Karlsruher Institut für Technologie

Institut für Theoretische Physik

On The Phenomenology Of Hadronization And Colour Reconnection

Zur Erlangung des akademischen Grades eines

DOKTORS DER NATURWISSENSCHAFTEN (DR. RER. NAT.)

von der KIT-Fakultät für Physik
des Karlsruher Instituts für Technologie (KIT)

genehmigte

DISSERTATION

von

M. Sc. Stefan Kiebacher

aus Bressanone/Brixen (Italien)

Referent:	PD Dr. Stefan Gieseke (ITP, KIT Karlsruhe)
Korreferentin:	Prof. Dr. Gudrun Heinrich (ITP, KIT Karlsruhe)
Berater:	Dr. Simon Plätzer (Institute for Physics, NAWI Graz)

Tag der mündlichen Prüfung: 07. February 2025

Eidesstattliche Versicherung gemäß § 13 Absatz 2 Ziffer 3 der Promotionsordnung des Karlsruher Instituts für Technologie (KIT) für die KIT-Fakultät für Physik:

1. Bei der eingereichten Dissertation zu dem Thema

   On The Phenomenology Of Hadronization And Colour Reconnection

   handelt es sich um meine eigenständig erbrachte Leistung.

2. Ich habe nur die angegebenen Quellen und Hilfsmittel benutzt und mich keiner unzulässigen Hilfe Dritter bedient. Insbesondere habe ich wörtlich oder sinngemäß aus anderen Werken übernommene Inhalte als solche kenntlich gemacht.

3. Die Arbeit oder Teile davon habe ich bislang nicht an einer Hochschule des In- oder Auslands als Bestandteil einer Prüfungs- oder Qualifikationsleistung vorgelegt.

4. Die Richtigkeit der vorstehenden Erklärungen bestätige ich.

5. Die Bedeutung der eidesstattlichen Versicherung und die strafrechtlichen Folgen einer unrichtigen oder unvollständigen eidesstattlichen Versicherung sind mir bekannt.

Ich versichere an Eides statt, dass ich nach bestem Wissen die reine Wahrheit erklärt und nichts verschwiegen habe.

Karlsruhe, den 18. Dezember 2024

. . . . . .

(Stefan Kiebacher)

”Colours are forces, radiant energies that affect us positively or negatively, whether we are aware of it or not.”

– *Johannes Itten* from ”The Art of Colour”

Abstract

The non-perturbative models for hadronization and colour reconnection of general purpose Monte Carlo event generators have been developed by theoretical motivation, but are ultimately phenomenological models with many free parameters. Although this allows for a good description of the measured data, the uncertainties associated with these models cannot be easily and reliably estimated. In addition, these models are very limited in their predictivity and can exhibit unphysical behaviour, especially in correlation observables. In this thesis we will show some of these shortcomings of the event generator `Herwig` with a particular focus on baryon production and provide an approach motivated by the colour evolution picture to resolve the encountered issues for the hadronization and colour reconnection models. We discuss the phenomenology of the developed models and study observables that are able to discriminate between different parts of the hadronization model. Additionally, we implement a new colour reconnection topology in order to boost the baryon production and support the measured near side suppression of baryon-baryon angular correlations. We show a colour reconnection algorithm to study its phenomenology and finally compute the momentum dependent dynamical transition probabilities calculated from soft gluon evolution. Finally, we urge the experimental community to measure many more correlation observables for different centre of mass energies and different collision systems in order to pin down the hadronization and colour reconnection models more reliably.

Zusammenfassung

Die nicht-störungstheoretischen Modelle für die Hadronisierung und Farbwiederverbindung von Mehrzweck-Monte-Carlo-Ereigniserzeugern sind entwickelt worden durch theoretische Motivation, sind aber letztendlich phänomenologische Modelle mit vielen freien Parametern. Obwohl dies eine gute Beschreibung von gemessenen Daten erlaubt, können die dazugehörigen Unsicherheiten nicht einfach und zuverlässig abgeschätzt werden. Zudem sind diese Modelle sehr beschränkt in deren Vorhersagbarkeit und können unphysikalisches Verhalten besonders in Korrelationsobservablen aufweisen. In dieser Doktorarbeit werden wir einige von diesen Unzulänglichkeiten von dem Ereigniserzeuger `Herwig` mit besonderem Fokus auf die Baryon-Produktion zeigen und einen Lösungsansatz motiviert durch das Farbevolutionsbild bereitstellen um die angetroffenen Probleme für die Hadronisierungs-und Farbwiederverbindungsmodelle zu beseitigen. Wir diskutieren die Phänomenologie der entwickelten Modelle und untersuchen Observablen, die in der Lage sind zwischen den verschiedenen Teilen des Hadronisierungsmodells zu unterscheiden. Zusätzlich implementieren wir eine neue Farbwiederverbindungstopologie um die Baryon-Produktion anzukurbeln und die gemessene Unterdrückung der diesseitigen Winkel-Korrelationen zu unterstützen. Wir zeigen einen Farbwiederverbindungsalgorithmus um die Phänomenologie zu untersuchen und berechnen letztendlich die impulsabhängigen dynamischen Übergangswahrscheinlichkeiten. Schließlich halten wir die Gemeinschaft der Experimentalteilchenphysik dazu an, viele weitere Korrelationsobservablen für verschiedene Massenschwerpunktsenergien und verschiedene Kollisionssysteme zu messen um die Hadronisierungs-und Farbwiederverbindungsmodelle zuverlässiger festlegen zu können.

Contents

CHAPTER 1

Introduction

The strong nuclear force - as the name suggests - is the strongest of the four fundamental forces of the Standard Model (SM) of particle physics. It is not only responsible for binding protons inside atomic nuclei against the Electro-Magnetic (EM) Coulomb repulsion, but also binds quarks inside hadrons at low energy scales. In fact, most of the mass of hadrons and thus atoms originates from the interactions of the fundamental quarks with the strong nuclear force. The fundamental description of the strong interaction is given by Quantum ChromoDynamics (QCD). This interaction allows due to its asymptotic freedom property for very precise perturbative calculations at high energy scales. However, at lower energy scales the strong interaction becomes Non-Perturbative (NP) and confines quarks and gluon into colourless hadrons.

In High Energy Particle (HEP) physics experiments only hadrons are observed in the detectors and not the underlying quarks and gluons. It is therefore essential to understand and especially also attempt to predict this transition from perturbatively calculable partons to NP observable hadrons. Since this so-called *hadronization* process is non-perturbative, computations become unfeasible for pragmatical simulations of QCD processes. Therefore usually phenomenological hadronization models such as the cluster or string model are used to describe this confinement process in general purpose event generators such as `Herwig` [1,2], `Pythia` [3] and `Sherpa` [4].

Such hadronization models - and more in general event generators - are used by experimentalists to estimate backgrounds, compute hadronization uncertainties and to test unfolding analysis and are therefore crucial for precision measurements and the search for new physics. In order to develop such simulations a detailed understanding of the underpinning theoretical physics is necessary to capture the multi-faceted features of a realistic high energy collision.

In particular, also so-called *Colour Reconnection* (CR), which attempts to rearrange the existing colour structure of partons via the exchange of soft gluons and tries to reconnect different QCD interactions of the same hadronic collision, is important and has become a substantial source of uncertainty e.g. for the top mass measurement [5]. In addition, for hadronic collisions it is still unclear how different partonic collisions of the same event interact with each other. For such cases, CR models try to restore their correlated colour structure from previously uncorrelated scatterings.

Both CR and hadronization models have been developed so far using theoretical motivation, but are ultimately phenomenologically descriptive models reliant on many free, a priori unknown so-called *tuning* parameters that are fitted or *tuned* to existing measured data. It is therefore difficult to truly extract hadronization uncertainties in a meaningful way as has been laid out in [6]. In particular, the long term goal would be to have sufficiently good control over the hadronization uncertainties such that e.g. jet sub-structure and correlation measurements could become more precise and reliable.

Reliable hadronization and CR models are also essential for studying heavy ion collisions to determine whether features of collectivity arise from thermal effects or pure microscopic QCD. In particular, the existence of a thermalized quark gluon plasma could be tested by comparing microscopic simulations without temperature with thermal simulations.

Therefore we attempt with this thesis to develop a hadronization and CR model that has more theoretical motivation from colour evolution [7] and is reliant on fewer tuning parameters. This thesis is structured as follows.

In **chapter** 2 we introduce the basic concepts of QCD, the infrared and collinear limits, the master formula for hadronic collisions and the basics of the colour flow basis, which will be needed later.

In **chapter** 3 we describe the typical structure of a general purpose event generator, where we describe especially in detail the event generator `Herwig` since we will be implementing changes in this model.

In **chapter** 4 we show some phenomenological studies of `Herwig` and in particular show some shortcomings in the description of correlation observables of baryons. We attempt a naive solution for the encountered problems, which is however not sufficient as it introduces other unphysical features.

In **chapter** 5 we present a new hadronization model based on the colour evolution picture and show that its phenomenology solves some of the encountered issues. We also introduce observables, which are able to discriminate between various parts of the hadronization model, which is crucial for pinning down the individual parts of the model.

In **chapter** 6 we develop a new CR topology and a corresponding phenomenological algorithm, that has not been yet available in `Herwig`, which boosts the formation of baryons and yields also some features reflected by measured correlation observables.

In **chapter** 7 we develop and implement a CR model, which is motivated by the soft gluon evolution picture [7, 8]. We discuss the approximations used and show its phenomenology for a two cluster system and the general algorithm. We supply multiple already existing CR algorithms of `Herwig` with the calculated probabilities and show their phenomenological differences.

We will be concluding with a more general outlook and show that our work has been a proof of concept that more predictive CR and hadronization models with fewer parameters are feasible and solve some unphysical behaviour.

CHAPTER 2

The Strong Interaction

In this chapter we introduce the fundamental Quantum Field Theoretical (QFT) description of the strong interaction, which is called Quantum ChromoDynamics (QCD) and discuss the confinement property. We briefly discuss the factorization property of QCD, which is the backbone of perturbative calculations for the proton proton collisions at the Large Hadron Collider (LHC). Furthermore, we discuss the colour flow basis and soft gluon evolution, which will be useful later for our work on colour reconnection.

2.1 Quantum Chromodynamics and Confinement

The fundamental constituents of hadrons are quarks bound together by the strong nuclear interaction mediated by gluons. This strong interaction is described in QFT by a non-abelian gauge theory of the gauge group $SU(N_c)$, where the number of "colours" N_c has been measured for example by the R-ratio [9] to be $N_c = 3$. Nonetheless, it is still instructive to keep N_c variable especially in the context of so-called large N_c theories [10] as approximations to real QCD with $N_c = 3$. Therefore, we will keep N_c variable in the equations[1] unless otherwise stated in this thesis. The QCD Lagrangian density for a $SU(N_c)$ theory is defined as the following according to [11,12], where we ignore the gauge fixing term and the Faddeev-Popov ghost term since those are not relevant for this thesis:

$$\mathcal{L}_{\text{QCD}} = -\frac{1}{2}\text{Tr}\left[F_{\mu\nu}F^{\mu\nu}\right] + \sum_{f\in\{\text{Flavours}\}} \bar{q}_f(i\not{D} - m_f)q_f, \tag{2.1}$$

with $\not{D} = D_\sigma\gamma^\sigma$ and m_f the quark current masses. Here $D_\mu = \partial_\mu - ig_sA_\mu$ is the covariant derivative and $F_{\mu\nu} = \frac{i}{g_s}[D_\mu, D_\nu] = \partial_\mu A_\nu - \partial_\nu A_\mu - ig_s[A_\mu, A_\nu]$ is the gluon field strength tensor with the corresponding gluon field A_μ and the strong coupling constant g_s describing the strength of the interaction. Note that in this notation $A_\mu = T^aA^a_\mu$, where T^a are the $(N_c^2 - 1)$ generators of the gauge group in the fundamental representation, which for QCD are $T^a = \lambda^a/2$, with the Gell-Mann matrices λ^a. Therefore, the commutator $[A_\mu, A_\nu] =$

[1] But of course for actual computations and plots we will set $N_c = 3$.

$A^a_\mu A^b_\nu i f^{abc} T^c$ can be further simplified using the structure constants f^{abc} of the gauge group defined as:

$$[T^a, T^b] = i f^{abc} T^c. \tag{2.2}$$

The quark Dirac fermions q_f are in the fundamental representation $\mathbf{N_c}$ of the gauge group leading to N_c coloured quarks, while the antiquark Dirac fermions $\bar{q}_f = q_f^\dagger \gamma^0$ are in the anti-fundamental representation $\overline{\mathbf{N}}_\mathbf{c}$ and carry anti-colour. The gluon fields A^a_μ are given in the adjoint representation $(\mathbf{N_c^2 - 1})$ in order to maintain local gauge invariance.

In the following we use the usual group normalization according to the following relations [13]:

$$\mathrm{Tr}(T^a T^b) = T_R \delta^{ab} = \frac{1}{2}\delta^{ab}, \tag{2.3}$$

$$\mathrm{Tr}(T^a_A T^b_A) = -f^{acd} f^{bdc} = C_A \delta^{ab} = N_c \delta^{ab}, \tag{2.4}$$

$$T^a T^a = C_F \mathbf{1} = \frac{N_c^2 - 1}{2N_c}\mathbf{1}, \tag{2.5}$$

where $(T^a_A)_{bc} = -i f^{abc}$ are the generators in the adjoint representation.

The order-by-order renormalization of QCD results in the so-called *running* of the strong coupling $\alpha_s(\mu) = g_s^2(\mu)/(4\pi)$ with the renormalization scale μ, where the change of the strong coupling follows the following Renormalization Group Equation (RGE), where N_f is the number of quark flavours [13, 14]:

$$\mu \frac{\mathrm{d}\alpha_s}{\mathrm{d}\mu} = \beta(\alpha_s), \tag{2.6}$$

$$\beta(\alpha_s) = -2\alpha_s \left[\left(\frac{\alpha_s}{4\pi}\right) \beta_0 + \left(\frac{\alpha_s}{4\pi}\right)^2 \beta_1 + \mathcal{O}\left(\frac{\alpha_s}{4\pi}\right)^3 \right], \tag{2.7}$$

$$\beta_0 = \frac{11}{3} C_A - \frac{4}{3} T_R N_f = \frac{11}{3} N_c - \frac{2}{3} N_f, \tag{2.8}$$

$$\beta_1 = \frac{34}{3} C_A^2 - T_R N_f \left(\frac{20}{3} C_A + 4 C_F \right) = \frac{1}{3}\left(34 N_c^2 - \frac{13 N_c^2 - 3}{N_c} N_f \right). \tag{2.9}$$

Here $\beta(\alpha_s)$ is the beta function of QCD, which can be calculated from the counter-terms of the renormalization procedure order-by-order and N_f is the number of active quark flavours at the relevant energy scale. The coefficients β_i are the $(i+1)$-loop order coefficients and are scheme independent for $i < 2$ and gauge covariant [14].

This RGE can be solved from a reference scale μ_0 to the scale of interest μ keeping only the leading order term in equation (2.6) to give the following [13]:

$$\alpha_s(\mu) = \frac{\alpha_s(\mu_0)}{1 + \frac{\beta_0}{2\pi}\alpha_s(\mu_0) \log\left(\frac{\mu}{\mu_0}\right)} = \frac{2\pi}{\beta_0} \frac{1}{\log\left(\frac{\mu}{\Lambda_{\mathrm{QCD}}}\right)}. \tag{2.10}$$

Note that in the last equivalence we have rewritten the equation by introducing the (lowest order) confinement scale $\Lambda_{\mathrm{QCD}} = \mu_0 \, e^{-\frac{2\pi}{\beta_0 \alpha_s(\mu_0)}}$ at which the coupling diverges since $\beta_0 > 0$ for QCD. For the Standard Model the running of α_s as a function of energy scale is displayed in figure 2.1 alongside with experimentally measured values. The leading coefficient $\beta_0 > 0$ in the Standard Model, which implies that QCD is asymptotically free i.e. at low enough scales the coupling has a Landau pole, invalidating the application of perturbative QCD methods at energy scales $\mu \lesssim \Lambda_{\mathrm{QCD}}$. This confinement scale is experimentally found to be $\Lambda_{\mathrm{QCD}} \sim 200$ MeV and sets the energy scale at which strongly charged particles confine into colourless hadrons.

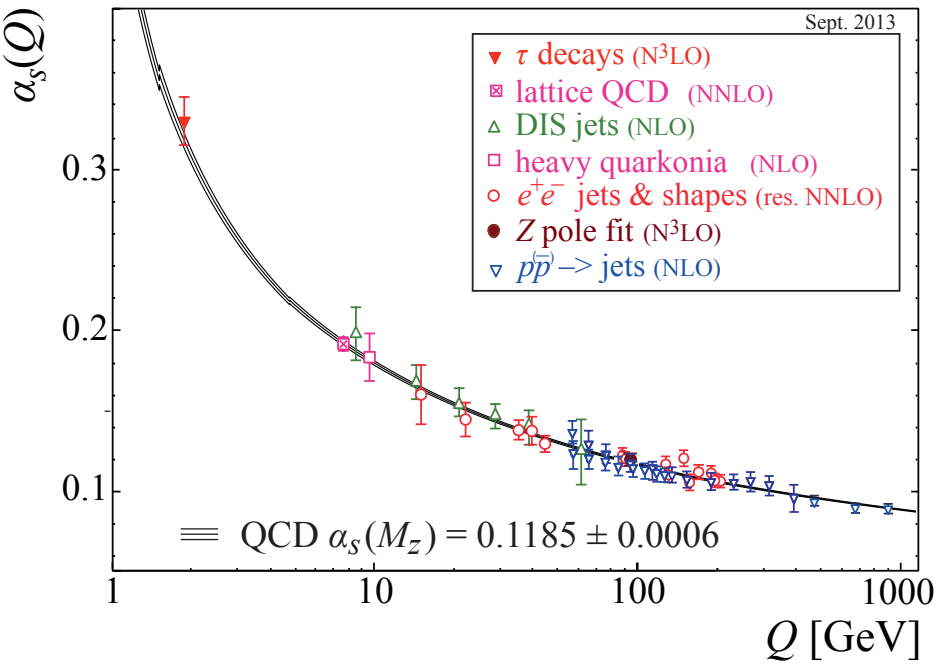

Figure 2.1: The predicted running of $\alpha_s(\mu = Q)$ at various energies (black lines) alongside with the different experimental measured values from [15].

Nonetheless, due to the asymptotic freedom of QCD it is possible to perform perturbative calculations of quark, antiquark and gluon, which are called *partons*, processes to very high accuracy at high energy scales $Q \gg \Lambda_{\text{QCD}}$, where the coupling is small. However, independently of how precise the perturbative calculation may be, what is measured in experiments are confined hadrons and not quarks and gluons. The transition from coloured partons to colourless hadrons is called *hadronization* and is a non-perturbative phenomenon, which is poorly understood and in practice relies on phenomenological models. Note that some aspects of non-perturbative QCD can be calculated using lattice QCD [16], but those are in practice often hard to transform into a pragmatic hadronization model.

2.2 Infrared and Collinear Limits of QCD

Processes in QCD[2] often involve *InfraRed* (IR) and *collinear* divergences, which can be attributed to an internal propagator going on-shell if partons become soft and/or collinear. These IR and collinear limits lead to the factorization of soft and collinear partons [11]. A manifestation of these divergences and the corresponding factorization can be seen in the process $e^+e^- \to q\bar{q}g$, whose cross section $\sigma_{q\bar{q}g}$ can be factorized into the cross section $\sigma_{q\bar{q}} = \sigma\left(e^+e^- \to q\bar{q}\right)$ in the IR and collinear limits, which is given by the following, showing only the divergent parts [11, 17]:

$$\frac{\mathrm{d}^2\sigma_{q\bar{q}g}}{\mathrm{d}\cos\theta \mathrm{d}z} = \sigma_{q\bar{q}} \times C_F \frac{\alpha_s(\mu)}{2\pi} \frac{2}{\sin^2\theta} \frac{(1-z)^2+1}{z} + \text{IR and collinear finite terms.} \quad (2.11)$$

Here θ is the angle between the quark q and the gluon g and $z = E_g/E_q$ is the energy fraction carried by the gluon. One can clearly see that for $\theta \to 0/\pi$ the expression diverges logarithmically, which exposes the collinear singularity. On the other hand if the gluon becomes soft in the limit $z \to 0$ the expression is IR divergent. Both of these divergences are related to the propagator of the internal (anti)quark line in the Feynman diagrams shown

[2]This feature is not exclusive to QCD, but also applies to any gauge theory with a massless vector boson.

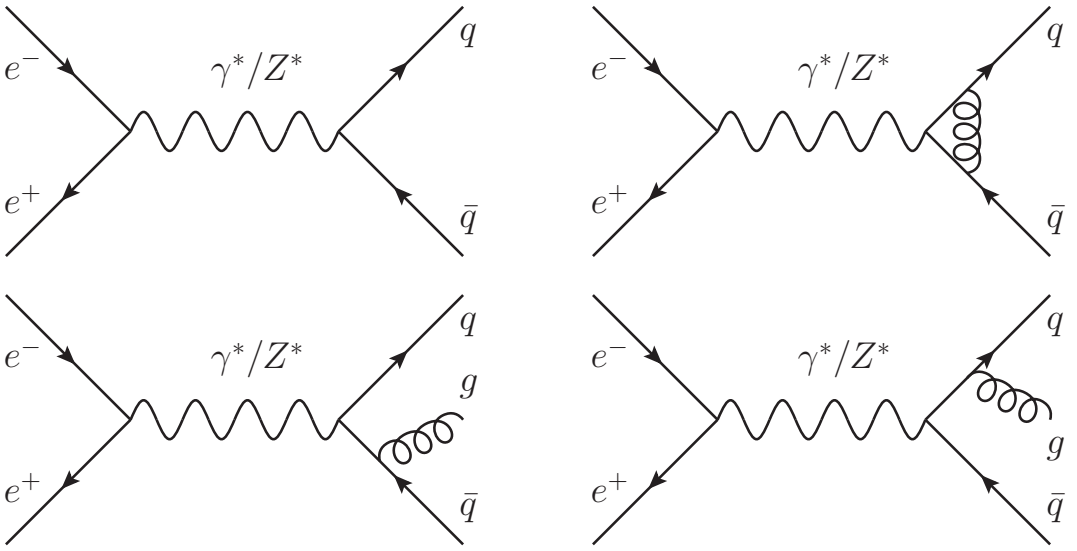

Figure 2.2: The contributing Feynman diagrams to the NLO fixed order cross section of $\sigma(e^+e^- \to q\bar{q})$. The top diagrams include just a $q\bar{q}$-pair in the final state, while the bottom diagram are the real emission diagrams, where an extra gluon is radiated off.

in figure 2.2 (bottom) going on-shell. In particular, assuming the gluon and the quarks to be massive with m_g and m_q respectively one can identify the IR divergence as the limit $m_g \to 0$, $m_q \neq 0$ and the collinear divergence as the limit $m_g = 0$, $m_q \to 0$ as shown in [18]. Note that m_g, $m_q \to 0$ corresponds to the IR and Collinear (IRC) limit.

When computing a fixed order NLO cross section $\sigma\left(e^+e^- \to q\bar{q}\right)$, all of the diagrams[3] in figure 2.2 are needed to give an IRC finite result, where the bottom *real* emission diagrams (after integration over the gluon momentum) cancel exactly the divergences of the top right *virtual* diagram, which is the manifestation of the KLN theorem [19, 20]. This admits the interpretation of this phenomenon as a built-in finite resolution criterion for the emitted gluon i.e. no detector can detect an infinitely soft and/or collinear gluon. Even though the IRC divergences cancel, the remaining real emission is still logarithmically enhanced if it is soft and/or collinear.

One should note that these logarithmic enhancements of the resulting real emission matrix elements are a generic feature of massless gauge theories, but the fact that the QCD coupling is quite large and that gluons interact with other gluons makes these enhancements much more significant than e.g. in QED. This feature of QCD leads to the notion of *jets*, which are sprays of collinear (and to some extent soft) particles originating from these logarithmically enhanced real emissions. These jets will be the motivation for introducing parton showers in the modelling of QCD interactions, which are able to *resum* these large logarithmic enhancements by recursively emitting partons in the correct soft and collinear pattern leading to a fully *exclusive* final state.

2.3 Infrared and Collinear Safety

As mentioned before the IR and collinear divergences have a huge impact on the phenomenology of high energy collisions. It is therefore useful to define observables which are relatively insensitive to these effects. Such observables $\mathcal{U}[\{p_i\}]$ for a set of final state particles $\{p_i\}$ are

[3] In principle also the self-energy corrections would be needed, but if one chooses dimensional regularization and works in the Landau gauge these corrections are zero as discussed in [18].

called IRC *safe* observables if they respect the IR safety condition and the collinear safety condition. For the IR safety condition to be satisfied, the observable must not change if a soft particle p_S - i.e. a particle with vanishing energy and momentum - is added to the set of particles [11]:

$$\mathcal{U}\left[\{p_i\} \cup p_S\right] \stackrel{!}{=} \mathcal{U}\left[\{p_i\}\right]. \tag{2.12}$$

For the collinear safety condition one requires that the observable does not change if each particle (but without loss of generality we can just exemplify it for one particle) $p_j \to \{\lambda p_j,\, (1-\lambda)p_j\}$ (for all $\lambda \in (0,\, 1)$) is replaced by two particles collinear to each other with the same total momentum such that the condition becomes [11]:

$$\mathcal{U}\left[\{p_i\}/\{p_j\} \cup \{\lambda p_j,\, (1-\lambda)p_j\}\right] \stackrel{!}{=} \mathcal{U}\left[\{p_i\}\right]. \tag{2.13}$$

If both of these properties are fulfilled[4] the observable is said to be IRC safe and can be computed to high accuracy analytically using resummation where only power corrections of order $\mathcal{O}\left(Q_0/Q\right)^p$ for $p \geq 1$ can be induced, where Q is the hard scale of the process and Q_0 is an IR cutoff [17].

2.4 Jet Algorithms

A jet algorithm is a useful tool for theoretical and experimental particle physics, which serves as a proxy for the inaccessible hard partons properties. We want to stress however that a parton and a jet are not identical e.g. the invariant mass of a jet is often far larger than the parton's on-shell mass. In principle a jet algorithm $\mathcal{J}$ is a mapping from a set of particle four-momenta $\{p_i\}$ to a set of (pseudo)jet four-momenta $\{j_i\}$, which can be represented by an appropriate algorithm $\mathcal{J}\left[\{p_i\}\right] = \{j_i\}$. Since it only depends on the set of momenta, it can be applied at parton level, hadron level or even at energy flow level. A good jet algorithm should be IRC safe, which means it has to satisfy the following in the same sense as we discussed in section 2.3:

$$\mathcal{J}\left[\{p_i\} \cup p_S\right] \stackrel{!}{=} \mathcal{J}\left[\{p_i\}\right], \tag{2.14}$$

$$\mathcal{J}\left[\{p_i\}/\{p_j\} \cup \{\lambda p_j,\, (1-\lambda)p_j\}\right] \stackrel{!}{=} \mathcal{J}\left[\{p_i\}\right]. \tag{2.15}$$

The IRC safety condition ensures that the IR and collinear divergences cancel properly. Here we will be discussing only sequential recombination algorithms, of which most obey the following algorithm, where we call all particles pseudojets in the following [21, 22]:

1. Each pseudojets is assigned a value $d_{i\mathrm{B}}$ associated to them and for each pair of pseudojets a distance measure d_{ij} is computed.
2. Find the minimum $d_{\min}$ of all $d_{i\mathrm{B}}$ and d_{ij}, i.e. $d_{\min} = \min\limits_{i,\,j}\{d_{i\mathrm{B}},\, d_{ij}\}$.
3. If $d_{\min} = d_{i^*\mathrm{B}}$ then the pseudojet i^* is removed from the set of pseudojets and moved to the set of finished jets if the algorithm is considering inclusive jets. In the case of considering only exclusive jets the pseudojet i^* is merged to the so-called beam jet (and discarded).
4. If $d_{\min} = d_{i^*j^*}$ then the pseudojet i^* and j^* are merged together to form a pseudojet k i.e. i^* and j^* are removed from the set of pseudojets and replaced by the merged pseudojet k. This is done according to a recombination scheme depending on the jet algorithm.

[4] In fact, for resummation a slightly stronger condition such as recursive IRC safety is necessary.

5. Repeat from step 1. until the set of pseudojets is empty or in the exclusive jets case if $d_{\min} > d_{\text{cut}}$ and only a number of finished jets remain. In the exclusive jets case, one can also require the algorithm to only stop after a given number of jets remain.

Now the difference between the jet algorithms remains in specifying $d_{i\text{B}}$, d_{ij}, d_{cut} and the recombination scheme. The recombination scheme is typically chosen to be the so-called E-scheme, which just merges the two pseudojets i and j by summing their four-momenta to obtain $p_k = p_i + p_j$. Another scheme that we will be using is the so-called *Winner-Takes-All* (WTA) $|\vec{p}|$ scheme [23, 24] of `FastJet` [21, 22], which assigns the merged pseudojet p_k the mass and direction of the pseudojet with $\max\{|\vec{p}_i|, |\vec{p}_j|\}$ and as a resulting $|\vec{p}_k| = |\vec{p}_i| + |\vec{p}_j|$. This ensures that the mass and direction is preserved exactly for the combination of a hard particle with a very soft one. There are also different schemes more important for pp collisions, but they are beyond of the scope of the necessary ingredients we will be needing later on. Regarding the distance measures d_{ij} and $d_{i\text{B}}$ there are several options that we list here for e^+e^- collisions:

- **JADE:** This algorithm has $d_{ij} = 2E_iE_j(1 - \cos\theta_{ij})$ and $d_{i\text{B}} > d_{ij}$ is irrelevant in this algorithm, which is valid only for exclusive jets [25]. The algorithm has a stopping criterion d_{cut} which has to be chosen.

- **Durham KT:** This algorithm has $d_{ij} = 2\min\{E_i^2, E_j^2\}(1 - \cos\theta_{ij})$ and $d_{i\text{B}} > d_{ij}$ is irrelevant in this algorithm, which is valid only for exclusive jets [26,27]. The algorithm has a stopping criterion d_{cut} which has to be chosen.

- **General KT:** This algorithm has $d_{ij} = \min\{E_i^{2p}, E_j^{2p}\}(1 - \cos\theta_{ij})/(1 + \cos R)$ and $d_{i\text{B}} = E_i^{2p}$, where R is the resolution parameter and p an arbitrary value. This algorithm works for inclusive and exclusive jets.

The above algorithms are sometimes called spherical algorithms since they use spherical coordinates θ_{ij}, while for their equivalent algorithms at pp collisions longitudinally (boost) invariant coordinates Δy_{ij} and $\Delta\phi_{ij}$ are used in the following manner with $\Delta R_{ij}^2 = \Delta y_{ij}^2 + \Delta\phi_{ij}^2$:

- **Longitudinally invariant KT:** This algorithm has $d_{ij} = \min\{p_{Ti}^2, p_{Tj}^2\}\Delta R_{ij}^2/R^2$ and $d_{i\text{B}} = p_{Ti}^2$ [27, 28]. The algorithm has the resolution parameter R, which controls the jet radius. This works for inclusive and exclusive jets, where in the latter case a d_{cut} has to be provided.

- **Anti-KT:** This algorithm has $d_{ij} = \min\{p_{Ti}^{-2}, p_{Tj}^{-2}\}\Delta R_{ij}^2/R^2$ and $d_{i\text{B}} = p_{Ti}^{-2}$ [29]. The algorithm has the resolution parameter R, which controls the jet radius.

- **Cambridge-Aachen:** This algorithm has $d_{ij} = \Delta R_{ij}^2/R^2$ and $d_{i\text{B}} = 1$ [30, 31]. The algorithm has the resolution parameter R, which controls the jet radius.

Note that the Durham k_T algorithm first clusters soft particles together, which is the reason why it is not used for pp collisions, where a lot of soft particles come from soft interactions. This problem is resolved by the anti-k_T algorithm, which first clusters the hard particles and forms circular shapes around them in the $y - \phi$ plane.

2.5 The Master Formula of High Energy Hadron Collisions

Hadronic inelastic cross sections $\sigma_{H_1H_2\to X}$ i.e. processes with hadrons H_1, H_2 in the initial state are in principle non-perturbative objects. Nonetheless at high enough energies due to collinear factorization of QCD these cross sections [32] - assuming a single hard process per

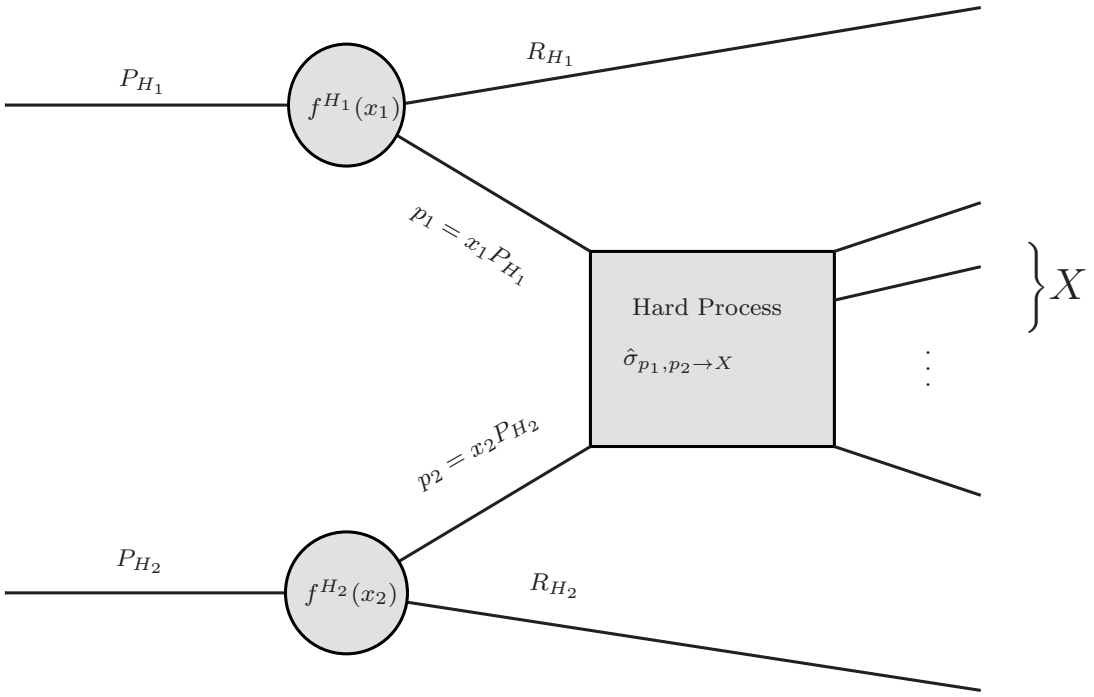

Figure 2.3: A schematic picture of the master formula (2.16). Note that the PDFs $f^{H_a}(x_i)$ and the hard partonic cross section $\hat{\sigma}_{p_1,p_2\to X}$ depend on the factorization scale μ_F and the in the latter case also on the renormalization scale μ_R.

hadron collision as sketched in figure 2.3 - can be computed perturbatively using the following master formula [11, 17]:

$$\sigma_{H_1H_2\to X} = \sum_{i,j} \int \mathrm{d}x_i \mathrm{d}x_j f_i^{H_1}(x_i,\, \mu_F) f_j^{H_2}(x_j,\, \mu_F) \hat{\sigma}_{p_i,p_j\to X} \left(\alpha_s(\mu_R),\, \frac{\mu_F}{\mu_R}\right) + \text{power corrections}, \tag{2.16}$$

$$\hat{\sigma}_{p_i,p_j\to X} = \frac{1}{2x_ix_j\ s} \int \mathrm{d}\Phi_X |\mathcal{M}_{p_i,p_j\to X}|^2. \tag{2.17}$$

Here the partonic cross section[5] $\hat{\sigma}_{p_i,p_j\to X}$ is convoluted with the so-called Parton Distribution Functions (PDFs) $f_i^{H_a}(x,\, \mu_F)$, which give the probability of extracting a parton i from hadron H_a with the momentum $p_i = x\, p_{H_a}$ at the factorization scale μ_F. Alongside the factorization scale, the cross section can also depend on a renormalization scale μ_R at which the UV divergences are subtracted, which in principle can be different from μ_F, but is mostly chosen to be equal to the factorization scale. Note that the power corrections that we omit in the master equation (2.16) stem from so-called higher *twist* terms, which are suppressed by inverse powers of the hard scale of the process Q, hence the name power corrections [33]. The sum over i, j runs over all possible partons pairs, which are contributing to the partonic cross section and Φ_X is the $|X|$-particle final state phase space.

While these cross sections can be computed to high accuracy, they are completely *inclusive* and give only the probability of measuring such a process, while being completely oblivious to the sub-structure of real events observed at e.g. the LHC. If we want to measure the property

[5] Note that here we use the ultra-relativistic approximation for the incoming flux in equation (2.17) as this is rarely unjustified

ξ of the final state X, we can do so by adding a measurement function $\mathcal{U}_\xi[X, \Phi_X]$ to the master formula (2.16) to obtain the following *differential* cross section:

$$\frac{\mathrm{d}\sigma_{H_1H_2\to X}}{\mathrm{d}\xi} = \sum_{i,j} \int \mathrm{d}x_i \mathrm{d}x_j f_i^{H_1} f_j^{H_2} \frac{1}{2\hat{s}} \int \mathrm{d}\Phi_X |\mathcal{M}_{p_i,p_j\to X}|^2 \mathcal{U}_\xi[X, \Phi_X]. \tag{2.18}$$

Typically the measurement function $\mathcal{U}_\xi[X, \Phi_X]$ is a complicated combination of delta functions and theta functions in order to represent projections and phase space cuts. The above observable can be computed in principle in Fixed Order (FO) calculations to an arbitrary[6] order k to give a N^{k}LO prediction which is accurate up to $\mathcal{O}(\alpha_s^{k+1})$ compared to the Leading Order (LO) and contains at most k real emissions. Note however that a general N^{k}LO process is a often a multi-scale process whose accuracy is often spoiled by the appearance of *large logs* $\log(\rho) \sim \alpha_s^{-1} \gg 1$ of scale ratios. In cases where these large logs are important for the measurement they need to be resummed to all orders and *matched* to the FO calculation to maintain a controlled result. So the task of N^{m}LL resummation is to sum all Leading large Logs (LL) of order m to *all* orders in α_s to include contributions of the form $\alpha_s^l \log^{l+1-m}(\rho)$ for all $l > m-1$, where ρ is a relevant ratio of scales [17].

Although for some processes and relatively simple measurement functions very precise FO perturbative QCD and resummation results exist, see e.g. this N^{3}LL+NNLO calculation for α_s determination [34] or this fiducial Drell-Yan ($pp \to l^-l^+$) cross section calculation at N^{4}LL$_p$+N^{3}LO [35], for more complicated $\mathcal{U}_\xi[X, \Phi_X]$ and especially also for not recursively IRC safe observables resummation is not possible. In these cases Monte Carlo event generators truly excel, due to their ability to completely *exclusively* simulate a hadronic collision with the full information about the final state.

2.6 The Colour Flow Basis

A crucial difference from QED to QCD is the non-abelian nature of $SU(N_c)$, which implies that gluons carry colour charge (in fact twice the charge compared to quarks for $N_c \to \infty$). This difference leads to a non-trivial colour structure for the strong interaction, which combined with the necessity for hadrons to form colourless states has a huge phenomenological impact on the overall structure of jets. It it therefore worth to examine the typical colour structures, which we will encounter in this thesis, e.g. a gluon exchange between a quark and an antiquark. We displayed the corresponding Feynman diagrams in figure 2.4 showing the colour structure, which can be conveniently written using the Fierz identity as the following:

$$T^a_{km} T^a_{ln} = \frac{1}{2}\left(\delta_{kl}\delta_{mn} - \frac{1}{N_c}\delta_{km}\delta_{ln}\right). \tag{2.19}$$

Note that the N_c suppressed term looks like a colour singlet gluon exchange, which is needed in order to satisfy the $SU(N_c)$ symmetry[7]. One can clearly see from equation (2.19) that the colour structure simplifies significantly in the limit $N_c \to \infty$, which is often also called the large N_c limit or the leading colour approximation [10]. However, one should also note that taking the large N_c limit implies the existence of infinite distinct colours without ever repeating, which of course is not true for QCD. Even though this approximation might seem completely unreasonable for QCD, at the observable level subleading colour terms will be of order $\mathcal{O}(N_c^{-2})$ according to [17]. Nonetheless, this approximation is still very crude and a systematic treatment for inclusion of some subleading N_c terms is sketched in [36].

[6] In practice this is very process dependent as well as computationally demanding.
[7] Without this contribution we would have a $U(N_c)$ gauge symmetry.

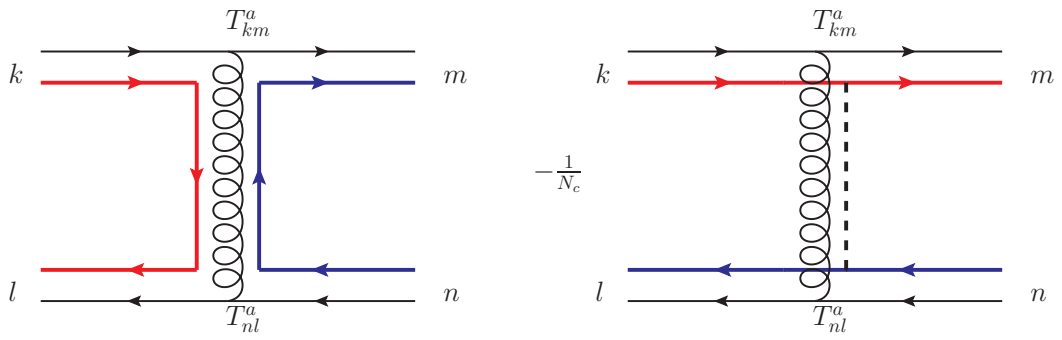

Figure 2.4: The Fierz identity pictorially with the N_c suppressed colour structure.

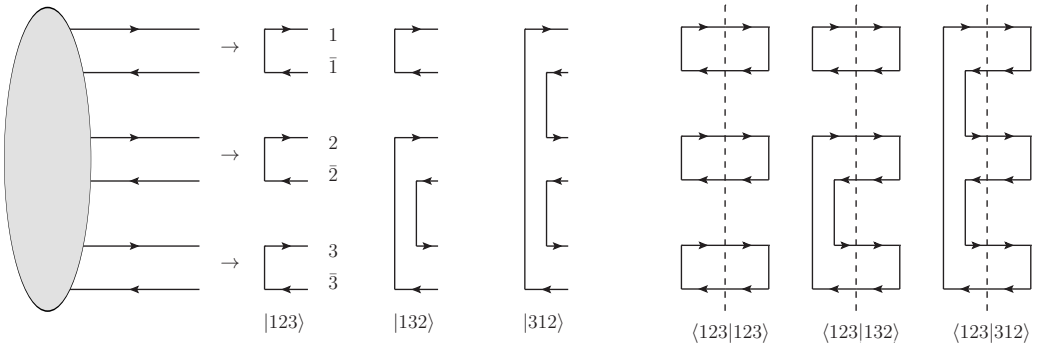

Figure 2.5: The exemplary 3 of the 3! colour flow states for 3 $q\bar{q}$ states.

For our further discussion it is very useful to introduce the so-called *colour flow* basis, which has been proven in [37] to be a very computationally efficient basis decomposition for evaluation of the colour structures of general amplitudes. From [37] a QCD matrix element $|\mathcal{M}\rangle$ can be decomposed into the following colour basis states, which we denote $|\rho\rangle$:

$$|\mathcal{M}\rangle = \sum_{\rho} \mathcal{M}_\rho |\rho\rangle. \tag{2.20}$$

Here the colour flow states $|\rho\rangle$ for $n = n_g + n_q = n_g + n_{\bar{q}}$ outgoing partons, i.e. n_g gluons and n_q quarks with $n_{\bar{q}}$ corresponding antiquarks, can be labeled by a permutation $\rho \in S(n)$ in the following manner:

$$|\rho\rangle = \left| \begin{smallmatrix} 1 & 2 & \cdots & n \\ \rho(1) & \rho(2) & \cdots & \rho(n) \end{smallmatrix} \right\rangle = |\rho(1)\ \rho(2)\ \ldots\ \rho(n)\rangle = \delta^{\alpha_1}_{\bar{\alpha}_{\rho(1)}} \delta^{\alpha_2}_{\bar{\alpha}_{\rho(2)}} \ldots \delta^{\alpha_n}_{\bar{\alpha}_{\rho(n)}}. \tag{2.21}$$

Note that here we assume that colour "flows" from the upper fundamental representation index α_i (colour) to the lower anti-fundamental index $\bar{\alpha}_i$ (anti-colour) for each leg. The indices $\alpha_i, \bar{\alpha}_i \in \{1, 2, \ldots, N_c\}$ represent the different colours and labels each leg as we display in figure 2.5, where gluons would carry a colour and anti-colour index. Note that any permutation is a valid colour flow state, which means that there are $n!$ different basis states for n colour flows. In fact, the colour flow basis is overcomplete and non-orthonormal, but nonetheless it is still very useful and about 60 times more efficient to compute than other bases as argued by [37]. Even though the basis is not orthogonal, the scalar products between two states take the following simple form:

$$\langle \rho|\tau\rangle = \delta^{\bar{\alpha}_{\rho(1)}}_{\alpha_1} \delta^{\bar{\alpha}_{\rho(2)}}_{\alpha_2} \ldots \delta^{\bar{\alpha}_{\rho(n)}}_{\alpha_n} \delta^{\alpha_1}_{\bar{\alpha}_{\tau(1)}} \delta^{\alpha_2}_{\bar{\alpha}_{\tau(2)}} \ldots \delta^{\alpha_n}_{\bar{\alpha}_{\tau(n)}} = N_c^{n-\#(\rho,\tau)}. \tag{2.22}$$

Here the function $\#(\rho, \tau)$ denotes the minimal amount of transpositions of state ρ to get to state τ or equivalently $(n - \#(\rho, \tau))$ is the number of loops if one contracts the two colour flow states pictorially [36, 38] as we display in figure 2.5.

In practice it is very useful to define a dual basis $|\rho]$, which forms an orthonormal basis with the colour flow states such that the following relations hold:

$$\langle\rho|\tau] = [\tau|\rho\rangle = \delta_{\rho\tau}, \tag{2.23}$$

$$\sum_{\alpha} |\alpha]\langle\alpha| = \mathbf{1}_{n!\times n!}. \tag{2.24}$$

Here in the first equation the $\delta_{\rho\tau}$ is only equal to 1 if both permutations ρ and τ are identical. The last equation defines the completeness relation in the $n! \times n!$ colour flow matrix space, which is useful to define projectors in the colour flow basis. Note that we will use this colour flow representation in chapter 7 extensively.

CHAPTER 3

Monte Carlo Simulations and Phenomenology of High Energy Collisions

The task of a Monte Carlo (MC) event generator is to simulate high energy particle collisions in order to generate fully exclusive events of such collisions. These event generators can be used by experimentalists to test their unfolding procedures of new measurements and give us also a theoretical prediction, which can be compared to the existing data. This allows also to feed-back potential disagreements with data in the context of a data-driven approach to further the theoretical development of MC event generators. There are three established general purpose event generators[8] available namely `Herwig` [1] (based on `ThePEG` [42, 43]), `Pythia` [3] and `Sherpa` [4]. Since the work in this thesis was done on `Herwig 7.3.0` [44], we will mostly describe the functioning of `Herwig` with only a few comments on the other codes.

The ultimate goal of a Monte Carlo (MC) simulation of High Energy Particle (HEP) collisions is to sample the probability density function $P(\mathcal{F}|\mathcal{I})$, where $\mathcal{I}$ is a given initial state - e.g. $\mathcal{I} = \{p, p\}$ colliding with $\sqrt{s} = 13$ TeV - and $\mathcal{F}$ is any fully differential final state. This goal is of course unachievable to perfection, but as we will see in this chapter several assumptions and approximations will allow us to approximately reach this goal for certain final states $\mathcal{F}$. The first assumption we already used in section 2.5 (or pictorially in figure 2.3) in the case of hadron-hadron collisions. There we assumed that through collinear factorization [32] we can factorize a high energy hadron-hadron collision into the convolution of a *hard partonic subprocess* with the universal process-independent non-perturbative Parton Distribution Functions (PDFs). Note that this factorization may also break for non-inclusive observables at higher orders as shown in [45], but for all further discussion we will assume that it holds.
The simulation of a hadron-hadron collision follows typically the following structure:

1. **Parton extraction using the PDFs:** The hard partons p_1, p_2 are extracted with momentum fraction $x_{1/2}$ from each hadron according to the PDFs[9] at a factorization scale μ_F. The hard partons are then evolved downwards using the DGLAP equation towards an IR cutoff at which the evolution stops [11].

[8] For heavy ion collisions there exists also `EPOS` [39] or only for pp collision `EPOS-LHC` [40], but these event generators are not general purpose. Another event generator `Whizard` [41] is also available, but relies on `Pythia` or `Herwig` for the parton shower and hadronization.
[9] Of course also the flavour of the partons is sampled if it contributes to the chosen hard process.

2. **Hard process generation:** Given the hard partons p_1, p_2 the final state of the chosen hard process is sampled according to its partonic cross section $\hat{\sigma}_{p_1,p_2\to\{q_i\}}$ at the drawn COM energy $\hat{s} = x_1 x_2 s$.

3. **Multiple Partonic Interactions (MPIs):** For hadron collisions a number of additional soft and semi-hard QCD interactions is drawn for the same event and their final state is sampled.

4. **Initial and final state shower:** All initial and final state hard partons[10] are showered until the parton shower cutoff. In particular, for the initial state shower the partons emitted during the DGLAP evolution are showered as well if they are at a high enough scale [11].

5. **Colour Reconnection (CR) and Hadronization:** After the parton shower all the partons are recombined into colourless clusters[11]. These clusters will have the chance to rearrange themselves during the CR according to the chosen CR model. Still heavy clusters are split into lighter clusters, which are decayed into hadrons.

6. **Hadron Decays:** Heavy or excited hadrons with small lifetimes will be further decayed to detector-level observable hadrons and particles.

We will discuss each of these steps in more detail in this chapter. Note however that for e.g. so-called *minimum bias* events, where we do not trigger on a hard process as will be discussed in section 3.7, the hard process stage is omitted since all processes are treated equal.

3.1 Hard Process

The goal of the hard process sampling is to sample the hard process from equation (2.18) with the observable function containing fiducial cuts, which are cuts that remove phase space regions, which are either inaccessible (or poorly predicted) by the detector or related to the physical necessity of resolving a final state [17]. We can either generate cross section weighted hard events $\mathcal{H}$ with weight $w_\mathcal{H}$ or generate unit weight hard events via unweighting weighted events through e.g. a rejection algorithm. Note here that if we are doing a NLO calculation with e.g. Catani-Seymour (CS) subtraction [46] the weight can be negative (in the unweighted case $w_\mathcal{H} = -1$). The latter is the preferred option for experimentalists unfolding their analyses through detector simulations such as `GEANT4` [47], which is computationally very expensive. In both cases the full integral over the hard final state with fiducial cuts are needed [17]. This integration is done by e.g. a sophisticated VEGAS algorithm or another integrator before running the event generation. There are several codes that have specialized on efficient generation of the corresponding Feynman diagrams and (tree and loop) matrix elements such as `Madgraph` [48] `OpenLoops` [49], `GoSam` [50], `NJet` [51], `VBFNLO` [52–54], `Whizard` [41] and many more. In `Herwig` the `Matchbox` module can be used with either internal matrix elements or with tree and one-loop matrix element providers to compute NLO cross sections.

At the end of this step we have generated a (weighted) hard event $\mathcal{H}$ with outgoing momenta alongside with a sampled flavour, helicity and colour flow state, which serves as an initial condition for the future event generation. This can be used as a FO prediction or - in most cases - is matched to the parton shower.

[10] Note that also leptons can develop a EM shower, but we will ignore this for brevity and especially since the initial state shower e.g. for LEP experiments is already subtracted by the measurements.

[11] Or strings in the case of `Pythia`.

3.2 Parton Showers

After the hard process has been generated, the parton shower dresses the partons with additional emissions. As we have seen in section 2.2 the cross section for an extra emission factorizes in the IR and collinear limit. This factorization can be generalized for any single final state emission according to [17] to the following, where we choose a generic evolution variable q:

$$\mathrm{d}\sigma(\mathcal{I} \to \{k_i\} + \text{emissions}) \simeq \sigma_0(\mathcal{I} \to \{k_i\}) \sum_{i \in \{k_i\}} \frac{\alpha_s}{2\pi} \frac{\mathrm{d}q^2}{q^2} \mathrm{d}z \; \mathrm{d}\phi P_{ji}(z, \phi), \tag{3.1}$$

$$P_{ji}(z) = \int_0^{2\pi} \frac{\mathrm{d}\phi}{2\pi} P_{ji}(z, \phi), \tag{3.2}$$

$$P_{qq}(z) = C_F \; \frac{1+z^2}{1-z}, \qquad P_{gg}(z) = C_A \; \frac{z^4+1+(1-z)^4}{z(1-z)}, \tag{3.3}$$

$$P_{gq}(z) = C_F \; \frac{1+(1-z)^2}{z}, \qquad P_{qg}(z) = T_R \; \left(z^2+(1-z)^2\right). \tag{3.4}$$

Here we defined the universal spin-averaged massless Altarelli-Parisi splitting functions $P_{ji}(z) = P_{i \to jk}(z)$ describing the branching of parton $i \to jk$, where the j parton carries momentum fraction z from the parent parton i and k is chosen such that the QCD vertex exists [55]. There exist also massive[12] [56] and spin-dependent [11] splitting functions.
Now the actual differential probability of a parton i to emit a parton j at evolution scale q can be written down as the following [17]:

$$q^2 \frac{\mathrm{d}\mathcal{P}}{\mathrm{d}q^2}(i \to jk) = \frac{\alpha_s}{2\pi} \int_{Q_{\mathrm{IR}}^2/q^2}^{1-Q_{\mathrm{IR}}^2/q^2} \mathrm{d}z \; P_{ji}(z). \tag{3.5}$$

Here Q_{IR} is the IR cutoff of the parton shower evolution, which acts as a definition for what a resolvable emission means. Furthermore we can write down the so-called *Sudakov equation* [17], where we define the Sudakov form factor $\Delta_i(Q^2, q^2)$ [57] for QCD:

$$q^2 \frac{\mathrm{d}\Delta_i}{\mathrm{d}q^2}(Q^2, q^2) = \Delta_i(Q^2, q^2) \; q^2 \frac{\mathrm{d}\mathcal{P}}{\mathrm{d}q^2}(i \to jk). \tag{3.6}$$

The Sudakov form factor $\Delta_i(Q^2, q^2)$ has a probabilistic interpretation, namely $\Delta_i(Q^2, q^2)$ is the probability for a parton i at evolution scale Q to not emit any additional partons k above q. The solution for the Sudakov form factor $\Delta_i(Q^2, q^2)$ can be written down as the following:

$$\Delta_i(Q^2, q^2) = \exp\left[-\int_{q^2}^{Q^2} \frac{\mathrm{d}t^2}{t^2} \frac{\alpha_s}{2\pi} \int_{Q_{\mathrm{IR}}^2/t^2}^{1-Q_{\mathrm{IR}}^2/t^2} \mathrm{d}z \; P_{ji}(z)\right]. \tag{3.7}$$

Assuming that α_s is constant, we get for the non-emission probability of a quark until the IR cutoff Q_{IR} the typical double logarithm structure originating from the soft and collinear divergences:

$$\Delta_q(Q^2, Q_{\mathrm{IR}}^2) \approx \exp\left[-C_F \frac{\alpha_s}{2\pi} \log^2 \frac{Q^2}{Q_{\mathrm{IR}}^2}\right]. \tag{3.8}$$

Note that here we assumed the scale separation is large i.e. $Q/Q_{\mathrm{IR}} \gg 1$. From the full Sudakov form factor in equation (3.7) one can sample the scale q at which a resolvable

[12] Which will depend on the evolution variable q.

emission is generated using the parton shower veto algorithm (see [17]). After that the z and ϕ can be sampled from the splitting functions of equation (3.3) to get the complete kinematics of the emission. Of course the assumptions we used in equation (3.8) give only a very crude estimate and in practice e.g. the running of α_s is taken into account using the so-called CMW scheme [58], which takes into account NLO corrections (for semi-inclusive deep inelastic scattering i.e. $e^- p \to e^- + X$ and Drell-Yan i.e. $pp \to e^+e^- + X$) by using a two-loop running α_s - i.e. keeping the $\beta_1 \neq 0$ in the equation (2.6)) - evaluated at a different scale discussed in [58].

There are many parton shower approaches and codes available such as the Angular Ordered (AO) shower of `Herwig` [59–61], the Dipole Shower (DS) of `Herwig` [62], the Catani Seymour (CS) and `Alaric` shower by `Sherpa` [63, 64], the `DIRE` and `Vincia` shower of `Pythia` [65, 66], the `PanScales` shower [67], the `CVolver` shower [68, 69] and the `Deductor` shower [70, 71]. The default shower of `Herwig` is the AO shower, which is based on colour coherence, which implies that all emissions must be ordered in angle, i.e. the largest angle emission is the first emission. In addition, the angular ordering exhibits the so-called *preconfinement* property [72] for $e^+e^- \to$ hadrons processes which will be the basis for the *cluster* hadronization model as we will discuss later. The DS of `Herwig` on the other hand is ordered in p_T and emits from the uniquely colour connected[13] dipoles like most of the above mentioned showers. Both of these showers contain spin-correlations [73] i.e. the full azimuthal dependence on ϕ for the splitting functions in equation (3.1).

We want to stress again that parton showers yield - in contrast to resummation approaches - fully differential final states and are useful beyond IRC safe observables. Furthermore some parton showers satisfy also some NLL accurate resummation properties, e.g. the AO shower of `Herwig` [59–61], the `PanScales` shower [67] and the `Alaric` shower [64] have been proven to give NLL accurate results for some observables according to the NLL criterion of [74].

It should be noted that most parton showers are only Leading Colour (LC) accurate[14] due to their assumption of independent evolution i.e. any emission, where a new different colour is drawn, never runs out of colours since the LC approximation implies never-repeating colours. Or in other words, the colour structure does not factorize (see appendix A of [46]) for more than 3 parton amplitudes. The `CVolver` shower [68, 69] and the `Deductor` shower [70, 71] projects are systematically expanding in $1/N_c$ to collect subleading N_c effects, while some approaches in the existing showers [75, 76] try to capture some of these effects.

3.3 PDFs and DGLAP Evolution

While we discussed the hard process and parton shower, we have not yet described how hard partons are extracted from the hadrons if we consider a hadron collision. In the master equation (2.16) we defined the PDFs $f_i^{H_1}(x_i, \mu_F)$, but we did not yet consider the initial state shower in this case. In fact, what happens for an initial state shower is that once the hard partons with $x_{1/2}$ are extracted at the factorization scale μ_F, the initial state shower needs to evolve the PDFs backwards towards lower scales $q' < \mu_F$ and harder partons $x'_{1/2} > x_{1/2}$. This can be achieved by the so-called DGLAP evolution equation, which essentially can be derived as a Renormalization Group Equation (RGE) generated by requiring the logarithmic

[13] The uniqueness is a consequence of the large N_c limit.

[14] Strictly speaking true LC would mean to use $C_F \approx N_c/2$ (compare equation (2.5)), but in practice this is never done due to the large impact.

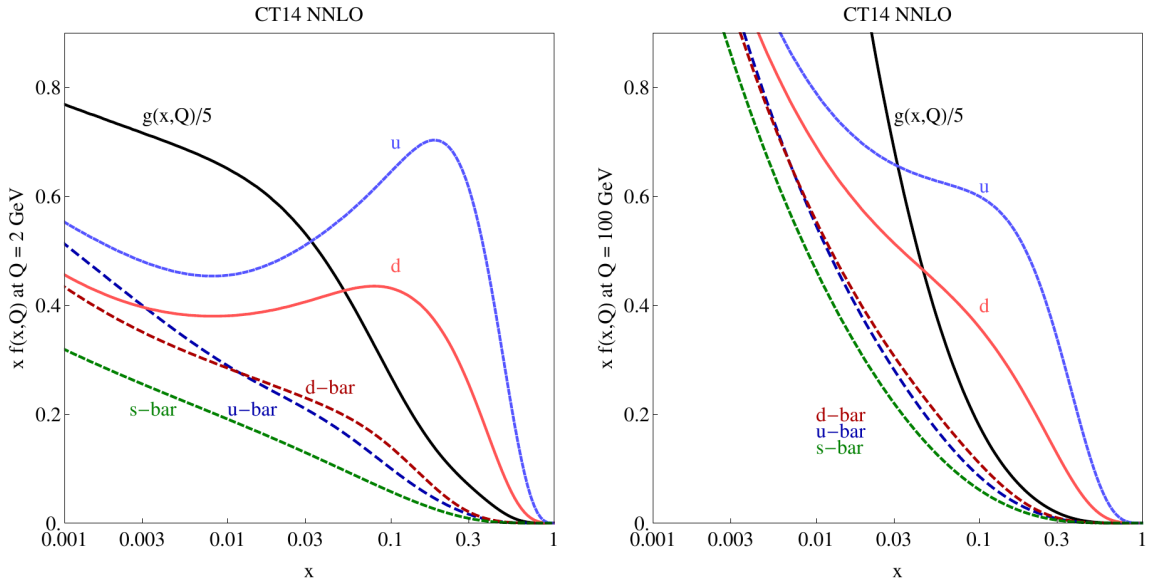

Figure 3.1: The NNLO PDF `CT14` set for $Q \in \{2\text{ GeV}, 100\text{ GeV}\}$ of [77].

derivative with respect to μ_F of equation (2.16) to be zero on both sides. This yields the following DGLAP equation - where we replaced $\mu_F \to Q$ - according to [11, 55]:

$$Q\frac{\mathrm{d}}{\mathrm{d}Q}\begin{pmatrix} f_{q_i}(x,\,Q) \\ f_g(x,\,Q)\end{pmatrix} = \frac{\alpha_s(Q)}{2\pi}\sum_j \int_x^1 \frac{\mathrm{d}z}{z}\begin{pmatrix} \tilde{P}_{q_iq_j}\left(\frac{x}{z}\right) & \tilde{P}_{q_ig}\left(\frac{x}{z}\right) \\ \tilde{P}_{gq_j}\left(\frac{x}{z}\right) & \tilde{P}_{gg}\left(\frac{x}{z}\right)\end{pmatrix}\begin{pmatrix} f_{q_j}(z,\,Q) \\ f_g(z,\,Q)\end{pmatrix}. \tag{3.9}$$

Note here that the index $q_{i,\,j}$ refers to both quarks and antiquarks. The splitting functions $\tilde{P}_{ji}$ here are almost the same as in equation (3.3) with the additional so-called *sum rules* built-in, which impose quark number conservation and momentum conservation for quarks and gluons [55]. To LO only $\tilde{P}_{q_jq_j}(z)$ and $\tilde{P}_{gg}(z)$ get an extra term proportional to $\delta(1-z)$ due to these sum rules. The DGLAP equation 3.9 can be solved similarly to the Sudakov equation and in a similar manner to the parton shower can be used to evolve the partons - in this case backwards - towards lower scales until some IR cutoff scale. The splitting functions $\tilde{P}_{ji}$ can be computed to higher orders and in particular for a full N^{k}LO cross section calculation it is necessary to match the order k of the splitting functions $\tilde{P}_{ji}$ to get a consistent result [17]. The additional emission produced during the DGLAP evolution, which are not connected to the hard process, will be showered according to the regular parton shower approach discussed before. This admits the classification of Initial State Radiation (ISR) coming from the IR and collinear limits of the incoming partons compared to the Final State Radiation (FSR) coming from the final state partons.

Since the PDFs are intrinsically non-perturbative objects which cannot be derived from first principle except by NP approaches such as lattice QCD [16], in practice they have to be fitted to data (typically Drell-Yan, DIS and di-jet processes). This is done by various PDF collaborations and the fitted PDFs set can be used by `Herwig` using the `LHAPDF6` [78] interface. The default PDF set for `Herwig` is `CT14` [77] from the CTEQ collaboration, which we display in figure 3.1 for the NNLO PDF set. In the case of very soft processes (and/or high energies) i.e. $x \ll 1$, the gluon PDF will grow very fast as can be seen in figure 3.1. In these cases of $x \lesssim 10^{-5} - 10^{-4}$ DGLAP evolution may not be appropriate any more and one would need to resum the large logs of $\log 1/x$, which can be done by so-called BFKL evolution in the context of Regge theory [79] such that the gluon PDF would be tamed in the low x

region [11]. However, since for our comparatively small COM of $\sqrt{s} \leq 14$ TeV this is mostly not the case and DGLAP evolution is sufficient.

3.4 Matching and Merging

Now we have generated the hard process and have a parton shower algorithm at our disposal, but we still need to combine the two properly. This combination algorithm is called *matching* a parton shower to a FO matrix element. It is worth mentioning that for a few well separated hard jets a FO prediction is sufficient, but problems arise when jets become collinear to each other or become soft. On the contrary the parton shower gives very good predictions for very collinear and or soft jets, while hard isolated jets are poorly modelled by a parton shower.

Furthermore, we want to stress that a (LO) FO calculation e.g. for $e^+e^- \to n$ partons is considered to be inclusive in the sense that we require the final state to consist of at least n partons dressed with additional soft and collinear radiation [17]. On the other hand the parton shower algorithm generates exclusive events i.e. the final state will emit exactly n_{em} partons additionally to the n partons of the (LO) FO matrix element.

Tree-level matching has been invented by [80] and essentially just corrects the first or hardest parton shower emission to the true real emission matrix element, which changes only the shape of differential distributions and leaves the normalization constant. For a NLO calculation, which has already one real emission, much more care is needed for matching it to a parton shower due to double counting and getting the correct normalization of the cross section. For NLO matching there are two approaches called MC@NLO [81,82] and POWHEG [83], which are both available matching strategies in the `Matchbox` module of `Herwig` .

Another difficulty is the simulation of multi-jet final states that are correct to their respective tree-level matrix element. This is resolved by so-called *multi-jet merging*, which recombines different multiplicity final state tree-level matrix elements at the cost of a merging scale μ_m, which is the resolution criterion determining whether an emission is generated by the parton shower or by the corresponding tree-level matrix element. Tree-level merging was invented in [84, 85] using the CKKW-L method and preserves the logarithmic accuracy of the parton shower. Furthermore, the `Matchbox` module [86] of `Herwig` offers also multi-jet NLO unitarized merging which is described in [87], which captures up to $(N-1)$ virtual contributions for N jet merging.

3.5 Hadronization Model

Hadronization is the transition process from parton to hadron level. This transition is non-perturbative and therefore not calculable from first principles using perturbative methods. While in lattice QCD correlation functions can be computed non-perturbatively [16,88] they are typically computed in imaginary time and not in a useful form for particle physics simulations. Therefore pragmatic phenomenological models for hadronization have been employed for MC event generators such as the Lund string model [89] used by `Pythia` and the cluster model [90] used by `Herwig` and `Sherpa`.

The Lund string model is based on the Cornell potential of QCD [91], which has the following form:

$$V_{\text{QCD}}(r) = -C_F \frac{\alpha_s}{r} + \kappa r. \tag{3.10}$$

Here $\kappa \approx 1$ GeV/fm is the so-called *string tension*, yielding a constant restoration force like a string at larger separations. In fact, lattice QCD computations of this potential [91]

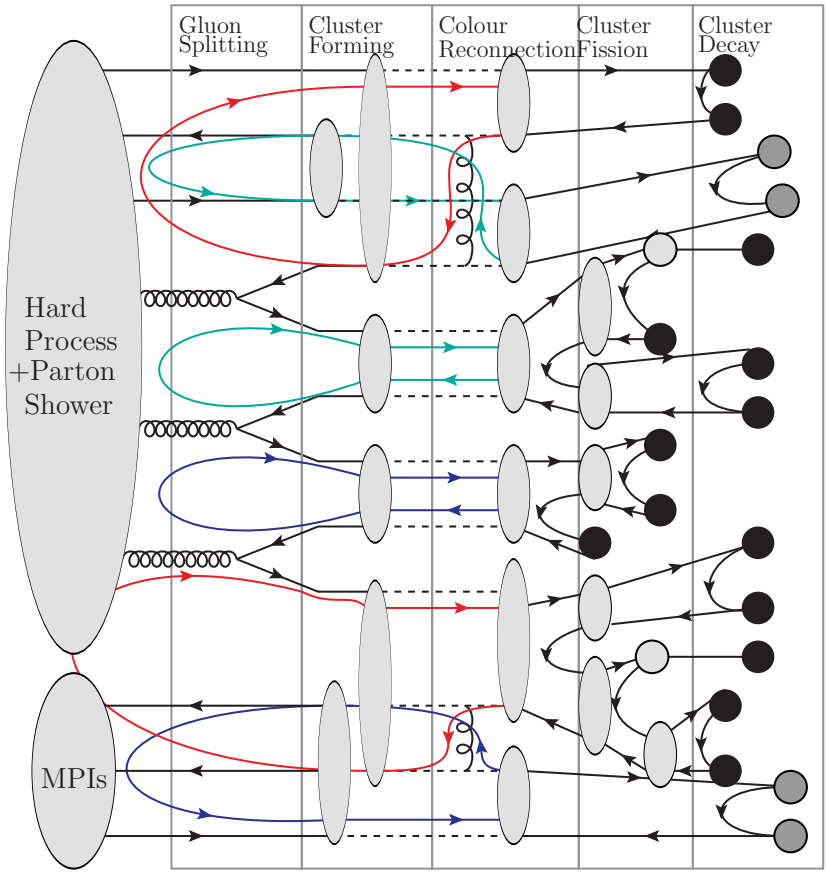

Figure 3.2: A sketch of the different stages of the cluster hadronization model of `Herwig`. Here the small light grey blobs are clusters, the black blobs are mesons and the dark grey blobs are baryons.

showed agreement. The actual string hadronization model starts by spanning a string from a quark[15] to its connected antiquark. If between the quark-antiquark endpoints real gluon emissions have occurred, e.g. from the parton shower, those gluons are interpreted as kinks on the string. These formed strings are then[16] fragmented using string fragmentation functions, which essentially start at the end point of a string and split hadrons off the string according to some kinematic prescriptions.

On the other hand we have the cluster model, which is based on the property of preconfinement [72], which states that if a $q\bar{q}$ singlet state has been produced at hard scale Q_H its perturbatively generated emissions form multiple colour singlets in leading colour and the mass distribution of these singlets is independent of the hard scale Q_H and peaks at around $Q_0 \sim 1$ GeV. The assumption that the hadronization mechanism is independent of the hard scale Q_H is called the *universality* of hadronization (see [92]), i.e. the hadronization should be independent of the hard processes and only be related to the parton shower cutoff. Note however that this is only true if the parton shower does emit partons. The `Herwig` cluster hadronization model is structured as:

1. **Reshuffling to constituent masses:** At the end of the parton shower the parton momenta are reshuffled to be on their respective constituent mass-shells. Note that gluons are

[15] Note that there can also exist so-called gluon loops if the gluons form a colour singlet.
[16] Before this step strings can colour reconnect.

given a non-perturbative constituent mass $m_g = 0.95$ GeV as well, which is dependent on the shower cutoff Q_{IR}.

2. **Non-perturbative gluon splitting:** The massive gluons are split non-perturbatively to a $q\bar{q}$ pair.

3. **Cluster formation:** Following the leading colour lines the clusters are formed by connecting the quark q through the colour line to the corresponding antiquark $\bar{q}$, where the momentum of the cluster is just the sum of the two constituents yielding the cluster $C(q\bar{q})$.

4. **Colour reconnection:** The clusters are allowed to rearrange themselves to a different singlet cluster set according to an algorithm, which we discuss in detail in section 3.9.

5. **Cluster fission:** Heavy clusters are split recursively to lighter clusters in order to avoid clusters decaying to high momentum hadrons.

6. **Cluster decay:** Last but not least all clusters are decayed to hadrons.

We display these steps pictorially in figure 3.2 and we will discuss the details of some of these stages more in detail in the next sections.

3.5.1 Non-Perturbative Gluon Splitting and Primordial Cluster Formation

After the parton shower has ended, we are left with n_q ($n_{\bar{q}}$) (anti)quarks and n_g gluons, which are on their current mass shells. As mentioned before these partons have to be reshuffled to their constituent masses, which for the light quarks u, d are $m_{u/d} = 0.325$ GeV$\simeq \Lambda_{\mathrm{QCD}}$. The non-perturbative constituent mass for the gluon m_g is in the default `Herwig` model a constant but tunable parameter correlated strongly with the parton shower cutoff.

Once all partons are on their constituent mass shell, the gluons are isotropically decayed to a $q\bar{q}$ pair, where the flavour of the quark is drawn using tunable weights $\mathbf{SplitPwt}(q)$ and only light quarks[17] (u, d or s) can be drawn. Note that there have been developments to allow for a dynamic gluon constituent mass distribution according to the integrated splitting function in [94]. Also anisotropic (biased towards the original gluon direction) decay of the quarks has been explored in [94], but these changes are not yet in the latest version of `Herwig`.

After the gluon splitting we are left with only (anti)quarks and potentially (anti)diquarks, which all have a colour connected partner in order to from a colour singlet. These preconfined pairings we call *primordial clusters* whose momentum is just the sum of the constituents. Note that we still keep track of the constituent momenta as they will give us a preferred direction since these clusters are composite objects. After these clusters are formed, they are given the chance to rearrange themselves during the so-called *colour reconnection* stage, which is discussed in more detail in 3.9. After colour reconnection we also have the chance of having generated a (anti)baryonic cluster with three (anti)quarks, but these clusters are subsequently reduced to a diquark-quark pair for easier handling.

3.5.2 Cluster Fission

After the colour reconnection we have a set of clusters $C(p_1, p_2)$ consisting of either a quark and antiquark or a (anti)quark and (anti)diquark, which are all on their respective constituent mass shells. The cluster fission model of `Herwig` 7.3.0 is described in [44] and fissions clusters recursively if their mass $M_C = \sqrt{(p_1 + p_2)^2}$ is above some probabilistic cutoff, but for this

[17] `Sherpa`'s cluster model allows for diquarks to be drawn at this stage [93], while in `Herwig` this is not allowed.

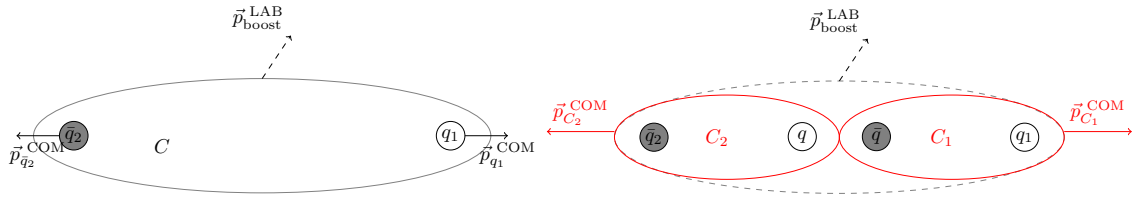

Figure 3.3: Sketch of current cluster fission model of `Herwig` with aligned splitting of the cluster.

thesis we will limit ourselves to the previous model of `Herwig` 7.2.X [95] with a static cutoff described in [2] as it facilitates the interpretation of our findings.

According to this model all clusters $C(q_1,\, \bar{q}_2)$ of mass M_C are forcibly and recursively fissioned if the following condition is satisfied:

$$M_C \geq \left[\mathbf{Cl_{max}}^{\mathbf{Cl_{pow}}} + (m_1 + m_2)^{\mathbf{Cl_{pow}}}\right]^{\frac{1}{\mathbf{Cl_{pow}}}} . \tag{3.11}$$

Here $m_{1/2}$ are the constituent masses of the q_1 and $\bar{q}_2$ respectively. Currently all clusters are fissioned into two clusters such as $C(q_1,\, \bar{q}_2) \to C_1(q_1,\, \bar{q}),\, C_2(q,\, \bar{q}_2)$, by drawing a $q\bar{q}$-pair from the vacuum, where the flavour is chosen according to some probability weight $\mathbf{Pwt}(q)$, where $q \in \{u,\, d,\, s\}$. The kinematics of the daughter clusters sketched in figure 3.3 are modelled according to the following algorithm based on the principle of Local Parton Hadron Duality (LPHD) first introduced in [96]:

1. Draw the daughter cluster masses $M_1,\ M_2$ from a power law distribution $(M_1 M_2)^{\mathbf{PSplit}-1}$.
2. Boost the cluster from the lab frame (LAB) into its rest frame (COM).
3. Compute the two-body decay for $C \to C_1,\, C_2$ to get the magnitude of the momentum. Set the direction of $C_1,\, C_2$ collinear to the original constituents $q_1,\, \bar{q}_2$.
4. Boost the cluster C_1 into its rest frame (COM1).
5. Compute the two-body decay for $C_1 \to q_1,\, \bar{q}$ to get the magnitude of the momentum. Set the direction of the constituents $q_1,\, \bar{q}$ of C_1 collinear to the original constituents q_1 and boost back from COM1 to COM.
6. Boost the cluster C_2 into its rest frame (COM2).
7. Compute the two-body decay for $C_2 \to q,\, \bar{q}_2$ to get the magnitude of the momentum. Set the direction of the constituents $q,\, \bar{q}_2$ of C_2 collinear to the original constituents $\bar{q}_2$ and boost back from COM2 to COM.
8. Boost all from COM to LAB.

Note that the phenomenological parameters $\mathbf{Cl_{max}}$, $\mathbf{Cl_{pow}}$ and $\mathbf{PSplit}$ are each a set of three parameters depending on whether the original cluster consists of only $\{u,\, d,\, s\}$ constituents or at least one c or b as constituents. In the case that one of the drawn cluster masses $M_i < M_{\mathrm{LHP}}(q_i,\, q)$, where $M_{\mathrm{LHP}}(q_i,\, q)$ is the summed mass of the lightest hadron pair to be produced from a cluster $C(q_i,\, q)$, a single hadron $h(q_i,\, q)$ is chosen instead i.e. the cluster undergoes the semi-hadronic process $C \to h(q_i,\, q),\, C'(q_j,\, \bar{q})$ with the fixed hadron mass $M_i = M_h$. If by doing so the drawn hadron mass violates the condition $M_{C'} + M_h < M_C$, the other daughter cluster is as well set to a chosen single hadron mass[18].

[18] If the condition is still violated, then the algorithm draws new masses and flavours.

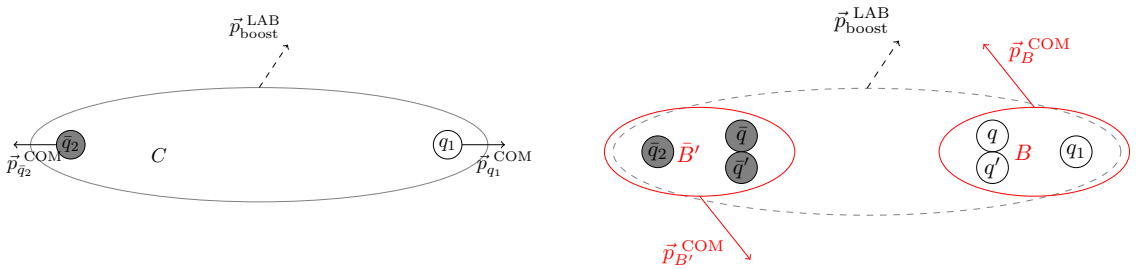

Figure 3.4: Sketch of current cluster decay model of `Herwig` for an exemplary decay of a mesonic cluster into a baryon-antibaryon pair.

In the special case of a beam cluster - i.e. a cluster consisting of a remnant (diquark) and its colour connected quark of a hadronic collision - the algorithm proceeds in the same way but the mass of the daughter cluster containing the remnant diquark is generated via the following:

$$M_{\mathrm{Beam}} = m_{\mathrm{diquark}} + m_q + \Delta M. \tag{3.12}$$

Here ΔM is a random variable sampled according to $\Delta M \sim \Delta M e^{-b\Delta M}$ with $b = 1$ GeV being a tunable parameter [2]. This will yield light - and therefore fast - remnant clusters, which go in the beam direction and thus do not contribute significantly to the central region, which is often of interest.

3.5.3 Cluster Decay

Now all clusters are light enough to be decayed into hadrons. Since we assume these clusters to be highly excited resonances, the decay kinematics are closely modelled according to resonance decay [90]. In `Herwig` all clusters that have a large mass ($M_C > M_{\mathrm{LHP}}(q_1, \bar{q}_2)$) are decayed to two hadrons $h_1(q_1, \bar{q})$, $h_2(q, \bar{q}_2)$. If the cluster is too light for such a decay the cluster reshuffles momentum with a neighbouring cluster in order to decay to a single hadron. For choosing the hadrons, one of the possible hadron combinations is drawn based on the Kupco model [97]. The total weight $w(h_1, h_2)$ for a hadron pair is given by the following:

$$w\left[h_1(q_1, \bar{q}), h_2(q, \bar{q}_2)\right] = \mathbf{Pwt}(q)\ w_{h_1} s_{h_1}\ w_{h_2} s_{h_2}\ p^*(M_C, m_{h_1}, m_{h_2}), \tag{3.13}$$

$$p^*(M_C, m_{h_1}, m_{h_2}) = \frac{\sqrt{\lambda(M_C^2, m_{h_1}^2, m_{h_2}^2)}}{2M_C}. \tag{3.14}$$

Here $\lambda(x^2, y^2, z^2) = (x^2-(y-z)^2)(x^2-(y+z)^2)$ is the Källén function, $\mathbf{Pwt}(q)$ is the weight for choosing a (di)quark-anti(di)quark pair $q\bar{q}$, $w_h = w_{\mathrm{mix,h}}(2J_h+1)$ is an individual hadron weight with the mixing weight for neutral mesons $w_{\mathrm{mix,h}}$ [2] and s_h are individual suppression factors to adjust meson multiplet and baryon singlet and/or decuplet production. Note that the $(2J_h+1)$ factor comes from the sum over final spin states.

Before drawing the hadron pair for a given a mesonic cluster it is decided with a probability[19] of $\dfrac{\mathbf{PwtDI}}{1+\mathbf{PwtDI}}$ if a diquark is draw i.e. if the cluster decays into a baryon-antibaryon pair as sketched in figure 3.4. After that the flavour weights $\mathbf{Pwt}(q)$ are defined as follows:

$$\mathbf{Pwt}(q) = \begin{cases} \mathbf{Pwt}_q & \text{for } q \text{ quark} \\ \left(1 - \dfrac{\delta_{s,0}}{2}\right) \mathbf{PwtDI} \times \mathbf{Pwt}_{q_1} \times \mathbf{Pwt}_{q_2} & \text{for } q = (q_1, q_2)_s \text{ diquark} \end{cases}. \tag{3.15}$$

[19] Of course only if this is kinematically possible.

Here $\mathbf{Pwt}_q$ are individual quark weights, **PwtDI** is a global diquark weight and the prefactor for diquarks comes from the different treatment of spin 0 or 1 diquarks. Then the hadron pair is drawn according to this probability:

$$P\left[h_i(q_1,\,\bar{q}),\,h_j(q,\,\bar{q}_2)|C(q_1,\,\bar{q}_2)\right] = \frac{w\left[h_i(q_1,\,\bar{q}),\,h_j(q,\,\bar{q}_2)\right]}{\sum_{n,\,m,\,q'} w\left[h_n(q_1,\,\bar{q}'),\,h_m(q',\,\bar{q}_2)\right]}. \tag{3.16}$$

Note that the sum over q' runs either over all light[20] quarks or light diquarks[21]. The sum over n, m runs over all possible hadrons, where there can be multiple hadrons per fixed q'.

After a hadron pair has been chosen we need to sample the direction of the two-body decay. For clusters whose constituents have been produced during the NP gluon splitting or cluster fission stage an isotropic direction in 3D space is sampled. If the cluster originates from the hard process or the parton shower the decay angle $\cos\theta^{\mathrm{COM}}_{\mathrm{smear}}$ is smeared with respect to the original direction of the constituents in the COM frame according to the following distribution:

$$f(\cos\theta^{\mathrm{COM}}_{\mathrm{smear}}) = \mathbf{ClSmr} \times \exp\left(\frac{\cos\theta^{\mathrm{COM}}_{\mathrm{smear}} - 1}{\mathbf{ClSmr}}\right), \tag{3.17}$$

$$\cos\theta^{\mathrm{COM}}_{\mathrm{smear}} = 1 + \mathbf{ClSmr} \times \log\xi. \tag{3.18}$$

Here $\xi \sim U_{[0,\,1]}$ is uniformly distributed in [0, 1]. The azimuthal angle for the cluster decay is in all cases drawn isotropically. After this stage all clusters have been transitioned into hadrons and the hadronization is completed.

3.6 Hadronic Decays

Even though we are now left with only hadrons, some of these hadrons are highly excited and therefore have very short lifetimes. These hadrons need to be decayed further into so-called *detector-stable* particles with lifetimes larger than $\mathcal{O}(30$ ps) [17]. This is done in `Herwig` via the hadronic decay models of [98], which also decay other unstable particles such as the τ lepton. The precise lifetime cut can be imposed in `Herwig`, which is necessary for comparing simulation and data unfolded to the proper lifetime cuts.

Various different hadronic matrix elements are contained in the decay model of `Herwig` to decay excited hadrons with complete spin correlations [99–102]. In `Herwig` 7.3.0 a Heavy Quark Effective field Theory (HQET) decayer [103] is also implemented to decay heavy quark containing hadrons.

Even though `Herwig` has its own decay model for some c, b containing mesons, many experiments prefer to use `EvtGen` [104], which is the reason why it is the default for `Herwig` even though it is based on the `Pythia` string model. In `Herwig` 7.3.0 a new Particle Data Group (PDG) [105] update on all masses, widths and decay channels has been done.

3.7 Minimum Bias and Diffraction

In this section we want to briefly discuss the concept of so-called *Minimum Bias* (MB) measurements. As the name suggests these MB measurements consist in triggering with as little bias as possible, i.e. essentially every inelastic pp collision is recorded [17]. Typically such events are selected by very inclusive cuts e.g. at least 1 charged particle $N_{\mathrm{ch}} \geq 1$ with $p_T > 100$ MeV. MB analyses measure often very inclusive quantities such as charged multiplicity N_{ch},

[20] No quark heavier than the s quark.

[21] Only the lowest possible spin state for the diquarks is allowed.

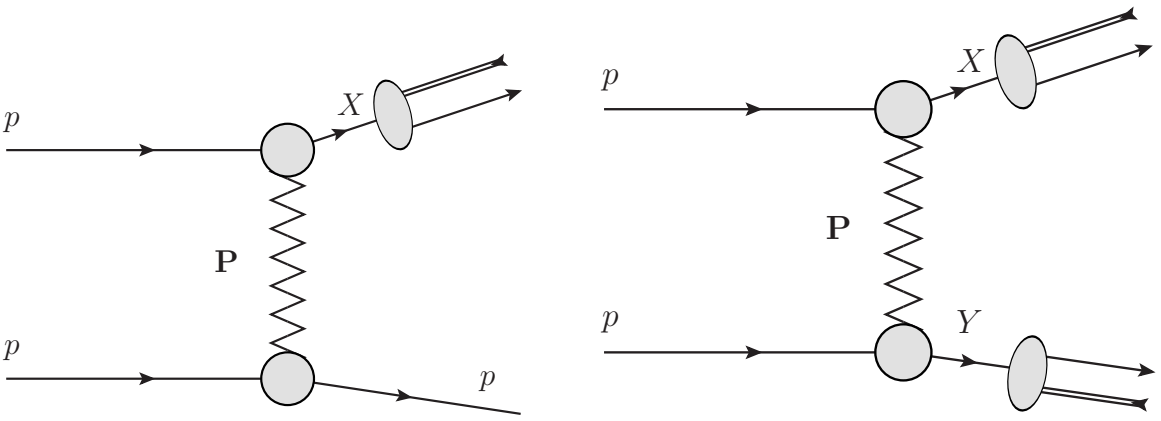

Figure 3.5: Sketch of the diffraction model of `Herwig` for a pp collision. We display single diffraction on the left and double diffraction on the right side. Note that double lines represent diquarks.

(pseudo)rapidity $y(\eta)$, transverse momentum p_T distributions (sometimes also for identified particles) and are useful for comparing the data to the soft QCD models of MPIs and Colour Reconnection (CR). Even though in most non MB measurements MPIs and CR are considered background and are attempted to be removed by imposing stringent cuts, these features of soft QCD still contribute to the final state. This contamination of soft (or semi-hard) QCD effects, which is not connected to the hard process of interest is called *Underlying Event* (UE). For jet measurements, e.g. there is the so-called jet pedestal effect that states that a hard jet in a high energy pp collision "sits" on top of a pedestal of UE activity [17]. Since jets are therefore contaminated with soft QCD effects it is important to model these aspects well. Therefore MB measurements are useful to test these models and in fact the free parameters of these models are tuned to such measurements. However, since in MB measurements so-called *diffraction* plays a big role (see e.g. the so-called "bump" problem [106, 107]), we will discuss what exactly is diffraction and how it is modelled in the following.

Diffractive events can be classified into three categories, namely Single-Diffractive (SD), Double-Diffractive (DD) and Central Exclusive Production (CEP). All of these are mediated by the $t-$channel exchange of the so-called *pomeron* $\mathbf{P}$, which is a pseudo particle with the quantum numbers of the vacuum and dominates the cross section in the large COM energy limit $s \gg |t|$ according to the Pomeranchuk theorem [108]. SD events are $pp \to pX$ collision events where one of the protons remains intact and transfers momentum to the other proton which becomes a highly excited state of mass M_X and dissociates resulting in particle production. Similarly, DD events are $pp \to X, Y$, where both protons become highly excited states of mass M_X and M_Y respectively. CEP production on the other hand is a $pp \to pXp$ event where both protons survive, but a highly excited state X of mass M_X is produced in the central region of the detector. All diffractive events lead to a so-called *large rapidity gap* $\Delta\eta_{\mathrm{LG}}$ i.e. the largest rapidity region in which no particles are detected. This signature comes firstly from the t-channel like pomeron exchange and from the fact that since the pomeron is a colour singlet, i.e. no colour exchange happens and therefore no colour connection is spanned between the final states. Therefore, diffractive events - with the exception of CEP - can be cut away relatively easily by a maximum rapidity cut.

Both SD and DD are modelled in `Herwig` by the following differential cross section in the approximation of large energy and small momentum transfer $s \gg M_{X,Y}^2 \gg |t|$ [107, 109, 110]

$$\frac{\mathrm{d}^2\sigma_{\mathrm{SD}}}{\mathrm{d}M_X^2\mathrm{d}t} \propto \left(\frac{s}{M_X^2}\right)^{\alpha_{\mathbf{P}}(0)} \exp\left[t\left(B_0 + 2\alpha' \log\frac{s}{M_X^2}\right)\right], \tag{3.19}$$

$$\frac{\mathrm{d}^3\sigma_{\mathrm{DD}}}{\mathrm{d}M_X^2\mathrm{d}M_Y^2\mathrm{d}t} \propto \left(\frac{s}{M_X^2}\right)^{\alpha_{\mathbf{P}}(0)} \left(\frac{s_0}{M_Y^2}\right)^{\alpha_{\mathbf{P}}(0)} \exp\left[t\left(b + 2\alpha' \log\frac{ss_0}{M_X^2 M_Y^2}\right)\right]. \tag{3.20}$$

Here $\alpha_{\mathbf{P}}(0)$ is the pomeron intercept, α' is the pomeron slope parameter, $B_0 \approx 10.1\ \mathrm{GeV}^{-2}$ is the proton-pomeron slope, $b = 0.1$ is a constant shift and s_0 is fixed according to the total normalization of the diffractive cross section. The pomeron intercept $\alpha_{\mathbf{P}}(0)$ and the slope parameter α' are connected to the pomeron's Regge trajectory $\alpha_{\mathbf{P}}(t) = \alpha_{\mathbf{P}}(0) + \alpha' t$. Note that the absolute and relative normalizations for the aforementioned cross sections are not fixed and are set approximately to the measured values of the ALICE experiment [111]. It is assumed that around $20-25\ \%$ of the total MB event rate are diffractive events. In practice in `Herwig` for sampling a SD or DD event the M_X, M_Y and t are sampled according to equations (3.19) or (3.20) and then the excited states are modelled as a cluster whose constituents are collinear to the direction of the excited state as displayed in figure 3.5. This cluster is handed over to the hadronization model and will in general fission to lighter clusters before decaying to hadrons.

3.8 Multiple Partonic Interactions

The total pp cross section $\sigma_{pp}^{\mathrm{tot}}$ in the limit $s \to \infty$ has been found to have the following form according to Regge theory, which is called the DL parameterization [112–115]:

$$\sigma_{pp}^{\mathrm{tot}} \approx (s) = \sigma_{\mathbf{P}}^{pp}\left(\frac{s}{\mathrm{GeV}^2}\right)^{\epsilon} + \sigma_{\mathbf{R}}^{pp}\left(\frac{s}{\mathrm{GeV}^2}\right)^{\eta}. \tag{3.21}$$

Here $\sigma_{\mathbf{P}}^{pp} = 21.7$ mb, $\sigma_{\mathbf{R}}^{pp} = 56.08$ mb, $\epsilon = 0.0808$ and $\eta = -0.4525$ are parameters fitted to experimental data [115]. Note that the first term in equation (3.21) is related to the pomeron intercept via $\epsilon \lesssim \alpha_{\mathbf{P}}(0) - 1$. The Pomeranchuk theorem states that the pomeron has the quantum numbers of the vacuum and dominates the cross section for large energies and therefore it cannot distinguish p and $\bar{p}$ i.e. $\sigma_{\mathbf{P}}^{pp} = \sigma_{\mathbf{P}}^{p\bar{p}} = \sigma_{\mathbf{P}}^{\bar{p}\bar{p}}$ [108]. The second term in (3.21) is related to the subleading *reggeon* $\mathbf{R}$, which does not have this property and will have different values for $\sigma_{\mathbf{R}}^{pp}$, $\sigma_{\mathbf{R}}^{p\bar{p}}$ and $\sigma_{\mathbf{R}}^{\bar{p}\bar{p}}$. Note that the DL parameterization and the fitted value did not require any perturbative QCD expansion and is only reliant on the analytic properties of the $\mathbf{S}$ matrix in the context of Regge theory.

We can now compare the experimental result $\sigma_{pp}^{\mathrm{tot}}(s)$ with the dominant perturbative QCD cross section of di-jet production $\sigma_{pp\to 2j}(p_{T,\min})$ with a lower cutoff $p_{T,\min}$ on the p_T of the jet to regulate the IR divergence. It is found that already for $p_{T,\min} \lesssim 2$ GeV for $\sqrt{s} = 1$ TeV unitarity is violated since $\sigma_{pp\to 2j}(p_{T,\min}) > \sigma_{pp}^{\mathrm{tot}}$ [116, 117]. This can be resolved by assuming that in one pp collision Multiple Partonic Interactions (MPIs) happen. These MPIs can be parametrized by the average number of partonic collisions per pp collision $\langle N_{\mathrm{col}}(p_{T,\min})\rangle$ in the following manner:

$$\langle N_{\mathrm{col}}(p_{T,\min})\rangle = \frac{\sigma_{pp\to 2j}(p_{T,\min})}{\sigma_{pp}^{\mathrm{inel}}(p_{T,\min})}. \tag{3.22}$$

Note that $\sigma_{pp}^{\mathrm{inel}}(p_{T,\min}) < \sigma_{pp}^{\mathrm{tot}}$ is the total inelastic hadronic cross section with a cut $p_T > p_{T,\min}$. This unitarizes the perturbative QCD (pQCD) cross section, where all MPIs are assumed to be sampled from the di-jet cross section $\sigma_{pp\to 2j}(p_{T,\min})$. Note that the actual

kinematics and in particular also the colour structure of the MPIs depend on the implementation details of the specific MPI model.

In `Herwig` a more sophisticated two component so-called *eikonal* model[22] is used for the MPI modelling [117]. Such eikonal models are based on the fact that the elastic amplitude $\mathcal{A}_{\text{el}}(s,\, t)$ can be written as the following Fourier transformation from impact parameter space $\mathbf{b}_\perp$ in the high energy limit [114, 118]:

$$\mathcal{A}_{\text{el}}(s,\, \mathbf{q}_\perp) = 4s \int \mathrm{d}^2\mathbf{b}_\perp a_{\text{el}}(s,\, \mathbf{b}_\perp) e^{i\mathbf{q}_\perp \cdot \mathbf{b}_\perp}, \tag{3.23}$$

$$a_{\text{el}}(s,\, \mathbf{b}_\perp) = \frac{1}{2i}\left[e^{-\frac{1}{2}\chi(s,\, \mathbf{b}_\perp)} - 1\right]. \tag{3.24}$$

Note that here we assumed implicitly the Regge limit of $s \gg |t|$ in the sense that $t \approx -\mathbf{q}_\perp^2$, where $\mathbf{q}_\perp$ is the transverse momentum of the momentum transfer $q = p_1 - p_3$. Here $\chi(s,\, \mathbf{b}_\perp)$ is the so-called *eikonal* function or opacity and ensures that the total cross section is unitary through the optical theorem [12, 114, 118] as can be seen by the following relations:

$$\sigma_{pp}^{\text{el}} = 4 \int \mathrm{d}^2\mathbf{b}_\perp |a_{\text{el}}(s,\, \mathbf{b}_\perp)|^2 = \int \mathrm{d}^2\mathbf{b}_\perp \left|1 - e^{-\frac{1}{2}\chi(s,\, \mathbf{b}_\perp)}\right|^2, \tag{3.25}$$

$$\sigma_{pp}^{\text{tot}} = \frac{1}{s}\Im\left\{\mathcal{A}_{\text{el}}(s,\, t=0)\right\} = 2 \int \mathrm{d}^2\mathbf{b}_\perp \left[1 - e^{-\frac{1}{2}\chi(s,\, \mathbf{b}_\perp)}\right], \tag{3.26}$$

$$\sigma_{pp}^{\text{ine}} = \sigma_{\text{tot}} - \sigma_{\text{el}} = \int \mathrm{d}^2\mathbf{b}_\perp \left[1 - e^{-\chi(s,\, \mathbf{b}_\perp)}\right]. \tag{3.27}$$

Here we defined the elastic σ_{pp}^{el}, the inelastic σ_{pp}^{ine} and the total cross section σ_{pp}^{tot}. In `Herwig` this eikonal function $\chi(s,\, \mathbf{b}_\perp) = \chi_{\text{soft}}(s,\, \mathbf{b}_\perp) + \chi_{\text{hard}}(s,\, \mathbf{b}_\perp)$ consists of a soft component $\chi_{\text{soft}}(s,\, \mathbf{b}_\perp)$ and a hard component $\chi_{\text{hard}}(s,\, \mathbf{b}_\perp)$. For both of these components the impact parameter dependent PDFs $F_i(x_i,\, Q,\, \mathbf{b}_\perp)$ are assumed to factorize into $F_i(x_i,\, Q,\, \mathbf{b}_\perp) = f_i(x_i,\, Q) \times G(\mathbf{b}_\perp)$, which allows the definition of a matter overlap function $A(b_\perp)$ in the following way:

$$A(b = |\mathbf{b}_\perp|) = \int \mathrm{d}^2\mathbf{b'}_\perp G\left(|\mathbf{b'}_\perp|\right) G\left(|\mathbf{b}_\perp - \mathbf{b'}_\perp|\right). \tag{3.28}$$

Now we need to make a choice for $G(\mathbf{b}_\perp)$ for which we choose the electromagnetic form factor according to [118–120] given as:

$$G(\mathbf{b}_\perp) = \int \frac{\mathrm{d}^2\mathbf{k}_\perp}{(2\pi)^2} \frac{e^{i\mathbf{b}_\perp \cdot \mathbf{k}_\perp}}{(1 + \mathbf{k}_\perp^2/\mu^2)^2}. \tag{3.29}$$

Here μ is the inverse effective radius of the proton, which in this model is a free parameter that needs to be tuned. The overlap function for a pp collision can therefore be computed analytically to be the following [118–120]:

$$A(b,\, \mu) = \frac{\mu^2}{96\pi}(\mu b)^3 K_3(\mu b). \tag{3.30}$$

Here $K_\nu(z)$ is the ν-th order modified Bessel function of the second kind. Note that $A(b,\, \mu)$ is properly normalized to unity. Now the soft and hard components of the MPI model can be expressed in the following form:

$$\chi_{\text{soft}}(s,\, b) = A(b,\, \mu_{\text{soft}})\ \sigma_{\text{soft}}(s), \tag{3.31}$$

$$\chi_{\text{hard}}(s,\, b) = A(b,\, \mu)\ \sigma_{\text{hard}}(s,\, p_{T,\,\text{min}}). \tag{3.32}$$

[22] More sophisticated compared to the simple dijet MPI model discussed before.

Here we choose $\sigma_{\text{hard}}(s,\, p_{T,\,\text{min}}) = \sigma_{pp\to 2j}(s,\, p_{T,\,\text{min}})$, which can be computed perturbatively to LO and $\sigma_{\text{soft}}(s)$ is chosen such that the total cross section condition (3.26) is fulfilled and therefore $\sigma_{\text{soft}}(s) = \sigma_{\text{soft}}(s,\, p_{T,\,\text{min}})$ depends on the soft cutoff. Note furthermore that for the soft MPIs we choose a different inverse proton radius μ_{soft} since the soft scatterings need not necessarily see the same matter distribution as the hard MPIs.

The eikonal functions $\chi_{\text{soft}}(s,\, b) = \langle n_{\text{soft}}(s,\, b)\rangle$ and $\chi_{\text{hard}}(s,\, b) = \langle n_{\text{hard}}(s,\, b)\rangle$ can be interpreted as the average number of soft $\langle n_{\text{soft}}(s,\, b)\rangle$ and hard scatterings $\langle n_{\text{hard}}(s,\, b)\rangle$. If we now assume that the soft and hard MPIs are completely uncorrelated for fixed $\mathbf{b}_\perp$ and the number of additional soft and hard scatterings is distributed according to Poissonian statistic, we can write down the cross section $\sigma_{n_h,\, n_s}(s)$ for exactly n_h hard and n_s soft MPIs as follows [2]:

$$\sigma_{n_h,\, n_s}(s) = \int \mathrm{d}^2\mathbf{b}_\perp \mathcal{P}(n_h; s,\, \mathbf{b})\mathcal{P}(n_s; s,\, \mathbf{b}), \tag{3.33}$$

$$\mathcal{P}(n_h; s,\, \mathbf{b}) = \frac{[\chi_{\text{hard}}(s,\, \mathbf{b})]^{n_h}}{n_h!} e^{-\chi_{\text{hard}}(s,\, \mathbf{b})}, \tag{3.34}$$

$$\mathcal{P}(n_s; s,\, \mathbf{b}) = \frac{[\chi_{\text{soft}}(s,\, \mathbf{b})]^{n_s}}{n_s!} e^{-\chi_{\text{soft}}(s,\, \mathbf{b})}. \tag{3.35}$$

With the above expressions we can derive an expression for the total inelastic cross section i.e. with at least one soft or hard scattering as the following:

$$\sigma_{pp}^{\text{ine}}(s) = \sum_{n_h+n_s\geq 1} \sigma_{n_h,\, n_s}(s) = \int \mathrm{d}^2\mathbf{b}_\perp \left[1 - e^{-\chi(s,\, \mathbf{b}_\perp)}\right]. \tag{3.36}$$

This yields the following probability $P(n_s,\, n_h; s)$ for a non-diffractive MB event of having n_s soft and n_h hard MPIs:

$$P(n_s,\, n_h; s) = \frac{\sigma_{n_h,\, n_s}(s)}{\sigma_{pp}^{\text{ine}}(s)} \text{ for } n_s + n_h \geq 1. \tag{3.37}$$

The above matrix in n_s and n_h is computed once before every run of the simulation and then n_h, n_s are drawn from this distribution.

In the case of an actual triggering hard process with cross section $\sigma_{\text{HP}}(s) \ll \sigma_{pp}^{\text{ine}}$ the above probability must be adapted to the following:

$$P(n_s,\, n_h = 1 + m; s) = \frac{\int \mathrm{d}^2\mathbf{b}_\perp \mathcal{P}(m; s,\, \mathbf{b})\mathcal{P}(n_s; s,\, \mathbf{b})A(b)\sigma_{\text{HP}}(s)e^{-A(b)\sigma_{\text{HP}}(s)}}{\int \mathrm{d}^2\mathbf{b}_\perp A(b)\sigma_{\text{HP}}(s)}, \tag{3.38}$$

$$\approx \int \mathrm{d}^2\mathbf{b}_\perp \mathcal{P}(m; s,\, \mathbf{b})\mathcal{P}(n_s; s,\, \mathbf{b})A(b), \tag{3.39}$$

$$= \frac{n_h}{\sigma_{\text{hard}}} \int \mathrm{d}^2\mathbf{b}_\perp \mathcal{P}(n_h; s,\, \mathbf{b})\mathcal{P}(n_s; s,\, \mathbf{b}). \tag{3.40}$$

Note that here we approximated the exponential as unity since the assumption is $\sigma_{\text{HP}}(s) \ll \sigma_{pp}^{\text{ine}}$ and the last equality was obtained by absorbing $A(b)$ in the Poissonian distribution for the hard scatterings.

The actual kinematics of the hard MPIs are determined by the perturbative di-jet matrix element and sampled accordingly. For the soft MPIs however no first principle kinematics are known and need to be imposed. In the current model the kinematics for the soft scatterings are sampled according to the multi-peripheral model based on [121] shown in figure 3.6 as a gluon ladder diagram with one valence quark and antiquark. In this framework a soft N

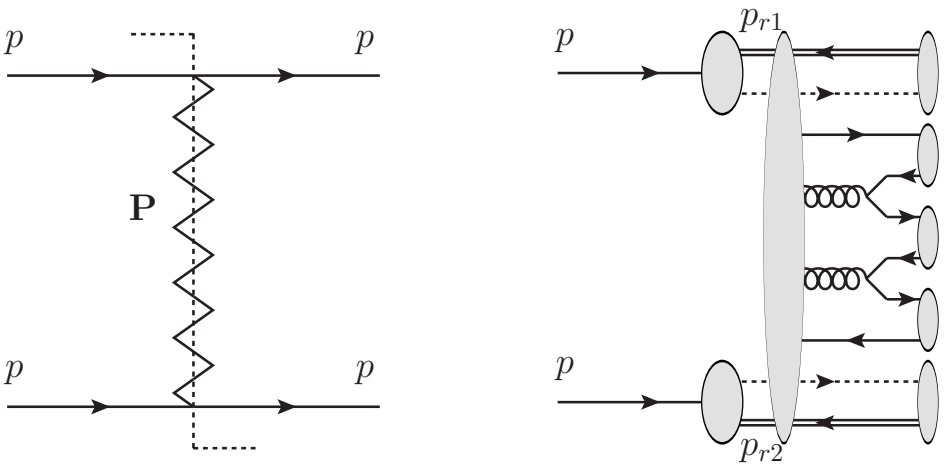

Figure 3.6: A sketch of the soft MPI type interaction (right), which is based on the idea of a cut pomeron (left). Here the grey blobs in the final state are the primordial clusters.

particle final state is generated, where N is sampled from a Poissonian distribution with the following mean:

$$\langle N \rangle = n_{\text{ladder}} \log \left[\frac{(p_{r1} + p_{r2})^2}{m_{\text{rem}}^2} \right]. \tag{3.41}$$

Here n_{ladder} is a free parameter of $\mathcal{O}(1)$, m_{rem} is the constituent mass of the remnants and p_{ri} are the initial state (i.e. just before this soft MPI has happened) remnant momenta. After that according to the multi-peripheral model the outgoing partons should be roughly equally distributed in rapidity and more uncorrelated the bigger their distance in the ladder. After that one random final state parton gets a transverse momentum p_T sampled from the distribution $\frac{\mathrm{d}\sigma_{\text{soft}}}{\mathrm{d}p_T^2} \propto e^{-\beta(p_T^2 - p_{T,\,\text{min}}^2)}$, where the normalization and the parameter β are fixed by the following two conditions:

$$\sigma_{\text{soft}}(s,\, p_{T,\,\text{min}}) \stackrel{!}{=} \int_0^{p_{T,\,\text{min}}^2} \mathrm{d}p_T^2 \frac{\mathrm{d}\sigma_{\text{soft}}}{\mathrm{d}p_T^2}(s,\, p_{T,\,\text{min}}), \tag{3.42}$$

$$\left.\frac{\mathrm{d}\sigma_{\text{soft}}}{\mathrm{d}p_T^2}\right|_{p_T = p_{T,\,\text{min}}} \stackrel{!}{=} \left.\frac{\mathrm{d}\sigma_{\text{hard}}}{\mathrm{d}p_T^2}\right|_{p_T = p_{T,\,\text{min}}}. \tag{3.43}$$

The other partons p_T's are sampled uniformly below the first sampled p_T. Note that for technical reasons in `Herwig` for a MB event the protons are split into a quark and a remnant diquark particle from which the remaining MPIs are drawn. Note furthermore that the colour flow of multiple MPIs is in general not unique and therefore a choice for the colour flow has to be made. Currently the colour structure is chosen such that e.g. for a hard MPI the DGLAP backwards evolution is forced to terminate on a gluon, which makes the colour structure unique to LC. For the soft MPIs this is done by drawing a $q\bar{q}$ valence quark pair with gluons in between in order to lead to a well defined (leading) colour structure as shown in figure 3.6. However, these choices are not very physically motivated as the colour structures of the MPIs cannot be determined from first principle. This is one of the reasons why so-called *Colour Reconnection* (CR) is needed to be able to restore the correct colour structure, which we will discuss in the next section.

3.9 Colour Reconnection

As already sketched before, the so-called *Colour Reconnection* (CR) is a crucial part for mostly hadronic collisions, but depending on the observable it can also impact high energy

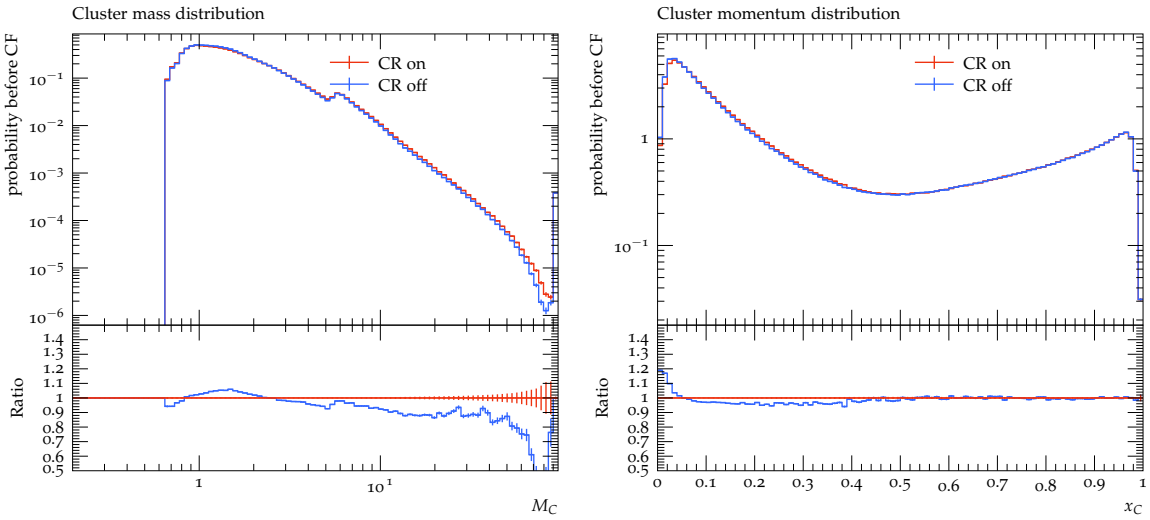

Figure 3.7: The primordial cluster mass (left) and momentum (right) distributions, where $x_C = 2|\vec{p}_C|/\sqrt{s}$ for $e^+e^- \to q\bar{q}$ at $\sqrt{s} = M_Z$ with and without CR.

(and therefore high multiplicity) e^+e^- collisions. One task of CR is an attempt to capture some subleading colour effects, which have been missed since the parton shower is LC only. However, by far the largest task for CR is to colour correlate the different MPIs and allow them to exchange colour with each other in a meaningful way. Therefore colour reconnection plays a much bigger role for high multiplicity hadronic collisions compared to leptonic collisions. In principle a lot of MB observables are strongly depending on CR e.g. observables related to multiplicity (see left plot of figure 3.8), p_T and η distributions, but a prime example of CR is the $\langle p_T \rangle (N_{\text{ch}})$ observable. As we can see in figure 3.8 on the right side in the absence of CR the $\langle p_T \rangle (N_{\text{ch}})$ observable is almost flat. This is due to the fact that the different MPIs form clusters, which hadronize completely independently of each other if CR does not reconnect them. Therefore the more MPIs are happening (strongly correlated to N_{ch}) the $\langle p_T \rangle$ changes only if the MPIs are interacting amongst themselves in some way. The fact that the observable increases can be explained by the fact that the singlet clusters might have close-by singlet clusters which would reduce the invariant mass of the clusters and release the available energy in the form of higher momentum.

As mentioned before, CR in `Herwig` is performed just after the primordial cluster formation. Even though the primordial mass distribution of clusters is peaked at a low energy scale related to the parton shower cutoff, the distribution does have a large power tail of high mass clusters. Typically CR tries to reduce the mass of these high mass clusters by exchanging constituents with close-by clusters in phase space. This effectively results a cluster mass spectrum with lighter but faster clusters as can be seen in figure 3.7. Note that the effect in figure 3.7 is quite small as expected for e^+e^- collisions at $\sqrt{s} = M_Z$, but is non-zero even without any MPIs. In principle the CR should restore here some subleading colour effects that would not have been captured by the leading colour parton shower. In `Herwig` currently there are four different CR algorithms available `Plain`, `Statistical` [122], `Baryonic` [123] and `BaryonicMesonic` [124]. We will now discuss the first three in a bit more detail since they have been longer available than the fourth. Also noteworthy is the so-called *space-time* CR algorithm [125, 126], which is determining closeness in not only in momentum space, but also considers relevant time scales to propose only causally allowed CR configurations.

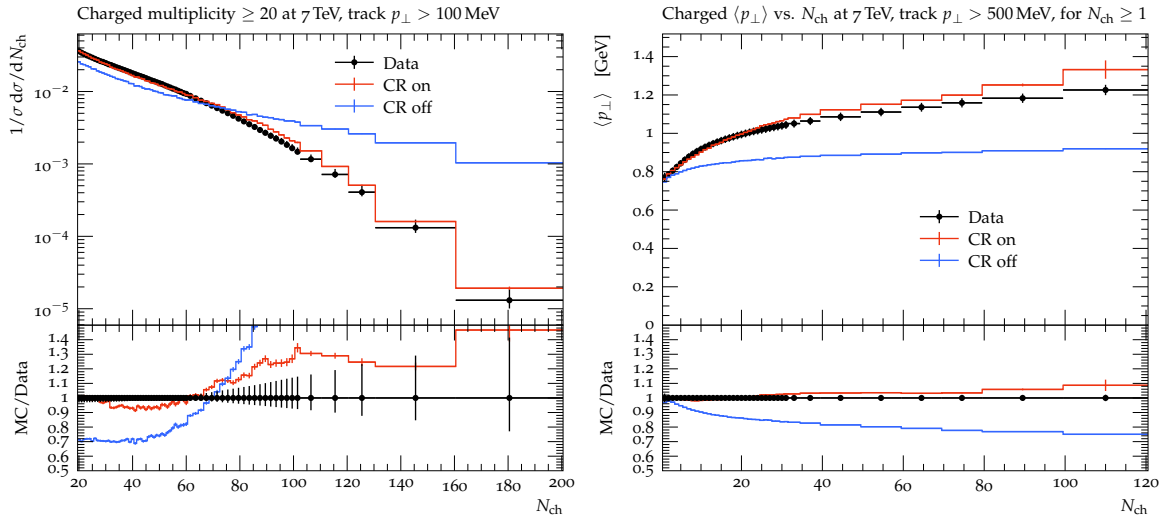

Figure 3.8: A minimum bias measurement of pp collisions at LHC with CR turned on and off [127] (public `Rivet` analysis `ATLAS_2010_S8918562`). This and almost all future histogram have been produced by `Rivet` [128].

3.9.1 Plain Colour Reconnection

The `Plain` CR algorithm is the simplest algorithm to obtain a reasonable description of e.g. the $\langle p_T \rangle(N_{\text{ch}})$. This algorithm starts by selecting the first cluster $C_s(q_s, \bar{q}_s)$ from all clusters[23] and goes through all remaining clusters $C_i(q_i, \bar{q}_i)$ and searches for the cluster with the minimal distance measure $\lambda_{si}(C_s, C_i)$ defined as follows:

$$\lambda_{si}(C_s, C_i) = \sqrt{(q_i + \bar{q}_s)^2} + \sqrt{(q_s + \bar{q}_i)^2}. \tag{3.44}$$

Here $q_{i/s}$, $\bar{q}_{i/s}$ are the constituent four-momenta. After that the cluster C_s and C_{i^*}, where $i^* = \text{argmin}_i\{\lambda_{si}\}$, are reconnected to the clusters $C_1(q_{i^*}, \bar{q}_s)$ and $C_2(q_s, \bar{q}_{i^*})$ with a probability of P_M, which is a tunable free parameter of the model. Then the next cluster on the list is selected and the algorithm repeats until every cluster on the list has been given the possibility to reconnect. Note that beam clusters are forbidden to reconnect to each other. Furthermore so-called *octet* clusters - i.e. clusters which originate from an octet gluon - are not allowed to form via CR. Note that here mesonic type clusters are reconnected only to mesonic clusters and no baryonic clusters are produced.

3.9.2 Statistical Colour Reconnection

The `Statistical` CR algorithm [122] is based on the minimization of the following global distance measure:

$$\lambda_\sigma = \sum_{i=1}^{N_{\text{cl}}} (q_i + \bar{q}_{\sigma(i)})^2. \tag{3.45}$$

Here $\sigma \in S(N_{\text{cl}})$ is a permutation. In practice we want to minimize λ_σ over all $N_{\text{cl}}!$ permutations, which is computationally too costly. For this reason the simulated annealing [129] algorithm is applied for finding the (hopefully global) minimum. This algorithm proposes a random transposition[24] $\tau_\sigma \in S(N_{\text{cl}})$ of the original state σ - i.e. the reconnection of two clusters - and accepts the reconnection with the following probability:

$$P_{\text{acc}}(\tau) = \min\left\{1, \exp\left(-\frac{\lambda_{\tau_\sigma} - \lambda_\sigma}{T}\right)\right\}. \tag{3.46}$$

[23] Where the list of all clusters has been shuffled to avoid a systematic bias.
[24] An exchange of two indices of a permutation.

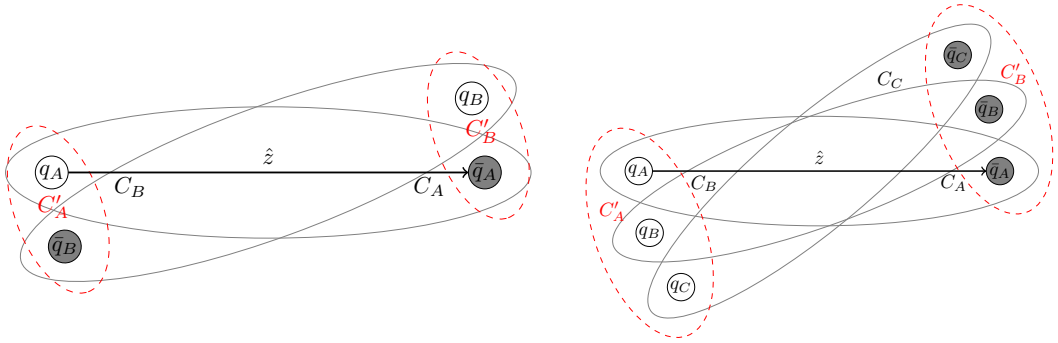

Figure 3.9: A sketch of mesonic CR (left) and baryonic CR (right).

Here T is a control parameter, which can be interpreted as a temperature of a statistical system. So if we reduce the distance measure the reconnection is always accepted, but if we do not reduce the distance then we are allowed to fluctuate outside of a potential local minima. The parameter T is at each step gradually reduced by a factor f (tunable parameter) - i.e. "cooled down" until some lower cutoff - where the algorithm terminates hopefully finding the global minimum. The starting temperature T_{start} is chosen by doing 10 transpositions and taking the median of the distance measure as $T_{\text{start}} = T_0$, where T_0 is a tunable parameter. Now even though T_0 and f are free parameters, they are only technical parameters for finding the minimum. So this model does not really have any free modelling parameters, but only the phenomenological choice of the distance measure λ_σ, which represents the physical input of what the CR should do. Nonetheless since these technical parameters are tuned to data they might capture some physics e.g. maybe the algorithm does terminate early because either the underlying physics does not want to find the global minimum or the distance measure is not representing the underlying physics very well. Note furthermore that here also only non-octet mesonic clusters are allowed to form and no baryonic clusters are generated.

3.9.3 Baryonic Colour Reconnection

The `Baryonic` CR algorithm [123] is the currently the default and most sophisticated algorithm. Since during the primordial cluster formation in the event generation we are only[25] left with quarks and antiquarks as constituents, no baryonic clusters have formed yet. However, with this algorithm baryonic clusters can be formed alongside also reconnecting mesonic clusters. This algorithm is based on rapidity in the cluster rest frame as it is motivated by the soft gluon evolution picture [8]. All clusters are shuffled to avoid any systematic bias and then the first one $C_A(q_A, \bar{q}_A)$ is boosted into its rest frame. The antiquark of this mesonic cluster determines the positive rapidity axis $\hat{z}$ as shown in figure 3.9. The next cluster on the list $C_B(q_B, \bar{q}_B)$ is boosted into the first cluster's rest frame and the rapidity of its quark y_q and antiquark $y_{\bar{q}}$ is calculated with respect to the $\hat{z}$ axis e.g. for the quark:

$$y_q = \frac{1}{2} \log \left[\frac{E_q + \hat{z} \cdot \vec{q}}{E_q - \hat{z} \cdot \vec{q}} \right]. \tag{3.47}$$

Now these rapidities y_q and $y_{\bar{q}}$ now fall into one of these three categories:

- **Mesonic:** For $y_q > 0$ and $y_{\bar{q}} < 0$ the quark of the second cluster alignes to the antiquark of the original cluster and vice-versa for the antiquark of the second cluster (see the left sketch of figure 3.9).
- **Baryonic:** For $y_q < 0$ and $y_{\bar{q}} > 0$ the quark of the second cluster alignes to the quark of the original cluster and vice-versa for the antiquark of the second cluster (see the right sketch of figure 3.9).

[25] With the exception of the remnant diquarks of hadronic collisions.

- **None:** For all other rapidities the clusters do not align properly.

We keep track of these configurations (except the trivial "none" configuration) alongside with the measure of closeness $y_{\text{sum}} = |y_q| + |y_{\bar{q}}|$, which the algorithm tries to maximize. Now we go through all of the remaining clusters and the one who gives the maximal y_{sum} will be attempted to reconnect. In the case the maximal y_{sum} is a Mesonic CR (MCR) topology (see the left sketch of figure 3.9) the proposed reconnection is accepted with a probability P_{MCR}, which is a free tunable parameter of the model. If the maximal y_{sum} is a Baryonic CR (BCR) topology (see the right sketch of figure 3.9) the two mesonic clusters are proposed alongside with the next to maximal cluster (in terms of y_{sum}) of baryonic type for a baryonic reconnection. This configuration is accepted with a probability P_{BCR}, which is a free tunable parameter of the model. After that all the participating reconnected clusters are removed from the list of clusters and the next cluster on the list is picked and the algorithm repeats.

We now have a mechanism to produce one baryonic and one antibaryonic cluster from three mesonic clusters. Now for this mechanism to produce baryons efficiently a lot of clusters are needed, but interestingly they do not need to be very massive to begin with in order to have sufficient mass left to be able to decay into two hadrons later on. After the algorithm has terminated, the baryonic type clusters are reduced to diquark-quark clusters to simplify the treatment during cluster fission and cluster decay later on. Note that the tuned parameters of this model P_{MCR} and P_{BCR} have a fixed value and ignore the kinematics of the participating clusters. This has been addressed theoretically in the context of soft gluon evolution in [8] to give a dynamic probability depending on the invariant masses of all constituents pairs, which we will develop and transform into a full CR model in chapter 7.

CHAPTER 4

Phenomenological Studies

The ultimate quest of theoretical particle physics is to explain and in the best case predict the outcome of experimental measurements. This means in practice developing testable models based on existing theoretical knowledge and data, which have the potential to predict future measurements. Such models we call *predictive* models and typically have as few as possible free parameters that need to be determined from (or fitted to) experimental measurements.

In practice however this is very difficult especially for non-perturbative effects, where *phenomenological* or *descriptive* models are used, which are defined as models that are able to describe the existing data, but do not necessarily claim to be able to predict new unseen data. These models are still mostly based on reasonable theoretical foundations, but often suffer from a large number of free parameters that have to be determined from fitting to data.

The aim of this chapter is to show and pinpoint some shortcomings of the current hadronization and CR model of `Herwig`. In this thesis we propose some attempted solutions for these shortcomings and at the same time either reduce the number of free parameters or keep them the same. These more predictive alternatives for the hadronization are discussed in chapter 5 and for the CR in chapter 7. However, we do not want to claim that these results are the final models since some crucial parts are still missing in order to capture the whole picture as we will discuss in the respective chapters.

Still, in the quest for a more predictive answer to hadronization and CR we assume the strong coupling in the following to be fixed to the PDG world average[26] $\alpha_s(M_Z) = 0.1185$ [15, 105] for the ISR and FSR instead of tuning both separately to different values. Therefore our results for the default `Herwig` 7.3.0 runs will differ from other sources e.g. the official `Herwig` website. Note that for all of the plots of LHC MB simulations we employ a maximum lifetime cut of $c\tau > 10$ mm (i.e. particles with longer average lifetimes are considered stable) as this is used by the ATLAS, ALICE and CMS LHC experiments. For the e^+e^- simulations for the BELLE, ARGUS and various LEP experiments we turn off the ISR photons since the data has been corrected for ISR effects.

Since we are studying hadronization and CR in terms of matrix elements we are considering only LO matrix elements with matrix element corrections for e^+e^- collisions [130] unless

[26] This is not the most recent value for α_s, but still close enough for our purposes.

otherwise stated. Similarly, for *pp* collisions the MPIs are all calculated to LO. Therefore the normalization of the (partonic) cross section computation will be a LO result, which should be kept in mind for all plots where the cross section is relevant.

4.1 Baryonic Angular Correlations at LHC

Correlations of hadrons have been gathering a lot of attention in the context of long ranged collectivity effects of high multiplicity events measured by ALICE, ATLAS and CMS [131–134] for *pp* MB events. The observed so-called *ridge* structure has been claimed to be a sign of the formation of a Quark Gluon Plasma (QGP). In this context also measurements for e^+e^- collisions of hadron correlations have been done by e.g. ALEPH [135] at LEP and by BELLE [136] at KEKB, which did not find any significant ridge yields.

However, also the near side correlations are a very valuable observable especially for hadronization and CR modelling. Such short range hadron correlations have been measured by BELLE [136] inclusively in flavour and by ALICE for identified hadrons $\pi^{\pm}$, $K^{\pm}$, p and Λ_0 in [137], for Λ_0 and K^0_S in [138] and for $\pi^{\pm}$, $K^{\pm}$, p, Ξ_0 and $\Xi^{\pm}$ in [139]. Unfortunately only the analysis [137] has a public `Rivet` [128] analysis available, which is the reason why we will mostly focus on this analysis in this section.

However, let us briefly discuss the method with which the measurement of [137] was made. If we look at the $\phi - \eta$ plane one can define correlations C_{ab} between two hadrons of type a and b respectively as a function of $\Delta\phi_{ij} = \phi_i - \phi_j$ and $\Delta\eta_{ij} = \eta_i - \eta_j$. These are measured e.g. in [137] experimentally by using so-called *event-mixing* techniques and can be expressed as the following:

$$C_{ab}(\Delta\eta,\, \Delta\phi) = \frac{S_{ab}(\Delta\eta,\, \Delta\phi)}{B_{ab}(\Delta\eta,\, \Delta\phi)}. \tag{4.1}$$

Here the signal correlation $S_{ab}(\Delta\eta,\, \Delta\phi)$ is computed for all particles in the same event, while the background correlation $B_{ab}(\Delta\eta,\, \Delta\phi)$ is determined by computing the correlation between each particle from the event and each particle from a different so-called mixing event, which yields the following [137]:

$$S_{ab}(\Delta\eta,\, \Delta\phi) = \frac{1}{N^{\text{sig}}_{ab}} \frac{\mathrm{d}^2 N^{\text{sig}}_{ab}}{\mathrm{d}\Delta\eta\, \mathrm{d}\Delta\phi}, \tag{4.2}$$

$$B_{ab}(\Delta\eta,\, \Delta\phi) = \frac{1}{N^{\text{mix}}_{ab}} \frac{\mathrm{d}^2 N^{\text{mix}}_{ab}}{\mathrm{d}\Delta\eta\, \mathrm{d}\Delta\phi}, \tag{4.3}$$

$$\frac{\mathrm{d}^2 N^{\text{sig}}_{ab}}{\mathrm{d}\Delta\eta\, \mathrm{d}\Delta\phi} = \sum_E \frac{1}{2} \sum_{i \in \{h_a\}_{\mathrm{E}}} \sum_{j \in \{h_b\}_{\mathrm{E}}} \delta(\Delta\eta_{ij} - \Delta\eta)\delta(\Delta\phi_{ij} - \Delta\phi), \tag{4.4}$$

$$\frac{\mathrm{d}^2 N^{\text{mix}}_{ab}}{\mathrm{d}\Delta\eta\, \mathrm{d}\Delta\phi} = \frac{1}{M} \sum_E \sum_M \frac{1}{2} \sum_{i \in \{h_a\}_{\mathrm{E}}} \sum_{j \in \{h_b\}_{\mathrm{M}}} \delta(\Delta\eta_{ij} - \Delta\eta)\delta(\Delta\phi_{ij} - \Delta\phi). \tag{4.5}$$

Here the factor of $1/2$ is due to double counting and $\{h_a\}_{\mathrm{E}}$ and $\{h_a\}_{\mathrm{M}}$ are the sets of hadrons of type a from the event E and the mixing event M respectively. The mixing events are selected randomly from a stack of mixing events with a similar multiplicity to avoid a systematic bias. For the analysis in [137] the mixing events M can only differ by at most 5 particles in terms of multiplicity compared to the original event E and the events are mixed with 10 different mixing events.

In ridge measurements the obtained correlation $C(\Delta\eta,\, \Delta\phi)$ is typically integrated in a region $a < |\Delta\eta| < b$ with large a and b to avoid the jet correlations region, but since we are more

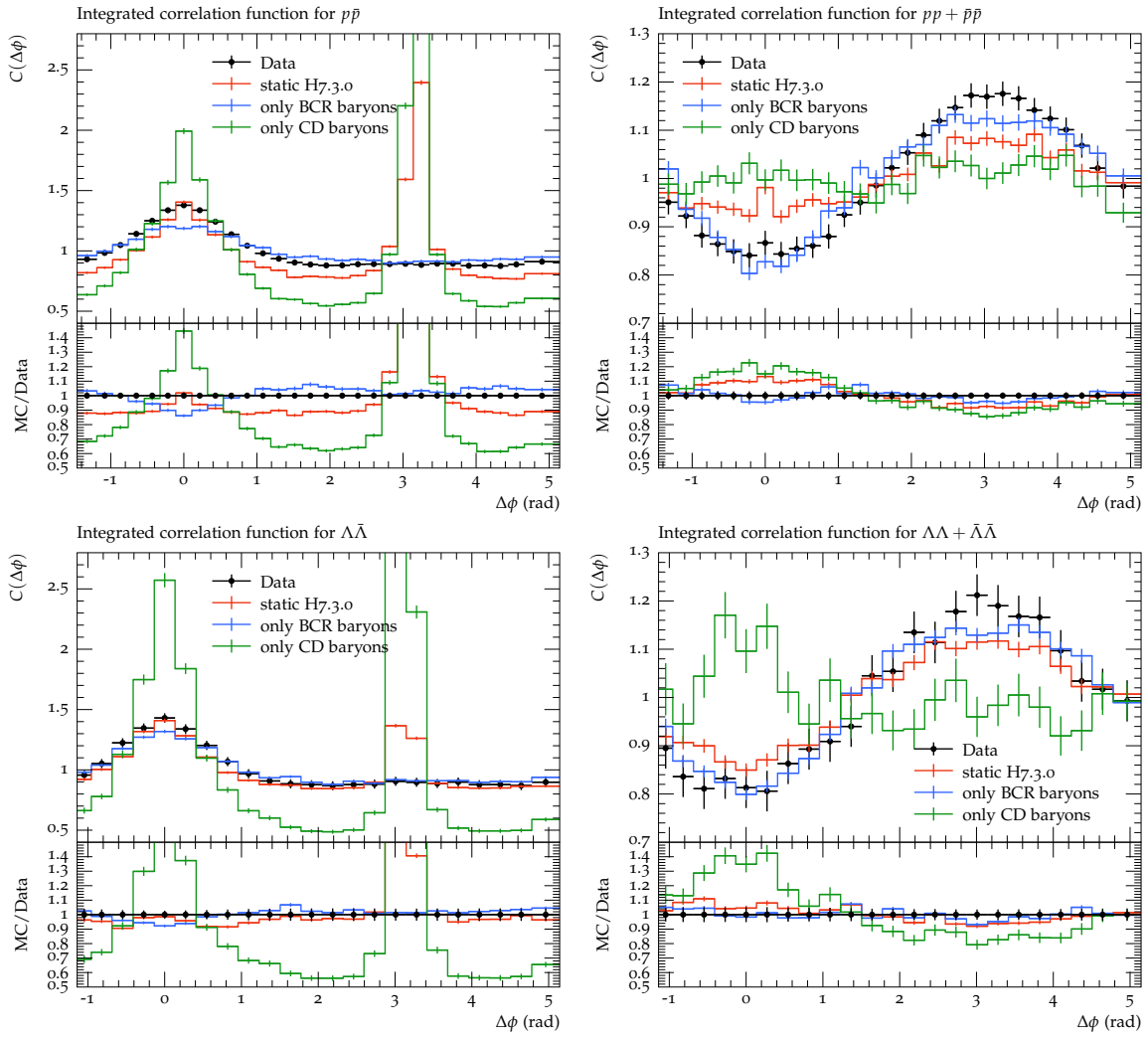

Figure 4.1: The azimuthal correlations of different baryon-antibaryon and baryon-baryon combinations comparing the default with only BCR baryons and only CD baryons for LHC MB runs at 7 TeV measured by ALICE [137] (public `Rivet` analysis `ALICE_2016_I1507157`).

interested in hadronization and CR, also within a jet, we are looking at the short range correlations where $a = 0$ and $b = 1.3$ [137].

We display the results for Baryon-Baryon (BB) and Baryon-Antibaryon (BA) correlations for this analysis in figure 4.1, where we compare the `Herwig` 7.3.0 default with the two production mechanisms for baryons available to `Herwig`. These two mechanisms are the baryon production from the Cluster Decay (CD), where a mesonic cluster decays into a baryon-antibaryon pair and the Baryonic Colour Reconnection (BCR), where three mesonic clusters recombine to a baryonic and an antibaryonic cluster. Note that in figure 4.1 for the default we have chosen the static cluster fissioning scheme, which we described in section 3.5.2 and for the CD we have increased the weight of drawing a baryon (**PwtDI** from section 3.5.3) from the tuned value of 0.33107 to 0.6 in order to boost the overall baryon production to compensate for the missing BCR baryons. In the same spirit, we increased the BCR reconnection probability P_{BCR} from section 3.9 from the tuned value of 0.7 to 1.0 for the same reason. Leaving it at its tuned value does require more events to give the same statistic and does not change the overall qualitative observation we want to make.

The near side depletion of BB correlations observed in [137, 140–143] has been shown to be badly modelled especially by `Pythia`, with several attempts to fix these issues (see e.g.

[144–146]). While `Herwig` does describe the data for BB correlations much better (see e.g. figure 4.1), for BA correlations there is some unphysical behaviour present.

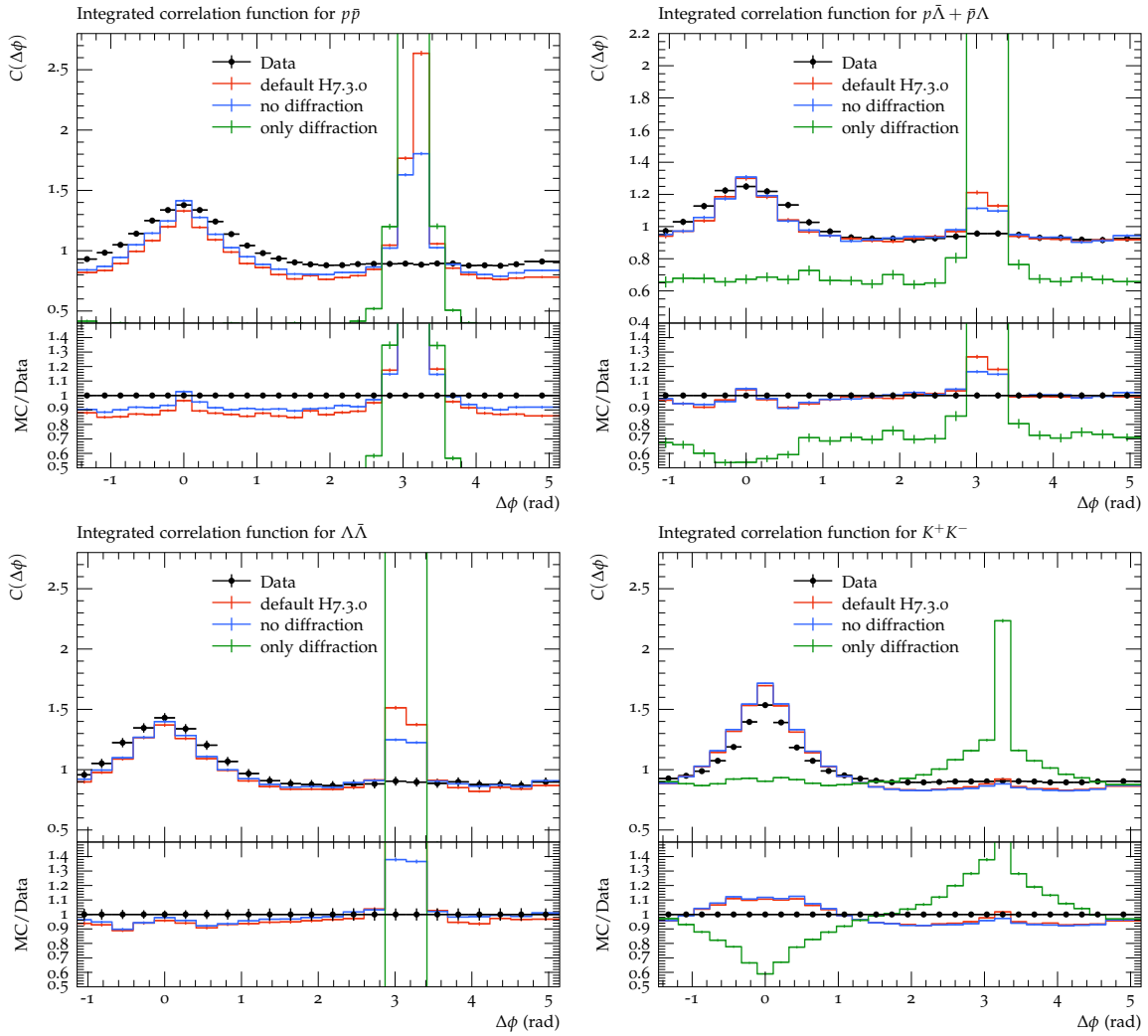

Figure 4.2: The azimuthal correlations of different hadron-antihadron combinations comparing the default with only diffractive and only non-diffractive processes for LHC MB runs at 7 TeV measured by ALICE [137] (public `Rivet` analysis `ALICE_2016_I1507157`).

One can clearly see that the default `Herwig` prediction for the BA correlations exhibits a huge far side peak in figure 4.1, which is not observed in the data. Disentangling the production mechanisms we can narrow down the origin of this unphysical behaviour to the CD baryon production mechanism. This should not be too surprising if we recall the cluster decay model from section 3.5.3, which decays light clusters isotropically to a baryon-antibaryon pair. Also the near side peak is way more pronounced in the BA correlations for the CD baryons, while for the purely BCR baryons it almost matches perfectly the data. Note that the diffraction model plays also an important role here, but it is not solely responsible for this unphysical behaviour as one can see in figure 4.2, where we display the correlations for only diffractive events and non-diffractive events. In fact, the diffraction model would produce a single cluster with aligned constituents, which (if the cluster is heavy enough) would fission recursively to further aligned clusters (yielding a cluster chain) close to the beam axis, which are then decayed isotropically to two hadrons. This would clearly lead to huge back-to-back correlations on the far side as one can see in the purely diffractive events plot in figure 4.2 also for the K^+K^- mesonic correlations. We want to stress here that it is at the same time

remarkable and worrisome that this one-dimensional cluster chain combined with isotropic cluster decay can be tuned to MB data such as rapidity gap data e.g. from ATLAS [147] to give a quite decent description of the data.

Examining the BB correlations in figure 4.1 one can clearly see the impact of the different baryon production mechanisms. In particular, again the BCR model seems to describe the data much better by itself, while the CD baryons yield a qualitatively wrong description. Now this should not come as a too big surprise for this observable, because it is sensitive to the correlation of baryon number. Let us assume a high multiplicity MB event before hadronization and CR is just a set of quarks and antiquarks[27] uniformly distributed in phase space, whose elements want to confine into a colour singlet state with their closest neighbours in phase space. If now in some small compact region of phase space a baryonic type configuration of e.g. three quarks will form a baryon the remaining partons are more likely to be antiquarks compared to quarks since the formation of the baryon has absorbed from the region three quarks. However, since baryon number is conserved an antibaryon has to be produced to maintain the balance as one can see in the BA correlations of 4.1. This can be done with the previously colour connected partners of the original quarks, which need to form an antibaryonic configuration. Of course, this is only reasonable if these three antiquarks are in reasonable proximity in phase space. This is exactly what the BCR model from section 3.9 describes including the balance peak at the far side. So what the depletion in the near side of figure 4.1 tells us is that we locally depleted the source of baryon number (i.e. quarks) in the close-by phase space.

In contrast to the BCR mechanism, the CD baryons seem to yield either no BB correlations or a near side correlation in figure 4.1, which does not agree at all with the data. However, also this should not be surprising since this mechanism is completely independent of the event. We need two clusters to decay into a baryon-antibaryon pair to compute this correlation, these two clusters are mostly[28] uncorrelated and therefore the BB correlations are mostly uncorrelated except for phase space effects. In contrast to this of course the BA correlations are strongly correlated, which is just a reflection of pure isotropic two-body decay phase space. In particular, we can say that the BCR mechanism is aware of the surrounding partons/clusters or the rest of the event, while the CD baryon mechanism is completely oblivious to the rest of the event and hadronizes independently. Note that similarly to the BCR model there exist also so-called *coalescence* models [148] such as `AMPT` [149], which essentially coalesce partons into hadrons and therefore are also able to reproduce the BB suppression, but those are not microscopic models like the BCR model.

Now the conjecture that nature prefers the BCR mechanism to produce baryons is supported by the measurement of $pp + \bar{p}\bar{p}$ correlations of ALICE (at 13 TeV) in [141][29], where more multiplicity corresponds to a higher depletion of BB correlations, which in our conjecture can be explained by more baryonic configurations for BCR can be found due to increased multiplicity.

Now one might want to just propose a purely BCR model for baryon production as it describes the qualitatively and in parts quantitatively the data very well, but what is not visible in the presented data is the overall number of baryons produced. In fact, purely BCR baryons cannot produce enough baryons for pp MB collisions and the situation is even worse for e^+e^- collisions without the MPI contributions. Therefore we propose a two-fold approach to address this problem:

[27] Assuming the gluons have already split to $q\bar{q}$ pairs.

[28] They both need to have sufficient mass to decay into two baryons.

[29] Note that in this analysis the correlations are rescaled to the correlation per particle instead of correlation per pair of particles in order to compare different multiplicity classes.

1. Turn off baryon production from the CD stage and allow CF baryon production.
2. Increased baryon production in CR using a new algorithm.

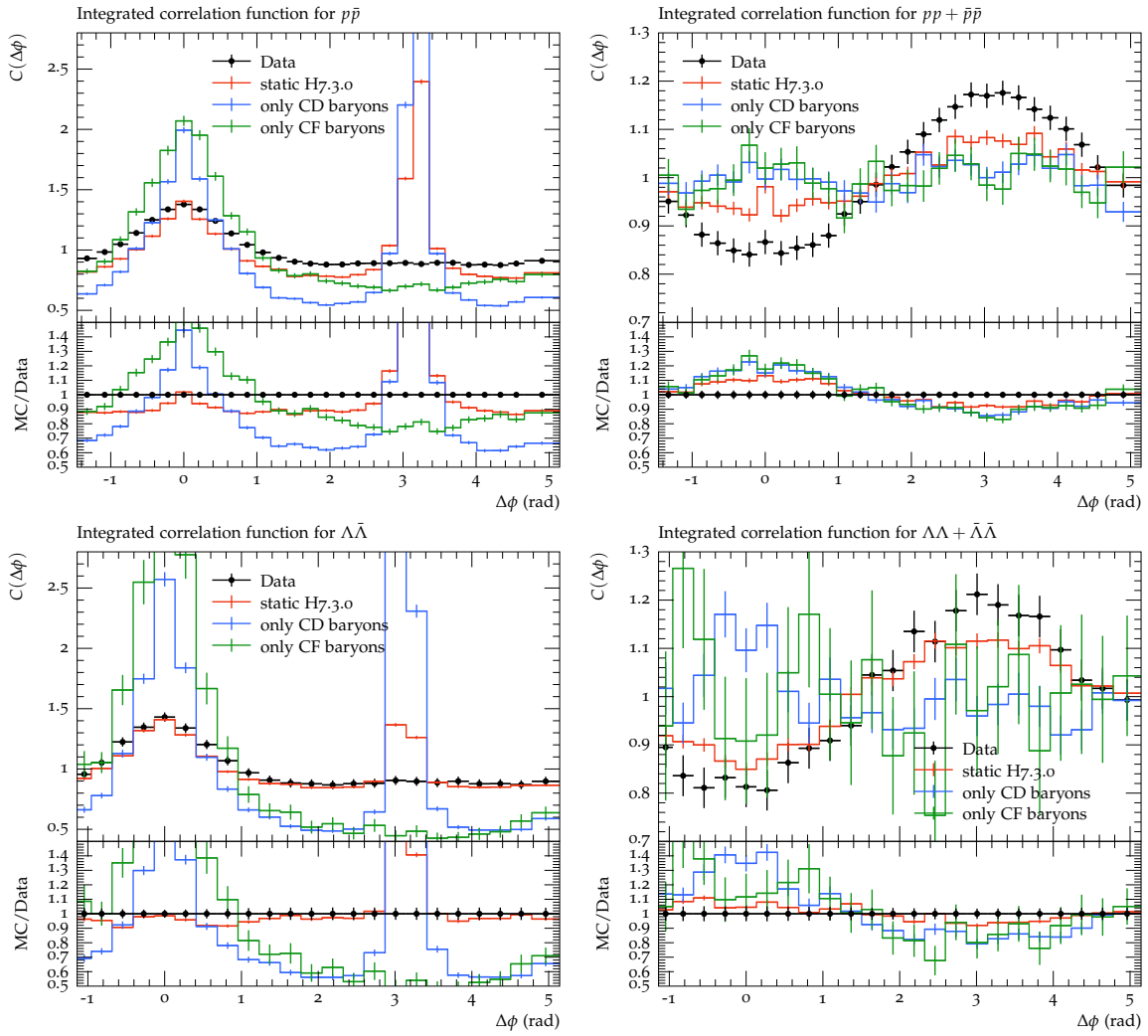

Figure 4.3: The azimuthal correlations of different baryon combinations comparing the default with only CD baryons and only CF baryons for LHC MB runs at 7 TeV measured by ALICE [137] (public `Rivet` analysis `ALICE_2016_I1507157`).

For the latter point, we will describe our new algorithm in chapter 6, but the former point is quite straightforward. We simply set the $\textbf{PwtDI}_{\text{CD}} = 0$ and set $\textbf{PwtDI}_{\text{CF}}$ to a similar value to the CD weight. In figure 4.3 we display the comparison of only CF baryons and only CD baryons, where for the case of only CF baryons we set the $\textbf{PwtDI}_{\text{CF}} = 0.9$ in order to boost the baryon production. One can clearly see that this eliminates the unphysical far side peak in the BA correlations even though it does not create the depletion of the BB correlations, but we would not expect this in any case since the CF is also an independent hadronization process. However, what we must note here is that the CF baryons exhibit very different p_T spectra as can be seen in figure 4.4. In fact, the soft peak of the baryon p_T spectra is related to the masses and momentum distributions of the underlying clusters, which means the production mechanism must reflect this somehow. Interestingly looking at the p_T spectra in figure 4.4 one can note that the BCR baryons by themselves yield a very good prediction of the shape of the Ξ and to a lesser extent the Λ baryon. However, the p spectrum is quite significantly underestimating the soft peak. This might also be a hint that multi-strange baryons are more easily formed via the BCR mechanism compared to light baryons.

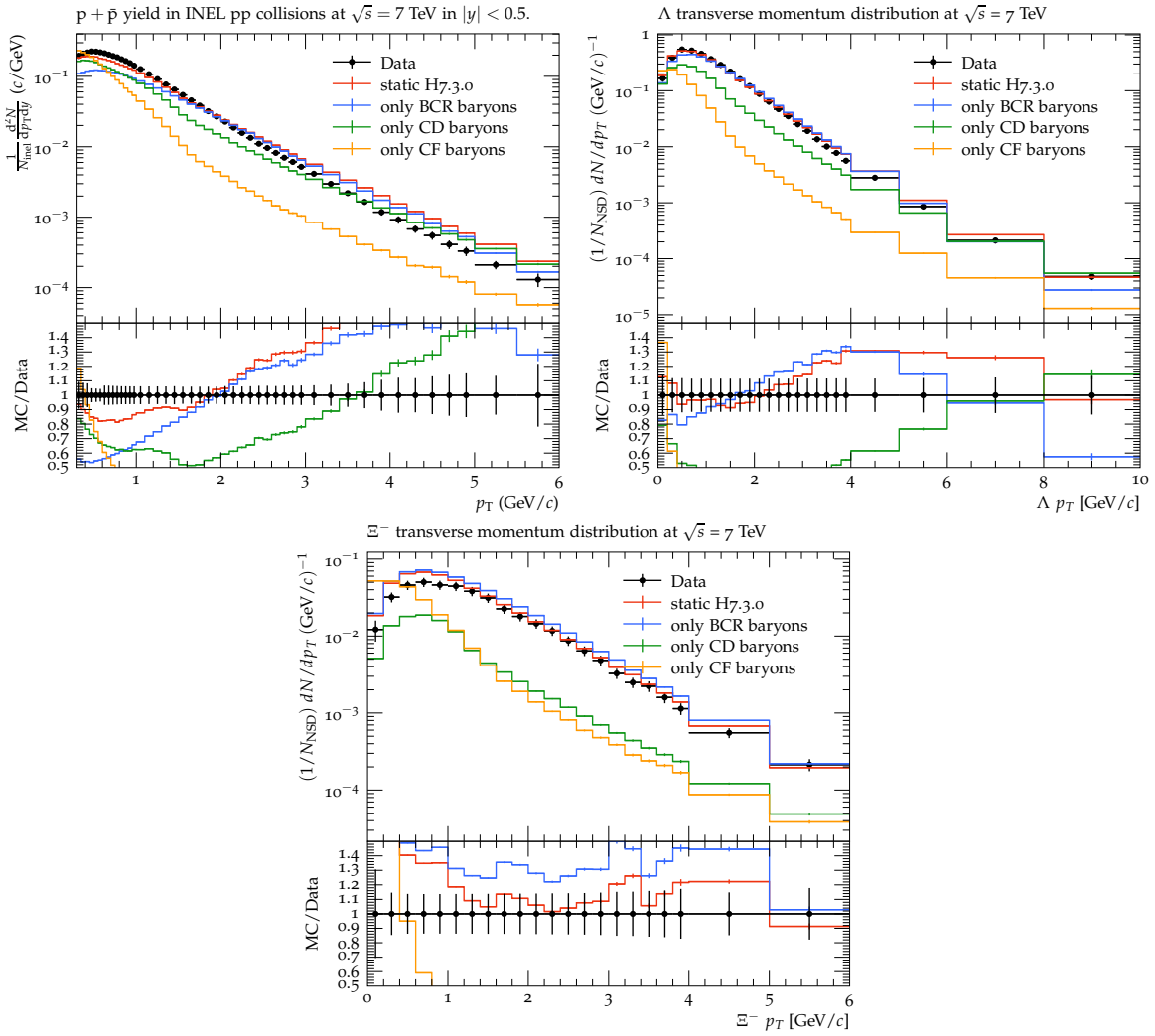

Figure 4.4: The p_T spectra of baryons of MB pp collisions at 7 TeV measured by CMS and ALICE [150, 151] (public `Rivet` analyses `CMS_2011_S8978280` and `ALICE_2015_I1357424`) for different baryon production mechanisms.

However, just producing all baryons using the BCR mechanism is not enough even for MB pp collisions let alone e^+e^- collisions. Furthermore, it is not necessarily clear if the improper modelling of the baryon-antibaryon correlations is only a feature of MB pp collisions or if it happens also at low energy e^+e^- collisions, which would consolidate our claim that this problem is in the universal hadronization model and not related to issues in the MPI model. In the next section we will therefore look at a similar observable for low energy e^+e^- collisions.

4.2 Baryon Correlations at ARGUS

In this section we want to cross-check our findings with low energy $\sqrt{s} = 10$ GeV e^+e^- collisions at the so-called *continuum* - above the $\Upsilon(1S)$ and below the $\Upsilon(2S)$ resonance - for a similar correlation observable measured by the ARGUS experiment at the DORISII collider. The measurement of [152] used the azimuthal angle $\phi_\perp$ between protons and antiprotons, where the angle is defined in the plane perpendicular to the thrust direction of the event. In fact, the conclusion of this analysis was that the simplistic diquark picture i.e. assuming diquarks to be just another parton in the string context is disfavoured by the data observed and the so-called *popcorn* model [153] for the case of `Pythia` is preferred.

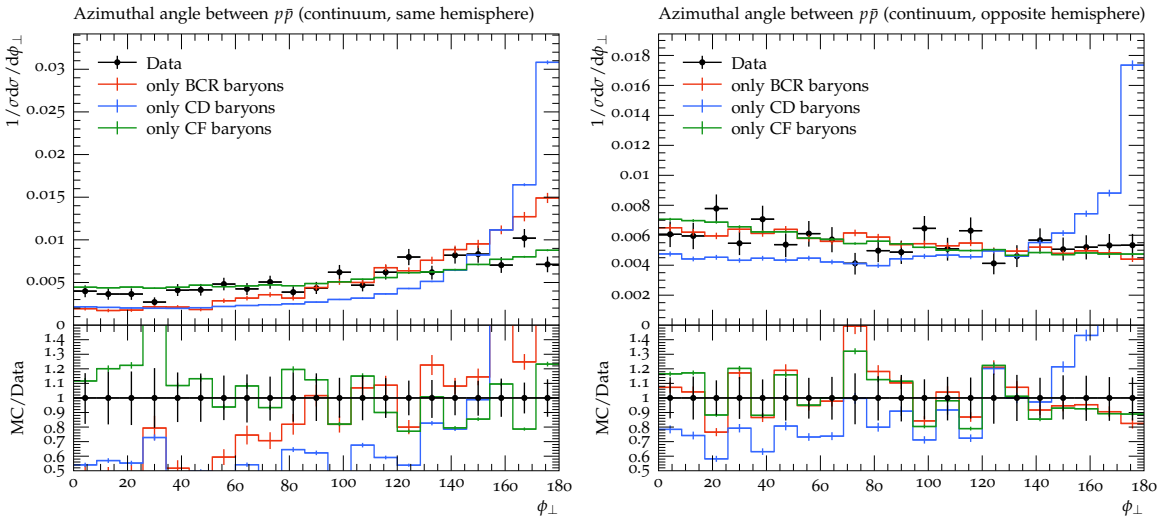

Figure 4.5: The $p\bar{p}$ azimuthal angular correlations for e^+e^- collisions at $\sqrt{s} = 10$ GeV measured by ARGUS [152] (public `Rivet` analysis `ARGUS_1988_I266892`) for the same and opposite hemisphere.

In figure 4.5 we display these correlations for the $p\bar{p}$ pairs in the same and opposite hemisphere for the aforementioned different baryon production mechanisms. Note that in the "only CD baryons" we disabled the BCR mechanism even though it does not have a substantial effect since not enough clusters are around. We can clearly see that this confirms our previous findings that the baryon correlations exhibit an unphysical far side peak for the CD baryon mechanism. Interestingly also the purely BCR baryons show a slight far sided peak for $p\bar{p}$ pairs in the same hemisphere, while the CF baryons yield excellent agreement. However, one should note that baryons originating purely from BCR at such low energies are highly unlikely as there are not many clusters produced, which could undergo BCR.

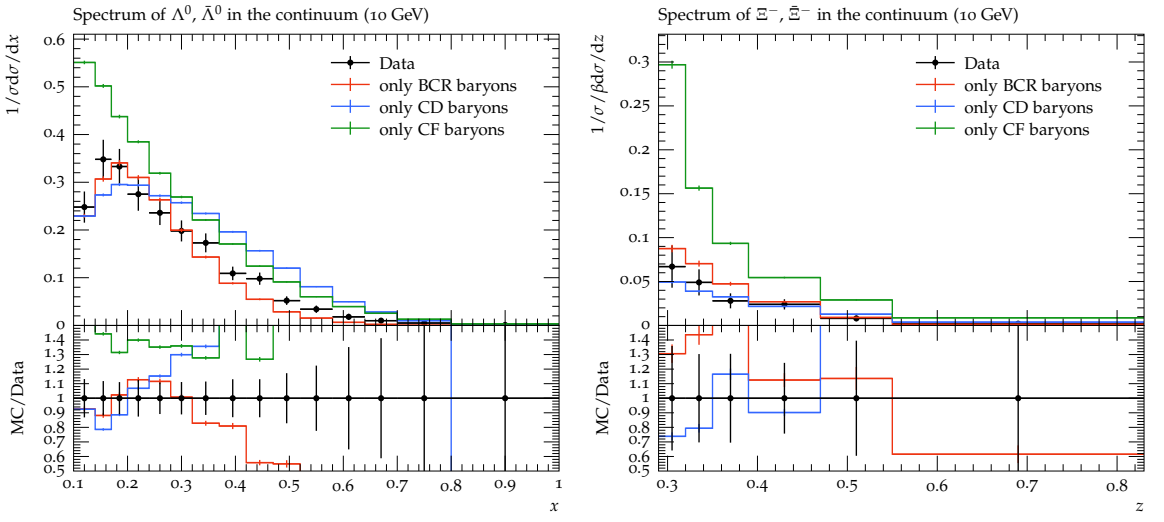

Figure 4.6: The Λ^0 and Ξ^- baryon $x = 2|\vec{p}|/\sqrt{s}$ and $z = 2E/\sqrt{s}$ distributions respectively for e^+e^- collisions at $\sqrt{s} = 10$ GeV measured by ARGUS [154] (public `Rivet` analysis `ARGUS_1988_I251097`). Note that here we have up-scaled the "only BCR baryons" by a factor of 30 in order to compare the shapes.

As before we would like to examine how the momentum spectra of baryons behave if we only consider CF baryon production. Therefore we display the $x = 2|\vec{p}|/\sqrt{s}$ and $z = 2E/\sqrt{s}$

spectra of the Λ^0 and Ξ^- baryons measured by ARGUS [154] in figure 4.6. Note that in figure 4.6 we rescaled the red BCR histogram by a factor of 30 for visibility. As in the previous section (see figure 4.4) we can see that the CF baryons produced do not form the characteristic soft peak, while the other mechanisms do. So we can conclude that this feature is generic for the default CF baryon production. However, one should note that this is all tied to the exact kinematics of the cluster model i.e. the mass and directional distributions sampled during CF and CD. It is therefore worth to closely examine the kinematics of the cluster hadronization model, which we will do in chapter 5 in more detail.

4.3 Di-Hadron Masses at BELLE

As we have seen some issues with the current CF model for baryons, we might expect similar issues to arise in different observables related to the CF kinematics. For this purpose we examine here the current cluster hadronization models kinematics by looking at the di-hadron fragmentation functions for the identified hadron pairs invariant mass measured by BELLE [155]. This observable is given by the following differential cross section:

$$\frac{\mathrm{d}^2\sigma(e^+e^- \to h_1,\, h_2,\, X)}{\mathrm{d}z\mathrm{d}m_{h_1h_2}}. \tag{4.6}$$

Here $m_{h_1h_2} = \sqrt{(p_{h_1} + p_{h_2})^2}$ is the invariant mass of two hadrons, which are coming from the same hemisphere (with respect to the thrust direction). The energy fraction $z = 2(E_{h_1} + E_{h_2})/\sqrt{s}$ is chosen such that $z = 1$ corresponds to the two hadrons having the total energy of one hemisphere. We can note therefore that for the continuum BELLE energy of $\sqrt{s}_{\mathrm{BELLE}} = 10.52$ GeV, where the COM energy is quite low (but still perturbative for the continuum measurement), the Parton Shower (PS) is practically absent or does not emit many particles and therefore partons transition directly to the hadronization model. If the PS does not emit any particles for the hard process $e^+e^- \to q\bar{q}$, we have to hadronize a cluster of mass $M_C = \sqrt{s}_{\mathrm{BELLE}}$. In particular, for $z \lesssim 1$ (almost) all the energy of the hemisphere is contained in the two hadrons, which means that we essentially only have those two hadrons in the hemisphere. These two hadrons have to originate in our cluster model from the cluster decay of a cluster into two hadrons, but for momentum balance reasons this cluster cannot be at rest in the LAB frame and must therefore itself arise from the cluster fission of (possibly) the primordial cluster of mass $M_C = \sqrt{s}_{\mathrm{BELLE}}$ if the PS has not emitted anything. Therefore the mass distribution of two hadrons for $z \lesssim 1$ (where the background from the PS is minimal) will give us a probe of the cluster mass spectrum after the cluster fission. It is crucial to note that what this observable at $z \lesssim 1$ shows is not necessarily a single CF process, but the recursive process of CF such that all clusters are below the cutoff in the case of a hard static cutoff.

In figure 4.7 we display the di-hadron invariant mass spectrum for $\pi^+\pi^-$ and π^+K^- for $z \in [0.95, 1]$ measured by BELLE for the default hadronization, pure hadronization without PS and pure PS without CF. Clearly, neither the default cluster model nor the purely hadronization model (without PS) is agreeing with the data qualitatively. The resonances in these spectra are clearly visible in the data, but are not captured by the pure hadronization approach. In fact, we see a slowly decreasing plateau at 650 MeV for $\pi^+\pi^-$ and at 775 MeV for π^+K^-, which are exactly the sum of the constituent masses of a cluster that can decay into the respective pairs of hadrons. This means the current CF model produces a lot of clusters $C(q, \bar{q}')$, which are barely above the minimal kinematic threshold $M_C^{\min} = m_q + m_{\bar{q}'}$.

We can easily verify this claim by varying the underlying light quark constituent masses by a factor of 0.75 and 1.25, which we display in figure 4.8. As expected the plateaus shift towards

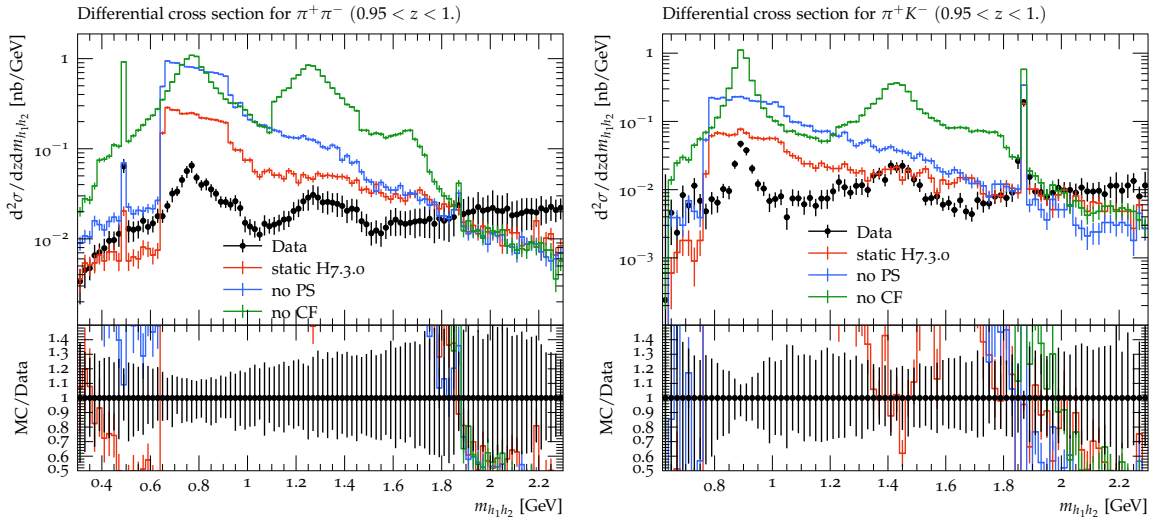

Figure 4.7: The di-hadron invariant mass spectrum for $\pi^+\pi^-$ and π^+K^- for $z \in [0.95, 1]$ measured by BELLE at $\sqrt{s} = 10.52$ GeV (below the $\Upsilon(4S)$ threshold) [155] (public `Rivet` analysis `BELLE_2017_I1607562`) for the default hadronization model, the model without parton shower and the model without cluster fission.

higher values for higher constituent masses and vice-versa. Comparing the purely CF model with the purely PS model in figure 4.7 furthermore confirms that the issue lies in the CF model since the "no CF" simulation shows qualitatively good agreement with the data. Note that the discontinuity in figure 4.8 at around 1.1 GeV for the $\pi^+\pi^-$ is most likely related to the cut on the width of the resonances that are imposed in the event generator.

Nonetheless, the qualitative agreement gives us evidence that the CF should most likely behave similarly to the PS, which we will further investigate in chapter 5. In figure 4.9 we display the mass spectrum of the clusters and their momentum in terms of $x_C = 2|\vec{p}_C|/\sqrt{s}$ both after CF for the cases where we have only CF and no PS and vice-versa. There one can clearly see that first of all the perturbative spectrum of the PS is not preserved during the CF and second of all the recursive CF essentially overlays its distribution on top of the perturbative mass spectrum. This hard transition from PS to CF is of course unphysical and leads to a huge and unpredictable dependence on the PS cutoff, which should just be a matching scale between the PS and CF as has been explored more in detail in [94]. Another possibility is that some heavy clusters should be given the possibility to directly decay into two hadrons instead of splitting into lighter clusters, which is a temporary fix to this issue proposed in [44, 103] at the cost of three tunable parameters.

4.4 Conclusions

In this chapter, we have seen some issues of the current cluster hadronization model of `Herwig` and investigated their potential origin. In this investigation it turned out that correlation observables are particularly useful since they truly probe the sub-structure of an event, which is very sensitive to hadronization and colour reconnection. In particular, we found that it is quite easily possible to have a hadronization model that gives reasonable results for a plethora of observables to which it has been tuned to, but clearly gives unphysical behaviour for correlation observables. Of course this makes sense since e.g. the di-hadron correlations we looked at (by ALICE, ARGUS and BELLE) are particularly sensitive to the production mechanism that generated these two hadrons i.e. hadronization and colour reconnection.

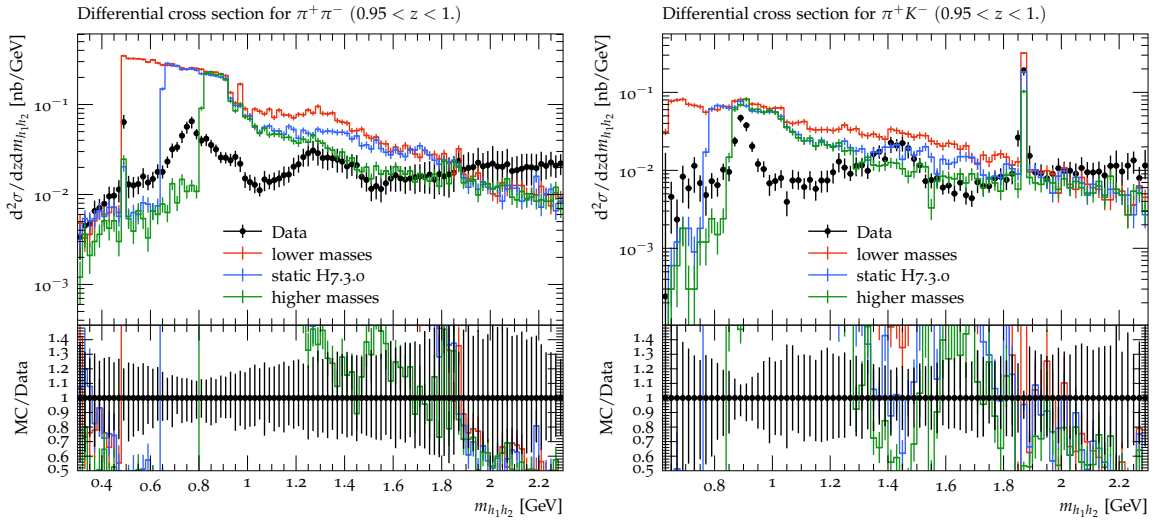

Figure 4.8: The di-hadron invariant mass spectrum for $\pi^+\pi^-$ and π^+K^- for $z \in [0.95, 1]$ measured by BELLE at $\sqrt{s} = 10.52$ GeV (below the $\Upsilon(4S)$ threshold) [155] (public `Rivet` analysis `BELLE_2017_I1607562`) for different values of the light *uds* constituent masses. For the "lower masses" we scaled the constituent masses by 0.75 of their default value and for the "higher masses" we scaled the constituent masses to 1.25 of their default value except for the *s* quark, which has been kept at the default value.

Furthermore, we showed that the modelling of baryon production is still not clearly understood and in particular that baryon observables are therefore a good probe for hadronization models especially also comparing different collision systems and energies. All of these observations are of course strongly tied to the hadronization model, the colour reconnection model and their interaction with each other. This is the motivation for this thesis to investigate deeply the current phenomenological hadronization and colour reconnection models and try to develop more predictive models.

In particular, we have already seen a hint for a new cluster fission model, which should behave more like an actual parton shower as can be seen in figure 4.7. In fact, we will propose a new matrix element cluster fission in chapter 5, which will be motivated by colour evolution and show its phenomenology. In addition, in chapter 7 we will be showing a more predictive colour reconnection model and discuss its phenomenology.

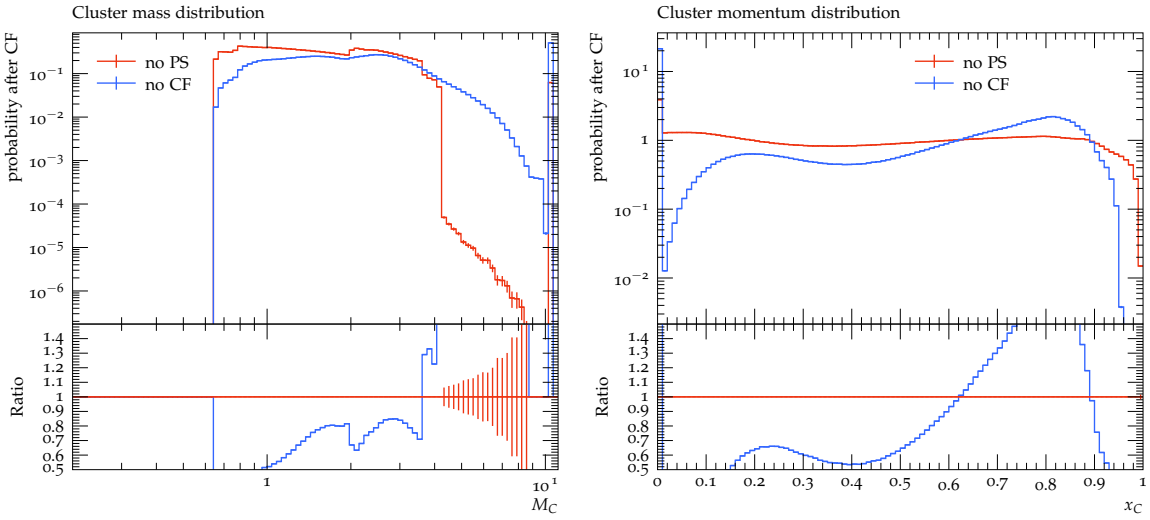

Figure 4.9: The (unobservable) mass spectrum of the clusters for $e^+e^- \to q\bar{q}$ at BELLE and their momentum in terms of $x_C = 2|\vec{p}_C|/\sqrt{s}$ both after CF for the cases where we have only CF and no PS and vice-versa.

CHAPTER 5

Hadronization Studies

Current cluster hadronization models (`Herwig` [2] and `Sherpa` [93]) rely on phenomenological cluster fission models with several free tuning parameters, which parametrize our lack of knowledge of the underlying mechanism. This is one of the down-sides of cluster hadronization compared to string hadronization models[30], which - based on the string assumption - get a prescription for the kinematics of hadronization.

In this chapter, we propose a perturbatively inspired matrix element for the cluster fission and a phenomenological matrix element for the cluster decay in order to reduce the number of free parameters [156]. This will not only yield a more predictive model for hadronization, but also lead in the long term towards more meaningful hadronization uncertainties on experimental measurements than the usual two point variations, where the hadronization uncertainty is defined as the envelope of the `Herwig` and `Pythia` simulation [6]. Additionally, fewer parameters should alleviate the need for sophisticated tuning strategies, which has been an issue at least for some parameters as shown in [94]. Furthermore, we will discuss the phenomenology of these new approaches on measured data and propose unmeasured and new correlation observables to examine their sensitivities on the different hadronization stages.

5.1 The Issues of the Current Cluster Fission Model

As already discussed in sections 3.5.2 and 3.5.3 theoretically and in chapter 4 phenomenologically with measured data we have seen several issues of the current CF and CD model in `Herwig`. The most important theoretical and phenomenological issues of the model are the following:

- No transverse momentum for the daughter clusters is added for the CF, i.e. it is a one-dimensional process as shown in figure 3.3.
- The Ansatz for the mass distribution as a power law neither captures threshold effects nor does it have a solid theoretical motivation.
- The biased treatment of different clusters undergoing either isotropic or smeared aligned CD.

[30] Even though for the hadron production fewer parameters are needed by the cluster model to describe the data.

- The correlations between baryons and antibaryons are way too strong if we only allow them in the CD.
- If we allow the baryons to be produced only during CF, their momentum spectra are disagreeing with data for the current hadronization model.

Note that the first issue results in a non-continuous transition from collinear CF to the later mostly isotropic CD, which is of course unphysical. The second issue also leads to difficulty in tuning the **PSplit** parameters since a tune may drive these parameters to unphysical values in the hope of trying to capture physics, which it cannot and should not describe as has been noted in [94]. With the work in section 5.2 we attempt to address these issues by describing the cluster fission of a cluster as a perturbative emission of a quasi-soft $q\bar{q}$-pair.

5.2 The Perturbative Matrix Element Cluster Fission model

The cluster model gives us a primordial set of clusters $\{C(q_1, q_2)\}$ consisting of either a quark and an antiquark or a (anti)quark and a (anti)diquark, which are all on their respective constituent mass shells and are denoted generically by q_1 and q_2 respectively. As mentioned before this cluster mass spectrum is universal for $e^+e^- \to q\bar{q}$ collisions and peaks at a low energy scale of the order of the PS cutoff Q_0. However, the cluster mass spectrum has a long tail at high masses and in particular also a significant number of events with only one cluster of mass $\sqrt{s}$ if the PS does not emit any partons. In such cases the heavy clusters need to meaningfully dissociate into lighter clusters. As a consequence of the colour evolution picture [7], the CF can evolve perturbatively from the PS cutoff scale down to a truly NP scale. Therefore the PS cutoff scale can be thought of as a matching scale between the PS and the perturbative CF evolution. Therefore a change in the PS cutoff must be picked up by the perturbative CF model such that the overall prediction changes only insignificantly, which we pictorially represent in figure 5.1. This was studied in the context of a dynamical gluon mass in [94] for an angular ordered CF model. However, our approach here differs from [94] by the generality of the actual matrix element instead of a PS like description.

In `Herwig` 7.3.0 the current cluster fission model [44] splits clusters recursively if their mass M is above some probabilistic cutoff, but for our study we will limit ourselves to the previous model of `Herwig` 7.2.3. with a static cutoff described in [2] unless otherwise stated, as it facilitates the interpretation of our findings.

5.2.1 Phase space effects

In order to generically describe the cluster fission in the aforementioned matrix element picture, we first employ the factorization of phase space in order to separate the phase space effects from the actual matrix element. We can write down a general $2 \to 4$ partonic process with a matrix element $\mathcal{M}_{2\to4}(p_1, p_2 \to q_1, q, \bar{q}, q_2)$, where the rate $\Gamma_{2\to4}$ can be written in this manner in $D = d + 1$ space-time dimensions [12]:

$$\Gamma_{2\to4} = \int |\mathcal{M}_{2\to4}|^2 \mathrm{d}\Phi_4, \tag{5.1}$$

$$\mathrm{d}\Phi_4 = \mathrm{d}\Pi_{q_1}\mathrm{d}\Pi_q\mathrm{d}\Pi_{\bar{q}}\mathrm{d}\Pi_{q_2}(2\pi)^D\delta^D(p_1 + p_2 - \sum_f q_f), \tag{5.2}$$

$$\mathrm{d}\Pi_{p_i} = \frac{\mathrm{d}^d p_i}{(2\pi)^d\ 2E_{p_i}}. \tag{5.3}$$

Note that in the above expression we choose the masses of the quarks to be the constituent masses instead of the current masses. This assumption was made since the cluster fission

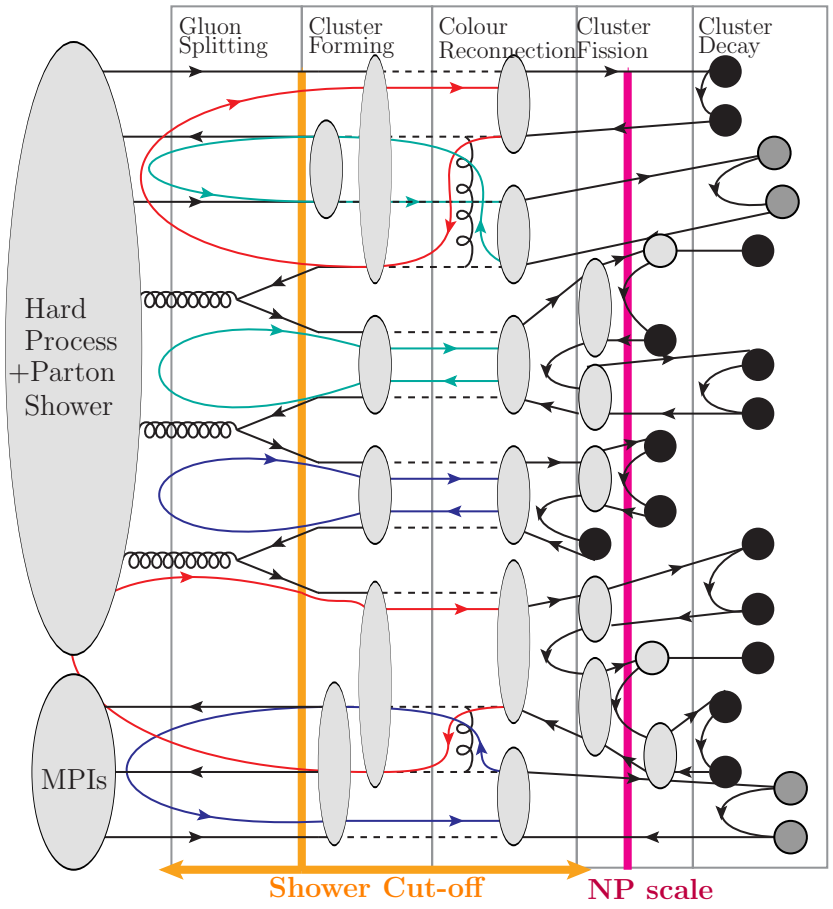

Figure 5.1: Sketch of the cluster hadronization model in the colour evolution picture [7].

happens at a stage, where the current mass description breaks down as it would lead to extremely light clusters. In this context the constituent masses are essentially the IR regulator for the cluster hadronization model.

Rearranging the above expression as described more in detail in the appendix B, we finally arrive at the following equation in 4 space-time dimensions:

$$\Gamma_{2\to4} = \int \mathrm{d}M_1 \mathrm{d}M_2 f_{\mathrm{PS}}(M_1,\, M_2)\; \mathrm{d}\Omega^{\mathrm{COM}} \mathrm{d}\Omega^{\mathrm{COM},1} \mathrm{d}\Omega^{\mathrm{COM},2} |\mathcal{M}_{2\to4}|^2, \tag{5.4}$$

$$f_{\mathrm{PS}} \propto \frac{\sqrt{\lambda(M^2,\, M_1^2,\, M_2^2)\lambda(M_1^2,\, m_1^2,\, m^2)\lambda(M_2^2,\, m_2^2,\, m^2)}}{2M_1 2M_2}. \tag{5.5}$$

Here $f_{\mathrm{PS}}(M_1,\, M_2)$ describes the mass distribution of clusters if the matrix element would have no implicit or explicit dependence on M_1, M_2 i.e. the distribution is coming purely from the 4-particle phase space. The pictorial representation of this factorization is displayed in figure 5.2. We define Ω^{COM} as the solid angle between the original constituent direction p_1 and the child cluster $Q_1 = (q_1 + q)$ in the COM frame of the original cluster. The solid angles $\Omega^{\mathrm{COM,i}}$ are the angles between the child cluster Q_i direction (in the cluster COM frame) and q_i in the COM frame of Q_i respectively.

We display the distribution $f_{\mathrm{PS}}(M_1,\, M_2)$ in figure 5.3 for $m_1 = m_2 = m = m_{u/d}$ at $M = \sqrt{s}_{\mathrm{BELLE/LEP}}$, where $m_{u/d}$ is the constituent mass value of u/d quarks and $\sqrt{s}_{\mathrm{BELLE/LEP}}$ is the COM energy of the BELLE experiment and the various LEP experiments at the Z pole respectively as we will later compare to BELLE and LEP data. One can clearly note that the distribution in 5.3 is very different from a simple power law due to the threshold effects of the

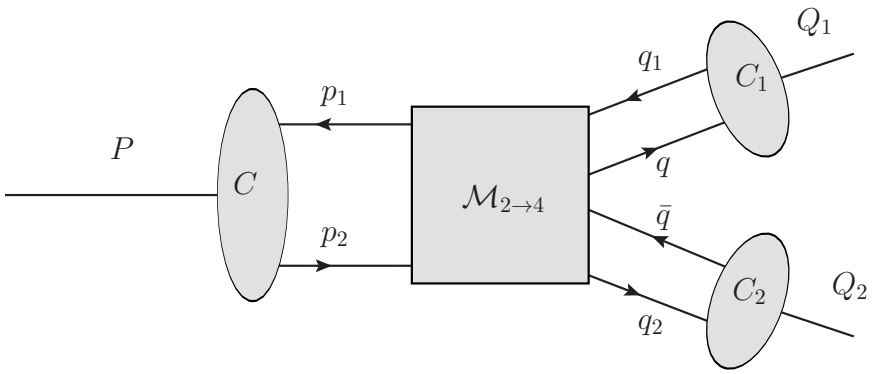

Figure 5.2: Pictorially representation of the phase space factorization for the CF. For details of the derivation we refer to the appendix B.

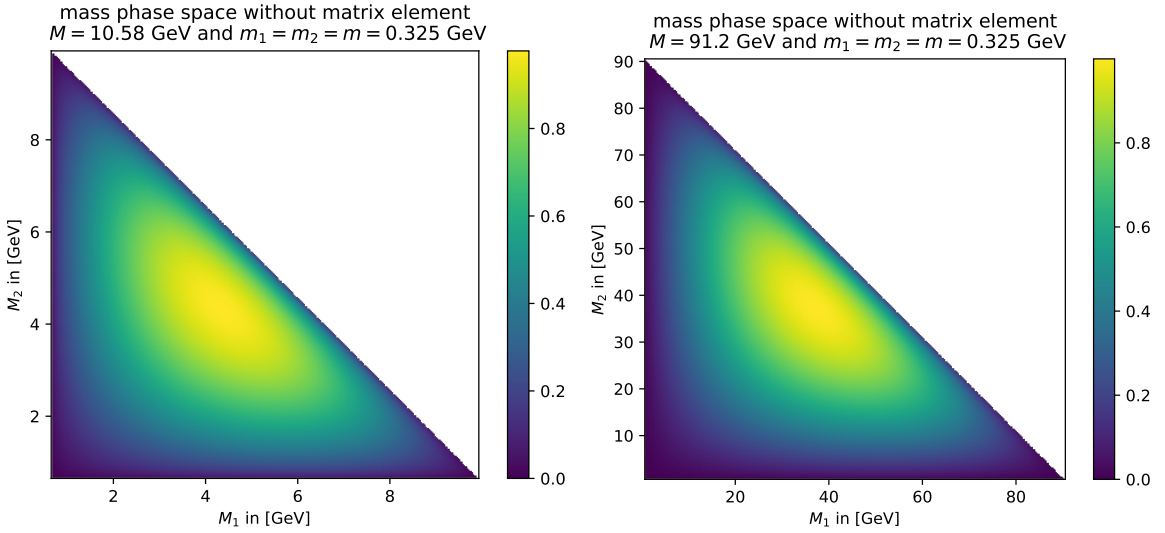

Figure 5.3: The distribution of flat mass phase space weight for a single CF for the maximally massive cluster at BELLE (left) and LEP (right) energies according to (5.5). The colour indicates the dimensionless weight of the flat phase space.

Källén functions in equation (5.5). Furthermore, the pure phase space is rather independent of the mass of the cluster (if it is heavy enough) as one can almost not see any difference between the $\sqrt{s}_{\text{BELLE}}$ mass CF and the $\sqrt{s}_{\text{LEP}}$ mass CF in figure 5.3.

Note that equation (5.4) with a trivial matrix element $|\mathcal{M}_{2\to4}|^2 = 1$ would sample the directions of clusters and their constituents completely isotropically, which is of course unphysical. This implies the necessity for a non-trivial matrix element.

5.2.2 Matrix Element

As an Ansatz for the cluster fission matrix element we choose a tree-level[31] soft $q\bar{q}$-emission, where a t-channel gluon exchange is needed in order to bias the original constituents of the cluster p_1, p_2 to point in a similar direction as the final state momenta q_1, q_2. Note that the s-channel contribution would be suppressed at least by $1/M_C^2$, which is the reason we do not

[31] In principle one could go beyond tree-level see e.g. [7, 157, 158], but since this is a first attempt to add perturbative QCD input to CF we will limit our discussion to tree level only.

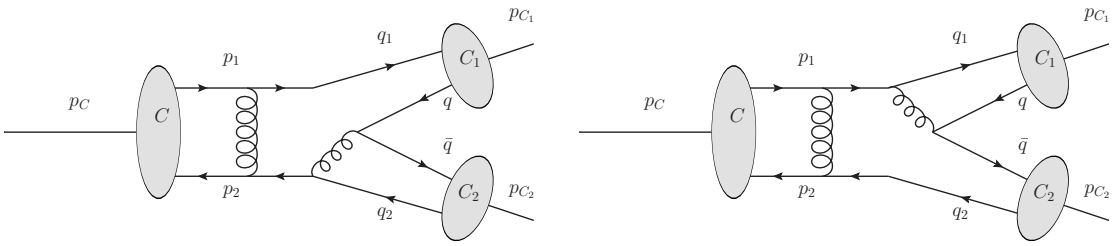

Figure 5.4: The Feynman diagrams of the chosen cluster fission matrix element.

consider it here. In order to simplify the matrix element, we employ the infrared factorization from [158] to factorize the t-channel from the soft function S, yielding in total the following:

$$|\mathcal{M}_{2\to4}|^2 \propto |\mathcal{M}_{2\to2}|_t^2 \times S(q_1,\, q_2,\, q,\, \bar{q}), \tag{5.6}$$

$$|\mathcal{M}_{2\to2}|_t^2 \propto \frac{(q_1\cdot q_2)(p_1\cdot p_2)+(q_1\cdot p_2)(p_1\cdot q_2)}{\left[(p_1-q_1)^2-\epsilon m_g^2\right]\left[(p_2-q_2)^2-\epsilon m_g^2\right]}. \tag{5.7}$$

Note that in our case we break this factorization explicitly by the non-zero constituent masses. This violation of factorization explicitly also breaks the momentum conservation, which we remedy by having the symmetrical denominator for the t-channel. In addition, to this we need to deal with the Coulomb divergence of the t-channel, which stems from the infinite range of the strong interaction if the gluon is massless. However, due to confinement the strong interaction is not even infinite range and therefore the regulator for this divergence should reflect this and be related to Λ_{QCD}. Since for the cluster model we put the gluons after the parton shower on a gluon constituent mass shell m_g, a reasonable regulator for our diagram shall be this gluon mass alongside a parameter ϵ, which we choose to be 1 for all further considerations. Note that the regulation parameter ϵ is in principle a free tunable parameter of the model and is not a RGE type scale that one could vary to estimate uncertainties.

The soft function $S(q_1,\, q_2,\, q,\, \bar{q})$ consists of the following eikonal functions I_{ij}, which are defined as the following in [158]:

$$I_{ij}(p_i,\, p_j,\, q,\, \bar{q}) = \frac{(p_i\cdot q)(p_j\cdot\bar{q})+(p_j\cdot q)(p_i\cdot\bar{q})-(p_i\cdot p_j)(q\cdot\bar{q})}{(q\cdot\bar{q})^2\,[p_i\cdot(q+\bar{q})]\,[p_j\cdot(q+\bar{q})]}, \tag{5.8}$$

$$S(q_1,\, q_2,\, q,\, \bar{q}) = (I_{11}+I_{22}-2I_{12}). \tag{5.9}$$

Note that we again explicitly break the momentum conservation since in the exact soft limit $p_i \to q_i$, but in practice we have $p_i \neq q_i$. For the case at hand we choose q_1, q_2 for the soft function since we want to consider the matrix element shown in figure 5.4, where the $q\bar{q}$-pair is emitted from the final state. The other convention was tried but did not significantly impact the results. Furthermore, we restored the mass dependence of the soft function by replacing $q\cdot\bar{q} \to q\cdot\bar{q}+m^2$, where $m^2 = q^2 = \bar{q}^2$. Even though we have restored the mass dependence in the eikonal functions, we did not introduce a gluon constituent mass parameter here, because it would yield a pole that would need to be regulated by the total decay width of gluon. The argument for this choice is that the process takes place at a high enough scale that this gluon of the matrix element can be treated perturbatively i.e. as massless.

This matrix element does not only have an impact on the directionality of cluster fission but also a significant contribution to the mass phase space. In particular, the soft function has an explicit dependence on M_1, M_2 through the functions $I_{ij} \propto (M_i^2+\ldots)^{-1}(M_j^2+\ldots)^{-1}$. This means that the matrix element impacts also the mass distributions of the clusters, which can be seen in figure 5.5, where we generated a weighted histogram of $\dfrac{1}{\Gamma_{2\to4}}\dfrac{\mathrm{d}^2\Gamma_{2\to4}}{\mathrm{d}M_1 dM_2}$, which

clearly differs from 5.3. The regulated poles of the soft function drive the masses down to lower values, while at the same time the phase space threshold functions forbid the region, where both clusters would be too light to be treated perturbatively. The most striking difference can be seen comparing the BELLE mass cluster splitting compared to a LEP mass cluster splitting. In stark contrast to the flat phase space shown in figure 5.3, which was rather independent of M, in figure 5.5 one can clearly see a narrowing of the distribution.

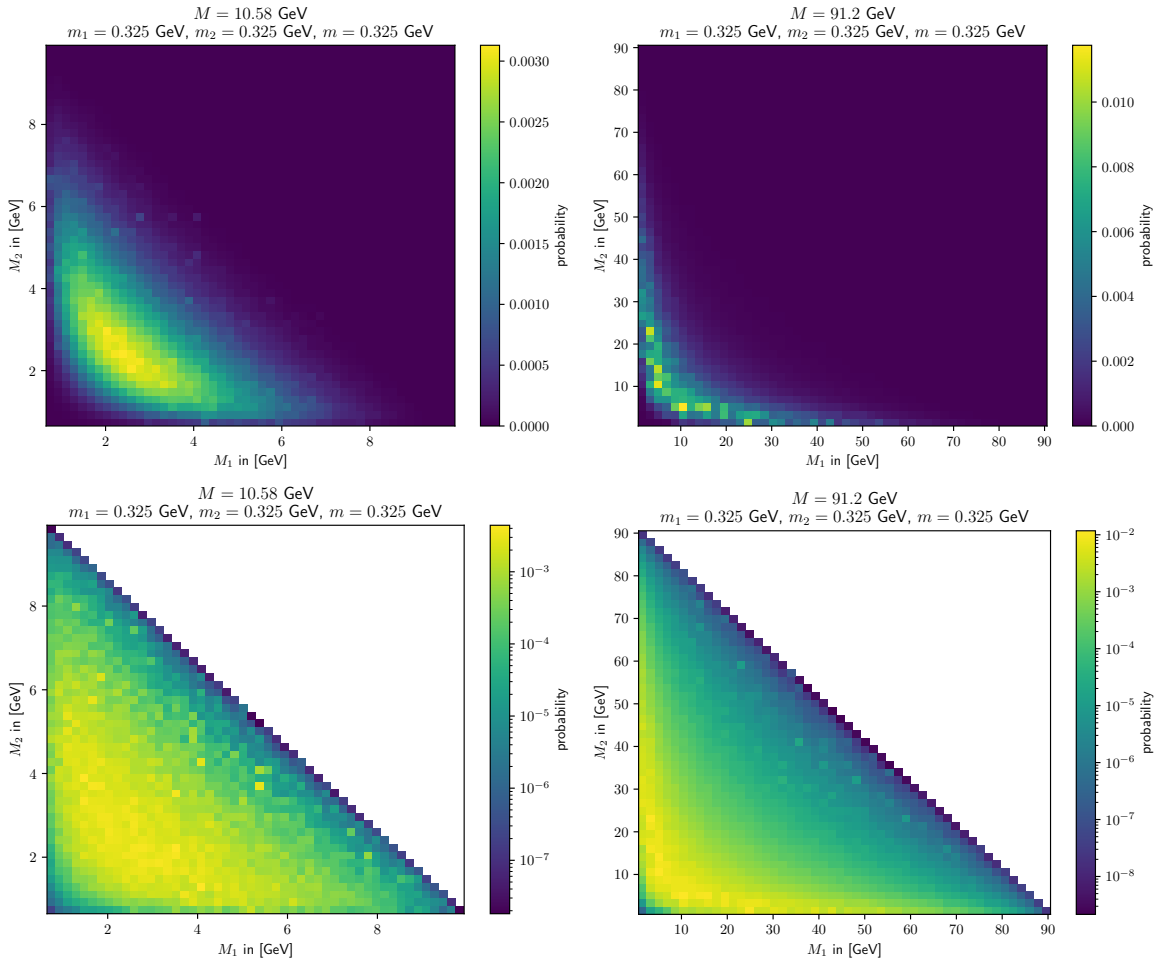

Figure 5.5: Plot of mass phase space according to the matrix element for a single CF for the maximally massive cluster at BELLE (left) and LEP (right) energies. The bottom plots are the same as the above but with a log scale for better visibility.

As we want to later sample also the angles efficiently, we display their distributions by using weighted histograms in figure 5.6. We can see that the angular distributions are indeed quite collinear. Note that here $\cos(\theta)$ is the angle defined in the original cluster mass frame (COM) between p_1 and Q_1 and $\cos(\theta_i)$ are defined in the final cluster Q_i rest frame (COMi) between the direction of Q_i in COM and q_i. For the normalized distribution $f_{\text{COM}}(\cos(\theta)|A)$ we assume the following type of distribution as this is motivated by the t-channel matrix element:

$$f_{\text{COM}}(\cos(\theta)|A) = \frac{A(2+A)}{[1+A-\cos(\theta)]^2}. \tag{5.10}$$

Here $A > 0$ is a parameter of the distribution, which needs to be fitted to the histogram of the angle, which is plotted in figure 5.6. On the other hand for $f_{\text{COM,i}}(\cos(\theta_i))$ we choose

an exponential Ansatz, which is motivated by the almost linear behaviour in the log plot of figure 5.6:

$$f_{\mathrm{COM,i}}(\cos(\theta_i)|\beta_i) = \frac{\beta_i}{1 - e^{-2\beta_i}} e^{\beta_i(\cos(\theta_i)-1)}. \tag{5.11}$$

Here we choose $\beta_i > 0$ and fit this as well to the histograms in figure 5.6 for obtaining the most efficient sampling later on. These parameters A, β_1 and β_2 are of course in general functions of M, m_1, m_2, m, which complicates getting good overall efficiency in the rejection sampling as we will discuss afterwards. Of course if $m_1 = m_2$ this implies that $\beta_1 = \beta_2$.

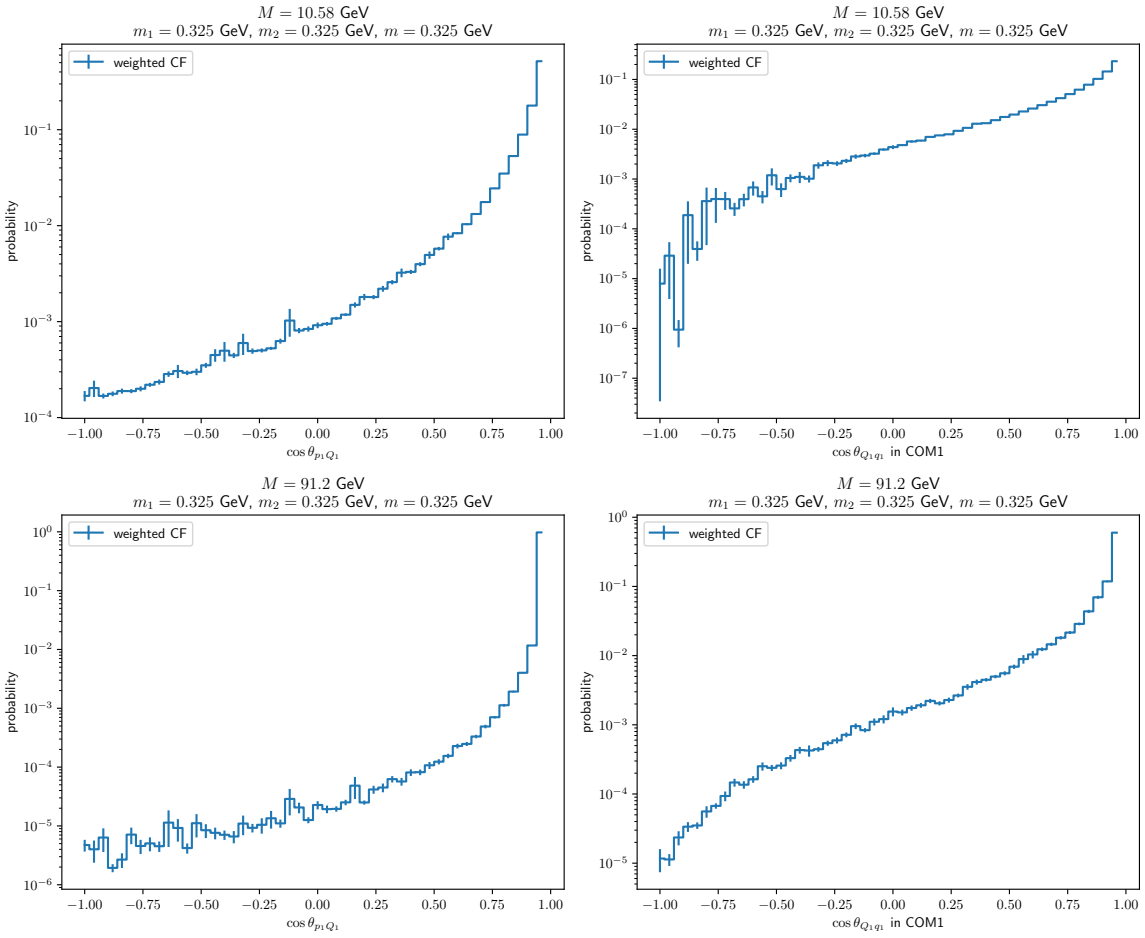

Figure 5.6: Plot of weighted histograms for the total distributions of the COM angle $\cos(\theta) = \cos\theta_{p_1Q_1}$ (left) and the COM1 angle $\cos(\theta_1) = \cos\theta_{Q_1q_1}$ at BELLE energies (top) and LEP energies (bottom).

From figure 5.6 one can clearly see that the more mass M a cluster has, the more aligned the CF will be in both the cluster COM frame (left) and the respective child cluster COM frames (right). This behaviour yields a reasonable interpolation from an essentially fully aligned CF mechanism (as in the `Herwig` default) at high cluster masses towards a more isotropic CD model for lower cluster masses. As the sampling for large cluster masses is quite inefficient even with the importance sampling discussed above, it is instructive to just test what the mass distributions would look like if we sample the angles fully aligned. Sampling the angles fully aligned of course changes the matrix element to the following:

$$|\mathcal{M}_{2\to4}|^2\,[M_1,\, M_2,\, \cos(\theta),\, \cos(\theta_1),\, \cos(\theta_2)] \to |\mathcal{M}_{2\to4}|^2\,[M_1,\, M_2,\, 1,\, 1,\, 1]\,. \tag{5.12}$$

We will therefore not get the same distributions, but a more efficient sampling and more importantly we can assess how much both differ. In figure 5.7 we display the same mass

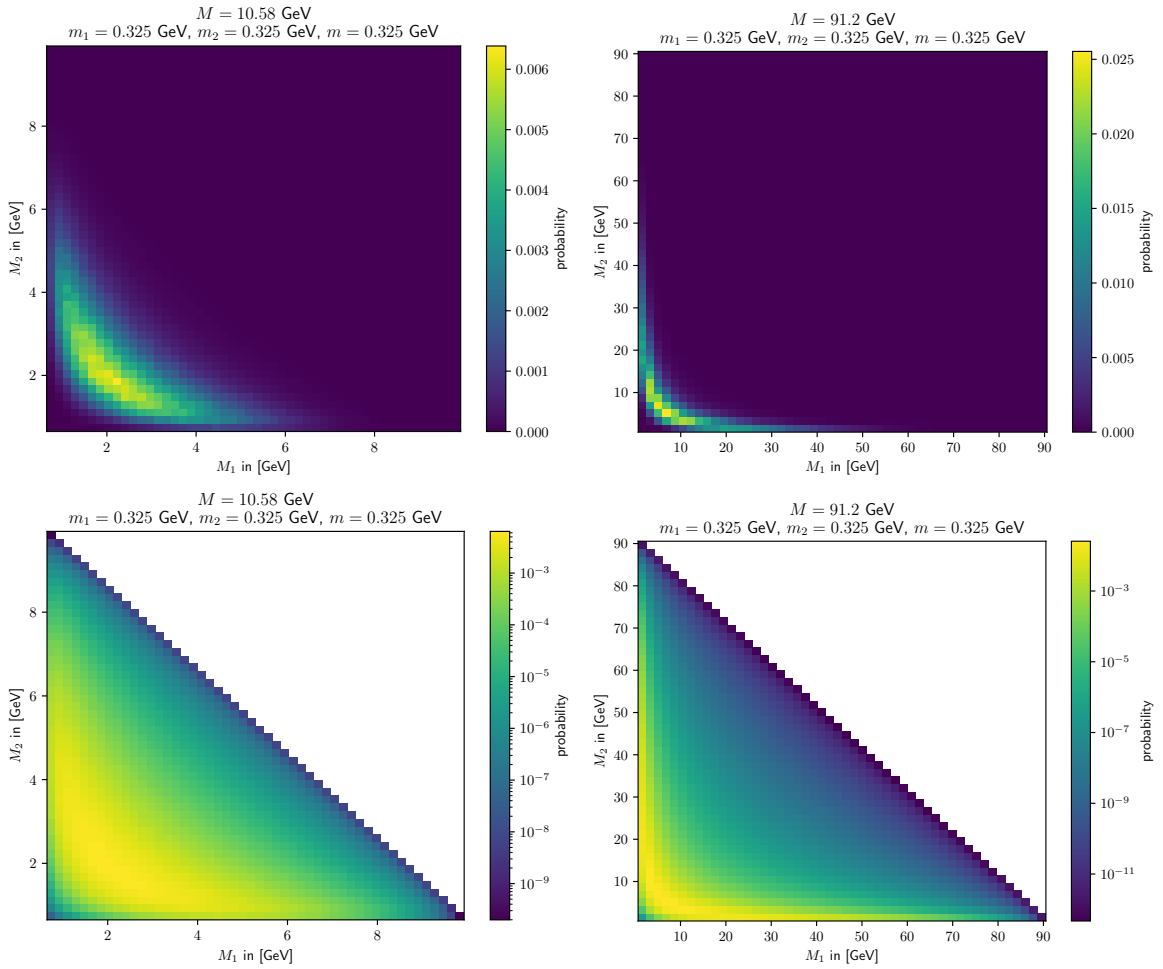

Figure 5.7: Plot of mass phase space according to the matrix element under the constraint of a fully aligned phase space for a single CF for the maximally massive cluster at BELLE (left) and LEP (right) energies. The bottom plots are the same as the above but with a log scale for better visibility.

phase space plots as before in figure 5.5 but for a fully aligned directional sampling. Of course, the difference is not huge between the sampling of the full matrix element in figure 5.5 and the fully aligned sampling in figure 5.7 since the dominant contribution of the full matrix element comes from the fully aligned region. Nonetheless, one can see that for low mass CF the peak of the full matrix element distribution is at higher values and extends more broadly towards large masses compared to the aligned matrix element. As similar feature can be spotted for the large mass CF, but the difference is substantially smaller, which of course is completely consistent with the observation we made before that higher mass clusters are splitting more aligned than lower mass clusters.

5.2.3 The Algorithm for Herwig

Now that we have factorized the phase space and made assumptions on the matrix element, we need to sample from equation (5.4) appropriately and with unit weights. Therefore we implemented the following importance sampling algorithm in `Herwig` for a single cluster fission:

1. **FlavourSampling:** Draw the flavour of the $q\bar{q}$-pair using the default weights $\mathbf{Pwt}(q)$.

2. **MassSampling:** Sample the masses M_1, M_2 uniformly in the allowed region of figure 5.3.

3. **PhaseSpaceSampling:**

   a) Boost from the lab frame LAB to the centre of mass frame of the original cluster (COM).

   b) Sample the direction of the child clusters according to $f_{\mathrm{COM}}(\cos(\theta))$.

   c) Boost in both child cluster's rest frames (COMi for $i \in \{1, 2\}$) respectively.

   d) Sample the direction of constituents according to $f_{\mathrm{COM,i}}(\cos(\theta_i))$ in the COMi frames.

   e) Boost both back to the original cluster rest frame COM.

   f) Boost all momenta from to the COM frame to the LAB frame.

4. Accept the sampled configuration with probability P_{acc}.

Note that we sample the masses M_1, M_2 uniformly, which - albeit not being the most sophisticated choice - is comparatively fast if the actual integrated mass distribution $\frac{1}{\Gamma_{2\to4}}\frac{\mathrm{d}^2\Gamma_{2\to4}}{\mathrm{d}M_1\mathrm{d}M_2}$ is not known or cannot be easily sampled. Furthermore, we always sample the azimuthal angles ϕ_{COM}, $\phi_{\mathrm{COM},1}$ and $\phi_{\mathrm{COM},2}$ uniformly in $[0, 2\pi]$. Note that the two boosts in the points 3e - 3f are necessary since we cannot simply boost from the COMi frames to the LAB frame as we will pick up a rotation since non-parallel Lorentz boosts do not commute. There are some more subtleties to this algorithm, which we discuss more in detail in the appendix A. For this algorithm we have to define P_{acc}, which is given by the following:

$$P_{\mathrm{acc}} = \frac{w_{\mathrm{acc}}}{\lambda_{\mathrm{OE}}} = \frac{f_{\mathrm{PS}}(M_1, M_2)|\mathcal{M}|^2_{2\to4}(\{p_i \cdot p_j\})}{\lambda_{\mathrm{OE}} f_{\mathrm{MS}}(M_1, M_2) f_{\mathrm{COM}}(c_\theta|A) f_{\mathrm{COM},1}(c_{\theta_1}|\beta_1) f_{\mathrm{COM},2}(c_{\theta_2}|\beta_2)}. \tag{5.13}$$

Here we abbreviated $\cos(\theta_i) = c_{\theta_i}$, $\{p_i \cdot p_j\}$ stands for the minimal set of all possible scalar products of the sampled set of four-momenta and λ_{OE} is the overestimate of the expression such that ideally $P_{\mathrm{acc}} \leq 1$ for all phase space. In addition, f_{MS} could be a pre-sampler of the masses M_1, M_2, but since we sample the masses uniformly we set $f_{\mathrm{MS}} = f_{\mathrm{PS,max}}(M)$, which is the overestimate of the mass phase space that we compute in the appendix B.

One should note however that the best overestimate λ_{OE} is a function of M, m_1, m_2 and m in general. Furthermore finding such an efficient overestimate is highly non-trivial especially due to the denominator probability density functions (PDFs) depending on a priori unknown parameters A and β_i. We therefore choose to get an estimate $\hat{\lambda}_{\mathrm{OE}}$ of the overestimate, by sampling the phase space and searching for a maximum of w_{acc} for fixed $m_1 = m_2 = m$ but variable M such that $\hat{\lambda}_{\mathrm{OE}}(M) = \max\{w_{\mathrm{acc}}(M)\}$. In practice, since we are not sure that the estimate for the overestimate is a true overestimate, we allow the user to choose a safety factor $f_{\mathrm{safety}} > 1$ such that we use $\lambda_{\mathrm{OE}}(M) = f_{\mathrm{safety}} \cdot \hat{\lambda}_{\mathrm{OE}}(M)$ in the expression for the probability in equation (5.13).

For the fixed constituent masses we choose the lightest u, d constituent masses because the lightest constituent masses give the largest enhancement. However, for the large range of possible cluster masses, fixed importance sampling parameters A and β_i are way too inefficient. Therefore the parameters $A = A(M)$ and $\beta_i = \beta_i(M)$ are defined as functions of M, which we estimate by plotting the M dependence of the best fits to the weighted CF distributions

of $\cos(\theta)$ and $\cos(\theta_i)$. We find that a decent estimate for the functional dependence on M of these parameters is given by the following power law:

$$A(M) = C_t \left(\frac{M}{1\ \text{GeV}}\right)^{P_t}, \tag{5.14}$$

$$\beta_i(M) = C_{\beta_i} \left(\frac{M}{1\ \text{GeV}}\right)^{P_{\beta_i}}. \tag{5.15}$$

Fitting the parameters C_t, C_{β_i}, P_t and P_{β_i} to weighted CF distributions, we find to a good approximation the values in table 5.1, which we will be using in all plots. However, one should note that we now also need a functional form for the overestimate $\lambda_{\text{OE}}(M)$, which is of course implicitly also a function of $A(M)$ and $\beta_i(M)$. We find that the following expression works for our purposes, where $M_{\min} = m_1 + m_2 + 2m$:

$$\lambda_{\text{OE}}(M) = f_{\text{safety}} w_{\text{acc}}(M_{\max}) \exp\left[\eta \left(\log^{P_{\text{OE}}}\left(\frac{M}{M_{\min}}\right) - \log^{P_{\text{OE}}}\left(\frac{M_{\max}}{M_{\min}}\right)\right)\right]. \tag{5.16}$$

Here $w_{\text{acc}}(M_{\max})$ is the maximal w_{acc} at the maximum mass of clusters $M_{\max}$ at which the fit has been performed. Furthermore, η and P_{OE} are determined from the fit and displayed in table 5.1 alongside the aforementioned parameters. Note that all of these fitted parameters are dependent on the pre-sampler parameters $A(M)$ and $\beta_i(M)$. Since this is still inefficient in general the f_{safety} factor can be chosen by the user to steer the overestimate. One should note however that $f_{\text{safety}} \lesssim 1$ is not giving exactly the correct distribution since it could lead to $P_{\text{acc}} > 1$, which is the reason why the user is informed if such $P_{\text{acc}} > 1$ samples are occurring. On the other hand, if the efficiency is too low and we try more than 10^7 times to sample a single CF process we allow for two options: Either reject the event altogether or revert to the default fully aligned CF. The first option biases the simulation towards more PS emissions (and thus lighter and easier to split clusters), but the second option gives us also a contamination of default CF, which is also not desirable. We choose in all future plots the first option, since we want to study the new CF model. Fortunately, this issue occurs mostly at large energies at e.g. the LEP Z pole. Since this is the bottleneck for this implementation, one would need to develop a more efficient approach for sampling the phase space e.g. using the `HAAG` method [159] for efficient sampling of eikonal matrix elements, which we leave for future work. Nonetheless, our implementation is more flexible in choices for mass and directional distributions and thus more useful as a phenomenological exploration tool of the impact of hadronization on certain observables.

5.3 The New Cluster Decay Kinematics

The current cluster decay (CD) model of `Herwig` [2] forces clusters to decay to two hadrons as already discussed in section 3.5.3. The kinematics of the decay depend on whether at least one of the cluster's constituents has originated from the hard process or the parton shower and has a virtuality $q > m_g$, where $m_g = 0.95$ GeV is the gluon constituent mass or the cluster has been produced during the cluster fission. In the latter case the cluster is decayed fully isotropically in its rest frame. In the first case the hadron directions $\cos(\theta_{p_1,h_1})$ with respect to the initial constituent partons is sampled according to the distribution in equation 3.17. This picture of treating clusters in a two-fold manner is contrary to the consequences from the colour evolution picture that the cluster fission should be treated perturbatively and the shower cutoff should be considered merely as a factorization scale [7].

We therefore present a new cluster decay model that tries to interpolate the cluster fission kinematics and the cluster decay kinematics in a more meaningful way. Similarly to the cluster fission we assume a phenomenological matrix element $\mathcal{M}_{p_1,p_2\to h_1,h_2}$, which in this

Table 5.1: The fitted technical parameters, which we used for the sampling in all future plots for the matrix element.

Parameter	Fitted value
C_t	9.78
P_t	-2.5
C_{β_i}	0.63
P_{β_i}	0.89
$w_{\text{acc}}(M_{\max})$	1.57×10^6 GeV^{-4}
$M_{\max}$	55 GeV
η	16.12
P_{OE}	0.3122

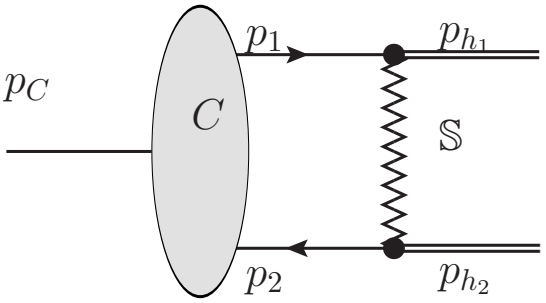

Figure 5.8: The (pseudo) Feynman diagram of the chosen CD matrix element.

case is however a NP $2 \to 2$ parton to hadron process. Due to local parton hadron duality we want the respective hadrons to be strongly aligned to the original partons, which is why we choose a $t-$channel like exchange of a pseudo particle $\mathbb{S}$ of the following form as displayed in figure 5.8:

$$|\mathcal{M}_{p_1,p_2\to h_1,h_2}|^2 \propto \frac{1}{[(p_1-h_1)^2-M_S^2]^2} \propto \frac{1}{[A-\cos(\theta_{p_1,h_1})]^2}. \tag{5.17}$$

Here M_S is a pseudo mass parameter that we set to $M_S = \max\{(m_1 - m_{h_1}), (m_2 - m_{h_2})\}$ in order to have the maximally aligned CD for small momentum constituents[32] without being singular. Note that this phenomenological matrix element completely ignores the spin information of the participating partons and hadrons. However, since we choose M_S to give us a strong alignment of the hadrons towards the constituent partons the dominant contribution comes from the enhancement of the denominator and the spin-dependent numerator is relatively irrelevant.

We can sample the direction very easily from the above matrix element since the masses of the hadrons are fixed. Therefore we can just integrate and invert the distribution for sampling the angle θ_{p_1,h_1} and use uniform sampling of the azimuthal angle in the COM frame of the cluster.

[32]Note that the maximum has to be taken since in general $p_1 \cdot h_1 > \max\{m_1 m_{h_1}, m_2 m_{h_2}\}$

5.4 Phenomenological Results

In this section we present some results of the newly proposed CF and CD model compared to BELLE data [155], which measured the hemisphere di-hadron fragmentation function as a function of $m_{h_1h_2}$ binned in $z = 2(E_{h_1} + E_{h_2})/\sqrt{s}_{\text{BELLE}}$. This observable is very sensitive to the CF model for $z \to 1$ since in this case the PS is essentially not able to emit any partons and the particle production comes mostly from hadronization. Therefore this region is dominated mostly by the recursive cluster fission of a $M_C \lesssim \sqrt{s}_{\text{BELLE}}$ mass cluster.

In figure 5.9 we compare the following three CF options with the new t-channel like CD model presented in section 5.3:

1. `Herwig` 7.3.0 default fully aligned CF (red).
2. New CF model with the flat mass phase space according to equation (5.5) and fully aligned directional sampling (blue).
3. New CF model with the full matrix element dependence (green) with underlying mass distributions as shown in figure 5.5 and angular distributions as shown in figure 5.6.

We can clearly see that the `Herwig` default forms a plateau starting from $(m_{q_1} + m_{q_2})$ until ~ 0.9 GeV, which can be explained by the fact that $\textbf{PSplit}_{\text{tuned}} \simeq 1.0$, which can be shown to yield a triangular distribution as can be seen in figure 4 of [94]. This plateau is not reflected in the data, which hints at a breakdown of the default model for cluster fission. On the other hand we can see that the full matrix element yields substantially better results except for the low $m_{h_1h_2}$ region, which we attribute to the deterministic cut-off in **ClMax**, which we chose for illustration. In addition, also the semi-hadronic decays of clusters $C \to C_1, h_2$ could contribute to that region, which are however suppressed in our case due to the phase space threshold functions.

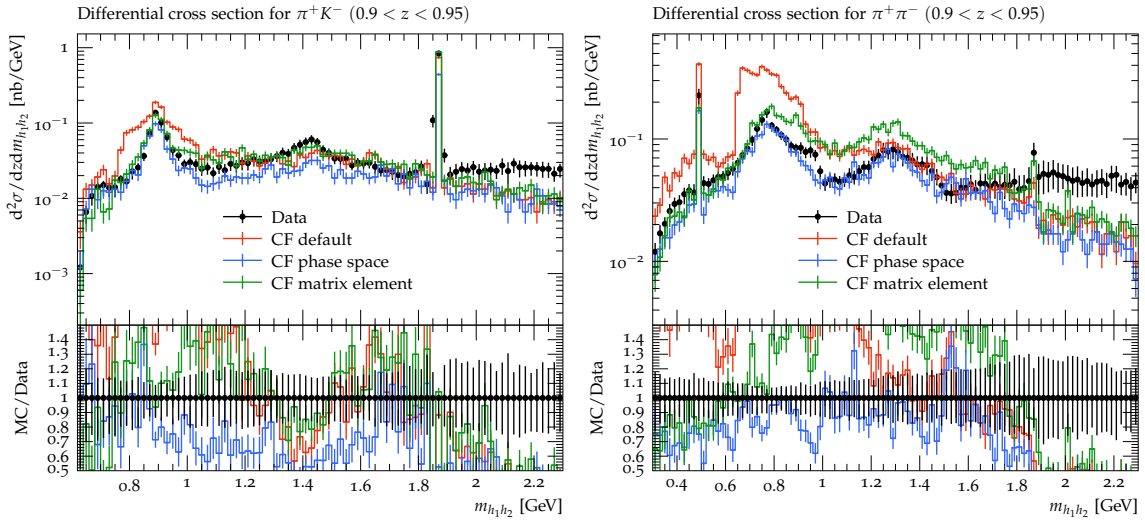

Figure 5.9: The comparison of the different CF models with respect to BELLE data from [155] (public `Rivet` analysis `BELLE_2017_I1607562`). Note that we used here already the t-channel like CD.

In order to further disassemble the CF model we plot the unphysical (but informative) cluster mass distribution $f(M_C)$ after the recursive CF binned in z. Looking at the cluster mass distributions, which we display in figure 5.10, one can clearly see that the CF is essentially regulated by the employed constituent mass thresholds, which is qualitatively the expectation of what the parton shower would do.

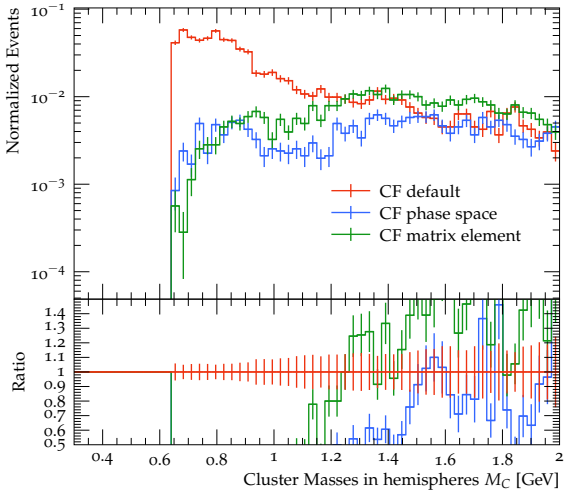

Figure 5.10: The mass distribution of clusters binned in $z \in [0.95, 1]$. Note that we used here already the t-channel like CD.

We can now also compare the different CD models fixing the default `Herwig` CF model. In figure 5.11 we compare the default CD model, the fully aligned CD, the fully isotropic and our new t-channel like CD model. As one can clearly see with the exception of the fully aligned CD the differences are relatively small. Note that the completely different behaviour of the fully aligned CD comes from the CD into two hadrons, which can move in the opposite hemispheres even though the cluster momentum points in the same hemisphere, which is most pronounced for the aligned CD.

The $p_T^{\text{in/out}}$ observable measures the hadron's momentum $\vec{p}$ transverse to the thrust (or sphericity) axis projected on the thrust-major (or sphericity-major) axis for p_T^{in} and projected on the thrust-minor (or sphericity-minor) axis for p_T^{out}. This observable is of course sensitive to the phase space extent of an event and in the soft region also strongly sensitive to hadronization. In figure 5.12 we display the variation of the CD model with the default CF model, where it can be seen that our new t-channel like CD model does describe the data better and reduces the enhancement at around 1 GeV. This effect of enhancing the lower momenta for a more aligned CD is expected and a general feature of boosted decays, which can be easily derived by considering a cluster of two on-shell constituents at rest with momenta $p_{1/2} = (E_{1/2}, \pm\vec{p})^T$, where $|\vec{p}| = \lambda(M_C^2, m_1^2, m_2^2)/(2M_C)$. We decompose their momenta in parallel and perpendicular components $\vec{p} = \vec{p}_\parallel + \vec{p}_\perp$ with respect to the boost direction in which we want to boost them. Now we boost both vectors in the lab frame of the cluster with the Lorentz transformation $\Lambda_\parallel(\eta)$, with the rapidity η defined as $\sinh\eta = |\vec{p}_C^{\,\text{LAB}}|/M_C$, where we assume the two extreme cases of $\vec{p}_\parallel = 0$ and $\vec{p}_\perp = 0$ yielding the following, where $||\cdot||_3$ is the norm of the spatial vector of a four momentum:

$$||\Lambda_\parallel(\eta)p_{1/2}||_3 = \begin{cases} \sqrt{(E_{1/2}\sinh\eta)^2 + \vec{p}_\perp^{\,2}} & \text{for } \vec{p}_\parallel = 0, \\ |E_{1/2}\sinh\eta \pm |\vec{p}_\parallel|\cosh\eta| & \text{for } \vec{p}_\perp = 0. \end{cases} \tag{5.18}$$

Now even though if both cases have the same magnitude, i.e. $|\vec{p}_\perp| = p$ and $|\vec{p}_\parallel| = p$ respectively, the magnitude of the boosted $\vec{p}_1$ will always be larger for the aligned decay, but for the aligned decay the magnitude of the boosted $\vec{p}_2$ a substantial cancellation is occurring, which is not

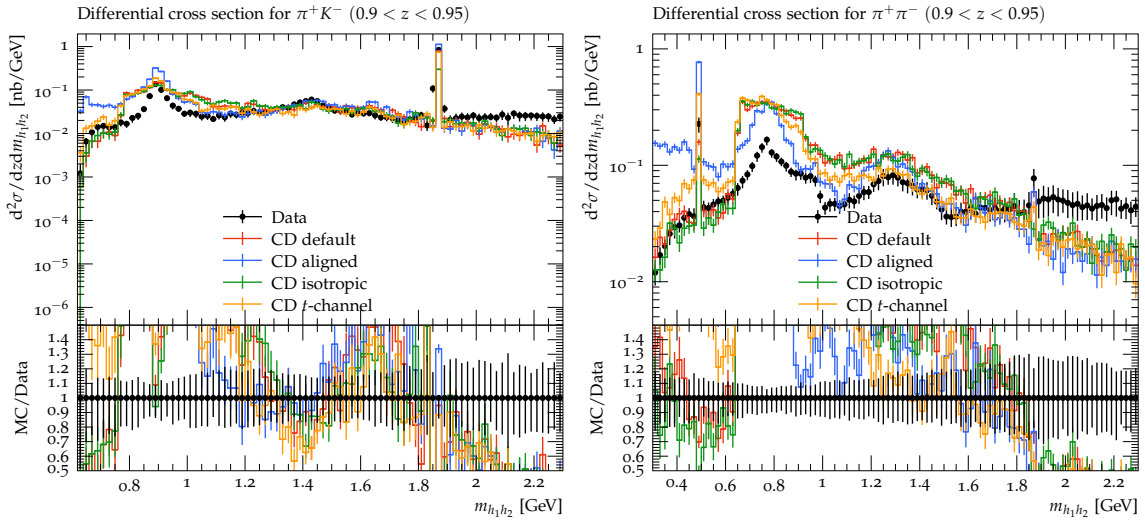

Figure 5.11: The comparison of the different cluster decay models with respect to BELLE data from [155] (public `Rivet` analysis `BELLE_2017_I1607562`). Note that we used the default cluster fission model.

the case for transverse decay. In fact, if we consider an expansion in $m_i/p \ll 1$ we get the following expression for the aligned boosted decay of $p_{1/2}$ for both cases:

$$\sqrt{(E_{1/2}\sinh\eta)^2 + p^2} \approx p\cosh\eta\left(1 + \frac{m_{1/2}^2}{2p^2}\tanh^2\eta\right), \tag{5.19}$$

$$|E_{1/2}\sinh\eta \pm p\cosh\eta| \approx p\ e^{\pm\eta} + \frac{m_{1/2}^2}{2p}\sinh\eta. \tag{5.20}$$

Here one can clearly see that the aligned boosted decay leads to one small momentum and one large momentum, while transverse boosted decay leads to two similar momenta if the mass difference is not large. This effect can be seen in the overall momentum distribution $x_p = 2|\vec{p}|/\sqrt{s}$ displayed in figure 5.12, which shows exactly the enhancement for low and high momenta (and reduction of medium momenta) the more aligned the CD becomes. This also explains the coincidence of multiple lines intersecting at similar values of the observables in all of the plots in figure 5.12.

In figure 5.13 we display the same $p\bar{p}$ correlations measured by ARGUS [152], which we showed in figure 4.5 for the new options of the CF model, where the "phase space CF" is just the flat mass phase space without matrix element and the "ME CF baryons only" is the full CF matrix element sampling. Note that in both cases only the CF model is allowed to produce baryons (but the CD model is the new t-channel like). Furthermore, we show also the new t-channel CD model for baryons, where of course all baryons are produced in the CD model.

One can see that this new CD model does not significantly improve the correlations, which we would not expect anyway. The new CF baryons with the flat phase space do seem to improve the situation even though the $\phi_T = 180°$ bin is higher than the default CF baryon model. The full matrix element CF for baryons appears to give a similar behaviour as the BCR in figure 4.5, which is most likely a coincidence though. Nonetheless, for ME CF baryons the same hemisphere correlations do deviate quite substantially from the data, but are still much better compared to the default CD baryons and the opposite hemisphere data matches very well the data. We want to stress that using the ME CF to produce baryons via an effective diquark-antidiquark pair is a very simplifying assumption, which limits the predictive power

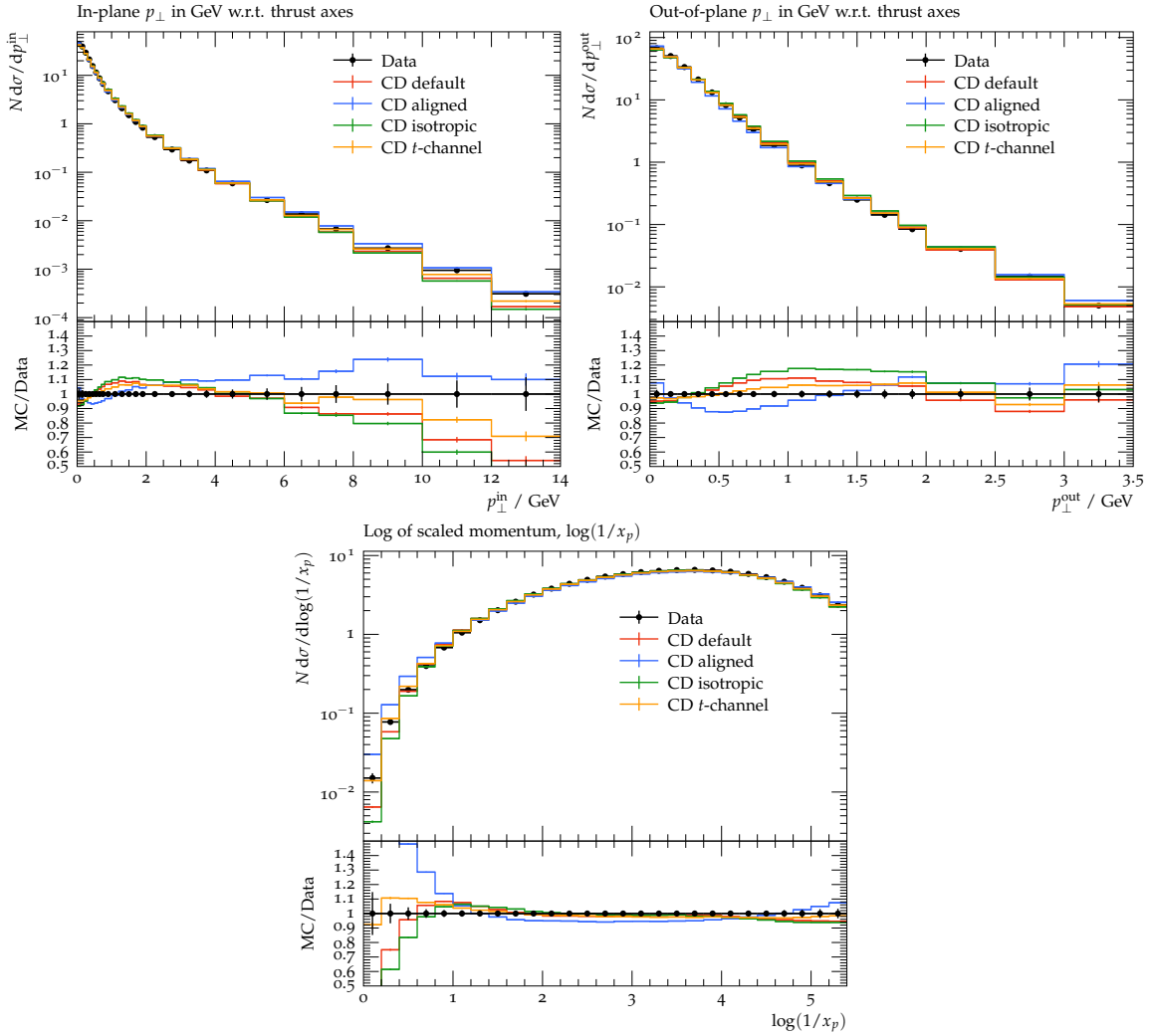

Figure 5.12: The $p_T^{\mathrm{in/out}}$ distribution and the $\zeta_p = -\log x_p$ distribution measured by DELPHI [160] (public `Rivet` analysis `DELPHI_1996_S3430090`). We show a variation of different CD models (keeping the `Herwig` default CF), where "default" is the `Herwig` default, "aligned" is a fully aligned CD, "isotropic" is a completely isotropic CD and "t-channel" is our phenomenological matrix element CD model.

of the baryon production from this mechanism. For a more detailed analysis one would need to study the emission of two soft $q\bar{q}$ pairs from a cluster and examine its limits to see whether one can draw conclusions on how baryon production during CF could look like. Also, the interleaving of the CF model with the CR model could have a substantial impact on the baryon production mechanism.

Correspondingly we display the momentum spectra of hyperons for the new models in figure 5.14, which we can compare to the default models with CF baryons from figure 4.6. As expected both CD baryon mechanisms deliver the soft peak in the momentum spectrum of the Λ^0 baryons. However, surprisingly the matrix element CF does also yield a clear soft peak and a less enhanced peak for the z distribution, while the pure flat phase space CF is not enough to ensure the formation of the soft peak. As before we want to stress that this CF model for baryons is very simplified, but it appears promising that the soft peak of the momentum distribution can in principle be modelled by this matrix element CF model.

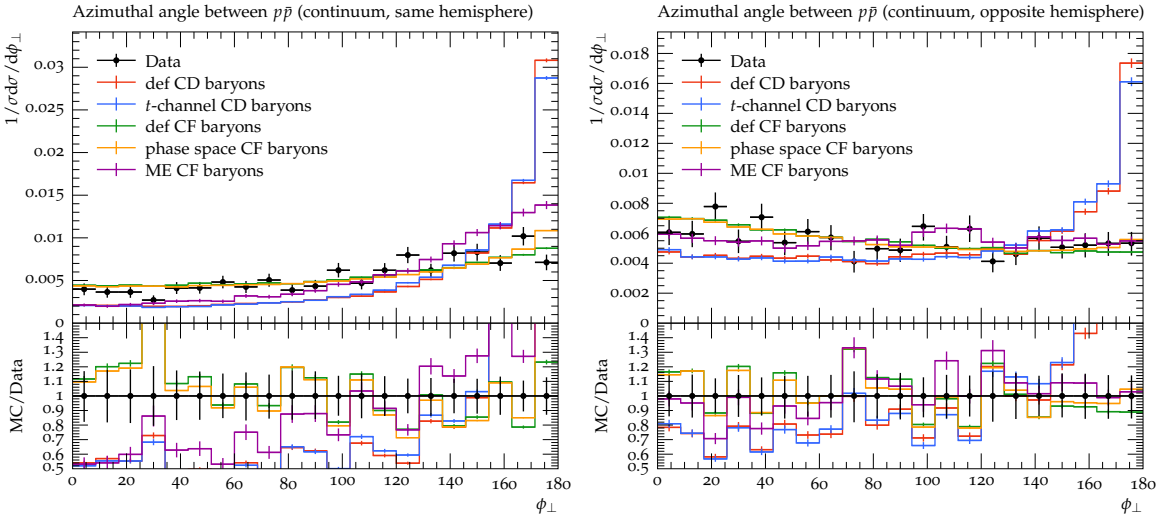

Figure 5.13: The $p\bar{p}$ azimuthal angular correlations for e^+e^- collisions at $\sqrt{s} = 10$ GeV measured by ARGUS [152] (public `Rivet` analysis `ARGUS_1988_I266892`) for the same and opposite hemisphere for various CF and CD models. Note that for the red line, baryons are only generated by the default CD model and for the blue line using the new t-channel CD model. For the green line baryons come only from the default CF model, while for the yellow line the flat mass phase space CF model was used and for the purple line the full matrix element CF model was used.

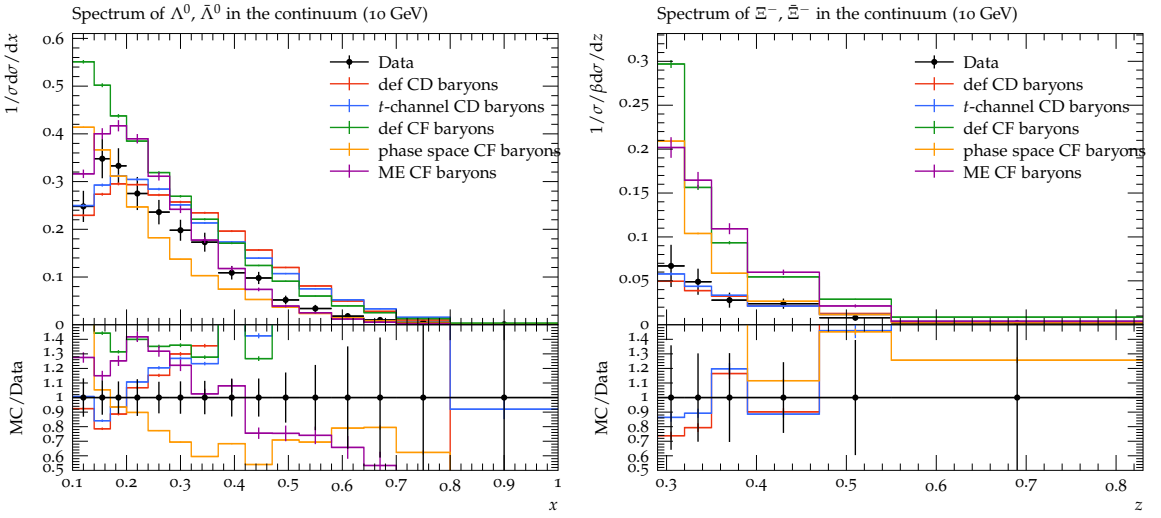

Figure 5.14: The Λ^0 and Ξ^- baryon $x = 2|\vec{p}|/\sqrt{s}$ and $z = 2E/\sqrt{s}$ distributions respectively for e^+e^- collisions at $\sqrt{s} = 10$ GeV measured by ARGUS [154] (public `Rivet` analysis `ARGUS_1988_I251097`) for various CF and CD models. Note that for the red line, baryons are only generated by the default CD model and for the blue line using the new t-channel CD model. For the green line baryons come only from the default CF model, while for the yellow line the flat mass phase space CF model was used and for the purple line the full matrix element CF model was used.

To examine the behaviour of the CF model it is instructive to show the cluster mass and momentum distributions after the CF and its ratio to the distributions before the CF has happened, which is exactly what we display in figure 5.15 for the ARGUS COM energy $\sqrt{s} = 10$ GeV. We can compare this to the BELLE energy distributions, which we displayed

in figure 4.9 for either no CF or no PS. As we claimed that our CF model should behave more similarly to the PS as its intrinsic motivation comes from the perturbative evolution, we expect that the distribution of clusters after CF should be somewhat similar to the distribution before the CF, which one can see clearly in figure 5.15.

While the default models yield a significantly different from unity ratio distribution, especially for low masses and low momenta, the matrix element CF yields a ratio very close to 1 except of course the $x_C = 0$ bin[33]. The bins above the threshold for the CF are also deviating, which is an unphysical relic of our static hard cutoff for the CF model. Interestingly the pure flat phase space CF is not enough to give a similar cluster mass/momentum distribution compared to the distribution before the CF has happened, but it gives a better (ratio close to 1) result for the cluster mass distribution. We should also note that in all of the plots that we have shown (and will be showing) the constant gluon constituent mass and isotropic NP splitting of the gluons have been used i.e. the gluons are on their constituent mass shell m_g and are isotropically decaying in the gluons' rest frame to a light $q\bar{q}$ pair, which could affect the whole discussion around cluster mass spectra as has been explored in [94].

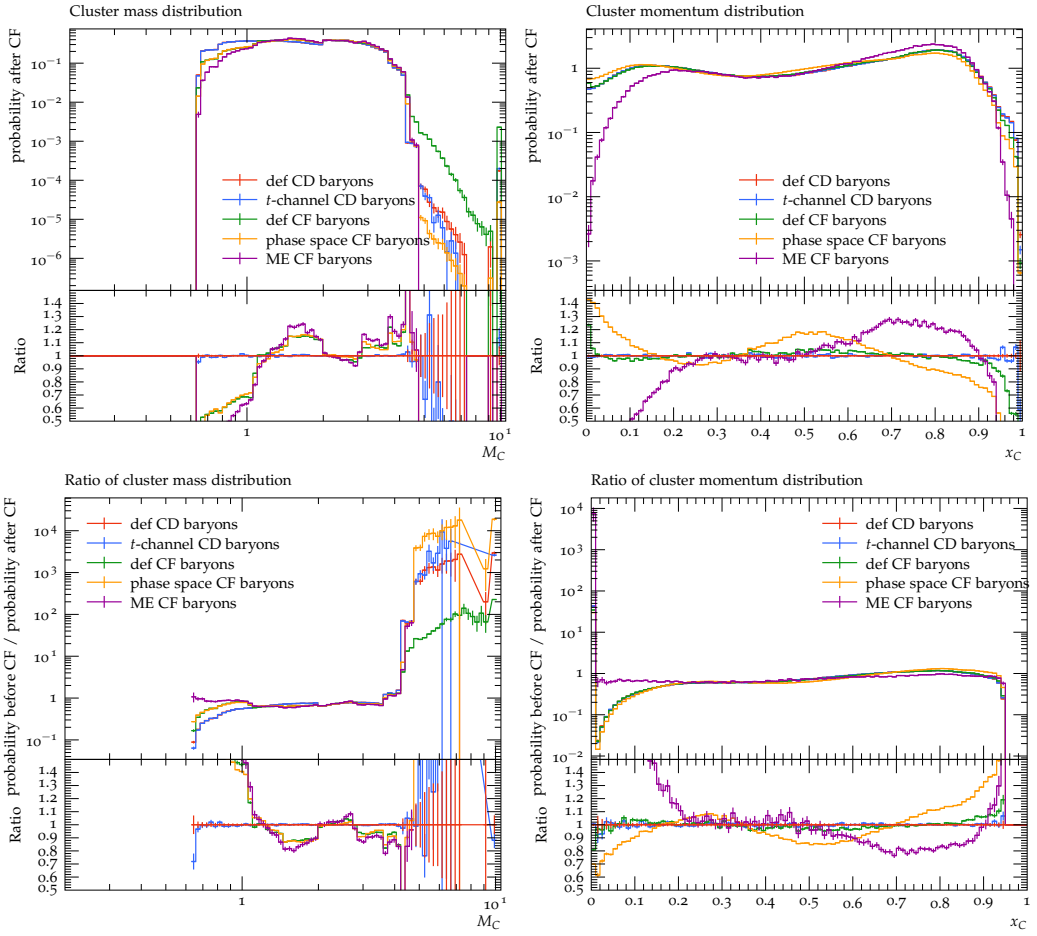

Figure 5.15: The cluster mass M_C (left) and momentum $x_C = 2|\vec{p}_C|/\sqrt{s}$ (right) distributions after the cluster fission for different CF models at the ARGUS COM energy $\sqrt{s} = 10$ GeV on the top plots. Correspondingly on the bottom we show the ratio of the normalized distributions before CF and after CF. Note that for the red line, baryons are only generated by the default CD model and for the blue line using the new t-channel CD model. For the green line baryons come only from the default CF model, while for the yellow line the flat mass phase space CF model was used and for the purple line the full matrix element CF model was used.

[33] Which comes from the existence of a single $q\bar{q}$ cluster with total momentum 0.

5.5 Sensitive Observables

In addition to the improved behaviour for the measured observables in figures 5.9, 5.12 and 5.14, we also want to propose sensitive observables to the CF and CD models respectively, which are able to discriminate between these two mechanisms to further refine the models. In particular, we want to examine the generalized angularities and multi-energy correlations, which are sensitive to the different stages of hadronization. The generalized angularities λ_β^α introduced by [161, 162] are defined as the following:

$$\lambda_\beta^\alpha = \sum_{i\in\{\text{jet}\}} z_i^\beta \theta_i^\alpha, \tag{5.21}$$

where $\theta_i := \sqrt{2(1-\cos(\hat{\theta}_i))}$ is defined with $\hat{\theta}_i$ being the angle between jet constituent i and the jet. The energy fraction $z_i = \dfrac{E_i}{E_{\text{vis}}}$ is defined with $E_{\text{vis}} = \sum_{i\in\{\text{jet}\}} E_i$ and gives a measure of hardness. Different powers of α and β provide different weighting of softness and collinearity and give insights into different regimes of the IR and collinear limits. In particular, note that for $\beta > 0$ IR safety is guaranteed and for $\beta = 1$ also collinear safety holds true, such that for $\beta = 1$ the angularities are IRC safe.

For the case of e^+e^- collisions we choose the Durham k_T-algorithm [26] with the E-recombination scheme and the Winner-Takes-All (WTA) generalized k_T-algorithm [23,24] from `FastJet` [21], where we ask for 2 exclusive jets.

We display the discriminative power of the angularities on different stages of the hadronization in figures 5.17 and 5.16, where we compare a variation of the CF model (left) and a variation of the CD model (right) for different values of α and β. In particular, one can clearly see in figure 5.17 that for $\alpha = \beta = 0.1$, which is close to the limit $\alpha, \beta \to 0$ to pure multiplicity, the CF model is very sensitive while the CD is fairly irrelevant. This should not come as a surprise since the CF is associated with particle production, while the different CD models are not producing new multiplicity, but only changing the final state momenta of the hadrons. Interestingly however the fully aligned CD does still deviate slightly from all of the remaining CD models, which is most likely an effect of the finite values of α and β, which leads to an expansion of the angularities in the following manner:

$$\begin{aligned}\lambda_\beta^\alpha \approx N_{\text{jet}} + \sum_{i\in\{\text{jet}\}} &\beta\log(z_i) + \alpha\log(\theta_i) + \alpha\beta\log(z_i)\log(\theta_i) \\ &+ \mathcal{O}\left[\alpha^2\log^2(\theta_i)\right] + \mathcal{O}\left[\beta^2\log^2(z_i)\right],\end{aligned} \tag{5.22}$$

where here N_{jet} is the multiplicity of the jet. Of course, this is only a good approximation if the logarithms here are sufficiently close to zero. Therefore the subleading contributions in equation (5.22) can depend on the momenta and can lead to small deviations.

Furthermore, we can also see in figures 5.17 and 5.16 that 3 or even 4 different simulations intersect at a common point of the observable, which we find in almost all plots of the angularities and later in the multipoint energy correlations, for which we do not have a good explanation.

On the contrary, if we look at figure 5.16, where we display the IRC safe angularity for $\alpha = 0.1$ and $\beta = 1$, we can see that albeit there is a strong dependence on different CD models (right), the dependence on the CF model is less strong especially the difference between the pure phase space effects and the matrix element is comparatively smaller. This might be a feature of the fact that this observable is IRC safe. This claim is supported by the comparison to lower

energies e.g. at BELLE results in which the CF is more sensitive, which could come from the hadronization power corrections of order $\left(\Lambda_{\mathrm{QCD}}/\sqrt{s}\right)^p$, which are larger for $p \geq 1$ at lower $\sqrt{s}$ energies. Interestingly the CD is nonetheless strongly sensitive to this observable, which might indicate that the CD is a truly NP phenomenon, whose effects on IRC safe observables are not protected by perturbative QCD arguments.

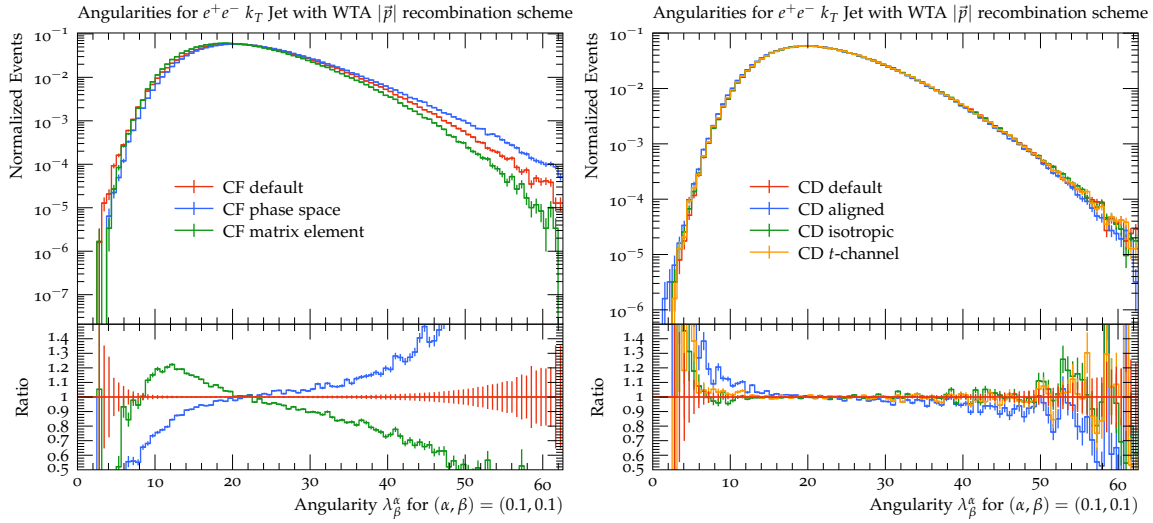

Figure 5.16: The generalized jet angularities for $\alpha = 0.1$, $\beta = 0.1$ for the KT WTA algorithm. We show a variation of the cluster fission models with the t-channel like cluster decayer (left) and the different cluster decay models with the `Herwig` default cluster fission (right).

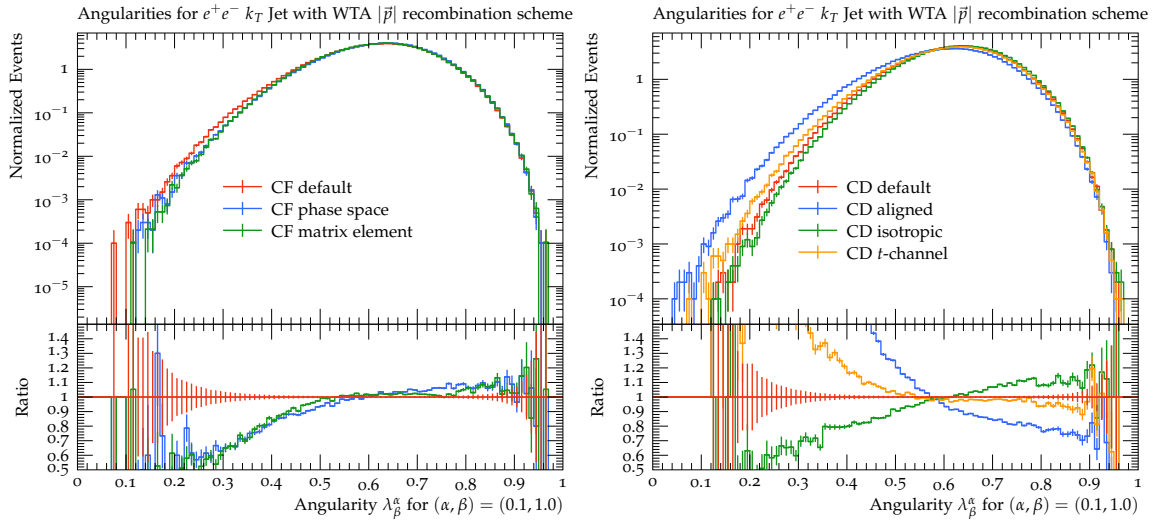

Figure 5.17: The generalized jet angularities for $\alpha = 0.1$, $\beta = 1.0$ for the KT WTA algorithm. We show a variation of the cluster fission models with the t-channel like cluster decayer (left) and the different cluster decay models with the `Herwig` default cluster fission (right).

We summarize our findings for the angularities in the α-β plane in the sketch of figure 5.18. We find that only for $\alpha \ll 1$ the angularities can discriminate between CF and CD effects. For larger α the general sensitivity decreases for all values of β. On the other hand for large $\beta \simeq 2$ we get angularities, which are sensitive to both CF and CD models. As discussed before for $\alpha = 0.1$ and $\beta = 0.1$ we get a discriminative observable that could be used to distinguish between CF models without precise knowledge about the CD model (see figure 5.16). Similarly for $\alpha = 0.1$ and $\beta = 1$ we get a discriminative observable that could be used

to distinguish between the CD models without precise knowledge about the CF model (see figure 5.17).

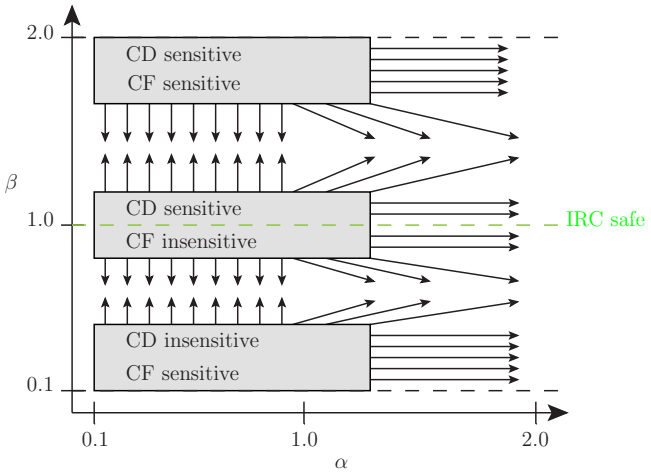

Figure 5.18: A summary sketch of the angularity parameter space of α, β with its corresponding sensitivities to the cluster fission and cluster decay. The arrows point towards decreasing sensitivities and the boxes represent the regions with the most sensitivity and discriminative power.

In addition, to the angularities we look at weighted multi-point energy correlations $\mathrm{ENC}_\gamma(\theta)$, which we define as follows similar to [163, 164]:

$$\mathrm{ENC}_\gamma(\theta) = \frac{1}{\sigma_{\mathrm{tot}}} \sum_{m=N}^{\infty} \int \mathrm{d}\sigma_m \mathcal{W}_m^\gamma[\theta, \{p_i\}_m], \tag{5.23}$$

$$\mathrm{d}\sigma_m = \mathrm{d}\sigma(e^+e^- \to p_1, \ldots, p_m), \tag{5.24}$$

$$\sigma_{\mathrm{tot}} = \sum_{m=2}^{\infty} \sigma_m, \tag{5.25}$$

$$\mathcal{W}_m^\gamma[\theta, \{p_i\}_m] = \frac{1}{D_m^\gamma} \sum_{i_1<\ldots<i_N}^{m} \left(\prod_{k=1}^{N} E_{i_k}^\gamma \right) \delta(\hat{\theta}(\{\hat{p}_{i_k}\}_N) - \theta), \tag{5.26}$$

$$D_m^\gamma = \sum_{i_1<\ldots<i_N}^{m} \left(\prod_{k=1}^{N} E_{i_k}^\gamma \right). \tag{5.27}$$

Here $\hat{\theta}(\{\hat{p}_i\}_N)$ is a symmetric function of the N particle directions on the subset $\{p_i\}_N \subseteq \{p_i\}_m$ of the m particle final state $\{p_i\}_m$. Note that the N-point correlations $\mathrm{ENC}_\gamma(\theta)$ are normalized to 1, where the total inclusive cross section σ_{tot} was defined in equation (5.25).

Due to the large computational cost of the $\mathrm{ENC}_\gamma(\theta)$ for large N, which is $\mathcal{O}(m^N)$, we limit ourselves to the cases $N \in \{2, 3\}$. For $N = 2$ the regular IRC safe[34] energy-energy correlations are recovered if the function $\hat{\theta}(\hat{p}_1, \hat{p}_2) = \theta_{12}$ and $\gamma = 1$ is chosen, but since we are not reliant on any recursive infrared safety condition the value of γ can be an arbitrary real number. In particular, for $\gamma > 0$ the observables are IR safe, for $\gamma = 0$ the observables are IR un-safe and for $\gamma < 0$ we call the observable IR "dangerous" since it would diverge in the IR limit[35]. Here we limit ourselves to $\gamma \in \{0, \pm 1, \pm 2, \pm\infty\}$ even though fractional values are of course also possible. In fact, we will display only the $\gamma = \pm\infty$ correlations since we found that the

[34] Here strictly speaking for true collinear safety the contact terms would need to be added (see later).
[35] Which in practice never happens with massive hadrons in the final state.

in-between values for γ are mostly an interpolation between $\gamma = -\infty$ and $\gamma = +\infty$ with no new insights. "Collinear safety" can only be guaranteed by $\gamma = 1$ and an appropriate choice of $\hat{\theta}$, where here we are ignoring the $\theta = 0$ bin i.e. neglecting the contact terms[36], which strictly speaking would not be collinear safe. Therefore we mark "collinear safety" in this sense under quotation marks to distinguish it from strict collinear safety. Note here that we will call $\gamma \to +\infty$ as the "Winner-Takes-All" (WTA) correlation and the $\gamma \to -\infty$ as the "Soft-Takes-All" (STA) correlation, which correspond to filling only the largest for WTA (smallest for STA) product of energies per event. For $N = 3$ we choose the function $\hat{\theta}(\hat{p}_1, \hat{p}_2, \hat{p}_3)$ as the minimum and maximum of the pair-wise angles θ_{ij} such that:

$$\hat{\theta}_{\min}(\hat{p}_1, \hat{p}_2, \hat{p}_3) = \min_{i \neq j}\{\theta_{ij}\}, \tag{5.28}$$

$$\hat{\theta}_{\max}(\hat{p}_1, \hat{p}_2, \hat{p}_3) = \max_{i \neq j}\{\theta_{ij}\}. \tag{5.29}$$

Note that only the choice of $\hat{\theta}_{\min}$ is a "collinear safe" choice, but in the quest for studying soft physics we are not limited to strictly or non-strictly collinear safe observables either.

In addition, to the inclusive final state energy correlations we looked at energy correlations within two exclusive jets clustered using the Durham k_T-algorithm and computed the ENC_γ on the set of particles within each jet and scaled the overall observable by 2 (the number of jets) such that the normalization to unity is recovered.

Note that unless otherwise stated all plots of the energy correlations were performed at the COM energy of the LEP Z pole measurements. In figure 5.19 we display the multiplicity distribution of each exclusive jet as a sanity check and to compare the results to the angularities for $\alpha = \beta = 0.1$ in figure 5.16. One can clearly see that for pure multiplicity the aligned CD does agree with the rest as expected, which proves that the angularities for $\alpha = \beta = 0.1$ are not exactly the same as the multiplicity distributions.

For the IR dangerous and not "collinear safe" STA $\mathrm{E3C}_\gamma(\theta_{\max})$ observable, which we present in figure 5.20 for the same CF (left) and CD (right) model variations, we can clearly see that the CF model is more sensitive than the CD model. Except for the fully aligned CD all CD models are essentially the same for large enough angles $\theta_{\max}$, while for the CF models there are some differences even though only < 20 %. Since this observable is IR-dangerous, we would expect large corrections also from the perturbative regime. Indeed the CF model seems to have quite an impact on the $\mathrm{E3C}_\gamma(\theta_{\max})$ observable. Interestingly however this particular observable seems to be quite indifferent to the CD model. This could originate from the fact that our CD model is only decaying clusters to two hadrons, which are most likely the closest in angle and therefore are ignored by $\theta_{\max}$.

If we compare these findings to the IR safe observable WTA $\mathrm{E3C}_\gamma(\theta_{\max})$ observable, which we show in figure 5.21, one can see that the CD model suddenly becomes sensitive to a similar extent as the CF model. Let us recall what the WTA (STA) scheme exactly means: We take only the triplet of hadrons from the jet (or an event) whose product $w_{ijk} = E_i E_j E_k$ is maximal (minimal for STA), which therefore tells us that the three hardest hadrons from a jet (or an event) are influenced much more strongly by the CD model because their corresponding clusters are carrying a large amount of momentum. On the contrary, the softest hadron triplet most likely originates from low momentum clusters and therefore its constituent's momentum is most likely isotropically distributed, which washes out any CD model effects. So in conclusion the STA $\mathrm{E3C}_\gamma(\theta_{\max})$ observable is able to discriminate between CF and CD models.

[36] Since the sums in equations (5.26) and (5.27) run only over non-equal particles compared to e.g. [165].

If we compare the three point correlations $\mathrm{E3C}_\gamma(\theta_{\max})$ with two point correlations $\mathrm{E2C}_\gamma(\theta)$, we can see some differences. Comparing STA $\mathrm{E3C}_\gamma(\theta_{\max})$ correlation in figure 5.20 with the STA $\mathrm{E2C}_\gamma(\theta)$ correlations, which we display in figure 5.22, we can see that there are very few differences, but the sensitivity of the CF model is more pronounced in the three-point correlations. This is expected since the maximum of the angular distances for a triplet of hadrons gives us a handle on earlier angular scales compared to the two-point correlations.

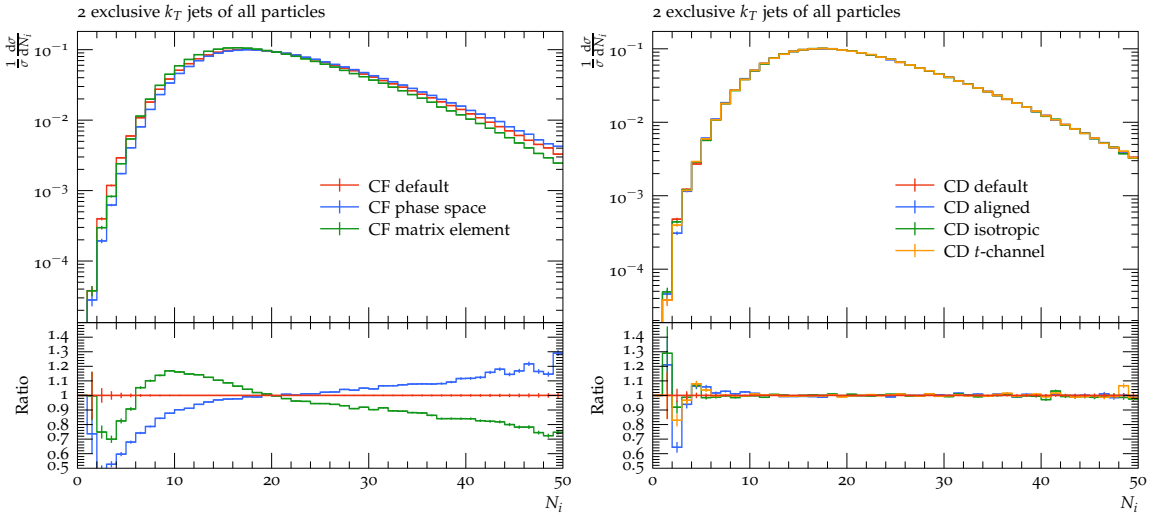

Figure 5.19: The normalized jet multiplicity of two exclusive KT jets. We show a variation of the cluster fission models with the t-channel like cluster decayer (left) and the different cluster decay models with the `Herwig` default cluster fission (right).

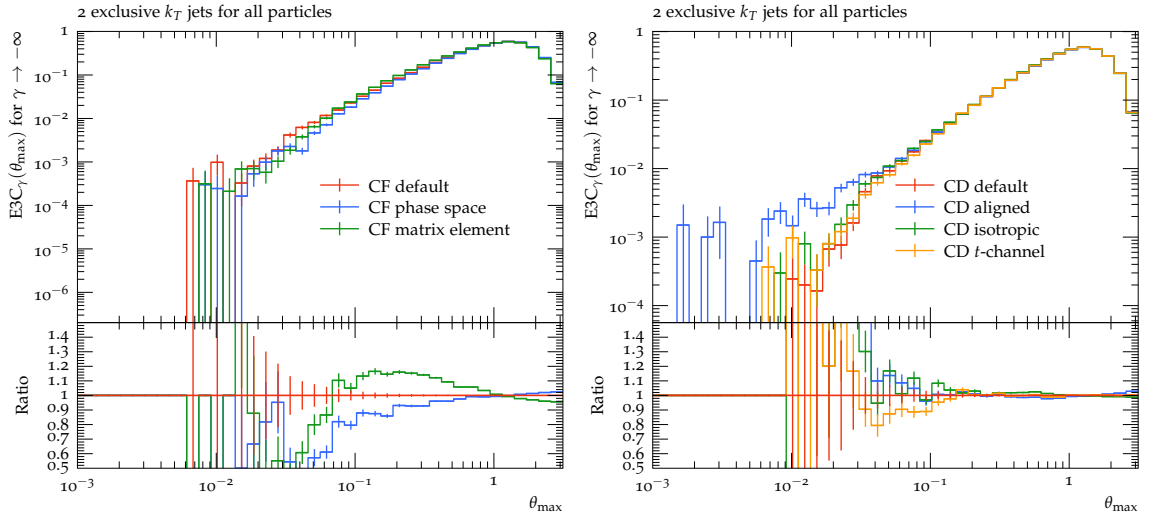

Figure 5.20: The energy correlator $\mathrm{E3C}_\gamma(\theta_{\max})$ of two exclusive KT jets using the STA scheme ($\gamma \to -\infty$). We show a variation of the cluster fission models with the t-channel like cluster decayer (left) and the different cluster decay models with the `Herwig` default cluster fission (right).

Similarly in figure 5.23 we display the WTA two point correlations $\mathrm{E2C}_\gamma(\theta)$, which compared to their corresponding WTA three point correlations $\mathrm{E3C}_\gamma(\theta_{\max})$ of figure 5.21 yields quite similar results, but again the three-point correlations do show a little bit stronger variation.

We now want to compare the difference of the three point correlations in the WTA scheme depending on $\theta_{\min/\max}$. Comparing figures 5.21 and 5.24 we can see that these observables

are indeed different, but overall they do agree in their response to different models qualitatively, even though the statistics are of course different[37]. We also compared the IR safe and "collinear safe" versions i.e. $\gamma = 1$, but did not find any significant difference compared to other values of γ.

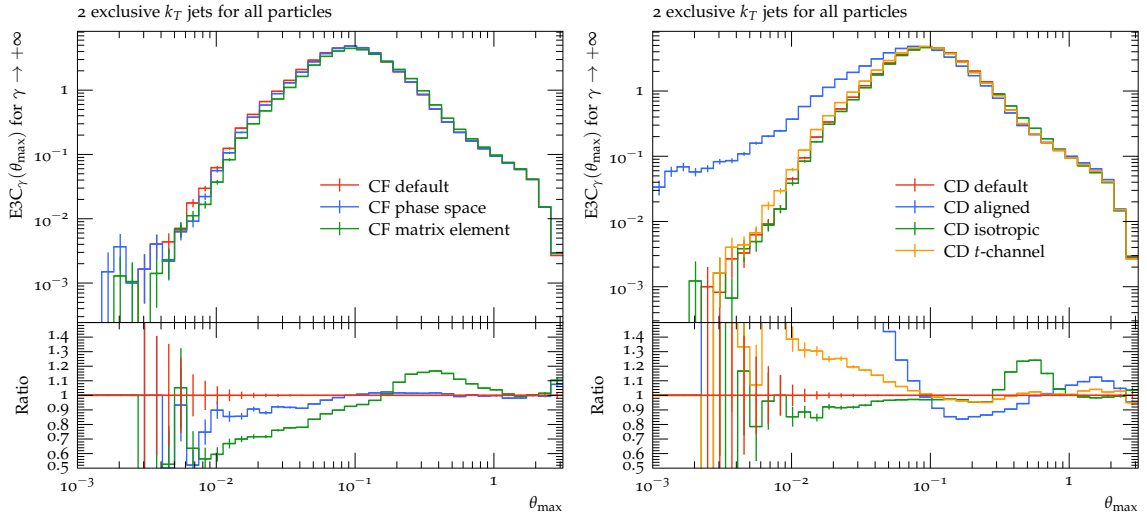

Figure 5.21: The energy correlator $\mathrm{E3C}_\gamma(\theta_{\max})$ of two exclusive KT jets using the WTA scheme ($\gamma \to +\infty$). We show a variation of the cluster fission models with the t-channel like cluster decayer (left) and the different cluster decay models with the `Herwig` default cluster fission (right).

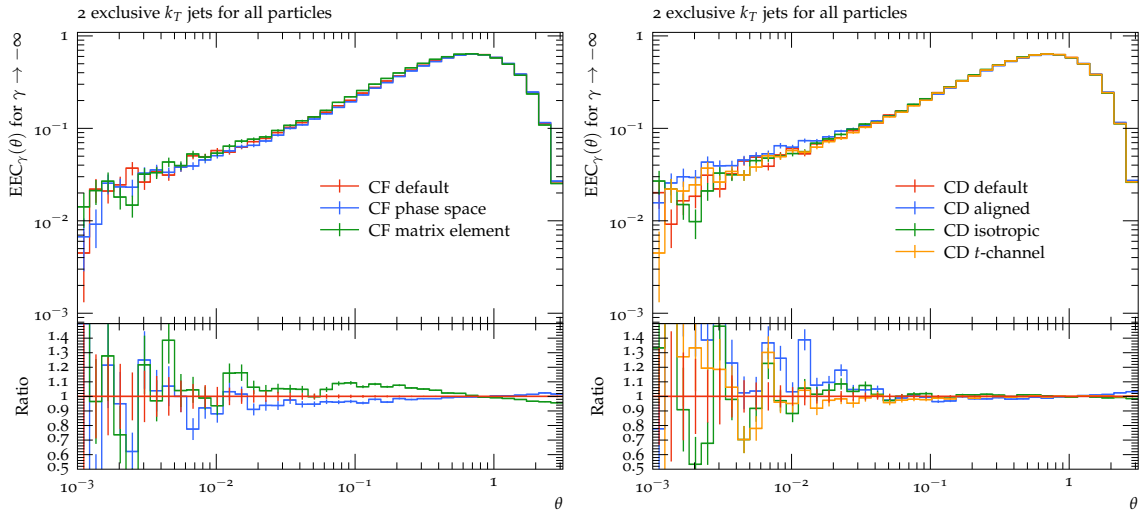

Figure 5.22: The energy correlator $\mathrm{EEC}_\gamma(\theta)$ of two exclusive KT jets using the STA scheme ($\gamma \to -\infty$). We show a variation of the cluster fission models with the t-channel like cluster decayer (left) and the different cluster decay models with the `Herwig` default cluster fission (right).

Another interesting observation is the behaviour of the correlations at different COM energies. Therefore we display the inclusive (no jet algorithm used) $\mathrm{E3C}_\gamma(\theta_{\min})$ and $\mathrm{EEC}_\gamma(\theta)$ in figure 5.26 for STA and in figure 5.25 for WTA at $\sqrt{s} \in \{10.58\ \mathrm{GeV}, 91.2\ \mathrm{GeV}\}$, which correspond to BELLE and LEP COM energies. One can clearly see as expected that the WTA correlations

[37] For $\theta_{\max}$ the small angles have poor statistics compared to $\theta_{\min}$, while for $\theta_{\min}$ the contrary is the case.

at different $\sqrt{s}$ in figure 5.25 are substantially different. This is expected since the hardest hadrons of course depend on the COM energy. However, it is far from trivial that the STA correlation comparison in figure 5.26 are supposed to be similar. Of course there are some differences in figure 5.26, but those might be explained by larger power corrections for the BELLE energy correlations. The fairly similar results in figure 5.26 seem to indicate however a vindication of hadronization universality since with the STA scheme we are probing the soft correlations of an event. One might be tempted to think that this happens due to the usage of energy weighting instead of $|\vec{p}|$ weighting, but this was cross-checked by running the simulation with both weighting schemes, which had an irrelevant impact on all correlations.

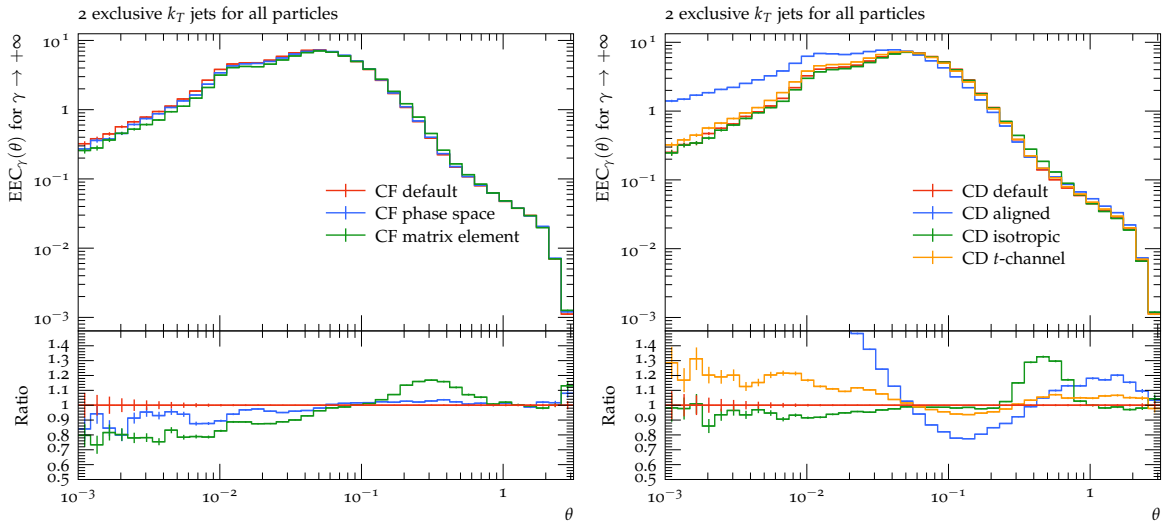

Figure 5.23: The energy correlator $\mathrm{EEC}_\gamma(\theta)$ of two exclusive KT jets using the WTA scheme ($\gamma \to +\infty$). We show a variation of the cluster fission models with the t-channel like cluster decayer (left) and the different cluster decay models with the `Herwig` default cluster fission (right).

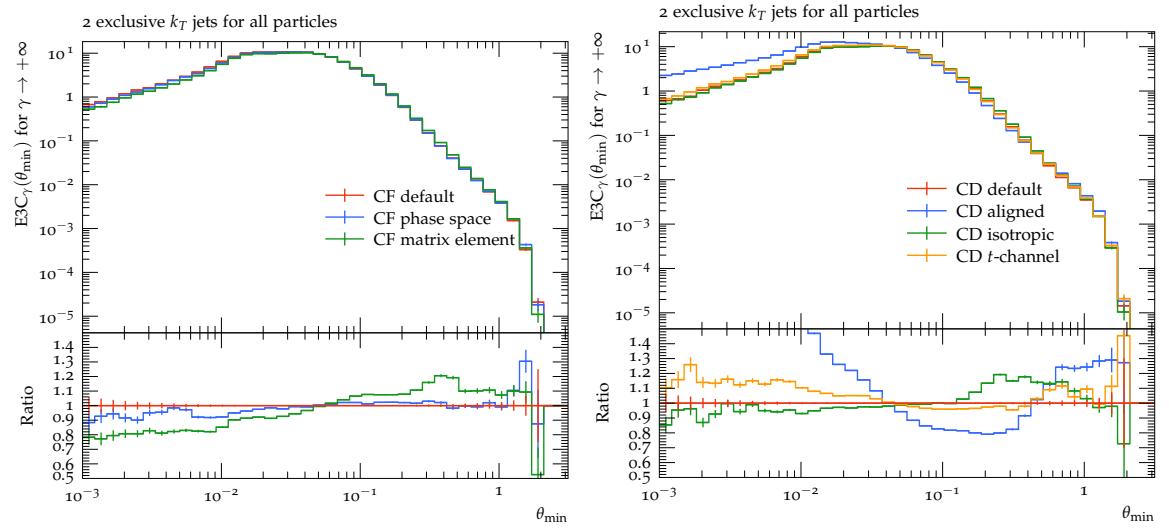

Figure 5.24: The energy correlator $\mathrm{E3C}_\gamma(\theta_{\mathrm{min}})$ of two exclusive KT jets using the WTA scheme ($\gamma \to +\infty$). We show a variation of the cluster fission models with the t-channel like cluster decayer (left) and the different cluster decay models with the `Herwig` default cluster fission (right).

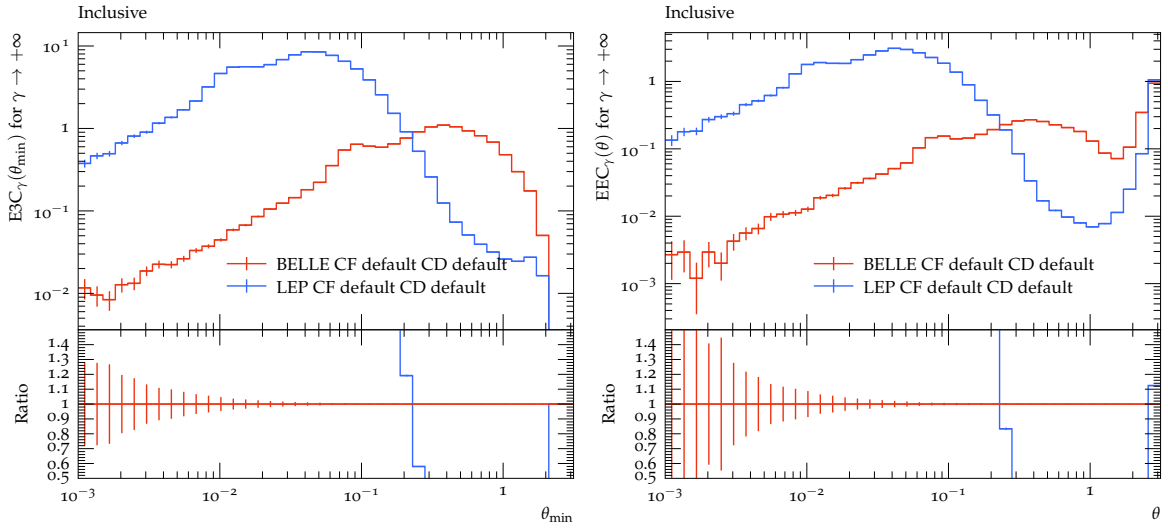

Figure 5.25: The energy correlators $\mathrm{E3C}_\gamma(\theta_{\min})$ (left) and $\mathrm{EEC}_\gamma(\theta)$ (right) inclusive over the whole event using the WTA scheme ($\gamma \to +\infty$) for $\sqrt{s} \in \{10.58\ \mathrm{GeV}, 91.2\ \mathrm{GeV}\}$. Here both plots are made with the `Herwig` default cluster fission and decay.

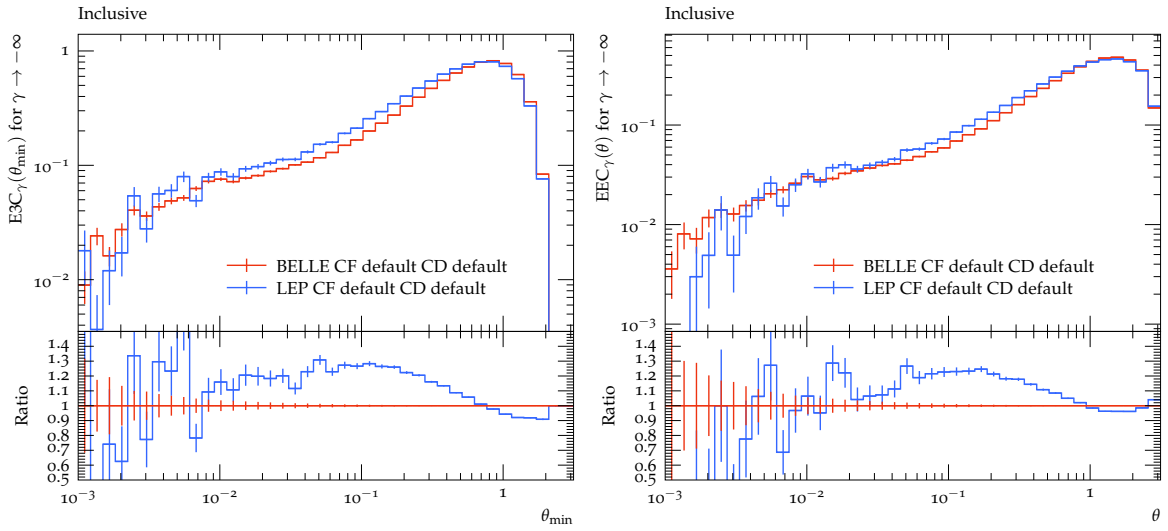

Figure 5.26: The energy correlators $\mathrm{E3C}_\gamma(\theta_{\min})$ (left) and $\mathrm{EEC}_\gamma(\theta)$ (right) inclusive over the whole event using the STA scheme ($\gamma \to -\infty$) for $\sqrt{s} \in \{10.58\ \mathrm{GeV}, 91.2\ \mathrm{GeV}\}$. Here both plots are made with the `Herwig` default cluster fission and decay.

5.6 Conclusions and Outlook

In this chapter, we have implemented a perturbatively inspired matrix element cluster fission model - via a quasi-soft $q\bar{q}$-emission - and a phenomenologically inspired matrix element cluster decay model, which was motivated by a more seamless transition from the CF model to the CD model [156]. We studied its phenomenology and discovered that some issues in correlation observables such as the di-hadron fragmentation functions could be resolved, while still maintaining agreement with the momentum spectra of baryons and minor improvements in some momentum dependent event shapes. In particular, we also showed in figures 5.14 that just the pure flat mass phase space is not enough if the directionality is sampled fully aligned for the cluster fission. In fact, we found in figure 5.15 as expected that the full matrix

element dependency leads the cluster fission to become very similar to the parton shower, which we already hinted at before.

In addition, we also explored the effects of the CF and CD models on more theoretical observables such as the generalized jet angularities and the weighted multi-point energy correlations. We found parameter ranges for these observables, which are able to discriminate between the CF and CD models i.e. observables that are either much more sensitive to the CF model or the CD model while at the same time being rather insensitive to the respective other model. In particular, we also explored the regime of IR dangerous observables in figures 5.20 and 5.22 for the correlations, which surprisingly appeared to be quite insensitive to the CD model. Additionally, we showed that the IR dangerous STA scheme correlations in figure 5.26 only depend weakly on the COM energy, which we interpret as a vindication for hadronization universality at least for the studied energies. It would be therefore very interesting to measure such correlations and the discriminating angularities in e^+e^- experiments also at varying COM energies.

We stressed however that in terms of baryon production, e.g. during CF, the model we provided crucially relies on the diquark assumption, i.e. that the matrix element cluster fission treats a diquark as an effective anti-triplet state with different mass without any substructure. In particular, it would be interesting to study the emission of two quasi-soft $q\bar{q}$ pairs and study its IR and collinear limits in order to have a clearer picture of more reasonable baryon production. Also, the interleaving of the CF with the CR model could be relevant to the baryon production, which we leave for future work. For this to happen however also the performance of the matrix element cluster fission has to be drastically enhanced, which would be also necessary to run this model for MB LHC observables in reasonable time scales.

There are also some other features that are still missing in the present model. We have kept the flavour sampling weights as tunable constants, but in principle these weights could be also computed by sampling them from the matrix element, which could lead to an even more predictive hadronization with fewer free parameters. Strongly related to this is the precise value and the potential scale dependence of the constituent masses, which in the new model are much more important for a reasonable description of the data.

So far we also implemented only a phenomenological matrix element for the cluster decay in order to give a smoother transition from the CF to CD model, but in principle the computation of such parton to hadron transition amplitudes is possible using so-called *Bethe-Salpeter* amplitudes as has been laid out in [7]. This could of course guide or even replace our phenomenological choice and tell us more about the actual process of confinement.

Additionally, we believe that one of the major goals in cluster hadronization is the development of a truly IR safe cluster hadronization model, which in its current form is not the case due to the forced NP gluon splitting. This thesis and plenty of other studies [7, 94] are trying to approach this goal.

CHAPTER 6

Diquark Colour Reconnection

Colour Reconnection (CR) is a crucial feature of QCD especially for high energy pp collisions, where the colour connections of different MPIs are ambiguous and CR tries to restore reasonable colour connections by rearranging colour singlets. CR is typically reducing soft particle multiplicity production resulting in increased average momentum. However, CR is not only important for soft particle production but also one of the dominant uncertainties of the top quark mass measurement [5]. In particular, determining the CR uncertainty is also a very active field of research as we have assessed in [6]. Furthermore, CR and its interplay with hadronization also plays a crucial role in Jet Sub-Structure (JSS) studies, which we have examined in an unpublished study starting from [6]. In fact, the interplay of CR and hadronization is also emergent from the colour evolution equations in [7].

Since the perturbative Parton Shower (PS) is in our case only LC accurate, baryonic singlets are not formed after the PS has finished and the gluons are split Non-Perturbatively (NP) to $q\bar{q}$ pairs. Therefore only mesonic primordial clusters are produced, which in our case are completely oblivious to the rest of the event if no CR is imposed. In fact, similar to CR there exist also so-called *coalescence* models [148] such as AMPT [149], which coalesce the partons to colour singlets in order to restore some subleading colour correlations. However, the formation of baryons in high energy collisions still remains a mystery as we have seen in chapter 4 that different baryon production mechanisms have different phenomenological consequences. In fact, in the large N_c limit a (anti)baryon, which is the totally antisymmetric combination of N_c (anti)quarks, is a possible state but has a mass proportional to N_c according to [166] and is therefore impossible to produce with a finite COM energy and a finite number of (anti)quarks. Therefore baryon production is a subleading colour effect, which can be achieved by CR as we already mentioned by e.g. BCR discussed in section 3.9. As also mentioned in section 3.9 the BCR model of `Herwig` has been quite successful in describing the observed baryon-baryon suppression in close-range correlations measured by ALICE [139–143], however it is still not able to produce enough baryons at LHC collisions let alone LEP collisions.

While in `Pythia` the new CR model [167, 168] has the so-called baryon junction-antijunction pair topology, the cluster equivalent CR topology has been missing in the current CR model of `Herwig`. It is noteworthy that due to the interpretation of the gluons as kinks in the string model, many more topologies are available in the string model case, while for the cluster

model due to the NP splitting of gluons to $q\bar{q}$, cluster colour singlets can only be formed from quarks and antiquarks.

This present study [169] aims at discussing the cluster equivalent of this junction-antijunction topology and the associated approximations used in order to build a viable CR model for such topologies. The goal of this chapter is to introduce this new so-called *diquark cluster* state and develop an algorithm that can produce all possible CR topologies including this new state in order to study its phenomenology.

6.1 The Diquark Cluster and The Diquark Approximation

As already mentioned before, after the primordial clusters are formed, we are left with only mesonic type clusters[38] consisting of a quark and an antiquark in the colour singlet state. In general, any type of cluster must be a colour singlet. Since in general we have an arbitrary - up to baryon number conservation - number of quarks n_q and antiquarks $n_{\bar{q}}$ in the event after the NP gluon splitting, colour reconnection would correspond to the task of finding all possible singlets $\mathbf{1}$ in the decomposition into irreducible representations of the following tensor representation:

$$\mathbf{3}^{\otimes n_q} \otimes \bar{\mathbf{3}}^{\otimes n_{\bar{q}}} = \bigoplus_{i=1}^{N_{\text{irrep}}} \mathbf{R}_i, \tag{6.1}$$

$$\mathbf{R}^{\otimes a} := \underbrace{\mathbf{R} \otimes \ldots \otimes \mathbf{R}}_{a \text{ times}}, \tag{6.2}$$

$$\bigoplus_{i=1}^{N} \mathbf{R}_i = \mathbf{R}_1 \oplus \ldots \oplus \mathbf{R}_N. \tag{6.3}$$

Here the specific values of the irreducible representations $\mathbf{R}_i$ can be computed by the usual Young tableau's. Of course for large numbers of n_q, $n_{\bar{q}}$ this is a difficult task even without gluons, which of course are in the adjoint $\mathbf{8}$ representation. In the case of finding all colour singlets in the n-th power of the adjoint tensor representation $\mathbf{8}^{\otimes n}$ the number of singlets grows quite fast as has been shown in [170], which makes the sampling space of all possible singlet configurations too large for practical purposes. Therefore it is useful to essentially employ a divide and conquer strategy to tackle this issue. In this spirit, the goal is to subdivide the total system of n_q quarks and $n_{\bar{q}}$ antiquarks into singlet subsystems of at most three mesonic clusters. It is useful to define the basic decompositions of the tensor products among the fundamental $\mathbf{3}$, the anti-fundamental $\bar{\mathbf{3}}$ and the adjoint $\mathbf{8}$ representation, which are given by [171]:

$$\mathbf{3} \otimes \bar{\mathbf{3}} = \mathbf{8} \oplus \mathbf{1}, \tag{6.4}$$

$$\mathbf{3} \otimes \mathbf{3} = \mathbf{6} \oplus \bar{\mathbf{3}}, \tag{6.5}$$

$$\bar{\mathbf{3}} \otimes \bar{\mathbf{3}} = \bar{\mathbf{6}} \oplus \mathbf{3}, \tag{6.6}$$

$$\mathbf{8} \otimes \mathbf{8} = \mathbf{27} \oplus \bar{\mathbf{10}} \oplus \mathbf{10} \oplus \mathbf{8} \oplus \mathbf{8} \oplus \mathbf{1}, \tag{6.7}$$

$$\mathbf{8} \otimes \mathbf{3} = \mathbf{15} \oplus \bar{\mathbf{6}} \oplus \mathbf{3}, \tag{6.8}$$

$$\mathbf{8} \otimes \bar{\mathbf{3}} = \bar{\mathbf{15}} \oplus \mathbf{6} \oplus \bar{\mathbf{3}}. \tag{6.9}$$

Note that here we find singlets only for a quark-antiquark pair and for a glue-ball i.e. two gluons. Furthermore, we find that the tensor product of two quarks decomposes into an

[38] For pp collisions we would also have two proton remnant clusters, which consist of a quark and a diquark, but the diquark is effectively treated as an antiquark with different mass.

antiquark representation and vice-versa. While on the other hand adding a gluon[39] to a (anti)quark still results in the same (anti)fundamental representation.

From these relations we can easily derive the baryon and antibaryon singlets as the following:

$$\mathbf{3} \otimes \mathbf{3} \otimes \mathbf{3} = \mathbf{10} \oplus \mathbf{8} \oplus \mathbf{8} \oplus \mathbf{1}, \tag{6.10}$$

$$\bar{\mathbf{3}} \otimes \bar{\mathbf{3}} \otimes \bar{\mathbf{3}} = \bar{\mathbf{10}} \oplus \mathbf{8} \oplus \mathbf{8} \oplus \mathbf{1}. \tag{6.11}$$

However, another possibility for generating a singlet is by tensor-multiplying equations (6.5) and (6.6) to get a so-called *tetraquark*:

$$\mathbf{3} \otimes \mathbf{3} \otimes \bar{\mathbf{3}} \otimes \bar{\mathbf{3}} = \mathbf{27} \oplus \bar{\mathbf{10}} \oplus \mathbf{10} \oplus \mathbf{8} \oplus \mathbf{8} \oplus \mathbf{8} \oplus \mathbf{8} \oplus \mathbf{1} \oplus \mathbf{1}. \tag{6.12}$$

Note that since such tetraquark configurations have been measured as a bound state by LHCb [172] we will call this cluster configuration *diquark cluster* since a cluster is an unbound colour singlet state and not an actual exotic hadron such as tetraquarks.

Now if we ignore the glueball states since we only have quarks and antiquarks, we have the following possible singlet states if we start from three mesonic clusters $C_i(q_i, \bar{q}_i')$:

1. Three different mesonic clusters.
2. One baryonic and one antibaryonic cluster.
3. One diquark cluster and one mesonic cluster.

Therefore we can identify all possible CR topologies for a three mesonic cluster subsystem as the following, where we denote mesonic clusters M/M′, baryonic/antibaryonic clusters B/$\bar{\text{B}}$ and diquark clusters as D:

- Mesonic CR: 3 M $\rightarrow$ 3 M′.
- Baryonic CR: 3 M $\rightarrow$ B, $\bar{\text{B}}$.
- Diquark CR: 3 M $\rightarrow$ D, M.

For the case of only two mesonic clusters we also get an additional diquark topology such that in total we get the following two options:

- Mesonic CR: 2 M $\rightarrow$ 2 M′.
- Diquark CR: 2 M $\rightarrow$ D.

So in fact we are able to generate a diquark cluster with only two mesonic clusters, which later will split into a baryon-antibaryon pair, with only two mesonic clusters.

Let us discuss what this tetraquark-like diquark cluster state actually is and how the hadronization model deals with diquark clusters in the aftermath. A primordial diquark cluster $C(q_1, q_2, \bar{q}_3, \bar{q}_4)$ consists of two quarks q_1, q_2 and two antiquarks $\bar{q}_3$, $\bar{q}_4$, which is then reduced to a true diquark cluster $C[(q_1q_2)_r, (\bar{q}_3\bar{q}_4)_s]$, where r, s are the lowest possible spin state. This diquark cluster is then treated - during the CF and the CD - as a two parton cluster, which completely loses the information of the individual constituents q_1, q_2 and $\bar{q}_3$, $\bar{q}_4$ respectively. This is of course a considerable assumption, which is not always guaranteed to hold. Therefore it is useful to introduce a measure on the constituents, which tells us how good this approximation actually is. Since a diquark is effectively a composite state of two quarks, which are close in phase space a reasonable measure is the total invariant mass

[39] In principle any number of gluons.

$M_{q_1q_2} = \sqrt{(q_1+q_2)^2}$ of the two-quark system and correspondingly for the two antiquark system. One can think of this measure as a closeness measure of the two (anti)quarks. However, since the constituents are not massless it is useful to scale out the masses in order to yield the following closeness measure $\Delta_{q_1q_2}$, defined as the following:

$$\Delta_{q_1q_2} = \frac{q_1 \cdot q_2 - m_{q_1} m_{q_2}}{m_{q_1} m_{q_2}} \geq 0. \tag{6.13}$$

Note that this dimensionless quantity is Lorentz invariant[40] and the equality to 0 holds for two quarks moving in the same direction with equal momenta, which is indistinguishable from an antiquark state with mass $(m_{q_1} + m_{q_2})$. The larger the value for $\Delta_{q_1q_2}$ becomes, the less reasonable the approximation of the two-quark system as a single diquark.

Note that we also use a similar approximation for baryonic clusters $C(q_1, q_2, q_3)$, which are reduced to two parton diquark-quark clusters $C[(q_iq_j)_r, q_k]$, where $i \neq k \neq j \neq i$. In the case of baryonic clusters however the diquark constituents are chosen such that the invariant mass of the diquark is minimal i.e. $(i, j) = \text{argmin}_{(l,m),\, l\neq m} \left\{ \sqrt{(q_l + q_m)^2} \right\}$. This choice still allows for potentially large diquark masses but is still better than the only choice available to diquark clusters. In particular, such quark diquark approximations have been also used in lattice QCD and other NP approaches such as solving the Bethe-Salpeter equations using functional methods (see the review [173]), but typically only for the actual NP formation of a baryon bound state and not like in our cases an unbound baryonic cluster state.

We want to stress however that there is nothing wrong with baryonic or diquark clusters violating the assumption that we can treat them as effective diquarks, but the reduction of baryonic and diquark clusters to two-component clusters gives us a much easier one-dimensional[41] handling for the CF and CD models. So ultimately if a CF and CD model is developed that can deal reasonably with three-dimensionally extended three and four component clusters, we would not be limited by this diquark approximation and could assess the phenomenological impact of the diquark approximation on the observables. In `Pythia` such a three-dimensional treatment is available by the string dynamics, but nonetheless some challenges and choices still remain an open field of research [89, 168].

6.2 The Diquark Colour Reconnection Algorithm

Since we have now determined all possible cluster singlets, we can try to incorporate the new diquark cluster into the existing baryonic CR model, which we briefly discussed in subsection 3.9.3 and is discussed in detail in [123]. We use the same rapidity based definition as in equation (3.47). Therefore if we have a cluster $C_A(q_A, \bar{q}_A)$ and compute the rapidities of a second cluster's $C_B(q_B, \bar{q}_B)$ constituents in the C_A COM frame we get the following:

$$y_{q_B} = \frac{1}{2} \log \left[\frac{E_{q_B} + \hat{z} \cdot \vec{q}_B}{E_{q_B} - \hat{z} \cdot \vec{q}_B} \right], \tag{6.14}$$

$$y_{\bar{q}_B} = \frac{1}{2} \log \left[\frac{E_{\bar{q}_B} + \hat{z} \cdot \vec{\bar{q}}_B}{E_{\bar{q}_B} - \hat{z} \cdot \vec{\bar{q}}_B} \right]. \tag{6.15}$$

Here as before $\hat{z}$ is the direction parallel to the first cluster's antiquark $\bar{q}_A$ in its COM frame. Similarly in the COM frame of C_A we define y_{q_C}, $y_{\bar{q}_C}$ for a third cluster $C_C(q_C, \bar{q}_C)$. In figure 6.1 we show a sketch of the COM frame choice and the possible CR topologies.

[40] and therefore frame independent.

[41] By one dimension we mean the original extend of the two parton cluster, which in its COM frame has only a one dimensional extend.

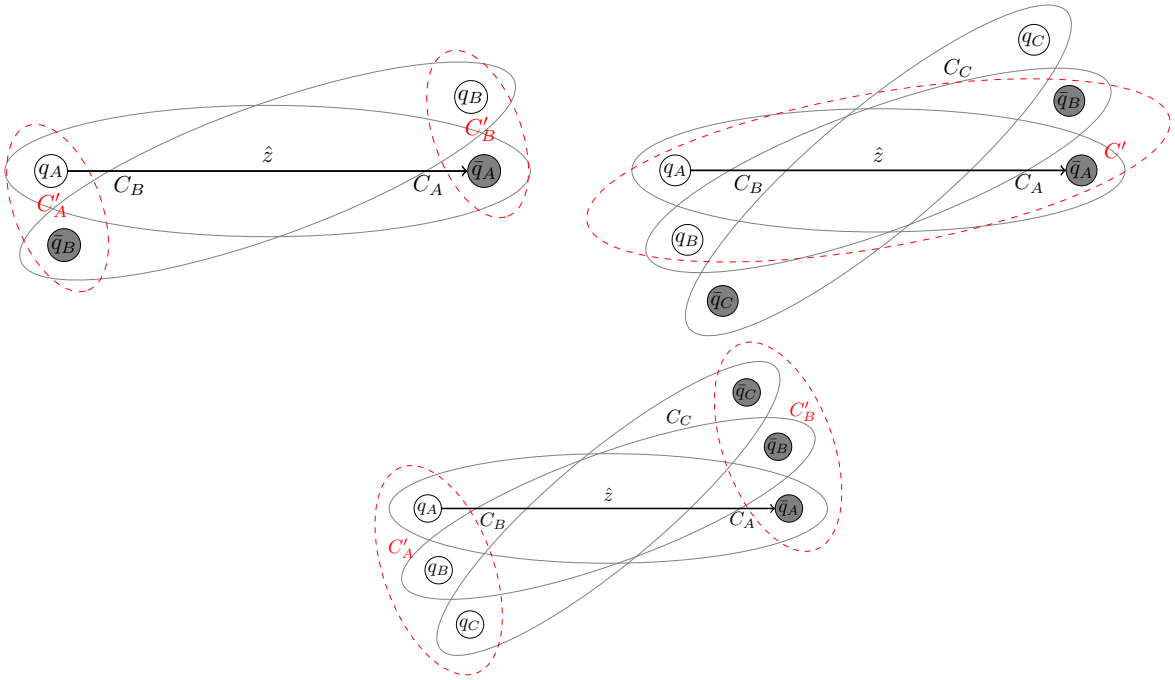

Figure 6.1: A sketch of the possible CR topologies for the diquark CR algorithm, where we can have mesonic CR (left), baryonic CR (bottom) and the new diquark CR (right).

For the diquark CR algorithm we have to colour reconnect the existing mesonic clusters[42], which we denote by the set $\mathcal{C}_{\text{start}}$, to a new set $\mathcal{C}_{\text{stop}}$, which contains mesonic, baryonic and diquark clusters. The algorithm then proceeds as follows:

1. Shuffle the set of clusters $\mathcal{C}_{\text{start}}$ to avoid a systematic bias.
2. Pick the next mesonic cluster C_A from the set $\mathcal{C}_{\text{start}}$.
3. Pick the next mesonic cluster $C_{B\neq A}$ from the set $\mathcal{C}_{\text{start}}$ and compute y_{q_B} and $y_{\bar{q}_B}$, which falls into one of the following categories:
   - Quark-Antiquark (QA) aligned for $y_{q_B} > 0$ and $y_{\bar{q}_B} < 0$ (left in figure 6.1).
   - Quark-Quark (QQ) aligned for $y_{q_B} < 0$ and $y_{\bar{q}_B} > 0$ (right in figure 6.1).
   - Neither for every other case. In this case, we continue and go to 3.
4. We compute the closeness measure $y_{\text{sum}} = |y_{q_B}| + |y_{\bar{q}_B}|$ between C_A and C_B and keep track of the maximal $y_{\text{sum}}^{\text{max}}$ and next-to-maximal $y_{\text{sum}}^{\text{Nmax}}$ value.
5. Go back to 3. and repeat until the all combinations have been tried.
6. If the maximum $y_{\text{sum}}^{\text{max}}$ is of QA-type mesonic CR is performed with a probability of P_M.
7. If the maximum $y_{\text{sum}}^{\text{max}}$ is of QQ-type and if $y_{\text{sum}}^{\text{Nmax}}$ is of QQ type baryonic CR is performed for the three clusters C_A, C_B, C_C with a probability of P_B (bottom in figure 6.1).
8. If the maximum $y_{\text{sum}}^{\text{max}}$ is of QQ-type and if $y_{\text{sum}}^{\text{Nmax}}$ is of QA type diquark CR is performed for the C_A, C_B clusters with a probability of P_D (bottom in figure 6.1). The third cluster C_C remains untouched.
9. Go back to 2 and repeat until every cluster has had the chance to be reconnected.

[42] We do not allow for the diquark containing beam remnant clusters to colour reconnect to diquark clusters.

Here we implicitly assume for the mesonic type CR that the reconnected clusters do not originate from a gluon, which is of course an octet and not a colourless singlet. This constraint can be alleviated by the interface `ColourReconnector:OctetTreatment`, which for the setting `All` prevents all octet clusters (default setting), for `Final` prevents only octet clusters that would originate from the last $g \to q\bar{q}$ splittings or for `None` allows all octet clusters to form. Note that the latter option is not meaningful since it will produce many clusters of exactly the gluon constituent mass m_g, since this is set to a static value by default even though the option for a dynamical gluon constituent mass has been explored in [94].

For diquark clusters there are no restrictions from possible octets since we could have either two gluon clusters - which are allowed to form a glueball singlet cluster - or a singlet cluster and a gluon, which also can form a singlet. For baryonic clusters similarly there are also no restrictions, where a baryonic singlet could consist of up to three gluon octets.

Note that this algorithm is very similar to the baryonic algorithm from [123], which makes it easier to discuss the phenomenology of these new diquark clusters relative to the baseline of the baryonic algorithm.

After the algorithm has terminated the baryonic and diquark clusters in $\mathcal{C}_{\text{stop}}$ are reduced all to two-component clusters using the diquark prescription discussed in section 6.1 before the clusters are passed on to the cluster fission. As discussed before this reduction to diquarks is needed by our hadronization model, which is the reason why we optionally allow imposing an additional cut $\Delta_{\max}$ on the $\Delta_{q_A q_B}$ and $\Delta_{\bar{q}_A \bar{q}_B}$ defined in equation (6.13) for all generated diquark clusters. In the code this cut $\Delta_{\max}$ can be set using the interface `ColourReconnector:CutDiquarkClusterFormation` such that $\Delta_{q_A q_B} < \Delta_{\max}$ and $\Delta_{\bar{q}_A \bar{q}_B} < \Delta_{\max}$ is guaranteed.

6.3 Phenomenology Of The Model

Now that we have defined the new Diquark CR (DCR) algorithm, we can explore its phenomenology and compare it to the Baryonic CR (BCR) algorithm. For this purpose, we use mostly MB data from LHC for pp collisions at 7 TeV as well as some custom `Rivet` [128] analyses to dissect the cluster distributions. In this section we used - unless otherwise stated - a maximum lifetime cut of $c\tau > 10$ mm, $\alpha_s(M_Z) = 0.1185$ for ISR and FSR in the CMW scheme, the `ColourReconnector:OctetTreatment All`, the static threshold option for the CF model and do not impose the diquark cluster formation cut $\Delta_{\max}$. Furthermore, we used the default CF and CD model for the plots of this section, which is the reason why caution is advised in the interpretation of all of the following results since all of the following observables are strongly correlated with the hadronization model that has been used. Since we are especially interested in the baryon production mechanism from the CR we also turn off all other baryon production mechanisms by setting **PwtDI** $= 0$ and therefore disabling the CF and the CD model baryons. Due to all of these settings our results will not agree precisely with the most recent tune of `Herwig 7.3.0` even though all remaining parameters used are set to their tuned values from the said version.

In figure 6.2 we display the BB and BA correlations varying the reconnection probabilities P_B and P_D for the new DCR model alongside the default BCR model in red. Since for the baryon production we are only interested in baryons we keep $P_M = 0$ for these plots. We can clearly see that consistency with the BCR model is achieved if no diquark clusters are produced $P_D = 0$ (blue), which is to be expected since also the selection of clusters is very similar. Furthermore, for increasing value of P_D, the suppression in the BB correlations is more and more reduced but still present. Also this should be expected since as already mentioned the suppression most likely originates from the fact that we generate a quark sink in the phase

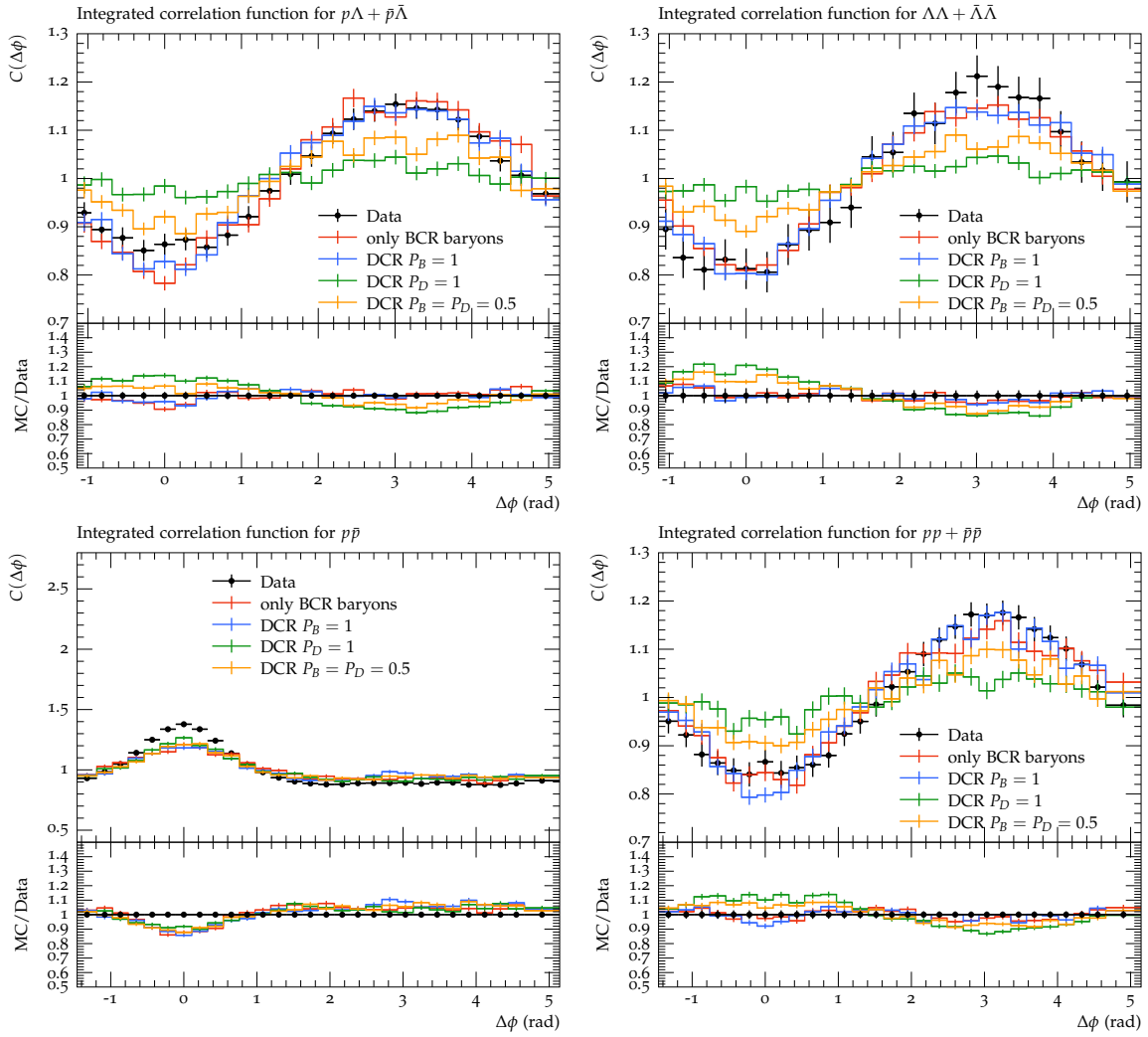

Figure 6.2: The BB and BA correlations of MB pp collisions at 7 TeV measured by ALICE [137] (public `Rivet` analysis `ALICE_2016_I1507157`) for different values of the reconnection probabilities P_M, P_B and P_D using the DCR algorithm. The red line corresponds to the default tuned BCR algorithm with **PwtDI** = 0. Note that for the DCR simulations, we display only the non-zero parameters for P_M, P_B and P_D.

space region, where the quarks of the diquark cluster are and vice-versa for the antiquarks, just that now only two instead of three quarks are recombined to a (future) baryon. Because of this it is expected that the suppression is smaller for diquark clusters compared to the baryonic clusters. Note however that in figure 6.2 the CF and/or CD model baryons are not included, which will have a negative impact on the BB correlations as we have already shown in figure 4.3 since they are responsible for slight near sided correlations. In figure 6.2 we also show exemplary with $C_{p\bar{p}}(\Delta\phi)$ that the BA type correlations do not show a significant change compared to the regular BCR algorithm with maybe the exception of the pure diquark CR (green), which appears to produce slightly more correlated $p\bar{p}$ pairs.

As mentioned before the CR is strongly correlated with the hadronization model as we already discovered in chapter 4. This is particularly problematic for correlation observables since they probe the correlations within an event. Therefore we examined the effect of the new t-channel CD model (described in section 5.3) on the BB and BA correlations, which are displayed in figure 6.3. One can clearly see that compared to the default isotropic CD model of figure 6.2 the BB correlations yield a much stronger suppression in the near side region and the BA

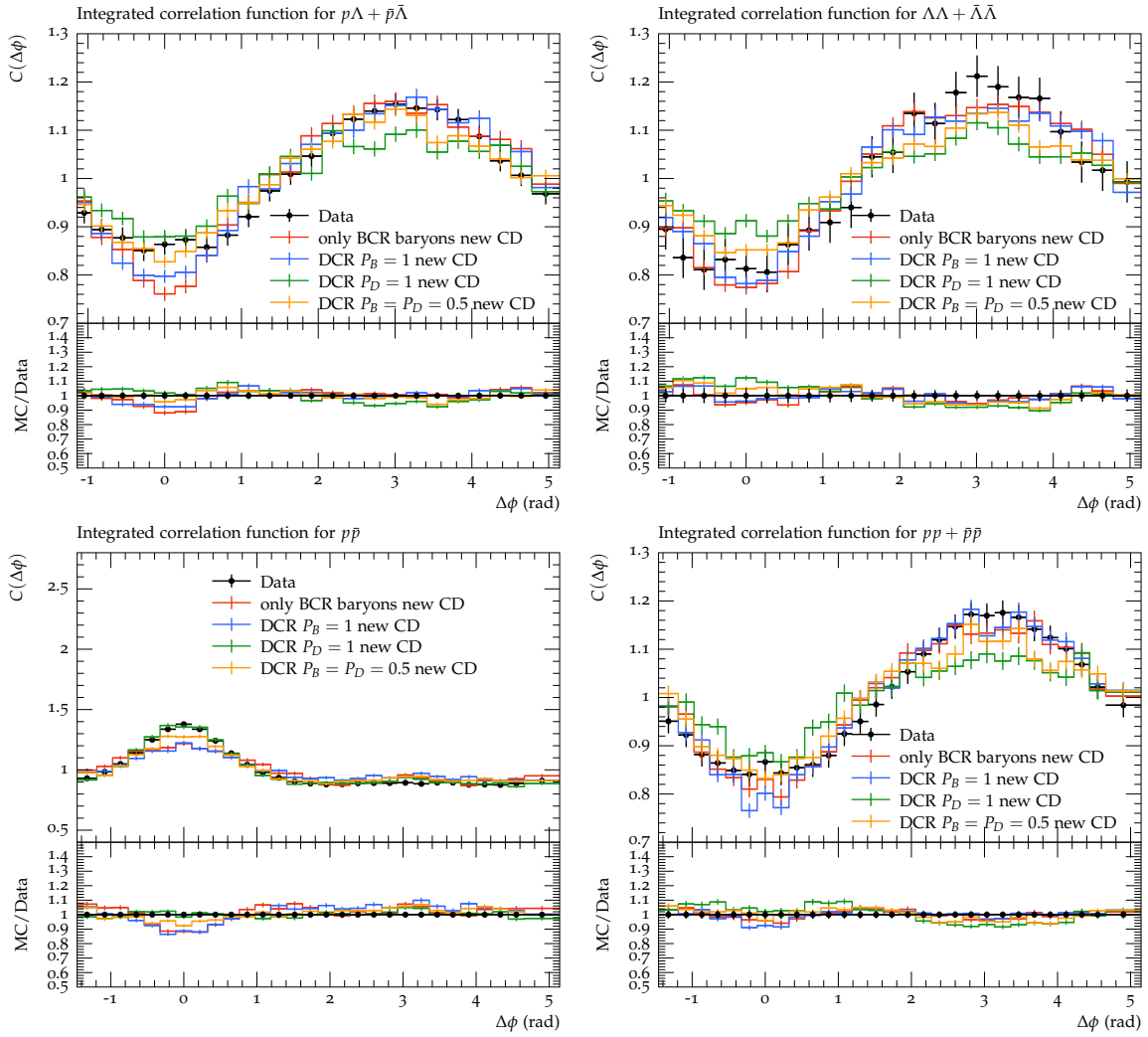

Figure 6.3: The BB and BA correlations of MB pp collisions at 7 TeV measured by ALICE [137] (public `Rivet` analysis `ALICE_2016_I1507157`) for different values of the reconnection probabilities P_M, P_B and P_D using the DCR algorithm with the new t-channel like CD discussed in 5.3. The red line corresponds to the default tuned BCR algorithm with **PwtDI** = 0. Note that for the DCR simulations we display only the non-zero parameters for P_M, P_B and P_D.

correlations form a stronger correlation in the near side. The overall phenomenology discussed before is still valid qualitatively, but quantitatively the variation is less strong among different parameter values. This can be explained by the fact that the diquark clusters are forced to go through the CD model and therefore would lose their correlation information if the CD model is sampling isotropic directions instead of having a bias aligned towards the constituents of the cluster. Note that this change in the CD model affects most strongly the correlation observables and to a lesser extent the other typical MB observables.

For the same model parameters we also plot in figure 6.4 the p_T distributions for the p, Λ and Ξ^- baryons and for the $\pi^\pm$ mesons as measured by ALICE and CMS [150, 151]. Regarding the baryons one can see that the BCR $P_B = 1$ baryons and the $P_D = 1$ diquark cluster baryons differ in the low p_T region, where the BCR baryons are too suppressed compared to the diquark baryons, which more closely match the data with the exception of the Ξ^- baryons. We can see again that many effects are at play here (in particular the diffraction and hadronization model) since what appears to be agreement with the data for protons

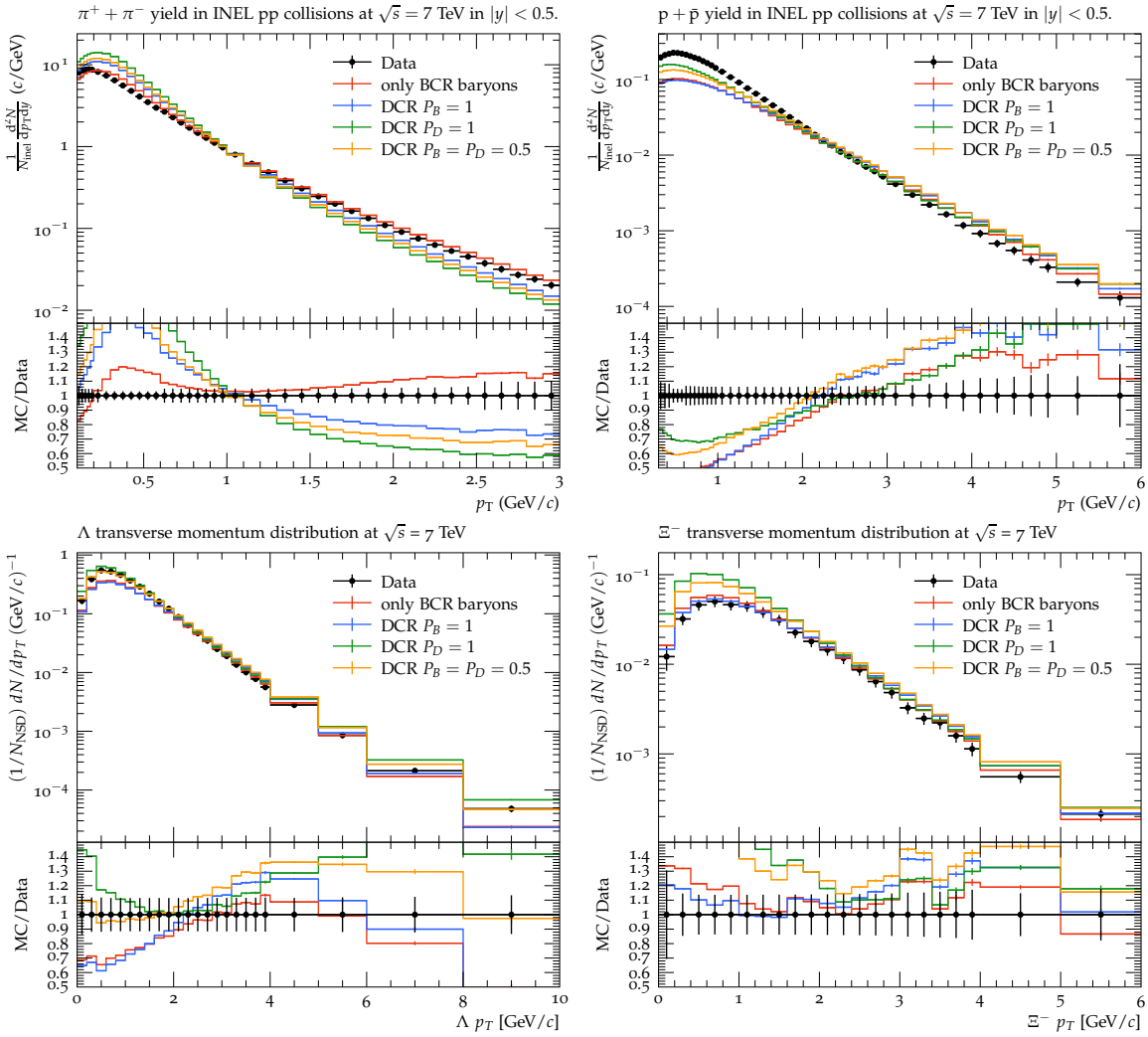

Figure 6.4: The p_T spectra of $\pi^{\pm}$, p, Λ and Ξ^- of MB pp collisions at 7 TeV measured by ALICE and CMS [150, 151] (public `Rivet` analyses `CMS_2011_S8978280` and `ALICE_2015_I1357424`) for different values of the reconnection probabilities P_M, P_B and P_D using the DCR algorithm. The red line corresponds to the default tuned BCR algorithm with **PwtDI** $= 0$. Note that for the DCR simulations we display only the non-zero parameters for P_M, P_B and P_D.

does not need to hold for Ξ^- baryons. Note however that the strangeness production of the hadronization can also be responsible for this difference and a proper retune is necessary in order to make claims on individual baryon species. However, what can be said is that relatively speaking the DCR mechanism produces more soft baryons. The pion distributions are substantially altered, but this can be explained by the fact that we choose $P_M = 0$, which does explain the difference compared to the default. Nonetheless, it appears that also for the pions the p_T distribution shifts to lower values the more P_D increases.

In order to assess the effects of this new DCR algorithm on more inclusive observables without Particle IDentification (PID) information we display in figure 6.5 the charged multiplicity N_{ch}, $\langle p_T \rangle (N_{\text{ch}})$ and p_T distributions for the same variations as before but with the additional purely mesonic CR $P_M = 1$ and $P_B = P_D = 0$ of the DCR algorithm (purple). It can be clearly seen that the mesonic CR is the backbone of these MB observables and shows a similar behaviour to the default BCR algorithm. Without mesonic CR the large rise of $\langle p_T \rangle (N_{\text{ch}})$ demanded by the data cannot be achieved and in particular the diquark clusters are almost

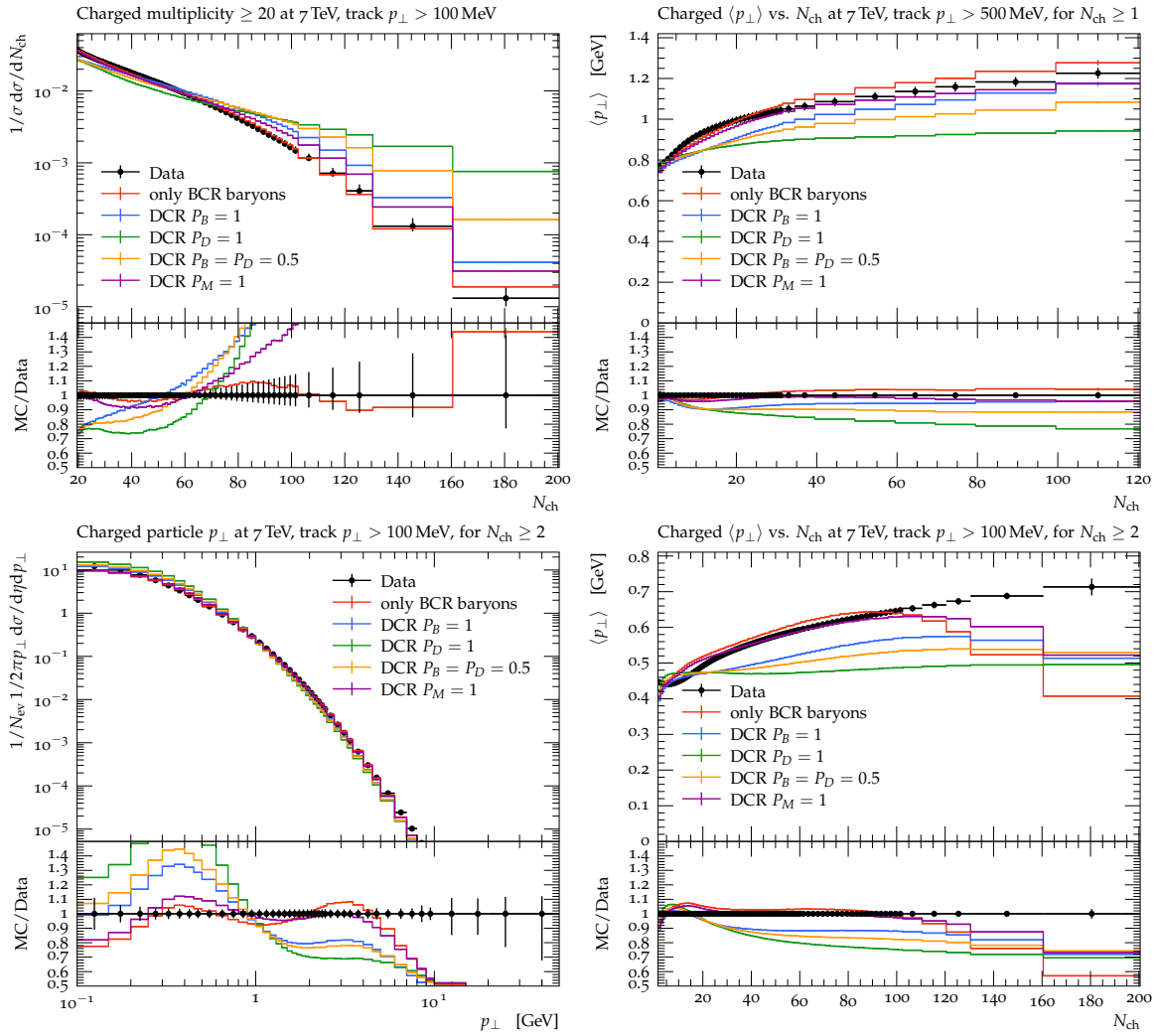

Figure 6.5: The N_{ch} and p_T ($p_\perp$ in plot) spectra (left) and the observable $\langle p_T \rangle (N_{ch})$ for different p_T cuts (right) of MB pp collisions at 7 TeV measured by ATLAS [127] (public `Rivet` analysis `ATLAS_2010_S8918562`). We varied the reconnection probabilities P_M, P_B and P_D using the DCR algorithm. The red line corresponds to the default tuned BCR algorithm with **PwtDI** $= 0$. Note that for the DCR simulations we display only the non-zero parameters for P_M, P_B and P_D.

completely unable to produce a rising $\langle p_T \rangle (N_{ch})$, while on the other hand the baryonic clusters do contribute to this observable. Note that for the $p_T > 100$ MeV we can observe a drop in $\langle p_T \rangle (N_{ch})$ towards large N_{ch}, which might be connected to our diffraction model, which produces a lot of low p_T hadrons, or to the specifics of our hadronization model, which does not produce enough p_T due to the aligned CF, or also to the remnant treatment of clusters.

Similar effects are also visible in the N_{ch} and p_T distribution (figure 6.5), which show too much high multiplicity and low p_T events for $P_D = 1$, which is typically resolved by CR reducing multiplicity and increasing p_T. One explanation for the inability of the diquark cluster CR could be that instead of actually producing two new clusters - like in the case of baryonic CR - two clusters are just stuck together such that their p_T does not really sum and therefore increase, since the diquark cluster has to first fission/decay, which costs momentum that needs to be invested in producing the mass of the $q\bar{q}$ pair that needs to be popped from the vacuum. In that sense this diquark CR is maybe more related to the *popcorn* mechanism in `Pythia` [153].

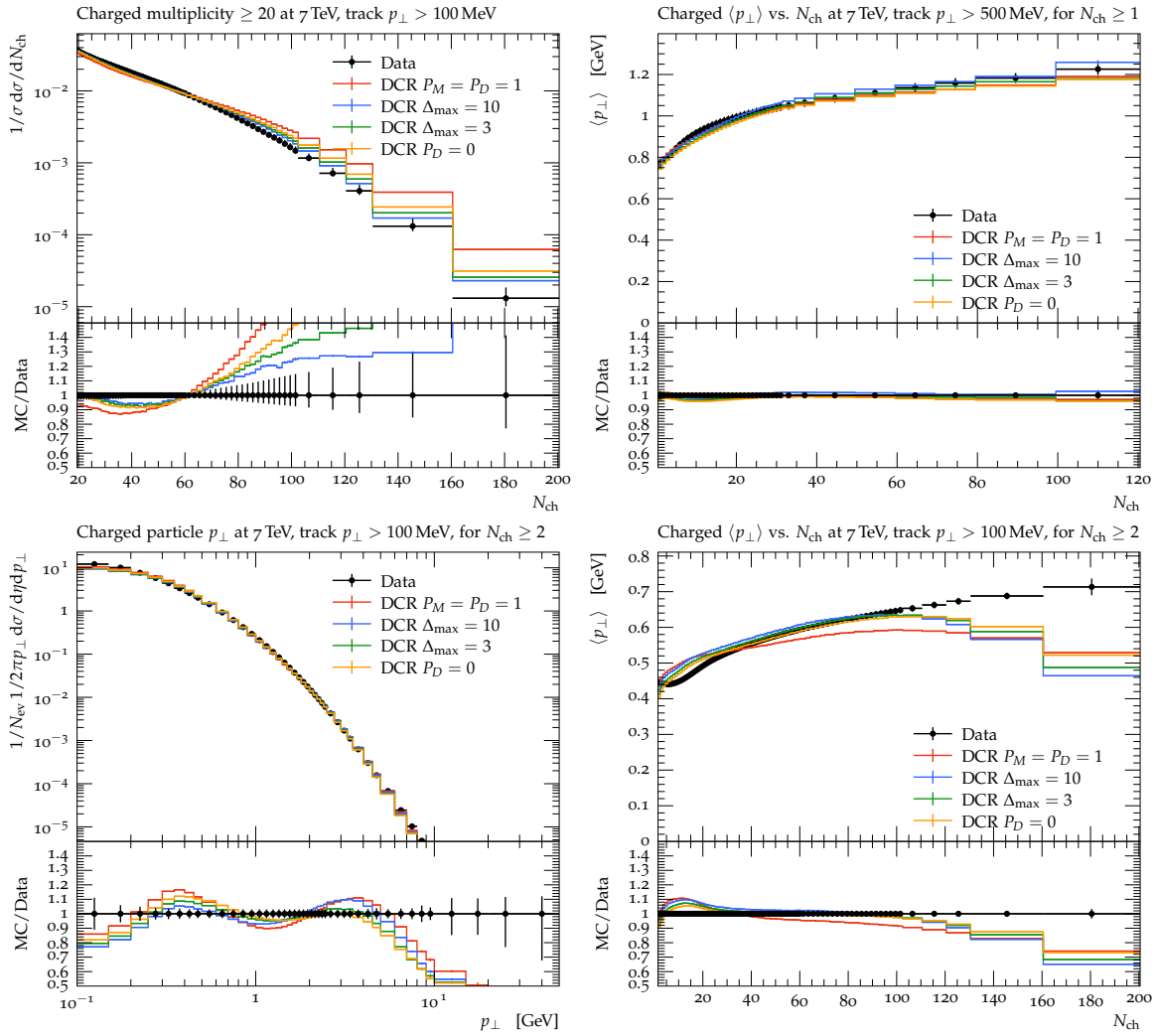

Figure 6.6: The N_{ch} and p_T ($p_\perp$ in plot) spectra (left) and the observable $\langle p_T \rangle (N_{ch})$ for different p_T cuts (right) of MB pp collisions at 7 TeV measured by ATLAS [127] (public `Rivet` analysis `ATLAS_2010_S8918562`). The reconnection probabilities $P_M = P_D = 1$ and $P_B = 0$ have been used with the DCR algorithm, varying the imposed cut on diquark cluster formation Δ_{max} from $\Delta_{max} = \infty$, i.e. no cut (red), $\Delta_{max} = 10$ (blue), $\Delta_{max} = 3$ (green) and $\Delta_{max} = 0 \Leftrightarrow P_D = 0$, i.e. no diquark CR (orange).

In order to assess if this behaviour of the diquark CR algorithm can be attributed to the diquark approximation that has been used, we displayed in figure 6.6 the DCR algorithm results for $P_M = P_D = 1$ applying and varying the cut on the Δ_{max}, which we defined previously. Since in these plots we have allowed for mesonic CR, the results are much closer to the data than in figure 6.5, but nonetheless we can see some differences in the multiplicity distribution. In fact, one can think of the plots in figure 6.6 as the variation of the $\Delta_{max} \in \{\infty, 10, 3, 0\}$ cut and we can see some interesting non-linear behaviour, which might be connected to the interplay of the diquark CR with the mesonic CR. One can see that the relatively inclusive $\Delta_{max} = 10$ cut is already sufficient to mostly restore the rise in $\langle p_T \rangle (N_{ch})$ in figure 6.6 compared to the default BCR simulation.

In the quest of dissecting the behaviour of this cut, we display in figure 6.7 the distribution of diquark cluster masses just after CR and the diquark cluster's originating clusters p_T distribution after the CF with different Δ_{max} cuts. As one would expect due to the cut on the invariant mass of two constituents the diquark cluster mass distribution gets shifted

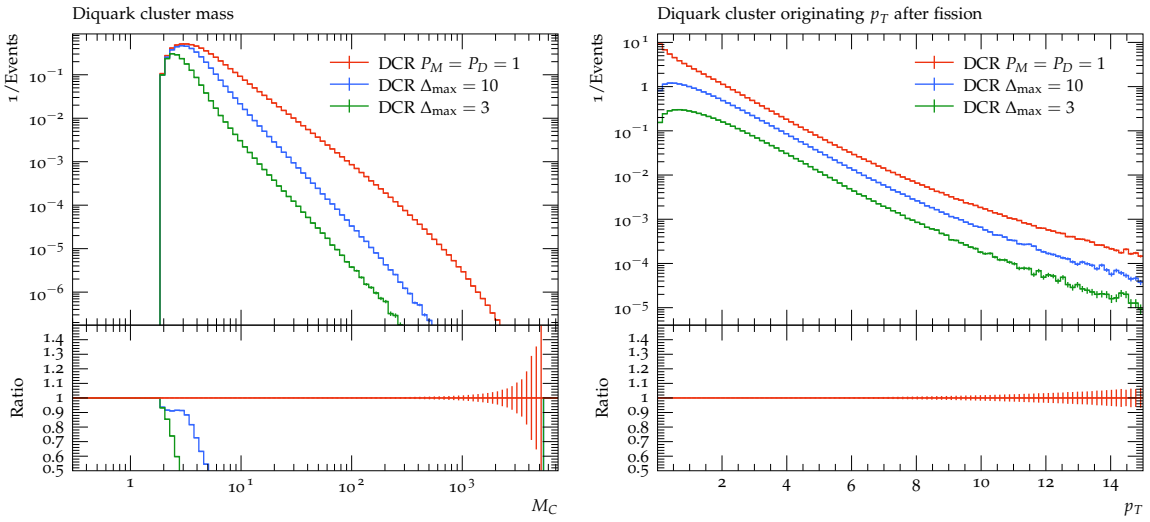

Figure 6.7: The diquark cluster mass M_C distribution after CR and the p_T distribution of all clusters that originate after CF from a diquark cluster of MB pp collisions at 7 TeV. The reconnection probabilities $P_M = P_D = 1$ and $P_B = 0$ have been used with the DCR algorithm varying the imposed cut on diquark cluster formation $\Delta_{\max}$ from $\Delta_{\max} = \infty$ (red), $\Delta_{\max} = 10$ (blue) and $\Delta_{\max} = 3$ (green).

towards lower masses the smaller the upper cut $\Delta_{\max}$ is. However, more interestingly is the effect on all clusters that originate from a diquark cluster, which appear to develop a soft peak the lower the cut is. This might also explain the difference in the $\langle p_T \rangle(N_{\text{ch}})$ for $p_T > 100$ MeV between the distribution without this cut (red) and the distribution with the cut in figure 6.6.

So in general the phenomenology of this DCR algorithm is quite similar to the BCR algorithm with the exception that it is now possible to more efficiently produce baryons also for lower multiplicity events, which can be used to reduce the CF/CD model baryons in order to be more consistent with the BB and BA correlations. To study more in detail the multiplicity dependence of CR and in particular for baryon correlations, we advocated for multiplicity binned analyses, which have been conducted in [139–141]. Although we have not provided yet a full tune of this model we still plan to do so with potentially the new matrix element CF model, which is however still too inefficient to attempt such a tuning endeavour.

We have now also seen that the baryon and diquark cluster CR have a substantial impact on the $\langle p_T \rangle(N_{\text{ch}})$ observable if they are not overpowered by mesonic CR. It would be very useful to have a measurement on the $\langle p_T \rangle_{\text{Baryons}}(N_{\text{ch}})$ observable, where the average runs only over the baryon p_T momenta such that we could get a better probe on how baryons are generated from CR. Some studies of this observable exist already e.g. [174] measured by ALICE and for the mean number of baryons as a function of multiplicity $\langle N_{\text{Baryons}} \rangle(N_{\text{ch}})$ from [175, 176] measured by ALICE, but unfortunately no public `Rivet` analysis is available yet.

6.4 Conclusions and Outlook

In this chapter, we have presented the diquark cluster singlet state and developed a new CR algorithm, which includes the efficient formation of such clusters. We have discussed the possible topologies and the selection algorithm of this new Diquark CR (DCR) algorithm and studied its phenomenology [169]. In particular, we found that the results are only reasonable if one imposes a cut on this diquark cluster formation, which is related to the approximation of this diquark cluster as a diquark-antidiquark cluster. However, we note that this is not

necessarily an issue since our hadronization model is just incapable in its current form of dealing with a diquark cluster which has a higher dimensional substructure.

We have also found that if we change e.g. the CD model to a more aligned t-channel like model (which we discussed in section 5.3), the resulting correlations are less washed out and the BA correlations exhibit a stronger suppression also for the new diquark topologies. We noted however that this is not yet the complete answer to the baryon production since the CF/CD baryon production has been turned off completely and for a more complete model a fully fledged tune will be needed. Therefore it should be clear that the hadronization and CR model are strongly correlated.

In fact, as mentioned previously the hadronization model should be interleaved with the CR model especially since this would also allow for the production of more mesonic clusters, which could be reconnected by the baryonic CR to new baryonic clusters. This interplay goes beyond this thesis but will be addressed in future work. However, it is also necessary to increase the performance of the matrix element cluster fission discussed before in order to study the interleaving of the CR and the CF model.

In terms of observables it would be very interesting to compare predictions for doubly or triply heavy quark baryons [177–179] from our microscopic model versus other statistical/thermal models e.g. [178] to assess whether thermal effects are responsible for the formation of multi heavy quark baryons.

CHAPTER 7

Dynamic Colour Reconnection from Soft Gluon Evolution

As we have seen in the previous chapters 4 and 6 phenomenological CR models are able to describe a plethora of MB observables such as charged multiplicities N_{ch}, p_T and η distributions, $\langle p_T \rangle (N_{\mathrm{ch}})$ and even multiplicity correlations for baryons. However, all of those models depend on phenomenological parameters, which need to be tuned to the available data and therefore limit the predictivity of such models. This tuning is typically performed mostly only with MB data and is therefore not guaranteed to yield a reasonable description for less inclusive and more differential observables. Furthermore, generalizing phenomenological models such as the model we presented in chapter 6 to more complicated CR topologies will increase the number of a priori not known parameters additionally. It is therefore important to develop CR models beyond phenomenological arguments based on their underlying theoretical mechanism, which in the case for CR is the colour exchanges between partons via soft gluons. The theoretical foundations of such a CR model have been laid in [8, 180], where also the systematic expansion in N_c has been discussed solidifying the claim that CR is a subleading colour effect. Based on this soft gluon evolution picture we will build on the results of [8] and develop an algorithm, which we will call dynamic CR, and discuss the necessary choices and approximations that are necessary. Additionally, we discuss the phenomenology of some of the already existing CR algorithms supplied with the dynamical CR probabilities.

In the following, we proceed with presenting the basis of soft gluon evolution from [8]. Afterwards we will define the new diquark colour flow states and the subdivision of the whole set of clusters into close-by sub-systems of clusters. Finally, we will describe the transition probabilities and the implementation before showing phenomenological results [169].

7.1 Soft Gluon Colour Evolution

A general matrix element $|\mathcal{A}(\{p_i\})\rangle$ can be expanded in the $n!$-dimensional overcomplete and non-orthonormal basis of colour flow states $|\sigma\rangle \in S(n)$ as follows, where n is the number of final state partons:

$$|\mathcal{A}(\{p_i\})\rangle = \sum_{\sigma} \mathcal{A}_\sigma(\{p_i\}) \, |\sigma\rangle \, , \tag{7.1}$$

where $\{p_i\}$ is the set of momenta and $\mathcal{A}_\sigma(\{p_i\})$ are the colour flow coefficients of the matrix element. A NLO matrix element $|\mathcal{A}(\{p_i\})\rangle$ has Ultra-Violet (UV) and IR divergences, where

the UV divergences can be absorbed into the counterterms and result in the running of the coupling through the usual renormalization procedure [13]. The IR divergences on the other hand cause the evolution of the initial amplitude, which resums the large IR logarithms to all orders in perturbation theory according to [181]. In Dimensional Regularization (DR) for the IR singularity with the space-time dimensions $D = 4 - 2\epsilon$, the IR renormalized matrix element $|\mathcal{A}(\{p_i\}; \mu^2)\rangle$ is defined as the following [8]:

$$|\mathcal{A}(\{p_i\}; \mu^2)\rangle = \mathbf{Z}^{-1}[\{p_i\}; \mu^2, \epsilon] \times |\mathcal{A}_{\text{bare}}(\{p_i\}; \epsilon)\rangle. \tag{7.2}$$

Here $|\mathcal{A}_{\text{bare}}(\{p_i\}; \epsilon)\rangle$ is the "bare" IR regulated matrix element and $\mathbf{Z}[\{p_i\}; \mu^2, \epsilon]$ is the renormalization constant encapsulating the IR divergence regulated in DR at the IR renormalization scale μ. Since the bare matrix element is oblivious to the IR renormalization scale μ, the logarithmic derivative with respect to μ^2 of $|\mathcal{A}_{\text{bare}}(\{p_i\}; \epsilon)\rangle$ must vanish, leading to the following evolution equation [8]:

$$\mu^2 \frac{\mathrm{d}}{\mathrm{d}\mu^2} |\mathcal{A}(\{p_i\}; \mu^2)\rangle = \mathbf{\Gamma}[\{p_i\}; \mu^2] \times |\mathcal{A}(\{p_i\}; \mu^2)\rangle, \tag{7.3}$$

$$\mathbf{\Gamma}[\{p_i\}; \mu^2] = - \lim_{\epsilon \to 0} \mathbf{Z}^{-1}[\{p_i\}; \mu^2, \epsilon] \; \mu^2 \frac{\mathrm{d}}{\mathrm{d}\mu^2} \mathbf{Z}[\{p_i\}; \mu^2, \epsilon]. \tag{7.4}$$

Here $\mathbf{\Gamma}[\{p_i\}; \mu^2]$ is the so-called *soft anomalous dimension* matrix, which contains the IR divergent structure as a residue. According to [8] the soft anomalous dimension $\mathbf{\Gamma}[\{p_i\}; \mu^2]$ in the colour flow basis is given by the following:

$$\mathbf{\Gamma}[\{p_i\}; \mu^2] = - \sum_{i \neq j} \mathbf{T}_i \cdot \mathbf{T}_j \; \gamma_{\text{cusp}}(\alpha_s) \; \log\left(-\frac{s_{ij}}{\mu^2}\right) + \sum_i \gamma^i(\alpha_s) \; \mathbf{1}_{n! \times n!}. \tag{7.5}$$

Here $\mathbf{T}_i$ is the colour charge operator generating a soft gluon emission off parton leg i, $\gamma_{\text{cusp}} = \alpha_s/(4\pi)$ is the cusp anomalous dimension to leading order and γ^i is the soft anomalous dimension of parton i, which is proportional to the identity in colour space. Since γ^i is proportional to the identity in colour space we neglect it, since we are interested in the transition between colour states. For the indices i, j we use the convention of [180], where i, j are defined as the ordered set $\{1, \bar{1}, 2, \bar{2}, \ldots n, \bar{n}\}$ and not the convention of [8, 117].

Note that the first sum runs over all quarks, antiquarks and gluons. The kinematic dependence is contained in $s_{ij} = (p_i + p_j)^2$ for p_i and p_j both outgoing or both incoming. In the case of one incoming and one outgoing momentum $s_{ij} \to -s_{ij}$ in the above equation. Since we will be assuming that all partons are outgoing, we can rewrite the logarithm as the following:

$$\log\left(-\frac{s_{ij}}{\mu^2}\right) = \log\left(\frac{s_{ij}}{\mu^2}\right) - i\pi. \tag{7.6}$$

Note that here the sign of the imaginary part comes from the Feynman prescription [182].

In order to calculate the soft anomalous dimension, we need to define the colour charge operator $\mathbf{T}_i$, which is a $n! \times (n+1)!$ dimensional matrix in colour flow space mapping a n colour flow state to a $n+1$ colour flow state. According to [183] one can write this colour operator as the following:

$$\mathbf{T}_i = \lambda_i \; \mathbf{t}_{c_i} - \bar{\lambda}_i \; \mathbf{t}_{\bar{c}_i} - \frac{1}{N_c}(\lambda_i - \bar{\lambda}_i) \; \mathbf{s}. \tag{7.7}$$

Here we define the quark (antiquark) emission operators $\mathbf{t}_{c_i}$ ($\mathbf{t}_{\bar{c}_i}$), which correspond to the emission off a quark leg c_i (an antiquark leg $\bar{c}_i$), as the following actions on colour flow states alongside with the singlet emission operator $\mathbf{s}$:

$$\mathbf{t}_{c_i}\,|\rho\rangle = \mathbf{t}_{c_i}\,\left|\begin{smallmatrix}1 & \dots & i & \dots & n\\ \rho(1) & \dots & \rho(i) & \dots & \rho(n)\end{smallmatrix}\right\rangle = \left|\begin{smallmatrix}1 & \dots & i & \dots & n & n{+}1\\ \rho(1) & \dots & n{+}1 & \dots & \rho(n) & \rho(i)\end{smallmatrix}\right\rangle, \tag{7.8}$$

$$\mathbf{t}_{\bar{c}_i}\,|\rho\rangle = \mathbf{t}_{\bar{c}_i}\,\left|\begin{smallmatrix}1 & \dots & i & \dots & n\\ \rho(1) & \dots & \rho(i) & \dots & \rho(n)\end{smallmatrix}\right\rangle = \left|\begin{smallmatrix}1 & \dots & \rho^{-1}(i) & \dots & n & n{+}1\\ \rho(1) & \dots & n{+}1 & \dots & \rho(n) & i\end{smallmatrix}\right\rangle = \mathbf{t}_{\rho^{-1}(c_i)}|\rho\rangle, \tag{7.9}$$

$$\mathbf{s}\,|\rho\rangle = \left|\begin{smallmatrix}1 & \dots & n & n{+}1\\ \rho(1) & \dots & \rho(n) & \rho(n{+}1)\end{smallmatrix}\right\rangle. \tag{7.10}$$

Note that here $\rho^{-1}(i)$ is defined as the inverse permutation such that $\rho^{-1}(\rho(i)) = i$.
Here we define the constants λ_i, $\bar{\lambda}_i$, which are defined as the following for convenience:

$$\lambda_i = \begin{cases}\sqrt{T_R} & \text{for } i \text{ gluon or quark}\\ 0 & \text{else}\end{cases}, \quad \bar{\lambda}_i = \begin{cases}\sqrt{T_R} & \text{for } i \text{ gluon or antiquark}\\ 0 & \text{else}\end{cases}. \tag{7.11}$$

Notice that the dot product defined in (7.5) is defined in such a way that the following relations hold [183]:

$$\mathbf{t}_{c_i}\cdot\mathbf{t}_{c_j}\,|\rho\rangle = \left|\begin{smallmatrix}1 & \dots & i & \dots & j & \dots & n\\ \rho(1) & \dots & \rho(j) & \dots & \rho(i) & \dots & \rho(n)\end{smallmatrix}\right\rangle = |\rho_{(ij)}\rangle, \tag{7.12}$$

$$\mathbf{t}_{c_i}\cdot\mathbf{t}_{\bar{c}_j}\,|\rho\rangle = N_c|\rho\rangle, \tag{7.13}$$

$$\mathbf{s}\cdot\mathbf{s}\,|\rho\rangle = N_c|\rho\rangle, \tag{7.14}$$

$$\mathbf{t}_{c_i}\cdot\mathbf{s}\,|\rho\rangle = \mathbf{t}_{\bar{c}_i}\cdot\mathbf{s}\,|\rho\rangle = \mathbf{s}\cdot\mathbf{t}_{c_i}\,|\rho\rangle = \mathbf{s}\cdot\mathbf{t}_{\bar{c}_i}\,|\rho\rangle = |\rho\rangle. \tag{7.15}$$

Here we define the *colour reconnection* operators $\mathbf{t}_{c_i}\cdot\mathbf{t}_{c_j}$, which are defined by exchanging colours i and j leading to the swapped state $|\rho_{(ij)}\rangle$.

A general endomorphic operator in colour space $\mathbf{O}$ can be expanded in the colour flow space in the following manner [38]:

$$\mathbf{O} = \sum_{\sigma,\,\rho\in S(n)} \mathcal{O}_{\sigma\rho}\,|\sigma\rangle\,[\rho|\,, \tag{7.16}$$

$$\mathcal{O}_{\sigma\rho} = [\sigma|\,\mathbf{O}\,|\rho\rangle\,. \tag{7.17}$$

With the actual matrix elements $\mathcal{O}_{\sigma\rho}$ given in an orthonormal basis. Thus using relations (7.12) we can get the matrix elements $[\tau|\mathbf{T}_i\cdot\mathbf{T}_j|\sigma\rangle$ for $i \neq j$ of the operator dot product $\mathbf{T}_i\cdot\mathbf{T}_j$ using the completeness relations (2.23), which yields:

$$\mathbf{T}_i\cdot\mathbf{T}_j = \sum_{\sigma,\,\tau\in S(n)} [\tau|\mathbf{T}_i\cdot\mathbf{T}_j|\sigma\rangle\;|\tau\rangle[\sigma|, \tag{7.18}$$

$$\begin{aligned}[\tau|\mathbf{T}_i\cdot\mathbf{T}_j|\sigma\rangle = &-N_c\;\delta_{\tau\sigma}\left[\lambda_i\bar{\lambda}_j\delta_{\sigma(c_i),\,\bar{c}_j} + \bar{\lambda}_i\lambda_j\delta_{\sigma(c_j),\,\bar{c}_i} + \frac{1}{N_c^2}(\lambda_i-\bar{\lambda}_i)(\lambda_j-\bar{\lambda}_j)\right]\\ &+\sum_{a<b}\delta_{\tau_{(ab)}\sigma}\Big(\lambda_i\lambda_j\delta_{(ab),\,(c_ic_j)} + \bar{\lambda}_i\bar{\lambda}_j\delta_{(ab),\,(\sigma^{-1}(\bar{c}_i)\sigma^{-1}(\bar{c}_j))}\\ &-\lambda_i\bar{\lambda}_j\delta_{(ab),\,(c_i\sigma^{-1}(\bar{c}_j))} - \bar{\lambda}_i\lambda_j\delta_{(ab),\,(c_j\sigma^{-1}(\bar{c}_i))}\Big)\,.\end{aligned} \tag{7.19}$$

Note that by (ab) the ordered pair of indices is meant such that $(ab) = ba$ if $b < a$. These matrix elements in the orthonormal basis will be useful for actual computations using matrices.

The solution of equation (7.3) can be written as the following using the evolution operator $\mathbf{U}$:

$$|\mathcal{A}(\{p_i\};\mu^2)\rangle = \mathbf{U}\left(\{p_i\};\mu^2,\,\{M_{ij}^2\}\right)|\mathcal{A}(\{p_i\};\{M_{ij}^2\})\rangle. \tag{7.20}$$

Here $\mathbf{U}\left(\{p_i\};\mu^2,\,\{M_{ij}^2\}\right)$ is the soft gluon evolution operator and $|\mathcal{A}(\{p_i\};\{M_{ij}^2\})\rangle$ is the matrix element after the parton shower with $M_{ij}^2 = (p_i + p_j)^2$ the invariant mass of the primordial leading colour singlet clusters. We assume here that the parton shower has already resummed the logarithms of the hard process of scale Q down to the typical PS cutoff of order Q_0, which then implies that $M_{ij} \sim \mathcal{O}(Q_0)$. Furthermore, we evolve the system down to a lower IR scale μ, which must satisfy $\mu^2 < M_{ij}^2$ for all possible kinematics. The soft gluon evolution operator is then defined as the following:

$$\mathbf{U}\left(\{p_i\};\mu^2,\,\{M_{ij}^2\}\right) = \exp\left(-\sum_{i\neq j}\mathbf{T}_i\cdot\mathbf{T}_j\int_{M_{ij}^2}^{\mu^2}\frac{\mathrm{d}q^2}{q^2}\,\frac{\alpha_s(q^2)}{4\pi}\,\left[\log\left(\frac{M_{ij}^2}{q^2}\right)-i\pi\right]\right), \tag{7.21}$$

$$\approx \exp\left(\sum_{i\neq j}\mathbf{T}_i\cdot\mathbf{T}_j\,\frac{\alpha_s}{4\pi}\,\left[\frac{1}{2}\log^2\left(\frac{M_{ij}^2}{\mu^2}\right)-i\pi\log\left(\frac{M_{ij}^2}{\mu^2}\right)\right]\right). \tag{7.22}$$

Note that in the last equation we approximate the running $\alpha_s(q)$ as constant, which allows us to explicitly perform the integral. Looking at the structure of equation (7.22), we assume that the imaginary part of the exponential - the so-called Coulomb term - is negligible as has been shown in [8]. This suppression can be clearly seen explicitly if the logarithm is large, but in addition also a lot of cancellation happens in the sum over partons in the off-diagonal entries of the final matrix.

Now we can define the transition amplitude $\mathcal{T}_{\sigma\to\tau}$ from an initial colour state $|\sigma\rangle$ at scales $\{M_{ij}^2\}$ evolved towards a state $|\tau\rangle$ at a lower scale μ^2 as the following:

$$\mathcal{T}_{\sigma\to\tau} = \langle\tau|\,\mathbf{U}\left(\{p_i\};\mu^2,\,\{M_{ij}^2\}\right)|\sigma\rangle\,, \tag{7.23}$$

$$= \sum_{\rho,\,\lambda\in S(n)}\langle\tau\mid\lambda\rangle\,[\lambda|\,\mathbf{U}\,|\rho\rangle\,[\rho\mid\sigma\rangle = \sum_{\lambda\in S(n)}\langle\tau\mid\lambda\rangle\,\mathcal{U}_{\lambda\sigma}. \tag{7.24}$$

These transition amplitudes can then be used to compute the CR probability $\mathcal{P}_{\sigma\to\tau}$ for going from state $|\sigma\rangle$ to $|\tau\rangle$ as follows:

$$\mathcal{P}_{\sigma\to\tau} = \frac{|\mathcal{T}_{\sigma\to\tau}|^2}{\sum_{\rho\in\mathcal{S}(n)}|\mathcal{T}_{\sigma\to\rho}|^2}. \tag{7.25}$$

Here the sum in the denominator runs over all possible singlet states, whose set we define as $\mathcal{S}(n)$, which contains also the original state $|\sigma\rangle$.

7.2 Mesonic, Diquark and Baryonic Cluster States

Since we have now defined the transition amplitudes, we can introduce the different types of singlet states we can project onto. We define mesonic colour flow states $|\sigma\rangle$ as the following:

$$|\sigma\rangle = \left|\begin{smallmatrix}1 & \cdots & n\\ \sigma(\bar{1}) & \cdots & \sigma(\bar{n})\end{smallmatrix}\right\rangle =: |\sigma(\bar{1})\ \ldots\ \sigma(\bar{n})\rangle\,, \tag{7.26}$$

which corresponds to the configuration of n mesonic clusters $C(q_k,\,\bar{q}_{\sigma(\bar{k})})$ consisting of quark q_k and antiquark $\bar{q}_{\sigma(\bar{k})}$. Note that in practice not all of the $N_{\text{mesonic}} = |S(n)| = n!$ possible permutations are allowed because they could originate directly or indirectly (depending on the `OctetTreatment` option) from a gluon octet. Without loss of generality[43] we define our

[43] Since we have only mesonic clusters before the CR.

primordial cluster configuration to be the identity permutation $|\mathbf{1}\rangle = |\bar{1} \ \ldots \ \bar{n}\rangle$, which allows us to define the mesonic CR probability as follows:

$$\mathcal{P}_{\mathbf{1}\to\tau} = \frac{|\mathcal{T}_{\mathbf{1}\to\tau}|^2}{\sum_{\rho\in\mathcal{S}(n)} |\mathcal{T}_{\mathbf{1}\to\rho}|^2}. \tag{7.27}$$

As already discussed in the previous chapter we can define a singlet diquark cluster state $\left|D^{ij}_{\bar{k}\bar{l}}\right\rangle$ consisting of two quarks q_i, q_j and two antiquarks $\bar{q}_{\bar{k}}$, $\bar{q}_{\bar{l}}$, for which we can express the colour flow state as the following:

$$\left|D^{ij}_{\bar{k}\bar{l}}\right\rangle = \frac{1}{N_D} \sum_{\pi\in S(2)} \operatorname{sgn}(\pi) \left| \begin{smallmatrix} i & j \\ \pi(\bar{k}) & \pi(\bar{l}) \end{smallmatrix} \right\rangle, \tag{7.28}$$

$$= \frac{1}{N_D} \left(\left| \begin{smallmatrix} i & j \\ \bar{k} & \bar{l} \end{smallmatrix} \right\rangle - \left| \begin{smallmatrix} i & j \\ \bar{l} & \bar{k} \end{smallmatrix} \right\rangle \right). \tag{7.29}$$

Here N_D is a normalization constant and the permutation π acts on the ordered set $\{\bar{k}, \bar{l}\}$. The normalization of the diquark state is set to be equal to the normalization of a general two colour flow state similar to [8] yielding the following:

$$\left\langle D^{ij}_{\bar{k}\bar{l}} \,\middle|\, D^{ij}_{\bar{k}\bar{l}} \right\rangle \overset{!}{=} N_c^2, \tag{7.30}$$

$$\Leftrightarrow N_D = \sqrt{\frac{2(N_c-1)}{N_c}}. \tag{7.31}$$

Note that even though we give the above expression for unspecified N_c, the diquark cluster treatment relies on the fact that $\mathbf{3}\otimes\mathbf{3} = \ldots \oplus \bar{\mathbf{3}}$ transform in the anti-fundamental representation and therefore requires $N_c = 3$ in order to be meaningful.

Now we can define the colour flow state, which consists of one diquark cluster configuration $\left|D^{ij}_{\bar{k}\bar{l}}\right\rangle$ and the remainder $\left|\tilde{\rho}^{ij}_{\bar{k}\bar{l}}\right\rangle$ being in some mesonic permutation state with the remaining partons as the following:

$$\left|D^{ij}_{\bar{k}\bar{l}}\right\rangle \ \otimes \left|\tilde{\rho}^{ij}_{\bar{k}\bar{l}}\right\rangle \in S(2)\otimes S(n-2), \tag{7.32}$$

$$\left|\tilde{\rho}^{ij}_{\bar{k}\bar{l}}\right\rangle = \left| \begin{smallmatrix} 1 & \ldots & n & \setminus & i & j \\ \rho(\bar{1}) & \ldots & \rho(\bar{n}) & \setminus & \bar{k} & \bar{l} \end{smallmatrix} \right\rangle. \tag{7.33}$$

Note that the permutation ρ acts on the set $\{\bar{1}, \ldots, \bar{n}\} \setminus \{\bar{k}, \bar{l}\}$ and therefore $(n-2)!$ different states are a priori possible. However, since we can choose a different set of partons as the diquark state the maximal number of single diquark states $N_{\text{diquark}}(n)$ is given by the following:

$$N_{\text{diquark}}(n) = (n-2)! \left[\binom{n}{2}\right]^2 = n!\frac{n(n-1)}{2!^2}. \tag{7.34}$$

Here the $(n-2)!$ comes from the remainder permutation group $S(n-2)$ and the binomial coefficient since we choose 2 from all n quarks and the same for the antiquarks to make one diquark cluster. It follows that $N_{\text{diquark}}(n) > N_{\text{mesonic}}(n)$ for $n \geq 3$, i.e. we have more diquark states associated with mesonic states than regular mesonic states[44].

Now we can define the diquark cluster transition probabilities as the following:

$$\mathcal{P}_{\sigma\to D^{ij}_{\bar{k}\bar{l}} \otimes \tilde{\rho}^{ij}_{\bar{k}\bar{l}}} = \frac{|\mathcal{T}_{\sigma\to D^{ij}_{\bar{k}\bar{l}} \otimes \tilde{\rho}^{ij}_{\bar{k}\bar{l}}}|^2}{\mathcal{N}_\sigma}, \tag{7.35}$$

$$\mathcal{N}_\sigma = \sum_{\rho\in\mathcal{S}(n)} |\mathcal{T}_{\sigma\to\rho}|^2 + \sum_{i<j}\sum_{\bar{k}<\bar{l}}\sum_{\rho\in\mathcal{S}(n-2)} |\mathcal{T}_{\sigma\to D^{ij}_{\bar{k}\bar{l}} \otimes \tilde{\rho}^{ij}_{\bar{k}\bar{l}}}|^2. \tag{7.36}$$

[44] Of course some mesonic states might be forbidden due to octets or the overcompleteness of the basis since the determinant of $\det(\langle\sigma \mid \tau\rangle) = 0$ for $n > 3$ and $N_c = 3$.

Note that here we define a generalized normalization $\mathcal{N}_\sigma$, which ensures that diquark and mesonic CR probabilities sum to unity.

As already discussed in [8] we can define a baryonic-antibaryonic cluster state $\left|B^{ijk}_{\bar{l}\bar{m}\bar{r}}\right\rangle$ consisting of three quarks q_i, q_j, q_k and three antiquarks $\bar{q}_{\bar{l}}$, $\bar{q}_{\bar{m}}$, $\bar{q}_{\bar{r}}$, which we can define in the colour flow basis as the following:

$$\left|B^{ijk}_{\bar{l}\bar{m}\bar{r}}\right\rangle = \frac{1}{N_B}\sum_{\pi\in S(3)}\operatorname{sgn}(\pi)\left|\begin{smallmatrix} i & j & k \\ \pi(\bar{l}) & \pi(\bar{m}) & \pi(\bar{r})\end{smallmatrix}\right\rangle. \tag{7.37}$$

Here N_B is a normalization constant and the permutation π acts on the ordered set $\{\bar{l}, \bar{m}, \bar{r}\}$. The normalization N_B of the baryonic state is set to be equal to the normalization of a general three colour flow state yielding the following:

$$\left\langle B^{ijk}_{\bar{l}\bar{m}\bar{r}} \,\middle|\, B^{ijk}_{\bar{l}\bar{m}\bar{r}}\right\rangle \stackrel{!}{=} N_c^3, \tag{7.38}$$

$$\Leftrightarrow N_B = \frac{\sqrt{6(N_c-1)(N_c-2)}}{N_c}. \tag{7.39}$$

Note that even though we give the above expression for unspecified N_c, we of course use the fact that we can recombine three quarks and antiquarks to a baryon and an antibaryon, which requires $N_c = 3$.

Now we can define the colour flow state, which consists of one baryonic-antibaryonic cluster pair configuration $\left|B^{ijk}_{\bar{l}\bar{m}\bar{r}}\right\rangle$ and the remainder $\left|\tilde{\rho}^{ijk}_{\bar{l}\bar{m}\bar{r}}\right\rangle$ being in some mesonic permutation state with the remaining partons as the following:

$$\left|B^{ijk}_{\bar{l}\bar{m}\bar{r}}\right\rangle \otimes \left|\tilde{\rho}^{ijk}_{\bar{l}\bar{m}\bar{r}}\right\rangle \in S(3)\otimes S(n-3), \tag{7.40}$$

$$\left|\tilde{\rho}^{ijk}_{\bar{l}\bar{m}\bar{r}}\right\rangle = \left|\begin{smallmatrix} 1 & \dots & n & \setminus & i & j & k \\ \rho(\bar{1}) & \dots & \rho(\bar{n}) & \setminus & \bar{l} & \bar{m} & \bar{r}\end{smallmatrix}\right\rangle. \tag{7.41}$$

Note that the permutation ρ acts on the set $\{\bar{1}, \dots, \bar{n}\} \setminus \{\bar{l}, \bar{m}, \bar{r}\}$ and therefore $(n-3)!$ different states are a priori possible. However, since we can choose different sets of (anti)quarks for the (anti)baryonic state the maximal number of baryonic-antibaryonic states $N_{\text{baryonic}}(n)$ is given by the following:

$$N_{\text{baryonic}}(n) = (n-3)!\left[\binom{n}{3}\right]^2 = n!\frac{n(n-1)(n-2)}{3!^2}. \tag{7.42}$$

Here the $(n-3)!$ comes from the remainder permutation group $S(n-3)$ and the binomial coefficient is present since we choose 3 from all n quarks and also 3 from all n antiquarks in order to make a baryonic-antibaryonic cluster pair. It follows that $N_{\text{baryonic}}(n) > N_{\text{mesonic}}(n)$ for $n \geq 5$, i.e. we have more baryonic states associated with mesonic states than regular mesonic states[45].

Now we can define the baryonic-antibaryonic cluster pair transition probabilities as the following:

$$\mathcal{P}_{\sigma\to B^{ijk}_{\bar{l}\bar{m}\bar{r}}\otimes\tilde{\rho}^{ijk}_{\bar{l}\bar{m}\bar{r}}} = \frac{|\mathcal{T}_{\sigma\to B^{ijk}_{\bar{l}\bar{m}\bar{r}}\otimes\tilde{\rho}^{ijk}_{\bar{l}\bar{m}\bar{r}}}|^2}{\mathcal{N}_\sigma}, \tag{7.43}$$

$$\begin{aligned}\mathcal{N}_\sigma = &\sum_{\rho\in\mathcal{S}(n)}|\mathcal{T}_{\sigma\to\rho}|^2 + \sum_{i<j}\sum_{\bar{k}<\bar{l}}\sum_{\rho\in\mathcal{S}(n-2)}|\mathcal{T}_{\sigma\to D^{ij}_{\bar{k}\bar{l}}\otimes\tilde{\rho}^{ij}_{\bar{k}\bar{l}}}|^2 \\ &+ \sum_{i<j<k}\sum_{\bar{l}<\bar{m}<\bar{r}}\sum_{\rho\in\mathcal{S}(n-3)}|\mathcal{T}_{\sigma\to B^{ijk}_{\bar{l}\bar{m}\bar{r}}\otimes\tilde{\rho}^{ijk}_{\bar{l}\bar{m}\bar{r}}}|^2.\end{aligned} \tag{7.44}$$

[45] Of course some mesonic states might be forbidden due to octets or the overcompleteness of the basis.

Note that here we include in the even more general normalization $\mathcal{N}_\sigma$ all CR topologies, which ensures that baryonic, diquark and mesonic CR probabilities sum to unity.

7.3 Phenomenology of Two Clusters

In this section we study the derived transition amplitudes for a two cluster system and examine how the diquark CR (DCR) probability behaves in contrast to mesonic CR (MCR). For a two cluster system $C_1(q_1, \bar{q}_2)$, $C_2(q_3, \bar{q}_4)$ we get the following matrix before the exponentiation:

$$\mathbf{\Omega} := \log \mathbf{U} = \begin{pmatrix} -N_c(\Omega_{12}+\Omega_{34}) & \Omega_{13}+\Omega_{24}-\Omega_{12}-\Omega_{34} \\ \Omega_{13}+\Omega_{24}-\Omega_{23}-\Omega_{14} & -N_c(\Omega_{14}+\Omega_{23}) \end{pmatrix}, \tag{7.45}$$

$$\Omega_{ij} = \frac{\alpha_s}{4\pi}\left[\frac{1}{2}\log^2\left(\frac{M_{ij}^2}{\mu^2}\right) - i\pi\log\left(\frac{M_{ij}^2}{\mu^2}\right)\right] \approx \frac{\alpha_s}{8\pi}\log^2\left(\frac{M_{ij}^2}{\mu^2}\right). \tag{7.46}$$

In the following, we will only work with the approximated Ω_{ij} as shown above by neglecting the imaginary part. We can explicitly exponentiate this matrix, which yields the following evolution operator $\mathbf{U}$:

$$\mathbf{U} = \frac{e^{-\frac{N_c}{2}(a+b)}}{\sqrt{\Delta}}\sinh\left(\frac{\sqrt{\Delta}}{2}\right)\begin{pmatrix} \sqrt{\Delta}\coth\left(\frac{\sqrt{\Delta}}{2}\right)+N_c(b-a) & 2(c-a) \\ 2(c-b) & \sqrt{\Delta}\coth\left(\frac{\sqrt{\Delta}}{2}\right)-N_c(b-a) \end{pmatrix}, \tag{7.47}$$

where the corresponding variables a, b, c and Δ are defined as the following:

$$a = \Omega_{34}+\Omega_{12}, \tag{7.48}$$

$$b = \Omega_{14}+\Omega_{23}, \tag{7.49}$$

$$c = \Omega_{13}+\Omega_{24}, \tag{7.50}$$

$$\Delta = a^2N_c^2 - 4c(a+b) - 2ab(N_c^2-2) + b^2N_c^2 + 4c^2. \tag{7.51}$$

Note here that all $\Omega_{ij} \geq 0$ since $\mu^2 \leq M_{ij}^2$. Now we can compute the three CR probabilities P_{noCR}, P_{MCR} and P_{DCR} for a general evolution matrix where we define $U_{ij} := \mathcal{U}_{\sigma\tau}$ with $|\sigma\rangle = |12\rangle \to 1$ and $|\tau\rangle = |21\rangle \to 2$ as the following:

$$P_{\text{noCR}} = \frac{|\mathcal{T}_{12\to 12}|^2}{\mathcal{N}} = N_c^2\frac{|N_cU_{11}+U_{21}|^2}{\mathcal{N}}, \tag{7.52}$$

$$P_{\text{MCR}} = \frac{|\mathcal{T}_{12\to 21}|^2}{\mathcal{N}} = N_c^2\frac{|U_{11}+N_cU_{21}|^2}{\mathcal{N}}, \tag{7.53}$$

$$P_{\text{DCR}} = \frac{|\mathcal{T}_{12\to D_{\bar{1}\bar{2}}^{12}}|^2}{\mathcal{N}} = \frac{N_c^3(N_c-1)}{2}\frac{|U_{11}-U_{21}|^2}{\mathcal{N}}, \tag{7.54}$$

$$\mathcal{N} = |\mathcal{T}_{12\to 12}|^2 + |\mathcal{T}_{12\to 21}|^2 + |\mathcal{T}_{12\to D_{\bar{1}\bar{2}}^{12}}|^2. \tag{7.55}$$

Here one can clearly see that a global factor of the matrix (like the prefactor of equation (7.47)) will scale out in the reconnection probabilities since all the probabilities are unitarized to yield $P_{\text{noCR}}+P_{\text{MCR}}+P_{\text{DCR}} = 1$. We can now assess how these probabilities depend on the kinematic variables a, b and c. Note that the definitions in equations (7.48)-(7.50) correspond essentially to a phase space distance measure of parton groupings e.g. a is related to the original cluster grouping $(q_1, \bar{q}_2)$ and $(q_3, \bar{q}_4)$, b is related to the Mesonic CR (MCR) configuration $(q_1, \bar{q}_4)$

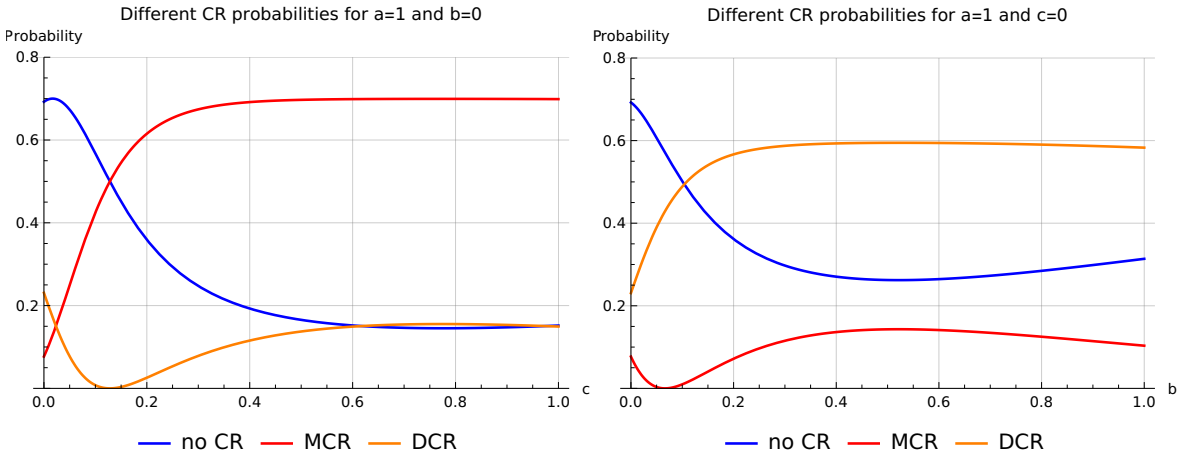

Figure 7.1: The different CR probabilities P_{noCR}, P_{MCR} and P_{DCR} for the kinematic configurations $a = 1$, $b = 0$ (left) as a function of c and $a = 1$, $c = 0$ (right) as a function of b.

and $(q_3, \bar{q}_2)$ and c is related to the Diquark CR (DCR) configuration (q_1, q_3) and $(\bar{q}_2, \bar{q}_4)$ corresponding to a diquark-antidiquark cluster. So effectively small a, b or c corresponds to their respective cluster configuration being very favourable and vice-versa.

In order to simplify our discussion we assume that the original cluster configuration is very unfavourable and therefore imposes the hierarchy $a > b, c$. Then we can assume "almost" without loss of generality that $a = 1$ and thus $b, c < 1$, which allows us to display the probabilities in figures 7.1-7.3 for different kinematic regimes. Note that the "almost" relates to the fact that we still assume that $\sqrt{\Delta} \gg 1$ such that the approximation $\coth\left(\sqrt{\Delta}/2\right) \approx 1$ is still valid since the coth term is the only term where a global factor of a cannot be scaled out of the evolution matrix.

In figure 7.1 we set $b = 0$ (left) corresponding to an efficient mesonic CR configuration as a function of c and $c = 0$ (right) corresponding to an efficient diquark CR configuration as a function of b. On the left we can clearly see that for an inefficient diquark configuration (large c) we get a large mesonic CR probability, which is as expected. For low c however the no CR topology dominates, which corresponds to the regime where both diquark and mesonic CR configurations are quite efficient. However, it may be that there are some phase space restrictions in this case since we would not expect to have unlikely CR if both mesonic and diquark configurations are favourable ($b = c = 0$).

In [8] the approximation $\cot\left(\sqrt{\Delta}/2\right) \approx 1$ was employed for the evolution matrix. In order to estimate the validity of this approximation we plot the same reconnection probabilities in figure 7.2 for the same limits. We can see quite some differences, which most likely can be attributed to our hierarchy choice $a = 1 > b, c$, which controls the magnitude of Δ and thus determines whether $\coth\left(\sqrt{\Delta}/2\right) \approx 1$ is a good approximation or not.

In figure 7.3 we set $b = 1$ (left) corresponding to an unfavourable mesonic CR configuration as a function of c and $c = 1$ (right) corresponding to an unfavourable diquark CR configuration as a function of b. One can clearly see that the no CR probability is dominant in both cases for large c and b respectively as expected. For low values of c (b) we see that the diquark (mesonic) CR dominates as one would expect.

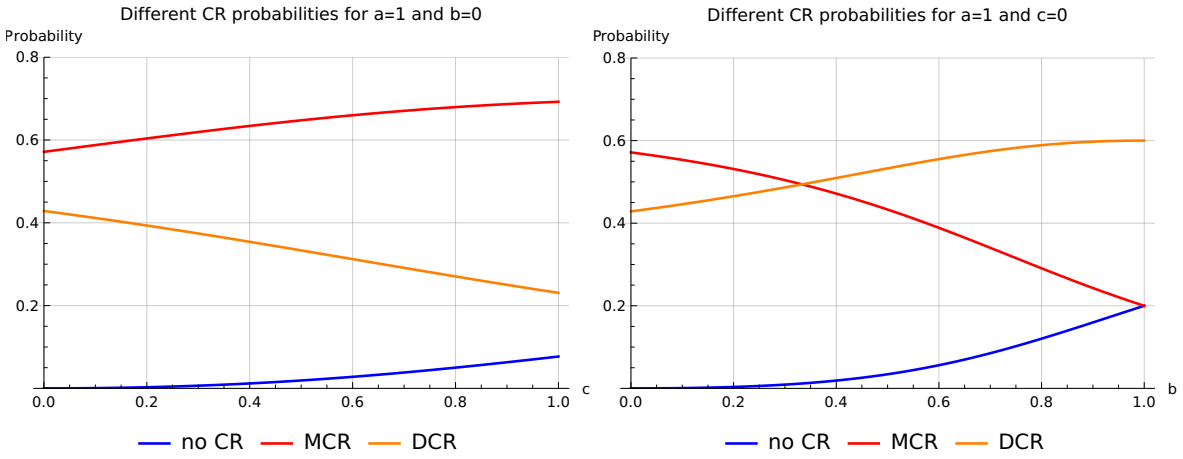

Figure 7.2: The different CR probabilities P_{noCR}, P_{MCR} and P_{DCR} for the kinematic configurations $a = 1$, $b = 0$ (left) as a function of c and $a = 1$, $c = 0$ (right) as a function of b. Here the approximation $\coth\left(\sqrt{\Delta}/2\right) \approx 1$ has been used.

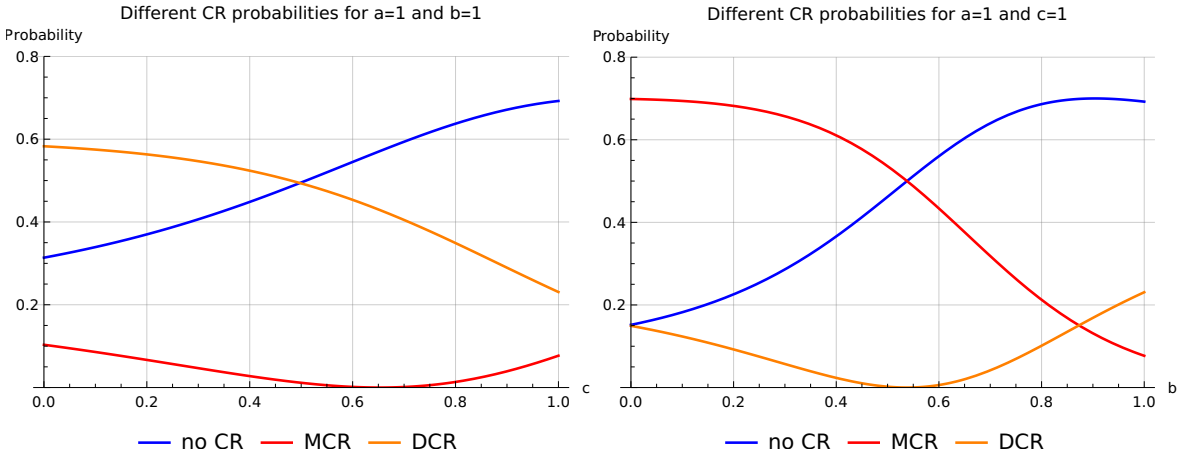

Figure 7.3: The different CR probabilities P_{noCR}, P_{MCR} and P_{DCR} for the kinematic configurations $a = b = 1$ (left) as a function of c and $a = c = 1$ (right) as a function of b.

7.4 Undiquarkization

As discussed in [8] there is of course also the possibility of an already existing baryonic-antibaryonic cluster pair to evolve into a set of three mesonic clusters. A similar effect appears for a single diquark cluster D, which can split into two mesonic clusters either in the $|12\rangle$ (original) or the $|21\rangle$ (mesonic CR'd) state. We call this mechanism *undiquarkization* and can easily write down the transition probabilities as follows:

$$P_{D\to D} = \frac{|\mathcal{T}_{D\to D}|^2}{\mathcal{N}} = \frac{N_c^4}{4}\frac{|\,(U_{11}+U_{22})-(U_{12}+U_{21})\,|^2}{\mathcal{N}}, \tag{7.56}$$

$$P_{D\to|12\rangle} = \frac{|\mathcal{T}_{D\to 12}|^2}{\mathcal{N}} = \frac{N_c^3}{2(N_c-1)}\frac{|\,N_c\,(U_{11}-U_{12})+(U_{21}-U_{22})\,|^2}{\mathcal{N}}, \tag{7.57}$$

$$P_{D\to|21\rangle} = \frac{|\mathcal{T}_{D\to 21}|^2}{\mathcal{N}} = \frac{N_c^3}{2(N_c-1)}\frac{|\,(U_{11}-U_{12})+N_c\,(U_{21}-U_{22})\,|^2}{\mathcal{N}}, \tag{7.58}$$

$$\mathcal{N} = |\mathcal{T}_{D\to D}|^2 + |\mathcal{T}_{D\to 12}|^2 + |\mathcal{T}_{D\to 21}|^2. \tag{7.59}$$

Note that in this case since we are not starting from the identity permutation state $|12\rangle$ but a superposition of both permutation states, the probabilities now depend on all entries of the evolution matrix.

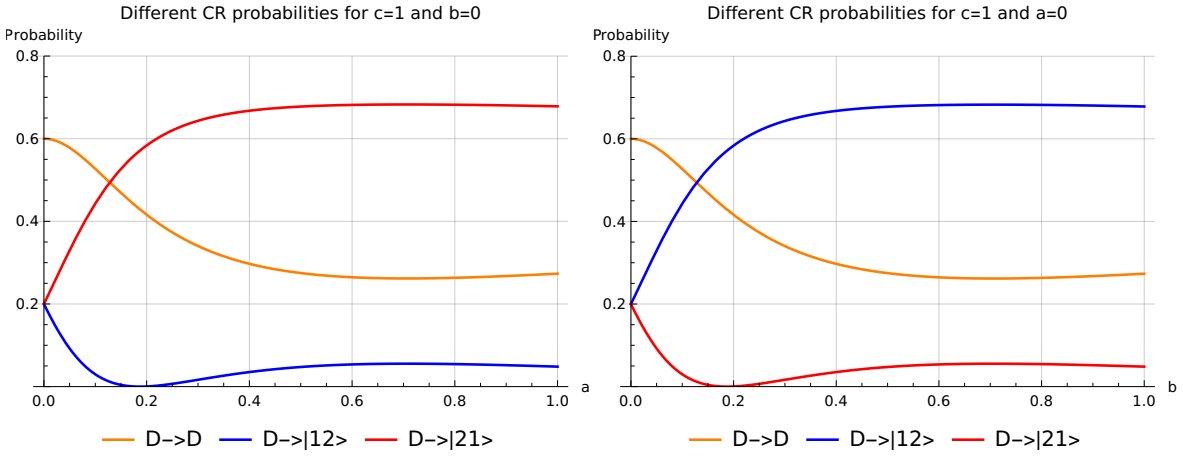

Figure 7.4: The different CR probabilities for a diquark cluster $P_{D\to D}$, $P_{D\to|12\rangle}$ and $P_{D\to|21\rangle}$ for the kinematic configurations $c = 1$, $b = 0$ (left) as a function of a and $c = 1$, $a = 0$ (right) as a function of b.

Now we assume again that there exists a hierarchy $c > a, b$ i.e. the diquark cluster configuration is more unfavourable than the rest and "almost" without loss of generality we set $c = 1$. We display the undiquarkization probabilities in figures 7.4 for the kinematic regime of $b = 0$ (left) corresponding to an efficient $|21\rangle$ configuration as a function of a and $a = 0$ (right) corresponding to an efficient $|12\rangle$ configuration as a function of b. We can see that the no undiquarkization probability $P_{D\to D}$ is exactly the same under the exchange of $a \leftrightarrow b$ and the other probabilities $P_{D\to|12\rangle}$ and $P_{D\to|21\rangle}$ exchange under the exchange $a \leftrightarrow b$. This symmetry can be explained by the fact that we start from a (anti-)symmetrized initial state. On the left (right) we can clearly see that for an inefficient $|12\rangle$ ($|21\rangle$) configuration i.e. large a (large b) we get a large reconnection probability to the state $|21\rangle$ ($|12\rangle$), which is as expected. For low a or b however the no CR topology dominates, which corresponds to the regime where both $|12\rangle$ and $|21\rangle$ configurations are equally favourable.

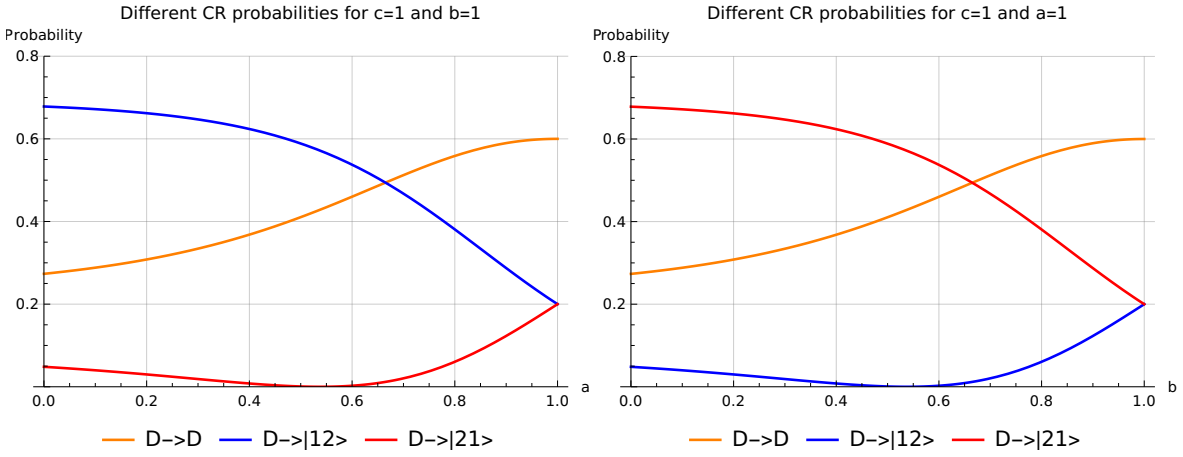

Figure 7.5: The different CR probabilities for a diquark cluster $P_{D\to D}$, $P_{D\to|12\rangle}$ and $P_{D\to|21\rangle}$ for the kinematic configurations $c = b = 1$ (left) as a function of a and $c = a = 1$ (right) as a function of b.

In figure 7.5 we show the different regime in which the $|12\rangle$ state is unfavourable i.e. $a = 1$ on the left and on the right where the $|21\rangle$ state is unfavourable i.e. $b = 1$. We can again see the same symmetry in these plots as in figure 7.4 and the behaviour appears to be almost mirrored between figures 7.4 and 7.5 as we would expect since we essentially are changing the hierarchy order between a and b.

Now even though we studied these undiquarkization probabilities, we remind the reader that these are only of relevance if there has been generated a diquark cluster state by e.g. some earlier stage (hard process, parton shower, NP gluon splitting or MPI) at the scale M_{ij}^2 and is needed to be evolved down to a lower common scale μ^2. Furthermore, one would also need to investigate if there is a better scale choice than M_{ij}^2 for such diquark states, which however does depend on their creation mechanism. Similar arguments hold of course also for the case of unbaryonization, which has already been discussed in [8]. In fact, for future work on interleaving the colour reconnection model with the cluster fission model these effects could be quite relevant since the CR evolution will only evolve towards an intermediate scale and then continue from that scale, where some states with diquark/baryonic clusters could have been produced.

7.5 The Subsystem Colour Reconnection Algorithm

Now that we have gained some intuition for a two cluster system we want to develop a pragmatical algorithm for a general n cluster system since of course numerical exponentiation of a $n! \times n!$ matrix is unfeasible for large n. We have seen in figures 7.3 and 7.5 that distant configurations in terms of large invariant masses M_{ij} are more unlikely to colour reconnect. In fact, the un-exponentiated matrix $\mathbf{\Omega}$ has typically negative eigenvalues, which means that larger Ω_{ij} correspond to larger suppression. This observation leads us to the assumption that the dominant contributions might be originating from close-by regions of phase space. We assume therefore that the $S(n)$ colour flow permutation space factorizes into a partition set $\mathcal{P}$ of $|\mathcal{P}|$ cluster subsystems such that we can write down the following approximation:

$$\sum_{p\in\mathcal{P}} p = n, \tag{7.60}$$

$$\left|\sigma^{\mathcal{P}}\right\rangle = \bigotimes_{p\in\mathcal{P}} \left|\sigma^{(p)}\right\rangle \in \bigotimes_{p\in\mathcal{P}} S(p) =: S(\mathcal{P}) \subset S(n), \tag{7.61}$$

$$\mathcal{T}_{\sigma^{\mathcal{P}}\to\tau^{\mathcal{P}}} = \left\langle\tau^{\mathcal{P}}\right| \mathbf{U}^{(n)} \left|\sigma^{\mathcal{P}}\right\rangle \approx \bigotimes_{p\in\mathcal{P}} \left\langle\tau^{(p)}\right| \mathbf{U}^{(p)} \left|\sigma^{(p)}\right\rangle, \tag{7.62}$$

$$\mathbf{U}^{(n)} \approx \bigoplus_{p\in\mathcal{P}} \mathbf{U}^{(p)} =: \mathbf{U}^{\mathcal{P}}. \tag{7.63}$$

Here $\mathbf{U}^{(p)}$ is computed in the $|S(p)| = p!$ dimensional subspace. Note that here the approximation of reducing the space from $S(n)$ to $S(\mathcal{P})$ and the approximation of $\mathbf{U}^{(n)} \approx \mathbf{U}^{\mathcal{P}}$ as block diagonal corresponds to the assumption that different subsystems are evolving completely independently. Furthermore, we assumed that the partitions are composed of colour singlets i.e. the subsystems cannot be coloured. We shall keep these assumptions in mind when discussing what physics we expect to describe e.g. we would not expect long ranged correlations to be described very well[46] since there would be no CR between different subsystems using this assumption.

Due to the rapid growth of $n!$ we decide to group at most $n = 3$ clusters into one subsystem. In fact, for three clusters we get also one possibility to get a baryonic colour reconnection and

[46] If CR effects are important for such correlations.

several possible diquark cluster configurations. The choice for $n = 3$ will potentially bias our algorithm towards diquark CR instead of baryonic CR due to the combinatoric possibilities. In fact, it has been shown in [8] that going to $n = 4$ or $n = 5$ substantially increases the baryonic CR probabilities compared to $n = 3$, which we will keep in mind for interpreting our results.

In order to then compute all possible mesonic $\mathcal{T}_{3M\to 3M'}$, diquark $\mathcal{T}_{3M\to DM'}$ and baryonic $\mathcal{T}_{3M\to B\bar{B}}$ transition amplitudes from equations (7.25), (7.35) and (7.43), we need to exponentiate the $3! \times 3!$ matrix $\mathbf{\Omega}$. While for $n = 2$ we can use the analytic expression for the exponentiation, for $n = 3$ we choose to use the Padé approximation [184] for computing the matrix exponential numerically.

Even though these transition amplitudes $\mathcal{T}_{3M\to 3M'}$, $\mathcal{T}_{3M\to DM'}$ and $\mathcal{T}_{3M\to B\bar{B}}$ are in general non-zero we set them to 0 if the final state configuration is invalid. This changes the total normalization given by equation (7.44) and is necessary since we have a transition probability of no CR happening $\mathcal{T}_{\sigma\to\sigma}$, which is not constructed from unitarity arguments. Examples of such invalid configurations are e.g. if a mesonic cluster configuration would lead to octets (depending on the flag `OctetTreatment`) or if for a diquark CR topology, the resulting diquark cluster could not be reduced[47] to a diquark-antiquark pair or does not pass the $\Delta_{\max}$ cut as discussed in the previous chapter. Similarly for baryonic clusters we impose also the requirement to have enough mass to be reduced to a diquark-quark cluster and to be decayed into at least a single baryon (reshuffling momentum with a nearby cluster), although this is almost always the case.

The CR algorithm for this subsystem soft gluon evolution CR approach, which we shall call *dynamic Colour Reconnection* (dynCR) then is almost the same as the Diquark Colour Reconnection (DCR) algorithm discussed in chapter 6. The difference is that the choice for the CR topology is not determined anymore by the configuration in rapidity of the three clusters, but rather one random selection is selected within the three cluster subsystem according to the computed unitary probabilities $P_{3M\to 3M'}$, $P_{3M\to DM'}$ and $P_{3M\to B\bar{B}}$. Note in particular this includes also "peripheral" CR i.e. from the cluster subsystem $\{C_1, C_2, C_3\}$ maybe only clusters C_2 and C_3 are reconnected, while C_1 is just a spectator cluster remaining unaltered. With this approach we are only left with the free parameters $\Delta_{\max}$, $\alpha_s \in [\alpha_s(M_Z), 1]$, which we choose as a NP constant[48], and the IR scale μ^2, which we redefine as $\mu^2 = 4m_{LCQ}^2\tilde{\mu}^2$ with m_{LCQ} being the lightest constituent quark mass[49] in order to guarantee $\mu^2 < M_{ij}^2$ for all possible invariant masses and $\tilde{\mu} \in (0, 1)$. This of course only holds if we assume that all partons are on their respective constituent mass shell, which can be guaranteed by the setting `ClusterFinder:DiQuarkOnShell=Yes`. Of course one can also numerically compute the integral in (7.21) also including the Coulomb term and use a running α_s, which needs however to be continued meaningfully into the IR regime, which is the reason why we leave this for further studies. In principle this whole framework can also deal with gluonic octet colour flow states, however the cluster model does need quarks or antiquarks in its current IR unsafe formulation.

7.6 Phenomenological Results

In this section we show and discuss the phenomenology of the new dynamic CR model on typical MB LHC observables at 7 TeV. In particular, we use as a baseline the `Herwig 7.3.0` tune with some additional options. As before we use the average lifetime cut $c\tau > 10$ mm, set

[47] If it would have not enough mass.
[48] Since we assumed no running coupling for now.
[49] In our case this will be the u/d quark with its constituent mass $m_{u/d} = 325$ MeV.

the ISR and FSR shower coupling to $\alpha_s(M_Z) = 0.1185$, use the static threshold for the default cluster fission and put all diquarks on their constituent mass shell. As we have seen before the correlations are strongly[50] impacted by the new t-channel like cluster decay (see section 5.3), which is the reason why we activate it for the following plots always. Furthermore, since we are interested in the baryon production we set **PwtDI** $= 0$, which turns off the CD baryon production. For the new dynamic CR parameters α_s, $\tilde{\mu}$ and $\Delta_{\max}$ we choose the default values $\alpha_s = 0.5$, $\tilde{\mu} = 0.5$ and $\Delta_{\max} = 10$ as a starting point.

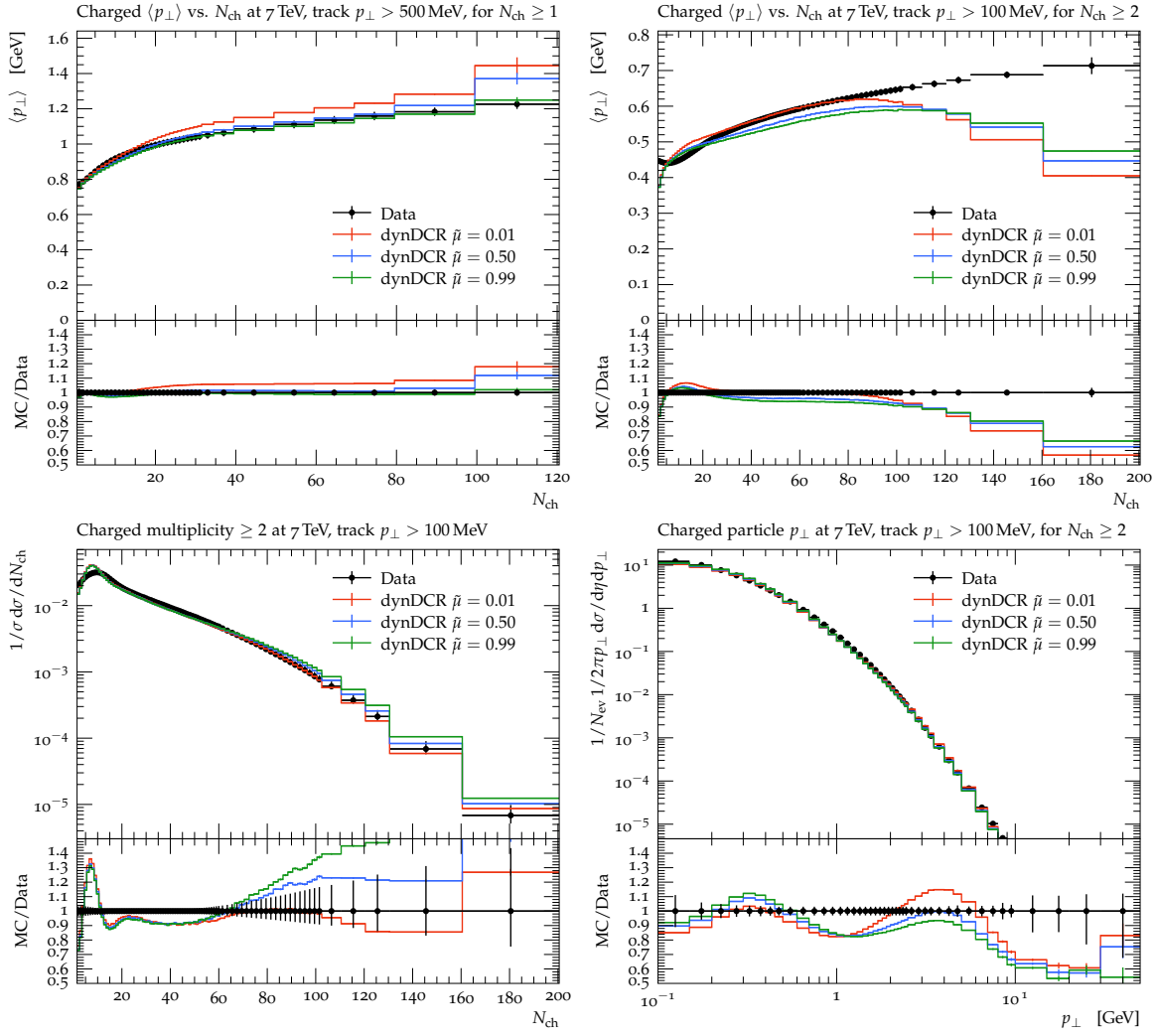

Figure 7.6: The $\langle p_T \rangle(N_{\text{ch}})$, N_{ch} and p_T ($p_\perp$ in the plots) spectra for different p_T cuts of MB pp collisions at 7 TeV measured by ATLAS [127] (public `Rivet` analysis `ATLAS_2010_S8918562`). All of these simulations have been performed using the dynamic DCR algorithm and the CR coupling $\alpha_s = 0.5$ and $\Delta_{\max} = 10$ at different CR scales $\tilde{\mu}$ given in the legend.

We again remind the reader that the plots we will be showing are untuned and strongly correlated to the hadronization model. Therefore it is not reasonable to expect substantial "improvement" in the data comparison. In particular, the new matrix element CF model (from 5.2) is unfortunately too slow to run at LHC energies and the aligned CF with only the phase space effects is not enough to yield decent results, which is the reason why we do not use it here.

[50] Here we mean that the default cluster decay washes out a lot of the correlations.

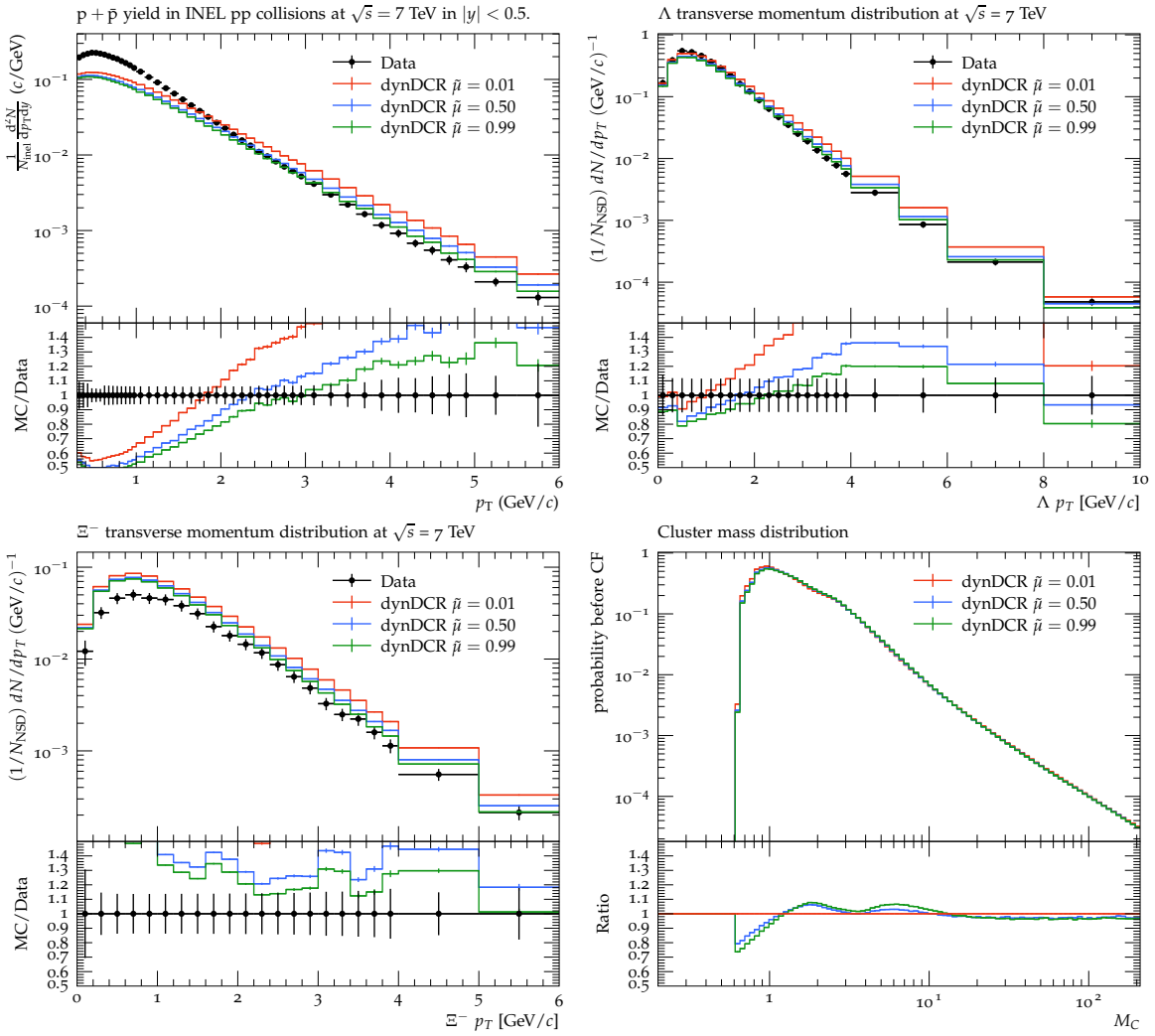

Figure 7.7: The p_T spectra of p, Λ and Ξ^- of MB pp collisions at 7 TeV measured by ALICE and CMS [150, 151] (public `Rivet` analyses `CMS_2011_S8978280` and `ALICE_2015_I1357424`) and the cluster mass spectrum of all clusters just after the CR has happened. All of these simulations have been performed using the dynamic DCR algorithm and the CR coupling $\alpha_s = 0.5$ and $\Delta_{\max} = 10$ at different CR scales $\tilde{\mu}$ given in the legend.

In figure 7.6 we display some MB observables for the dynamic DCR algorithm at different IR CR scales $\tilde{\mu}$ in order to determine the scale dependency of the new CR model. We can see that there are some variations, but overall the effect of varying the scale is a quite small effect. In practice the scale $\tilde{\mu}$ controls the "ideal" cluster mass i.e. the lower $\tilde{\mu}$, the lower cluster masses are preferred by the CR. Therefore we get more CR if the scale is small, which reduces the high multiplicity events and gives the hadrons more p_T leading to higher $\langle p_T \rangle (N_{\text{ch}})$.

In figure 7.7 we plot different baryon p_T spectra and the cluster mass spectrum just after the CR (bottom right). We can see that lower scales $\tilde{\mu}$ lead to overall more baryons (since it leads to more CR in general) and produce them also at slightly higher p_T as one can see in the different slopes. Note that similarly to our previous results we have seen that also in this case with kinematic dependence of the CR probabilities we are unable to produce the soft peak of the protons properly. The cluster mass distributions in figure 7.7 confirm our claim that for smaller $\tilde{\mu}$ the cluster masses are driven towards lower cluster masses. The BB and BA correlations measured by ALICE [137] do not significantly depend on the scale variation, which is the reason we omit showing them.

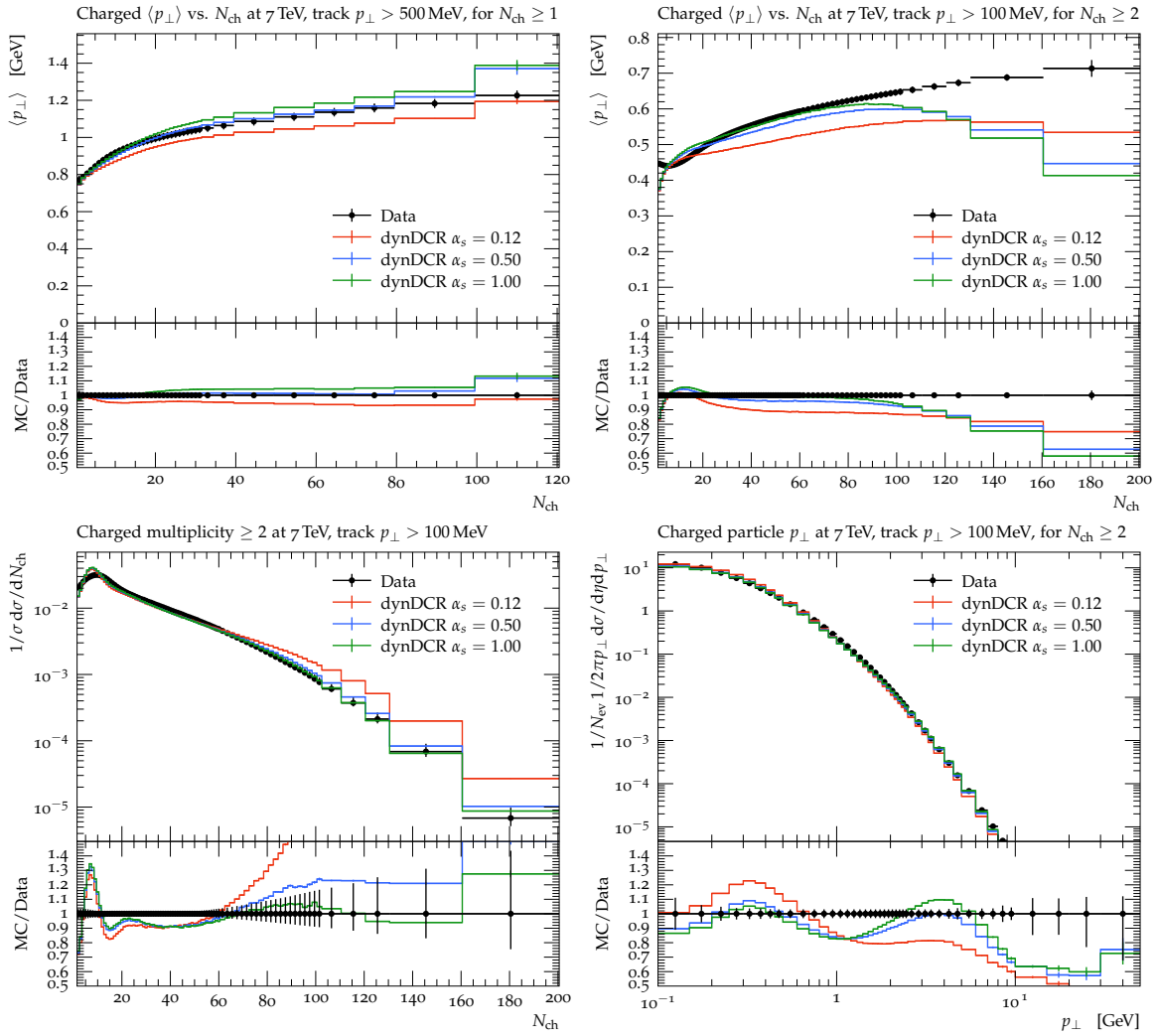

Figure 7.8: The $\langle p_T \rangle(N_{\text{ch}})$, N_{ch} and p_T ($p_\perp$ in the plots) spectra for different p_T cuts of MB pp collisions at 7 TeV measured by ATLAS [127] (public `Rivet` analysis `ATLAS_2010_S8918562`). All of these simulations have been performed using the dynamic DCR algorithm with the CR scale $\tilde{\mu} = 0.5$ and $\Delta_{\text{max}} = 10$ at different CR couplings α_s given in the legend.

In figures 7.8 and 7.9 we show the variation of the NP CR α_s for the dynamic DCR algorithm. As one would expect the higher the value of the strong coupling, the more CR is performed, which is clearly visible in figure 7.8. In fact, the variation with respect to α_s is much stronger than for the CR scale.

The baryon p_T spectra in figure 7.9 however are impacted quite similarly strongly under the α_s variation as under the $\tilde{\mu}$ variation even though the absolute magnitude is different. Also different α_s cannot reproduce the soft proton peak. The cluster mass distributions are consistent with the reasonable expectation that more CR implies lower cluster masses, where the inflexion point is around $2 - 3$ GeV. Similarly to the variation of the scale $\tilde{\mu}$ we do not see significant differences in the BA and BB correlations.

In figures 7.10 - 7.12 we display the dynamic DCR algorithm for varying values of the diquark production cut Δ_{max}. As already mentioned previously this cut acts only as a temporary limitation since diquark clusters cannot be treated by our current CF and CD model in a meaningful manner. The $p\bar{p}$ and pp correlations displayed in figure 7.10 are of course impacted by this cut, but interestingly not as much as we would have anticipated. It is of course difficult to assess the behaviour of the pp correlations due to the deteriorating statistics

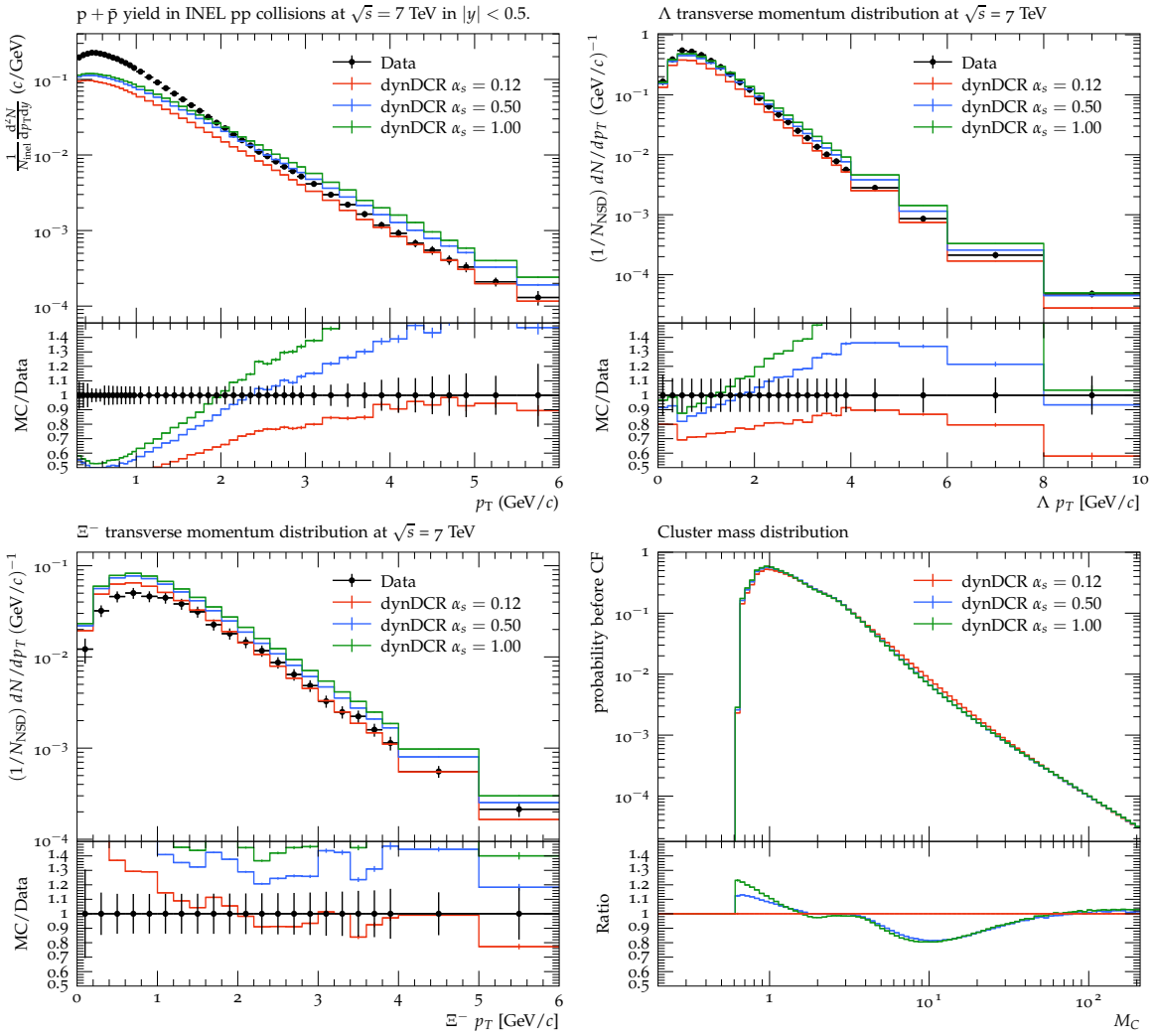

Figure 7.9: The p_T spectra of p, Λ and Ξ^- of MB pp collisions at 7 TeV measured by ALICE and CMS [150, 151] (public `Rivet` analyses `CMS_2011_S8978280` and `ALICE_2015_I1357424`) and the cluster mass spectrum of all clusters just after the CR has happened. All of these simulations have been performed using the dynamic DCR algorithm with the CR scale $\tilde{\mu} = 0.5$ and $\Delta_{\max} = 10$ at different CR couplings α_s given in the legend.

for more stringent cuts, but for the $p\bar{p}$ correlation it appears that the more stringent the cut, the more near side correlations are produced.

In figure 7.11 the impact of the $\Delta_{\max}$ cut is interestingly quite substantial. In particular, it appears that the $\langle p_T \rangle (N_{\text{ch}})$ for $p_T > 500$ MeV exhibits a huge spike at large multiplicities not reflected in the data, the more loose the $\Delta_{\max}$ cut is. This might come from the diquark reduction if we imagine a diquark cluster that has been produced with two quarks (and antiquarks) being back to back in the lab frame close to the beam direction with large invariant mass (since no $\Delta_{\max}$ would prevent this) would be reduced to a diquark with relatively small constituent mass, which would rescale its momentum to give a large component maybe in the transverse region. However, it is unclear why this effect does not appear to happen similarly for the $\langle p_T \rangle (N_{\text{ch}})$ at $p_T > 100$ MeV. Contrary to the naive expectation that a more stringent cut would lead to less CR, we can see that the behaviour of the N_{ch}, p_T and $\langle p_T \rangle (N_{\text{ch}})$ at $p_T > 100$ MeV observables appear have a non-linear dependence on the cut. This might originate from the delicate balance between DCR and MCR. Nonetheless, the unphysical feature observed without this $\Delta_{\max}$ cut does confirm the need for introducing this cut.

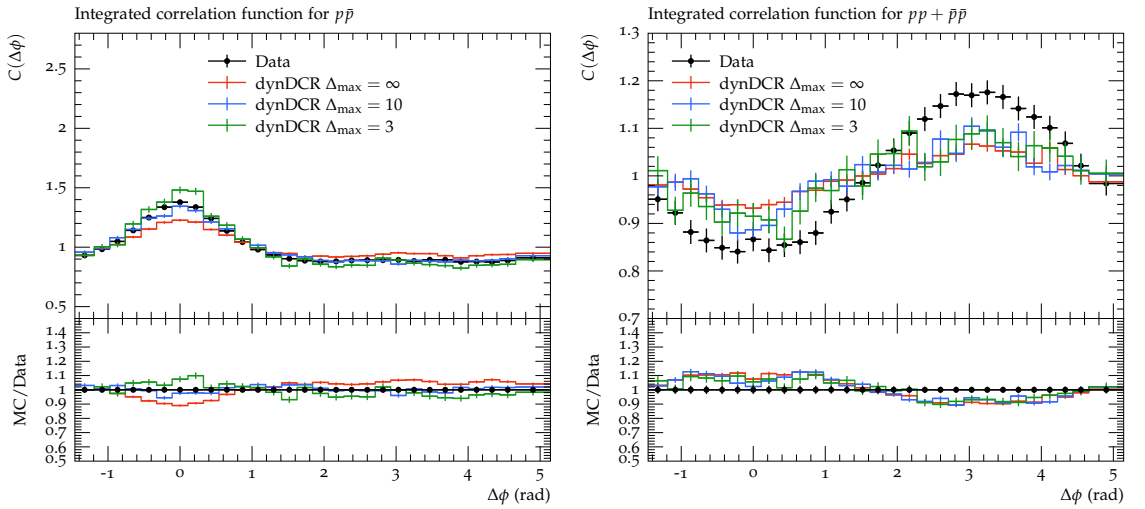

Figure 7.10: The BB and BA correlations of MB pp collisions at 7 TeV measured by ALICE [137] (public `Rivet` analysis `ALICE_2016_I1507157`). All of these simulations have been performed using the dynamic DCR algorithm with the CR scale $\tilde{\mu} = 0.5$ and the CR coupling $\alpha_s = 0.5$ for different $\Delta_{\max}$ given in the legend.

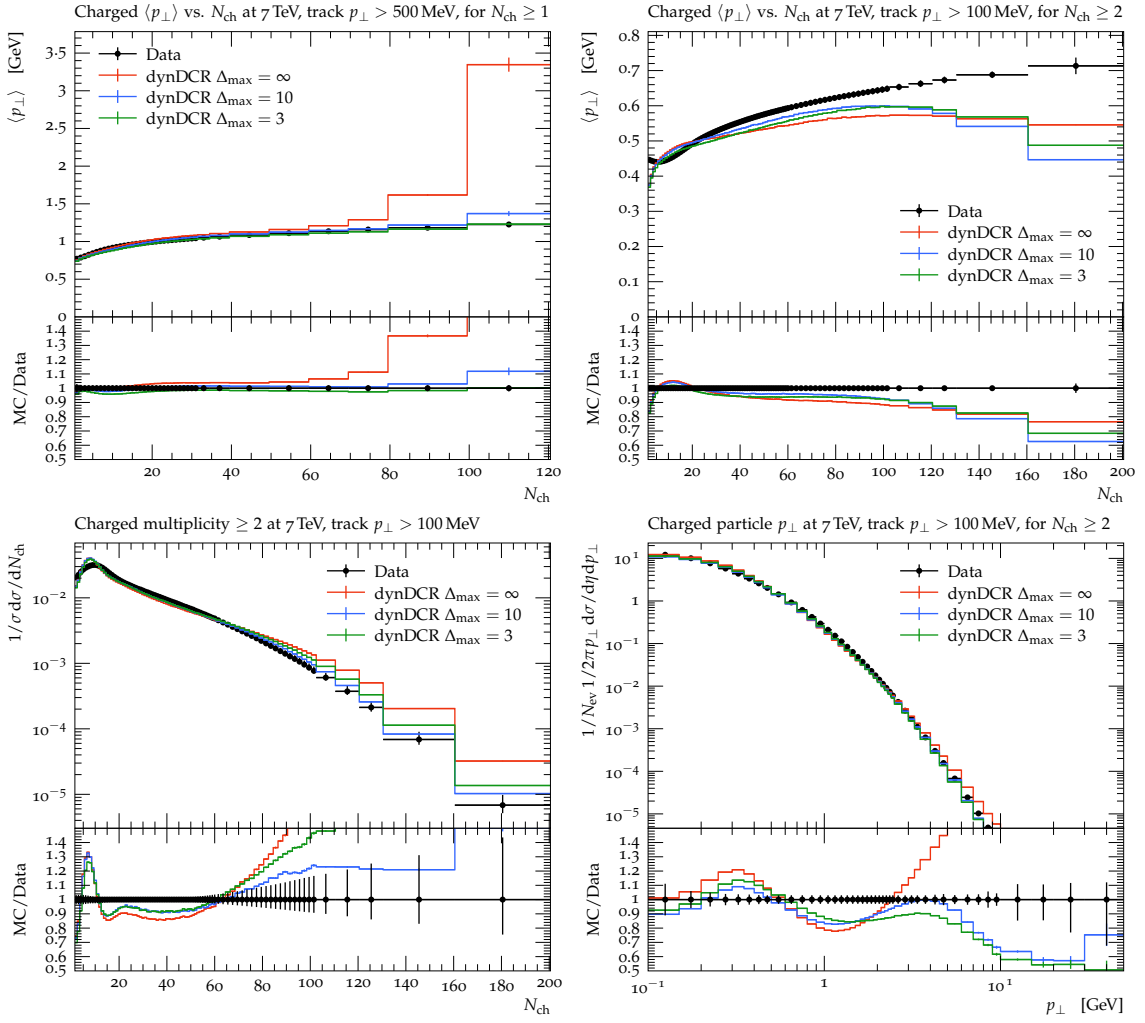

Figure 7.11: The $\langle p_T \rangle(N_{\text{ch}})$, N_{ch} and p_T ($p_\perp$ in the plots) spectra for different p_T cuts of MB pp collisions at 7 TeV measured by ATLAS [127] (public `Rivet` analysis `ATLAS_2010_S8918562`). All of these simulations have been performed using the dynamic DCR algorithm with the CR scale $\tilde{\mu} = 0.5$ and the CR coupling $\alpha_s = 0.5$ for different $\Delta_{\max}$ given in the legend.

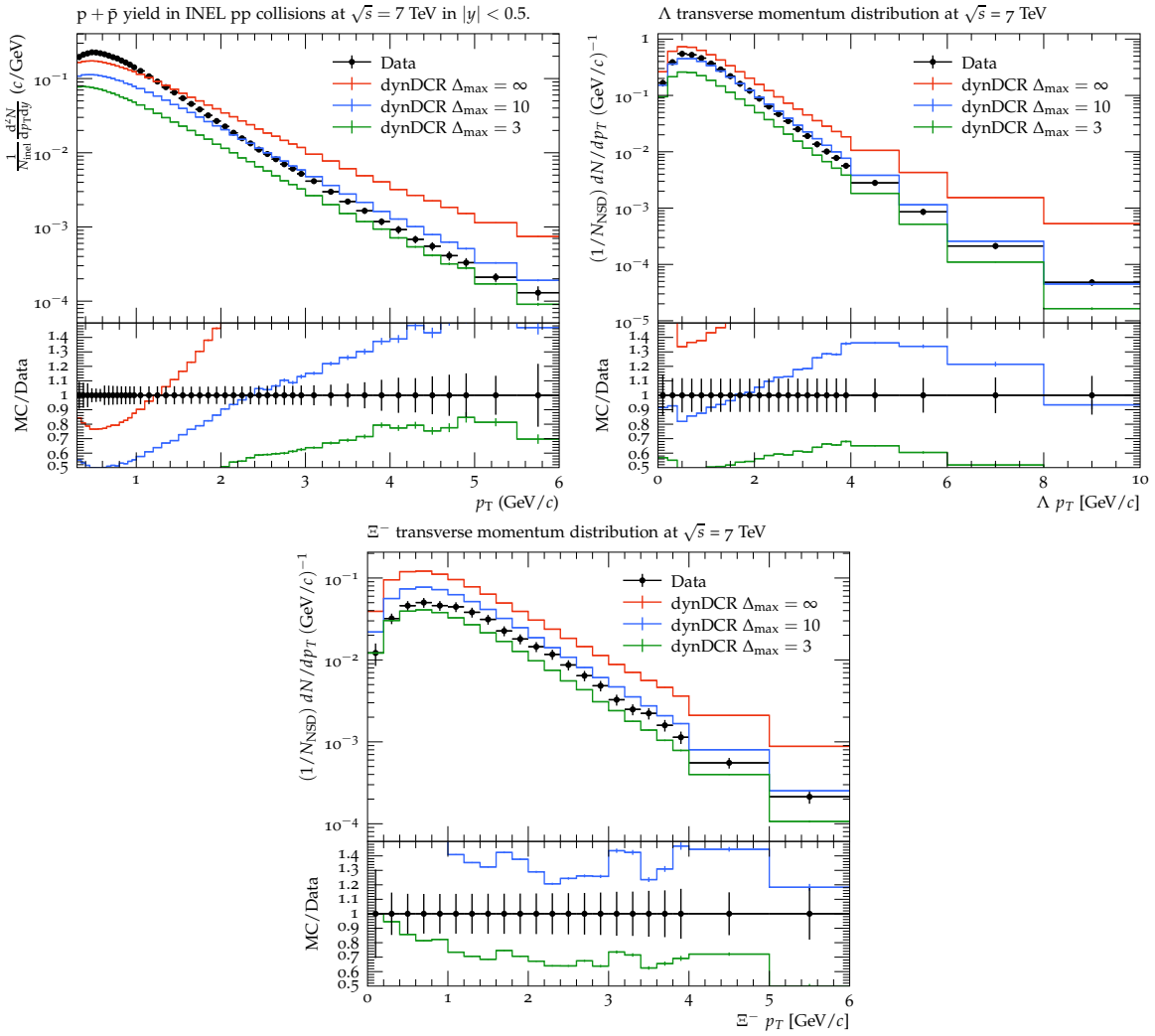

Figure 7.12: The p_T spectra of p, Λ and Ξ^- of MB pp collisions at 7 TeV measured by ALICE and CMS [150,151] (public `Rivet` analyses `CMS_2011_S8978280` and `ALICE_2015_I1357424`). All of these simulations have been performed using the dynamic DCR algorithm with the CR scale $\tilde{\mu} = 0.5$ and the CR coupling $\alpha_s = 0.5$ for different $\Delta_{\max}$ given in the legend.

In order to further investigate this behaviour we again display the baryon p_T spectra with varying $\Delta_{\max}$ cut in figure 7.12. Of course the looser the cut, the more baryons and with higher p_T we get. In fact, it could be that the sheer abundance of baryons with appreciable p_T are dominating the $\langle p_T \rangle (N_{\text{ch}})$ for the $p_T > 500$ MeV cut and thus leading to the observed unphysical feature. Such cross effects can of course happen as we have already seen and shown in chapter 4, which is the reason why such phenomenological studies are crucial for assessing whether a feature of the simulations is a physics effect that we expect or a shortcoming of our physics model.

Note that even though so far we only discussed the dynamic DCR algorithm, there exist also the previous CR models of `Herwig` e.g. the very primitive `Plain` and the current default `Baryonic` CR algorithm. These algorithms rely on the phenomenological parameters for the static colour reconnection, which are the probability P_M for both and P_B for the `Baryonic` algorithm. We can very easily replace these static parameters with their dynamic version from the soft gluon evolution approach discussed in this chapter. Therefore we introduced the global option `DynamicCR`, which when turned on uses the dynamic probabilities for the `Plain` and `Baryonic` algorithms depending on the parameters α_s and $\tilde{\mu}$.

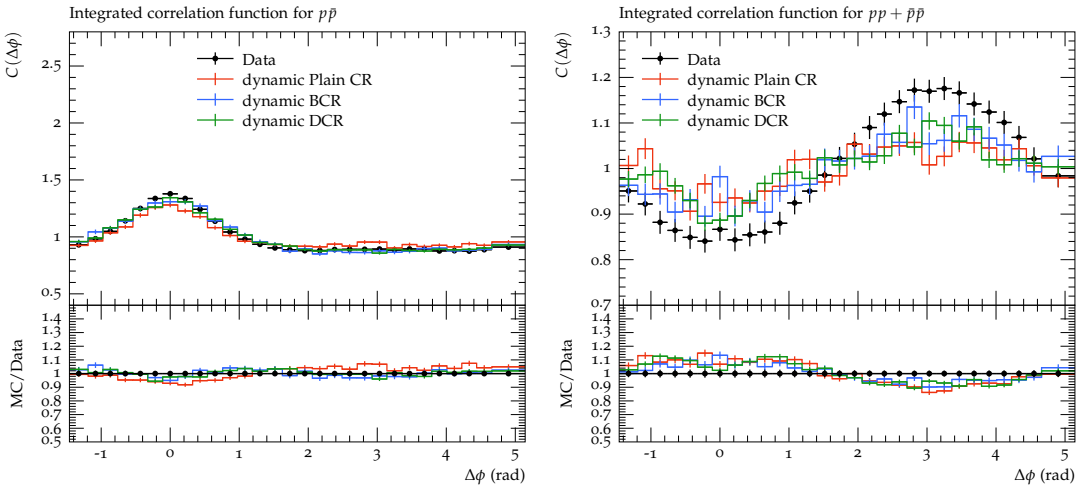

Figure 7.13: The BB and BA correlations of MB pp collisions at 7 TeV measured by ALICE [137] (public `Rivet` analysis `ALICE_2016_I1507157`). All of these simulations have been performed with the CR coupling $\alpha_s = 0.5$, the CR scale $\tilde{\mu} = 0.5$ and $\Delta_{\max} = 10$ using the `Plain`, `Baryonic` and Diquark CR algorithms. Note that here the `Plain` and `Baryonic` algorithms are also allowed to produce diquark clusters.

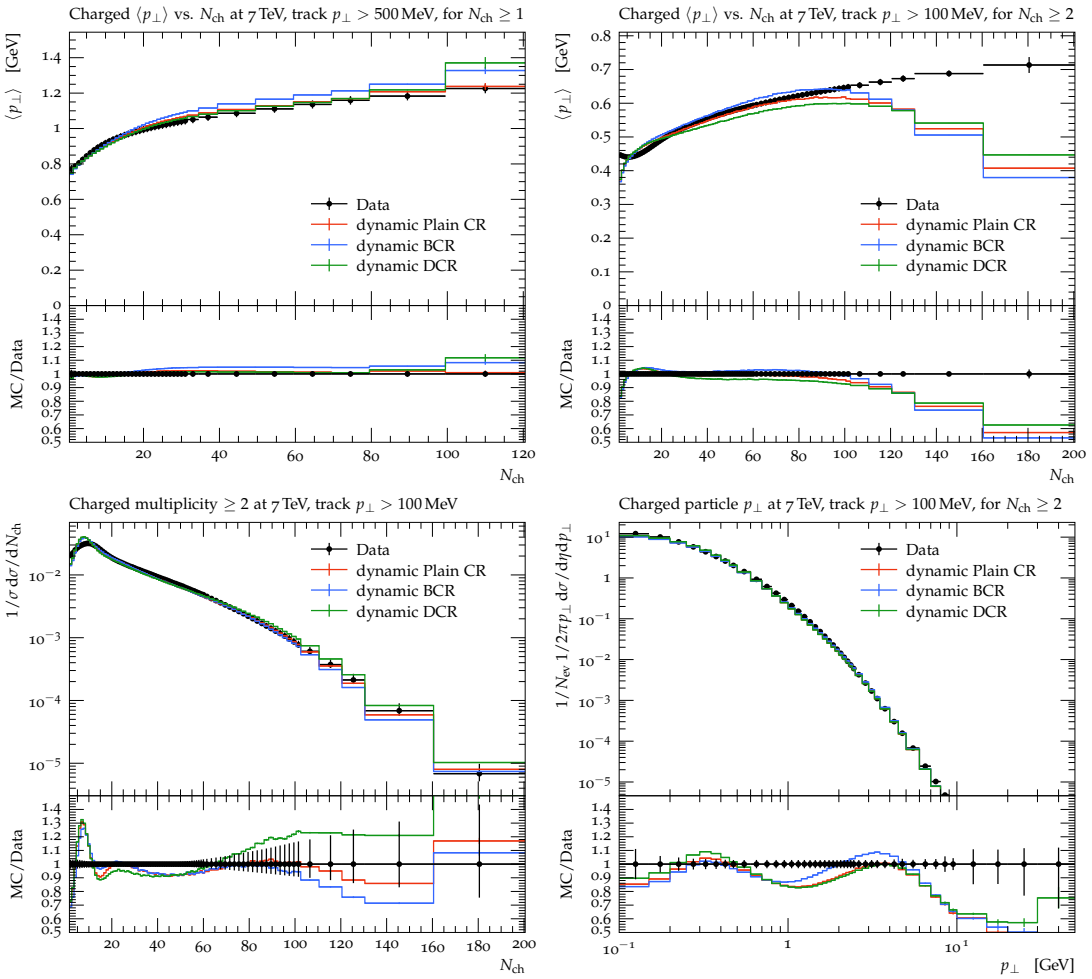

Figure 7.14: The $\langle p_T \rangle (N_{\text{ch}})$, N_{ch} and p_T ($p_\perp$ in the plots) spectra for different p_T cuts of MB pp collisions at 7 TeV measured by ATLAS [127] (public `Rivet` analysis `ATLAS_2010_S8918562`). All of these simulations have been performed with the CR coupling $\alpha_s = 0.5$, the CR scale $\tilde{\mu} = 0.5$ and $\Delta_{\max} = 10$ using the `Plain`, `Baryonic` and Diquark CR algorithms. Note that here the `Plain` and `Baryonic` algorithms are also allowed to produce diquark clusters.

This was implemented such that for the proposed selection of clusters of the CR topology (also the no CR topology) is chosen entirely from the discussed unitarized transition amplitudes. Note that therefore a baryonic configuration for the `Baryonic` algorithm can also undergo mesonic CR and vice versa. For the `Plain` algorithm we edited the cluster selection algorithm in order to pick the two clusters, which have the least probability of not undergoing any CR. In addition, we can also add the diquark topology to both of these algorithms by the flag `DiquarkCR`, which allows for CR baryon production also with the simplistic `Plain` CR model, which only selects two clusters for which we compute the transition probabilities.

In figures 7.13 - 7.15 we show the dynamic `Plain`, `Baryonic` and Diquark CR algorithm with the `DiquarkCR` option turned on. In figure 7.13 we can see only very few differences, but it appears that the `Plain` CR algorithm produces less $p\bar{p}$ correlations than the other ones. For the pp correlations we do not see substantial differences due to statistics, even though we would expect the `Plain` CR to have less near side suppressed correlations since it has only the diquark topology available to produce baryons.

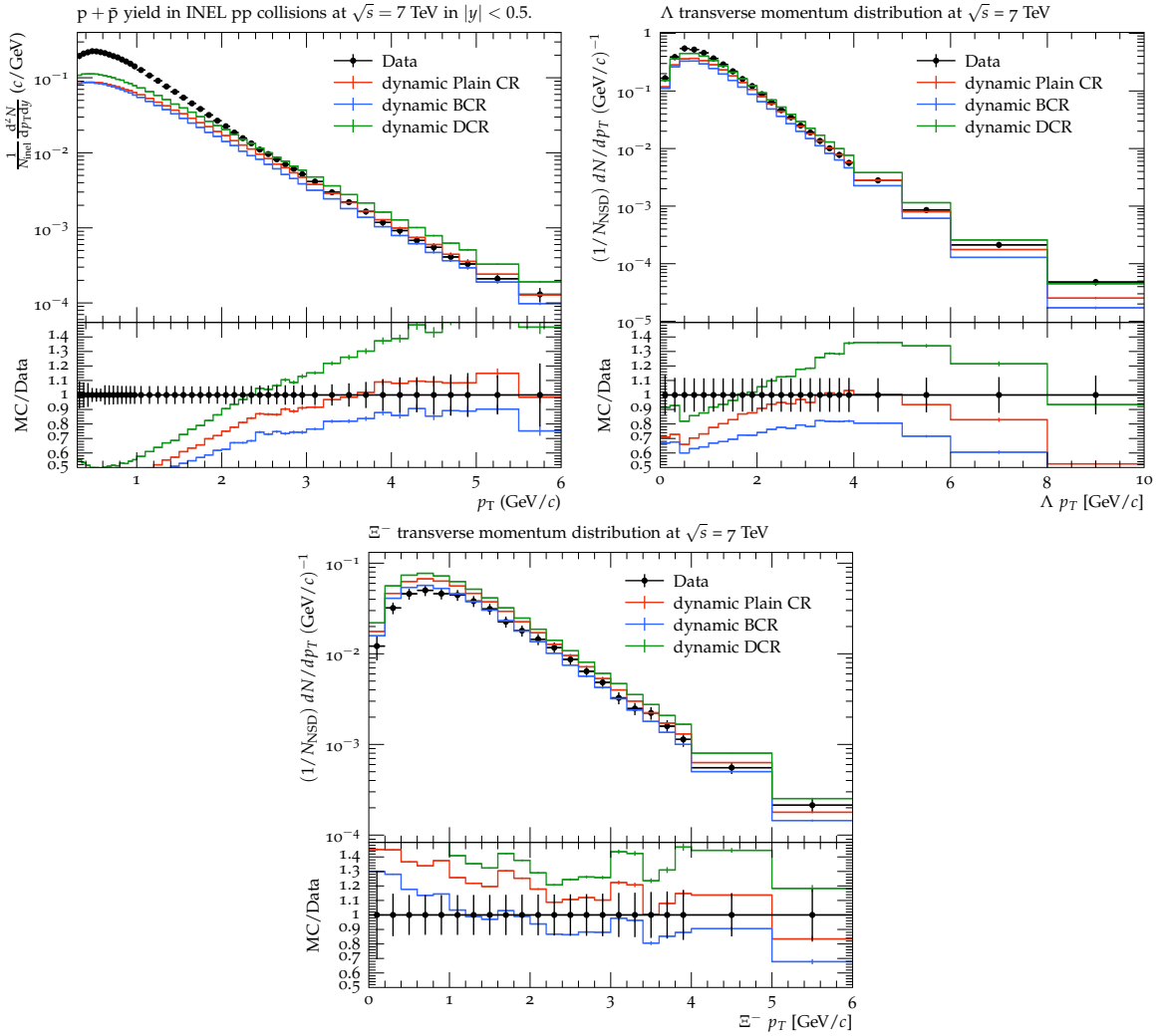

Figure 7.15: The p_T spectra of p, Λ and Ξ^- of MB pp collisions at 7 TeV measured by ALICE and CMS [150,151] (public `Rivet` analyses `CMS_2011_S8978280` and `ALICE_2015_I1357424`). All of these simulations have been performed with the CR coupling $\alpha_s = 0.5$, the CR scale $\tilde{\mu} = 0.5$ and $\Delta_{\max} = 10$ using the `Plain`, `Baryonic` and Diquark CR algorithms. Note that here the `Plain` and `Baryonic` algorithms are also allowed to produce diquark clusters.

The MB observables displayed in figure 7.14 show some difference in the $\langle p_T \rangle(N_{\mathrm{ch}})$, where the BCR algorithm appears to produce generally a larger rise compared to the rest. This is most likely due to the selection criterion for the BCR algorithm, which will not select clusters, which would be in a diquark cluster configuration. Therefore we expect few diquark type reconnections, which as already mentioned in the previous chapter lead to a smaller rise in the $\langle p_T \rangle(N_{\mathrm{ch}})$ since invariant mass is needed to produce the $q\bar{q}$ pair in order to decay to a baryon-antibaryon pair and cannot be invested in increased p_T.

In figure 7.15 we show the baryon spectra of the different dynamic algorithms. Clearly, the DCR algorithm produces the most baryons, which of course is expected since its selection algorithm searches explicitly also for diquark type configurations. Since we adapted the `Plain` CR selection algorithm to pick the pairs of clusters with the minimal no CR probability, we also get a substantial baryon production, which is even larger than the baryon production from the `Baryonic` CR algorithm. In any case it appears that the DCR algorithm gives more baryons forming the soft peak in the p_T distributions than all of the other algorithms.

7.7 Conclusions and Outlook

In this chapter, we presented the dynamical CR model starting from soft gluon evolution [169]. We discussed also the different CR topologies and in particular the diquark and baryonic clusters' colour flow states. The momentum dependent CR unitarized transition probabilities were defined for all possible CR topologies up to three colour flow systems. Studying the two cluster system we have found that closeness in phase space of cluster configurations corresponds to high CR probability, which has also been found in [8].

Building on this finding we approximated the general evolution operator as the direct sum of a suitable partition of the whole system into colourless subsystems of clusters with at most three colour flows (or three mesonic clusters). With this approximation we used the cluster selection algorithm of the DCR algorithm to partition the total cluster set into subsystems and perform the soft gluon evolution CR on each subset according to the transition probabilities. Thereby we allow also for peripheral CR, which has not been possible with the previous algorithms. The undiquarkization was also discussed in principle, although for the current implementation it has been found to not be relevant. Additionally, we also supplied these dynamical momentum dependent CR transition probabilities to the `Plain` and `Baryonic` CR algorithms with the option of generating diquark clusters themselves.

We showed the phenomenology of these dynamic CR algorithms and have found the possibility to get a reasonable description with three "free" parameters. However, one should keep in mind that these three "free" parameters should not be considered as bland phenomenological parameters since they have either a physical interpretation like α_s and $\tilde{\mu}$ or are a technical cutoff like Δ_{max}, which reflects the shortcomings of the current hadronization model.

Now this work is of course not yet the full model since many things could be improved here. In particular, one could compute the integral of the evolution matrix more precisely also with a running α_s if a reasonable continuation of α_s could be found and re-examine the impact of the Coulomb terms in the evolution. One could also increase the maximal subsystem size, which has been studied in [8] for up to 5 mesonic clusters to give a higher baryonic type CR probability.

Ultimately the overarching goal should be to interleave this dynamical CR model with a suitable cluster fission model in the context of colour evolution. This of course requires an efficient and reasonable cluster fission model motivated by colour evolution. Also, the IR safety for the cluster model has to be addressed in the same context, which would also impact

the dynamic CR model since it would need to be able to treat gluons, which has not yet been discussed.

Of course, it would be also very important to more clearly study the impact of our approximation that the subsystems are completely decoupled from each other. This could be particularly interesting for assessing the impact of CR (in microscopic simulations) on long ranged correlations such as ridge searches compared to statistical/thermal models.

CHAPTER 8

Final Conclusion and Outlook

In this thesis we have examined many correlation observables and found multiple shortcomings in the cluster hadronization and colour reconnection model of `Herwig` 7.3.0 for multiple centre-of-mass energies and different collision systems. In order to address these issues we provided several solutions with a deeper theoretical motivation coming from the colour evolution picture.

In chapter 4 we made a first solution attempt using the simplistic approach of moving the baryon production from the cluster decay model to the cluster fission model. However, this was not sufficient without producing unphysical momentum spectra for baryons, which forced us to investigate the kinematics of the cluster fission model much more in depth. In fact, we have already found in chapter 4 that the unphysical plateau from the di-hadron fragmentation functions could be avoided if the cluster fission model behaves more parton shower like.

Therefore in chapter 5, we developed a perturbatively inspired matrix element cluster fission model and a phenomenological matrix element cluster decay model, which is motivated by colour evolution. This model is more predictive and has fewer phenomenological parameters that would need to be tuned to data. We have shown that indeed this cluster fission model behaves more parton shower like if the full matrix element is taken into account. Nonetheless, the sampling of the cluster fission model is still quite inefficient especially for large cluster masses and will need to be accelerated in the future if we want to use it for minimum bias LHC collisions. The new t-channel like cluster decay model on the other hand has been introduced to have a smoother transition from the more aligned cluster fission to the more isotropic cluster decay. We have shown also in chapter 6 that the original cluster decay model washes out the baryon-baryon correlations, while the more aligned t-channel cluster decay model preserves more of the near side suppression, which is also observed in the data. In future studies it would be interesting to replace the phenomenological matrix element for the cluster decay with a Bethe-Salpeter amplitude, which is a non-perturbative parton to hadron transition amplitude, as has been laid out in [7].

Additionally, we introduced the generalized angularities and weighted multi-point energy correlations in chapter 5 and discussed the impact of the different cluster fission and cluster decay model options. We have found several parameters of these observables, which proved to be able to discriminate between cluster fission and cluster decay models. Measuring these

observables would give us the possibility to test which cluster fission/cluster decay model could deliver agreement with the data and therefore guide the development of hadronization models. We made it clear that these observables need not be infrared safe and in fact can also be infrared dangerous. In particular, we have found that for the soft-takes-all infrared dangerous energy correlations the dependence on the centre-of-mass is quite reduced, which suggests that hadronization universality holds for such observables. Therefore it would be very interesting to also measure such observables at e^+e^- and pp collision systems with varying centre-of-mass energies.

Of course, there are still a lot of features missing from the hadronization models. In particular, it would be interesting to study the infrared and collinear limits of a double quasi-soft $q\bar{q}$ emission matrix element to assess how diquark-antidiquark production in the cluster fission model will work. Also the currently static flavour weights could be generalized to dynamical weights, which could be derived from the actual matrix element and thus eliminating the need for tuning these parameters. In that case however, also the tuning and the potential scale dependence of the constituent masses needs to be investigated thoroughly, which goes beyond the scope of this thesis.

In chapter 6 we discussed the new diquark cluster state and designed a colour reconnection algorithm, which takes into account this new state and unlocks new colour reconnection topologies for the cluster model. In particular, it allows for a more efficient baryon production from colour reconnection, which results in less near side suppression of baryon-baryon correlations, but at the same time does not require as many clusters to be able to produce baryonic clusters. We found that the diquark approximation, which is needed by the cluster fission and cluster decay model gives unphysical features if we do not reject some diquark clusters using a cut on the future diquark's invariant mass. So for this diquark colour reconnection algorithm to work in completeness, we would need a hadronization model, which can deal with three and four component clusters, which we leave for future studies. Nonetheless, it would be interesting to test this colour reconnection algorithm on the production of doubly or triply heavy quark baryon production, which could tell us about the balance between the diquark cluster and baryonic cluster formation and hadronization. Also the $\langle p_T \rangle_{\text{Baryons}}(N_{\text{ch}})$ observable would be very useful to be measured more in detail for inclusive baryons as this could tell us more about the balance between baryon production from hadronization and colour reconnection.

In chapter 7 we developed a dynamic colour reconnection model using the soft gluon evolution from [7, 8]. In particular, we limited ourselves to a maximum of three colour flows (or three mesonic clusters) and defined the diquark and baryonic cluster colour flow states alongside with the unitarized transition probabilities. We broke down the total system of clusters into smaller cluster subsystems of at most three clusters and in this first implementation we just assumed that the different subsystems do not interact among themselves. The computed transition probabilities have been supplied to the already existing colour reconnection algorithms and their impact has been studied phenomenologically. Also in the dynamic colour reconnection models the diquark cluster formation cut was crucial to get a reasonable description of the data.

However, there is still room for improvement, e.g. the computation of the soft gluon evolution matrix could be performed with the running of the strong coupling if one has a reasonable continuation of the running of α_s into the infrared regime. Also going beyond the maximum of three colour flows could have some impact on high multiplicity events, but that would also mean more complicated topologies would arise and the numerical computation of the transition probabilities would become more challenging.

The overarching long-term goal in terms of hadronization and colour reconnection of the cluster model should be to develop an infrared safe model that interleaves hadronization and colour reconnection in such a way that the parton shower cutoff is merely a renormalization group evolution like scale, which just determines how the hadronization model should react to a parton shower at the chosen cutoff. In order to achieve this goal, the measurement of the discriminative observables we presented in chapter 5 would be very helpful in pinning down the cluster fission and cluster decay models at various centre-of-mass energy e^+e^- collisions. Such observables would be also very interesting for pp collisions in order to study multiple partonic interactions and colour reconnection with a more solid hadronization model.

For the soft gluon evolution colour reconnection model it would be very interesting to examine the long ranged correlations, which could be introduced if one goes beyond the completely independent subsystem evolution of this thesis. In particular, one could compare the long ranged correlations of our microscopic models with statistical/thermal hadronization models in order to assess whether thermal effects could emerge from microscopic colour reconnection.

Overall, we showed that non-perturbative effects can have a large impact on a plethora of observables and are necessary to define reasonable uncertainties for experimental measurements. The continuous improvement - both theoretically and phenomenologically - of the hadronization and colour reconnection models is crucial for understanding the process of QCD confinement and the collective phenomena emerging from high energy collisions.

APPENDIX A

Cluster Fission Algorithm

Here we describe the pseudo code for the cluster fission for `Herwig` in more detail. We fission a Cluster of Mass M (constituents q_1, q_2 with constituent masses m_1, m_2) to two new clusters $C_1(q_1, q)$, $C_2(\bar{q}, q_2)$ with masses M_1, M_2 respectively. $M_{\mathrm{LHP}}(q_i, q_j)$ is the lightest hadron pair mass, i.e. the sum of the two lightest hadrons, that can be formed from the cluster decay of the cluster $C = (q_i, q_j)$. $M_{\mathrm{LH}}(q_i, q_j)$ is the lightest hadron mass, that can be formed from the cluster $C = (q_i, q_j)$.

The pseudo code implemented is the following:

counterMEtry$\leftarrow 0$
FlavourSampling: Sample Flavour $q \in \{u, d, s\}$ according to static probability weights Pwt(q)
if $M < (m_1{+}m_2{+}2m)$ or $M < \max\{(m_1 + m), M_{\mathrm{LHP}}(q_1, q)\}{+}\max\{(m_2 + m), M_{\mathrm{LHP}}(q_2, q)\}$ **then**

Go to **FlavourSampling** or escape (no Cluster fission) if no Flavour can satisfy the condition
end if
MassSampling: Sample the Masses M_1, M_2 from uniform distribution in the region $M_1 \in [m_1 + m, M - (m_2 + m)]$ and $M_2 \in [m_2 + m, M - (m_1 + m)]$ and $M < M_1 + M_2$
▷ If the last condition fails we keep the flavour fixed and go to **MassSampling**
if $M_1 < M_{\mathrm{LH}}(q_1, q)$ **then**
MC1Max $\leftarrow \min\{M - (m_2 + m), M - M_{\mathrm{LHP}}(q_2, q)\}$
if MC1Max$-M_{\mathrm{LHP}}(q_1, q) < 10^{-2}$GeV **then**
Go to **FlavourSampling**
else
Go to **MassSampling**
end if
end if
if $M_2 < M_{\mathrm{LH}}(q_2, q)$ **then**
MC2Max $\leftarrow \min\{M - (m_1 + m), M - M_{\mathrm{LHP}}(q_1, q)\}$
if MC2Max$-M_{\mathrm{LHP}}(q_2, q) < 10^{-2}$GeV **then**
Go to **FlavourSampling**

else
Go to **MassSampling**
end if
end if
PhaseSpaceSampling: Sample isotropically Phase Space as discussed before give the masses M_1, M_2 sampled previously
$$\mathrm{P}_{\mathrm{acc}} = \frac{|\mathcal{M}|^2(p_i \cdot p_j)\tilde{\Phi}(M,\, M_1,\, M_2,\, m_1,\, m_2,\, m)}{|\mathcal{M}|^2_{\mathrm{over}}(M,\, m_1,\, m_2,\, m)\tilde{\Phi}_{\mathrm{over}}(M)}$$
▷ If one would like to take flavour properly into account $|\mathcal{M}|^2_{\mathrm{over}}$ need not depend on m
counterMEtry++
if counterMEtry>MaxLoopCount **then**
escape, print warning and do the old style of cluster fission
end if
if $P_{\mathrm{acc}} > 1$ **then**
Throw a warning exception, but don't reject sample
end if
Sample r uniformly $\in (0,\, 1)$
if $r < P_{\mathrm{acc}}$ **then**
accept the fission products
else
Go back to **MassSampling**
end if

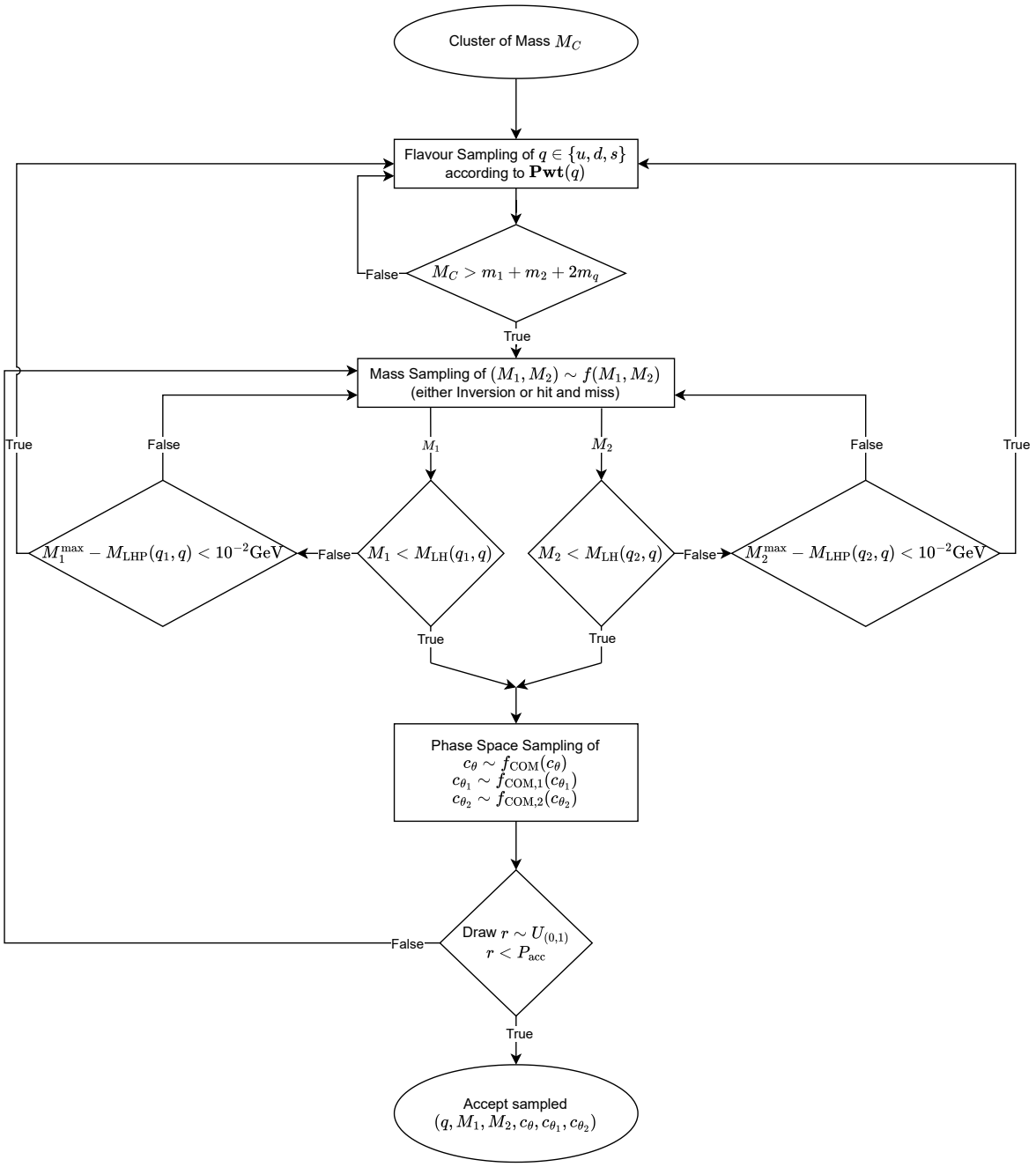

Figure A.1: Flowchart for the matrix element cluster fission algorithm.

APPENDIX B

Phase Space Factorization

The phase space factorization which were used for the cluster fission algorithm. We start with a general $2 \to 4$ partonic process with a matrix element $\mathcal{M}_{2\to4}(p_1,\, p_2 \to q_1,\, q,\, \bar{q},\, q_2)$, where the rate $\Gamma_{2\to4}$ can be written in this manner in $D = d + 1$ spacetime dimension [12]:

$$\Gamma_{2\to4} = \int |\mathcal{M}_{2\to4}|^2 d\Phi_4, \tag{B.1}$$

$$d\Phi_4 = \frac{d^d q_1}{2E_1}\frac{d^d q}{2E_q}\frac{d^d \bar{q}}{2E_{\bar{q}}}\frac{d^d q_2}{2E_2}\delta^D(p_1 + p_2 - q_1 - q - \bar{q} - q_2), \tag{B.2}$$

$$d\Phi_4 = d\Pi_{q_1} d\Pi_q d\Pi_{\bar{q}} d\Pi_{q_2} (2\pi)^D \delta^D(p_1 + p_2 - \sum_f q_f), \tag{B.3}$$

$$d\Pi_{p_i} = \frac{d^d p_i}{(2\pi)^d\ 2E_{p_i}}. \tag{B.4}$$

Now let us introduce some identities, where we define Q_1, Q_2 as the children cluster momenta and M_1, M_2 as their masses:

$$\int d^D Q_1 \delta^D(Q_1 - q_1 - q) = 1, \quad \int dM_1^2 \delta(Q_1^2 - M_1^2) = 1,$$
$$\int d^D Q_2 \delta^D(Q_2 - q_2 - \bar{q}) = 1, \quad \int dM_2^2 \delta(Q_2^2 - M_2^2) = 1.$$

Now we can reorder equation (B.1) with the above identities and use the Mass delta functions to perform the integral of Q_i^0, obtaining the following:

$$\begin{aligned}\int dM_1^2 dM_2^2 |\mathcal{M}_{2\to4}|^2 \delta^D(p_1 + p_2 - Q_1 - Q_2)\frac{d^d Q_1}{2E_{Q_1}}\frac{d^d Q_2}{2E_{Q_2}} \\ \times \delta^D(Q_1 - q_1 - q)\frac{d^d q_1}{2E_1}\frac{d^d q}{2E_q} \\ \times \delta^D(Q_2 - q_2 - \bar{q})\frac{d^d \bar{q}}{2E_{\bar{q}}}\frac{d^d q_2}{2E_2},\end{aligned} \tag{B.5}$$

$$d\Phi_2(P; q_1,\, q_2) = \delta^D(P - q_1 - q_2)\frac{d^d q_1}{2E_{q_1}}\frac{d^d q_2}{2E_{q_2}}. \tag{B.6}$$

We have now factorized the integration over 4-particle phase space Φ_4 into 3 two-particle phase spaces Φ_2 and two mass integrals:

$$\Gamma_{2\to4} = \int dM_1^2\, dM_2^2\, d\Phi_2(P; Q_1, Q_2)\, d\Phi_2(Q_1; q_1, q)\, d\Phi_2(Q_2; q_2, \bar{q})\, |\mathcal{M}_{2\to4}|^2. \tag{B.7}$$

Each of the two-particle phase spaces can be evaluated in its respective centre-of-mass frame in the following way, where we define the Källén function $\lambda(x, y, z)$ as the following:

$$\Phi_2(M, m_1, m_2) = \int \frac{d\Omega_{d-1}^{\mathrm{COM}}}{4M} \left(\frac{\sqrt{\lambda(M^2, m_1^2, m_2^2)}}{2M} \right)^{d-2}, \tag{B.8}$$

$$\lambda(M^2, m_1^2, m_2^2) = \left[M^2 - (m_1 - m_2)^2\right] \left[M^2 - (m_1 + m_2)^2\right]. \tag{B.9}$$

As we aim to sample the masses M_1, M_2 later, we collect all mass dependent factors such that we get the following:

$$\Gamma_{2\to4} = \int dM_1 dM_2 f_{\mathrm{PS}}(M_1, M_2) d\Omega_{d-1}^{\mathrm{COM}} d\Omega_{d-1}^{\mathrm{COM},1} d\Omega_{d-1}^{\mathrm{COM},2} |\mathcal{M}_{2\to4}|^2, \tag{B.10}$$

$$f(M_1, M_2) = \frac{1}{256M} \left(\frac{\sqrt{\lambda(M^2, M_1^2, M_2^2)\lambda(M_1^2, m_1^2, m_q^2)\lambda(M_2^2, m_2^2, m_q^2)}}{8MM_1M_2} \right)^{d-2}. \tag{B.11}$$

We can compute an overestimate for the flat phase space mass distribution $f(M_1, M_2)$ if we assume $d > 2$, which yields:

$$f(M_1, M_2) = \frac{M^{d-3}}{256 \cdot 8^{(d-2)}} \tilde{f}(M_1, M_2), \tag{B.12}$$

$$\tilde{f}(M_1, M_2) \leq (M_1 M_2)^{(d-2)} \left[\lambda \left(1, \frac{M_1^2}{M^2}, \frac{M_2^2}{M^2} \right) \right]^{\frac{(d-2)}{2}}. \tag{B.13}$$

Here we used the fact that $\lambda(x^2, y^2, z^2) \leq \lambda(x^2, 0, 0)$. Now we can use the following transformation and use the fact that $(M_1 - M_2)^2 \geq 0$:

$$M_\pm = M_1 \pm M_2, \tag{B.14}$$

$$M_{1/2} = \frac{M_+ \pm M_-}{2}, \tag{B.15}$$

$$\tilde{f}(M_1, M_2) \leq \left(\frac{M_+^2 - M_-^2}{4} \right)^{(d-2)} \left[\left(1 - \frac{M_-^2}{M^2} \right) \left(1 - \frac{M_+^2}{M^2} \right) \right]^{\frac{(d-2)}{2}}, \tag{B.16}$$

$$\leq \left[\left(\frac{M_+^2}{4} \right) \sqrt{1 - \frac{M_+^2}{M^2}} \right]^{(d-2)} = g(M_+), \tag{B.17}$$

$$\leq \left[\frac{M^2}{6\sqrt{3}} \right]^{(d-2)}. \tag{B.18}$$

Here in the last inequality we find analytically the maximum of the function $g(M_+)$, which is located at $M_+ = M\sqrt{\frac{2}{3}}$, which is the more efficient overestimate.

Acknowledgements (Danksagungen)

Zu Beginn möchte ich meinem Doktorvater, PD Dr. Stefan Gieseke, meinen aufrichtigen Dank aussprechen, da er mir die Möglichkeit gegeben hat diese Doktorarbeit zu verfassen und mich stets optimistisch und geduldig begleitet hat.

Zusätzlich möchte ich mich bei Prof. Dr. Gudrun Heinrich bedanken für die Übernahme der Rolle der Korreferentin und das kurzfristige Korrekturlesen.

Ein großes Dankeschön an Dr. Simon Plätzer, der mir die Möglichkeit geboten hat eine Zeit lang in Graz zu forschen um an interessanten Themen arbeiten zu können.

Außerdem bin ich dem "KHYS research travel grant" zu Dank verpflichtet, der meinen Aufenthalt in Graz finanziert hat.

Ich möchte mich ganz herzlich bei meiner Familie und meinen Freunden bedanken für die jahrelange Unterstützung und das Vertrauen in meine Fähigkeiten auch wenn ich selbst oft daran gezweifelt hatte.

Vorrei ringraziare Juline per avermi supportato durante questo lungo viaggio, anche se a volte è stato difficile.

I am deeply grateful to the Herwig and MCnet members for the fruitful often late-night discussions, which have furthered my understanding and stimulated my creativity.

A special thanks to Cody Duncan for helping me a lot in the beginning and for the interesting discussions about physics and computing.

I am immensely grateful to all ITP members for the friendly work environment and the time spent together. In particular, I would like to thank Anton Olsson, Christoph Borschensky and Sauro Carlotti for proofreading my English, German and Italian respectively on very short notice.

Furthermore, I would like to thank all of the ITP and TTP admins for solving all issues very swiftly.

I would like to express my gratitude to KSETA for providing a hospital and prosperous environment for discussions beyond my field of research.

At last, I want to thank good music, Italian coffee and delicious food for making this Ph.D. journey less dire.

References

[1] J. Bellm, S. Gieseke, D. Grellscheid, S. Plätzer, M. Rauch, C. Reuschle, P. Richardson, P. Schichtel, M. H. Seymour, A. Siódmok, A. Wilcock, N. Fischer, M. A. Harrendorf, G. Nail, A. Papaefstathiou, and D. Rauch, "Herwig 7.0/herwig++ 3.0 release note," The European Physical Journal C **76** no. 4, (Apr., 2016) . http://dx.doi.org/10.1140/epjc/s10052-016-4018-8.

[2] M. Bahr et al., "Herwig++ Physics and Manual," Eur. Phys. J. C **58** (2008) 639–707, arXiv:0803.0883 [hep-ph].

[3] C. Bierlich, S. Chakraborty, N. Desai, L. Gellersen, I. Helenius, P. Ilten, L. Lönnblad, S. Mrenna, S. Prestel, C. T. Preuss, T. Sjöstrand, P. Skands, M. Utheim, and R. Verheyen, "A comprehensive guide to the physics and usage of PYTHIA 8.3," SciPost Phys. Codebases (2022) 8. https://scipost.org/10.21468/SciPostPhysCodeb.8.

[4] **Sherpa** Collaboration, E. Bothmann et al., "Event Generation with Sherpa 2.2," SciPost Phys. **7** no. 3, (2019) 034, arXiv:1905.09127 [hep-ph].

[5] **ATLAS** Collaboration, "Measurement of the top-quark mass in $t\bar{t} \to$ dilepton events with the ATLAS experiment using the template method in 13 TeV pp collision data,".

[6] J. Andersen et al., "Les Houches 2023: Physics at TeV Colliders: Standard Model Working Group Report," in Physics of the TeV Scale and Beyond the Standard Model: Intensifying the Quest for New Physics. 6, 2024. arXiv:2406.00708 [hep-ph].

[7] S. Plätzer, "Colour evolution and infrared physics," JHEP **07** (2023) 126, arXiv:2204.06956 [hep-ph].

[8] S. Gieseke, P. Kirchgaeßer, S. Plätzer, and A. Siodmok, "Colour Reconnection from Soft Gluon Evolution," JHEP **11** (2018) 149, arXiv:1808.06770 [hep-ph].

[9] **Particle Data Group** Collaboration, S. Navas et al., "Review of particle physics," Phys. Rev. D **110** no. 3, (2024) 030001.

[10] G. 't Hooft, "A Planar Diagram Theory for Strong Interactions," Nucl. Phys. B **72** (1974) 461.

[11] R. K. Ellis, W. J. Stirling, and B. R. Webber, QCD and Collider Physics. Cambridge Monographs on Particle Physics, Nuclear Physics and Cosmology. Cambridge University Press, 1996.

[12] M. E. Peskin and D. V. Schroeder, An Introduction to Quantum Field Theory. Westview Press, 1995. Reading, USA: Addison-Wesley (1995) 842 p.

[13] M. D. Schwartz, Quantum Field Theory and the Standard Model. Cambridge University Press, 3, 2014.

[14] T. van Ritbergen, J. A. M. Vermaseren, and S. A. Larin, "The Four loop beta function in quantum chromodynamics," Phys. Lett. B **400** (1997) 379–384, arXiv:hep-ph/9701390.

[15] T. Carli, K. Rabbertz, and S. Schumann, Studies of Quantum Chromodynamics at the LHC, pp. 139–194. 2015. arXiv:1506.03239 [hep-ex].

[16] R. Gupta, "Introduction to lattice qcd," 1998. https://arxiv.org/abs/hep-lat/9807028.

[17] A. Buckley et al., "General-purpose event generators for LHC physics," Phys. Rept. **504** (2011) 145–233, arXiv:1101.2599 [hep-ph].

[18] R. D. Field, Applications of Perturbative QCD, vol. 77. 1989.

[19] T. Kinoshita, "Mass singularities of Feynman amplitudes," J. Math. Phys. **3** (1962) 650–677.

[20] T. D. Lee and M. Nauenberg, "Degenerate systems and mass singularities," Phys. Rev. **133** (Mar, 1964) B1549–B1562. https://link.aps.org/doi/10.1103/PhysRev.133.B1549.

[21] M. Cacciari, G. P. Salam, and G. Soyez, "FastJet User Manual," Eur. Phys. J. C **72** (2012) 1896, arXiv:1111.6097 [hep-ph].

[22] M. Cacciari, G. P. Salam, and G. Soyez, FastJet User Manual 3.4.3, 2012. https://fastjet.fr/repo/fastjet-doc-3.4.3.pdf.

[23] D. Bertolini, T. Chan, and J. Thaler, "Jet observables without jet algorithms," Journal of High Energy Physics **2014** no. 4, (Apr., 2014) . http://dx.doi.org/10.1007/JHEP04(2014)013.

[24] A. J. Larkoski, D. Neill, and J. Thaler, "Jet shapes with the broadening axis," Journal of High Energy Physics **2014** no. 4, (Apr., 2014) . http://dx.doi.org/10.1007/JHEP04(2014)017.

[25] **JADE** Collaboration, W. Bartel et al., "Experimental Studies on Multi-Jet Production in e+ e- Annihilation at PETRA Energies," Z. Phys. C **33** (1986) 23.

[26] S. Catani, Y. L. Dokshitzer, M. Olsson, G. Turnock, and B. R. Webber, "New clustering algorithm for multi - jet cross-sections in e+ e- annihilation," Phys. Lett. B **269** (1991) 432–438.

[27] S. D. Ellis and D. E. Soper, "Successive combination jet algorithm for hadron collisions," Phys. Rev. D **48** (1993) 3160–3166, arXiv:hep-ph/9305266.

[28] S. Catani, Y. L. Dokshitzer, M. H. Seymour, and B. R. Webber, "Longitudinally invariant K_t clustering algorithms for hadron hadron collisions," Nucl. Phys. B **406** (1993) 187–224.

[29] M. Cacciari, G. P. Salam, and G. Soyez, "The anti-k_t jet clustering algorithm," JHEP **04** (2008) 063, arXiv:0802.1189 [hep-ph].

[30] Y. L. Dokshitzer, G. D. Leder, S. Moretti, and B. R. Webber, "Better jet clustering algorithms," JHEP **08** (1997) 001, arXiv:hep-ph/9707323.

[31] M. Wobisch and T. Wengler, "Hadronization corrections to jet cross-sections in deep inelastic scattering," in Workshop on Monte Carlo Generators for HERA Physics (Plenary Starting Meeting), pp. 270–279. 4, 1998. arXiv:hep-ph/9907280.

[32] J. C. Collins, D. E. Soper, and G. Sterman, "Factorization of hard processes in qcd," 2004. https://arxiv.org/abs/hep-ph/0409313.

[33] V. M. Braun, "Higher Twists," EPJ Web Conf. **274** (2022) 01012, arXiv:2212.02887 [hep-ph].

[34] T. Becher and T. Neumann, "Fiducial q_T resummation of color-singlet processes at $N^3LL+NNLO$," JHEP **03** (2021) 199, arXiv:2009.11437 [hep-ph].

[35] T. Neumann and J. Campbell, "Fiducial Drell-Yan production at the LHC improved by transverse-momentum resummation at N4LLp+N3LO," Phys. Rev. D **107** no. 1, (2023) L011506, arXiv:2207.07056 [hep-ph].

[36] M. De Angelis, J. R. Forshaw, and S. Plätzer, "Resummation and Simulation of Soft Gluon Effects beyond Leading Color," Phys. Rev. Lett. **126** no. 11, (2021) 112001, arXiv:2007.09648 [hep-ph].

[37] F. Maltoni, K. Paul, T. Stelzer, and S. Willenbrock, "Color Flow Decomposition of QCD Amplitudes," Phys. Rev. D **67** (2003) 014026, arXiv:hep-ph/0209271.

[38] M. De Angelis, QCD Evolution At Amplitude Level. PhD thesis, University of Manchester, 2021. https://users.hep.manchester.ac.uk/u/forshaw/Thesis-DeAngelis-Final-Corrected-Submitted.pdf.

[39] K. Werner, B. Guiot, I. Karpenko, and T. Pierog, "Analysing radial flow features in p-Pb and p-p collisions at several TeV by studying identified particle production in EPOS3," Phys. Rev. C **89** no. 6, (2014) 064903, arXiv:1312.1233 [nucl-th].

[40] T. Pierog, I. Karpenko, J. M. Katzy, E. Yatsenko, and K. Werner, "Epos lhc: Test of collective hadronization with data measured at the cern large hadron collider," Physical Review C **92** no. 3, (Sept., 2015) . http://dx.doi.org/10.1103/PhysRevC.92.034906.

[41] W. Kilian, T. Ohl, and J. Reuter, "WHIZARD: Simulating Multi-Particle Processes at LHC and ILC," Eur. Phys. J. C **71** (2011) 1742, arXiv:0708.4233 [hep-ph].

[42] L. Lonnblad, "THEPEG: Toolkit for High Energy Physics event generation," in HERA and the LHC: 4th Workshop on the Implications of HERA for LHC Physics, pp. 733–736. 3, 2009.

[43] L. Lonnblad, "Development strategies for PYTHIA version 7," Comput. Phys. Commun. **118** (1999) 213–228, arXiv:hep-ph/9810208.

[44] G. Bewick et al., "Herwig 7.3 Release Note," arXiv:2312.05175 [hep-ph].

[45] J. R. Forshaw, M. H. Seymour, and A. Siódmok, "On the breaking of collinear factorization in qcd," Journal of High Energy Physics **2012** no. 11, (Nov., 2012) . http://dx.doi.org/10.1007/JHEP11(2012)066.

[46] S. Catani and M. Seymour, "A general algorithm for calculating jet cross sections in nlo qcd," Nuclear Physics B **485** no. 1–2, (Feb., 1997) 291–419. http://dx.doi.org/10.1016/S0550-3213(96)00589-5.

[47] **GEANT4** Collaboration, S. Agostinelli et al., "GEANT4–a simulation toolkit," Nucl. Instrum. Meth. A **506** (2003) 250–303.

[48] J. Alwall, M. Herquet, F. Maltoni, O. Mattelaer, and T. Stelzer, "Madgraph 5: going beyond," Journal of High Energy Physics **2011** no. 6, (June, 2011) . http://dx.doi.org/10.1007/JHEP06(2011)128.

[49] F. Buccioni, J.-N. Lang, J. M. Lindert, P. Maierhöfer, S. Pozzorini, H. Zhang, and M. F. Zoller, "OpenLoops 2," Eur. Phys. J. C **79** no. 10, (2019) 866, arXiv:1907.13071 [hep-ph].

[50] **GoSam** Collaboration, G. Cullen et al., "G*OSAM*-2.0: a tool for automated one-loop calculations within the Standard Model and beyond," Eur. Phys. J. C **74** no. 8, (2014) 3001, arXiv:1404.7096 [hep-ph].

[51] S. Badger, B. Biedermann, P. Uwer, and V. Yundin, "Numerical evaluation of virtual corrections to multi-jet production in massless qcd," Computer Physics Communications **184** no. 8, (Aug., 2013) 1981–1998. http://dx.doi.org/10.1016/j.cpc.2013.03.018.

[52] K. Arnold, M. Bähr, G. Bozzi, F. Campanario, C. Englert, T. Figy, N. Greiner, C. Hackstein, V. Hankele, B. Jäger, G. Klämke, M. Kubocz, C. Oleari, S. Plätzer, S. Prestel, M. Worek, and D. Zeppenfeld, "Vbfnlo: A parton level monte carlo for processes with electroweak bosons," Computer Physics Communications **180** no. 9, (Sept., 2009) 1661–1670. http://dx.doi.org/10.1016/j.cpc.2009.03.006.

[53] J. Baglio, F. Campanario, T. Chen, H. Dietrich-Siebert, T. Figy, M. Kerner, M. Kubocz, L. D. Ninh, M. Löschner, S. Plätzer, M. Rauch, I. Rosario, R. Roth, and D. Zeppenfeld, "Vbfnlo: A parton level monte carlo for processes with electroweak bosons – manual for version 3.0," 2024. https://arxiv.org/abs/1107.4038.

[54] J. Baglio et al., "Release Note – VBFNLO 3.0," arXiv:2405.06990 [hep-ph].

[55] G. Altarelli and G. Parisi, "Asymptotic freedom in parton language," Nuclear Physics B **126** no. 2, (1977) 298–318. https://www.sciencedirect.com/science/article/pii/0550321377903844.

[56] S. Catani, S. Dittmaier, and Z. Trócsányi, "One-loop singular behaviour of qcd and susy qcd amplitudes with massive partons," Physics Letters B **500** no. 1–2, (Feb., 2001) 149–160. http://dx.doi.org/10.1016/S0370-2693(01)00065-X.

[57] V. V. Sudakov, "Vertex parts at very high-energies in quantum electrodynamics," Sov. Phys. JETP **3** (1956) 65–71.

[58] S. Catani, B. R. Webber, and G. Marchesini, "QCD coherent branching and semiinclusive processes at large x," Nucl. Phys. B **349** (1991) 635–654.

[59] S. Gieseke, P. Stephens, and B. Webber, "New formalism for qcd parton showers," Journal of High Energy Physics **2003** no. 12, (Dec., 2003) 045–045. http://dx.doi.org/10.1088/1126-6708/2003/12/045.

[60] G. Marchesini and B. R. Webber, "Simulation of QCD Jets Including Soft Gluon Interference," Nucl. Phys. B **238** (1984) 1–29.

[61] G. Marchesini and B. R. Webber, "Monte Carlo Simulation of General Hard Processes with Coherent QCD Radiation," Nucl. Phys. B **310** (1988) 461–526.

[62] S. Plätzer and S. Gieseke, "Coherent parton showers with local recoils," Journal of High Energy Physics **2011** no. 1, (Jan., 2011) . http://dx.doi.org/10.1007/JHEP01(2011)024.

[63] S. Schumann and F. Krauss, "A parton shower algorithm based on catani-seymour dipole factorisation," Journal of High Energy Physics **2008** no. 03, (Mar., 2008) 038–038. http://dx.doi.org/10.1088/1126-6708/2008/03/038.

[64] S. Höche, F. Krauss, and D. Reichelt, "The alaric parton shower for hadron colliders," 2024. https://arxiv.org/abs/2404.14360.

[65] S. Höche and S. Prestel, "The midpoint between dipole and parton showers," The European Physical Journal C **75** no. 9, (Sept., 2015) . http://dx.doi.org/10.1140/epjc/s10052-015-3684-2.

[66] H. Brooks, C. T. Preuss, and P. Skands, "Sector showers for hadron collisions," Journal of High Energy Physics **2020** no. 7, (July, 2020) . http://dx.doi.org/10.1007/JHEP07(2020)032.

[67] M. van Beekveld et al., "Introduction to the PanScales framework, version 0.1," arXiv:2312.13275 [hep-ph].

[68] S. Plätzer and M. Sjödahl, "Subleading nc improved parton showers," Journal of High Energy Physics **2012** no. 7, (July, 2012) . http://dx.doi.org/10.1007/JHEP07(2012)042.

[69] S. Plätzer, "Amplitude and colour evolution," SciPost Phys. Proc. **15** (2024) 007, arXiv:2210.09178 [hep-ph].

[70] Z. Nagy and D. E. Soper, "Effects of subleading color in a parton shower," 2015. https://arxiv.org/abs/1501.00778.

[71] Z. Nagy and D. E. Soper, "Effects of subleading color in a parton shower," JHEP **07** (2015) 119, arXiv:1501.00778 [hep-ph].

[72] D. Amati and G. Veneziano, "Preconfinement as a Property of Perturbative QCD," Phys. Lett. B **83** (1979) 87–92.

[73] P. Richardson and S. Webster, "Spin Correlations in Parton Shower Simulations," Eur. Phys. J. C **80** no. 2, (2020) 83, arXiv:1807.01955 [hep-ph].

[74] M. Dasgupta, F. A. Dreyer, K. Hamilton, P. F. Monni, G. P. Salam, and G. Soyez, "Parton showers beyond leading logarithmic accuracy," Phys. Rev. Lett. **125** no. 5, (2020) 052002, arXiv:2002.11114 [hep-ph].

[75] J. Bellm, "Colour rearrangement for dipole showers," The European Physical Journal C **78** no. 7, (July, 2018) . http://dx.doi.org/10.1140/epjc/s10052-018-6070-z.

[76] J. Isaacson and S. Prestel, "Stochastically sampling color configurations," Physical Review D **99** no. 1, (Jan., 2019) . http://dx.doi.org/10.1103/PhysRevD.99.014021.

[77] S. Dulat, T.-J. Hou, J. Gao, M. Guzzi, J. Huston, P. Nadolsky, J. Pumplin, C. Schmidt, D. Stump, and C.-P. Yuan, "New parton distribution functions from a global analysis of quantum chromodynamics," Physical Review D **93** no. 3, (Feb., 2016) . http://dx.doi.org/10.1103/PhysRevD.93.033006.

[78] A. Buckley, J. Ferrando, S. Lloyd, K. Nordström, B. Page, M. Rüfenacht, M. Schönherr, and G. Watt, "LHAPDF6: parton density access in the LHC precision era," Eur. Phys. J. C **75** (2015) 132, arXiv:1412.7420 [hep-ph].

[79] E. A. Kuraev, L. N. Lipatov, and V. S. Fadin, "The Pomeranchuk Singularity in Nonabelian Gauge Theories," Sov. Phys. JETP **45** (1977) 199–204.

[80] M. Bengtsson and T. Sjöstrand, "Coherent parton showers versus matrix elements - implications of petra/pep data," Physics Letters B **185** no. 3, (1987) 435–440. https://www.sciencedirect.com/science/article/pii/0370269387910318.

[81] S. Frixione and B. R. Webber, "Matching nlo qcd computations and parton shower simulations," Journal of High Energy Physics **2002** no. 06, (June, 2002) 029–029. http://dx.doi.org/10.1088/1126-6708/2002/06/029.

[82] S. Frixione and B. R. Webber, "The mc@nlo 3.3 event generator," 2006. https://arxiv.org/abs/hep-ph/0612272.

[83] P. Nason, "A new method for combining nlo qcd with shower monte carlo algorithms," Journal of High Energy Physics **2004** no. 11, (Nov., 2004) 040–040. http://dx.doi.org/10.1088/1126-6708/2004/11/040.

[84] S. Catani, F. Krauss, B. R. Webber, and R. Kuhn, "Qcd matrix elements + parton showers," Journal of High Energy Physics **2001** no. 11, (Nov., 2001) 063–063. http://dx.doi.org/10.1088/1126-6708/2001/11/063.

[85] L. Lönnblad, "Correcting the colour-dipole cascade model with fixed order matrix elements," Journal of High Energy Physics **2002** no. 05, (May, 2002) 046–046. http://dx.doi.org/10.1088/1126-6708/2002/05/046.

[86] S. Platzer and S. Gieseke, "Dipole Showers and Automated NLO Matching in Herwig++," Eur. Phys. J. C **72** (2012) 2187, arXiv:1109.6256 [hep-ph].

[87] J. Bellm, S. Gieseke, and S. Plätzer, "Merging NLO Multi-jet Calculations with Improved Unitarization," Eur. Phys. J. C **78** no. 3, (2018) 244, arXiv:1705.06700 [hep-ph].

[88] **Flavour Lattice Averaging Group** Collaboration, S. Aoki et al., "FLAG Review 2019: Flavour Lattice Averaging Group (FLAG)," Eur. Phys. J. C **80** no. 2, (2020) 113, arXiv:1902.08191 [hep-lat].

[89] B. Andersson, G. Gustafson, G. Ingelman, and T. Sjöstrand, "Parton fragmentation and string dynamics," Physics Reports **97** no. 2, (1983) 31–145. https://www.sciencedirect.com/science/article/pii/0370157383900807.

[90] B. Webber, "A qcd model for jet fragmentation including soft gluon interference," Nuclear Physics B **238** no. 3, (1984) 492–528. https://www.sciencedirect.com/science/article/pii/055032138490333X.

[91] E. Eichten, K. Gottfried, T. Kinoshita, J. Kogut, K. D. Lane, and T. M. Yan, "Spectrum of charmed quark-antiquark bound states," Phys. Rev. Lett. **34** (Feb, 1975) 369–372. https://link.aps.org/doi/10.1103/PhysRevLett.34.369.

[92] A. Bassetto, M. Ciafaloni, and G. Marchesini, "Color singlet distributions and mass damping in perturbative qcd," Physics Letters B **83** no. 2, (1979) 207–212. https://www.sciencedirect.com/science/article/pii/0370269379906877.

[93] G. S. Chahal and F. Krauss, "Cluster Hadronisation in Sherpa," SciPost Phys. **13** no. 2, (2022) 019, arXiv:2203.11385 [hep-ph].

[94] A. H. Hoang, O. L. Jin, S. Plätzer, and D. Samitz, "Matching Hadronization and Perturbative Evolution: The Cluster Model in Light of Infrared Shower Cutoff Dependence," arXiv:2404.09856 [hep-ph].

[95] J. Bellm et al., "Herwig 7.2 release note," Eur. Phys. J. C **80** no. 5, (2020) 452, arXiv:1912.06509 [hep-ph].

[96] Y. I. Azimov, Y. L. Dokshitzer, V. A. Khoze, and S. I. Troyan, "Similarity of Parton and Hadron Spectra in QCD Jets," Z. Phys. C **27** (1985) 65–72.

[97] A. Kupco, "Cluster hadronization in herwig 5.9," 1999. https://arxiv.org/abs/hep-ph/9906412.

[98] D. Grellscheid and P. Richardson, "Simulation of tau decays in the herwig++ event generator," 2007. https://arxiv.org/abs/0710.1951.

[99] P. Richardson, "Spin correlations in monte carlo simulations," Journal of High Energy Physics **2001** no. 11, (Nov., 2001) 029–029. http://dx.doi.org/10.1088/1126-6708/2001/11/029.

[100] I. Knowles, "A linear algorithm for calculating spin correlations in hadronic collisions," Computer Physics Communications **58** no. 3, (1990) 271–284. https://www.sciencedirect.com/science/article/pii/0010465590900637.

[101] I. Knowles, "Spin correlations in parton-parton scattering," Nuclear Physics B **310** no. 3, (1988) 571–588. https://www.sciencedirect.com/science/article/pii/0550321388900922.

[102] J. C. Collins, "Spin correlations in monte carlo event generators," Nuclear Physics B **304** (1988) 794–804. https://www.sciencedirect.com/science/article/pii/0550321388906542.

[103] M. R. Masouminia and P. Richardson, "Hadronization and decay of excited heavy hadrons in Herwig 7," JHEP **07** (2024) 278, arXiv:2312.02757 [hep-ph].

[104] D. J. Lange, "The EvtGen particle decay simulation package," Nucl. Instrum. Meth. A **462** (2001) 152–155.

[105] **Particle Data Group** Collaboration, T. P. collaboration, "Review of particle physics," Phys. Rev. D **98** (Aug, 2018) 030001. https://link.aps.org/doi/10.1103/PhysRevD.98.030001.

[106] **ATLAS** Collaboration, G. Aad et al., "Rapidity gap cross sections measured with the ATLAS detector in pp collisions at $\sqrt{s} = 7$ TeV," Eur. Phys. J. C **72** (2012) 1926, arXiv:1201.2808 [hep-ex].

[107] S. Gieseke, F. Loshaj, and P. Kirchgaeßer, "Soft and diffractive scattering with the cluster model in Herwig," Eur. Phys. J. C **77** no. 3, (2017) 156, arXiv:1612.04701 [hep-ph].

[108] V. B. Berestetsky and I. Y. Pomeranchuk, "On the asymptotic behaviour of cross sections at high energies," Nucl. Phys. **22** (1961) 629–639.

[109] S. Gieseke, F. Loshaj, and M. Myska, "Towards diffraction in herwig," 2016. https://arxiv.org/abs/1602.04690.

[110] V. Barone and E. Predazzi, High-Energy Particle Diffraction, vol. v.565 of Texts and Monographs in Physics. Springer-Verlag, Berlin Heidelberg, 2002.

[111] T. A. collaboration, "Measurement of inelastic, single- and double-diffraction cross sections in proton–proton collisions at the lhc with alice," The European Physical Journal C **73** no. 6, (June, 2013) . http://dx.doi.org/10.1140/epjc/s10052-013-2456-0.

[112] T. Regge, "Introduction to complex orbital momenta," Nuovo Cim. **14** (1959) 951.

[113] M. Baker and K. A. Ter-Martirosian, "Gribov's Reggeon Calculus: Its Physical Basis and Implications," Phys. Rept. **28** (1976) 1–143.

[114] J. Campbell, J. Huston, and F. Krauss, The Black Book of Quantum Chromodynamics : a Primer for the LHC Era. Oxford University Press, 2018.

[115] A. Donnachie and P. Landshoff, "Total cross sections," Physics Letters B **296** no. 1–2, (Dec., 1992) 227–232. http://dx.doi.org/10.1016/0370-2693(92)90832-O.

[116] M. Bähr, Underlying Event Simulation in the Herwig++ Event Generator. PhD thesis, Karlsruhe U., 2008. https://www.itp.kit.edu/prep/phd/PSFiles/Diss_Baehr.pdf.

[117] P. Kirchgaeßer, Non-perturbative Models for the Simulation of Hadronic Collisions at the LHC. PhD thesis, KIT, Karlsruhe, 2020.

[118] M. Bahr, S. Gieseke, and M. H. Seymour, "Simulation of multiple partonic interactions in Herwig++," JHEP **07** (2008) 076, arXiv:0803.3633 [hep-ph].

[119] I. Borozan and M. H. Seymour, "An Eikonal model for multiparticle production in hadron hadron interactions," JHEP **09** (2002) 015, arXiv:hep-ph/0207283.

[120] J. M. Butterworth, J. R. Forshaw, and M. H. Seymour, "Multiparton interactions in photoproduction at HERA," Z. Phys. C **72** (1996) 637–646, arXiv:hep-ph/9601371.

[121] D. Amati, A. Stanghellini, and S. Fubini, "Theory of high-energy scattering and multiple production," Nuovo Cim. **26** (1962) 896–954.

[122] S. Gieseke, C. Röhr, and A. Siódmok, "Colour reconnections in herwig++," The European Physical Journal C **72** no. 11, (Nov., 2012) . http://dx.doi.org/10.1140/epjc/s10052-012-2225-5.

[123] S. Gieseke, P. Kirchgaeßer, and S. Plätzer, "Baryon production from cluster hadronisation," Eur. Phys. J. C **78** no. 2, (2018) 99, arXiv:1710.10906 [hep-ph].

[124] R. Zimmermann, "Aspects of Hadron Production in Herwig," 2021. https://www.itp.kit.edu/_media/publications/Masterthesis_Ronja_Zimmermann.pdf.

[125] J. Bellm, C. B. Duncan, S. Gieseke, M. Myska, and A. Siódmok, "Spacetime colour reconnection in herwig 7," The European Physical Journal C **79** no. 12, (Dec., 2019) . http://dx.doi.org/10.1140/epjc/s10052-019-7533-6.

[126] S. Ferreres-Solé and T. Sjöstrand, "The space–time structure of hadronization in the lund model," The European Physical Journal C **78** no. 11, (Nov., 2018) . http://dx.doi.org/10.1140/epjc/s10052-018-6459-8.

[127] **ATLAS** Collaboration, G. Aad et al., "Charged-particle multiplicities in pp interactions measured with the ATLAS detector at the LHC," New J. Phys. **13** (2011) 053033, arXiv:1012.5104 [hep-ex].

[128] C. Bierlich et al., "Robust Independent Validation of Experiment and Theory: Rivet version 3," SciPost Phys. **8** (2020) 026, arXiv:1912.05451 [hep-ph].

[129] N. Metropolis, A. W. Rosenbluth, M. N. Rosenbluth, A. H. Teller, and E. Teller, "Equation of state calculations by fast computing machines," The Journal of Chemical Physics **21** no. 6, (1953) 1087–1092. http://link.aip.org/link/?JCP/21/1087/1.

[130] M. H. Seymour, "Matrix-element corrections to parton shower algorithms," Computer Physics Communications **90** no. 1, (Sept., 1995) 95–101. http://dx.doi.org/10.1016/0010-4655(95)00064-M.

[131] **ALICE** Collaboration, S. Acharya et al., "Investigations of Anisotropic Flow Using Multiparticle Azimuthal Correlations in pp, p-Pb, Xe-Xe, and Pb-Pb Collisions at the LHC," Phys. Rev. Lett. **123** no. 14, (2019) 142301, arXiv:1903.01790 [nucl-ex].

[132] **ATLAS** Collaboration, G. Aad et al., "Observation of Long-Range Elliptic Azimuthal Anisotropies in $\sqrt{s}$ =13 and 2.76 TeV pp Collisions with the ATLAS Detector," Phys. Rev. Lett. **116** no. 17, (2016) 172301, arXiv:1509.04776 [hep-ex].

[133] **ATLAS** Collaboration, "Measurements of long-range azimuthal anisotropies and associated Fourier coefficients in pp collisions at $\sqrt{s} = 5.02$ and 13 TeV and p+Pb collisions at $\sqrt{s_{\rm NN}} = 5.02$ TeV with the ATLAS detector,".

[134] **CMS** Collaboration, V. Khachatryan et al., "Evidence for collectivity in pp collisions at the LHC," Phys. Lett. B **765** (2017) 193–220, arXiv:1606.06198 [nucl-ex].

[135] Y.-C. Chen, Y.-J. Lee, Y. Chen, P. Chang, C. McGinn, T.-A. Sheng, G. M. Innocenti, and M. Maggi, "Analysis note: two-particle correlation in e^+e^- collisions at 91-209 GeV with archived ALEPH data," arXiv:2309.09874 [hep-ex].

[136] **Belle** Collaboration, Y. C. Chen et al., "Two-particle angular correlations in e^+e^- collisions to hadronic final states in two reference coordinates at Belle," JHEP **03** (2023) 171, arXiv:2206.09440 [hep-ex].

[137] **ALICE** Collaboration, J. Adam et al., "Insight into particle production mechanisms via angular correlations of identified particles in pp collisions at $\sqrt{s} = 7$ TeV," Eur. Phys. J. C **77** no. 8, (2017) 569, arXiv:1612.08975 [nucl-ex]. [Erratum: Eur.Phys.J.C 79, 998 (2019)].

[138] **ALICE** Collaboration, S. Acharya et al., "K_S^0- and (anti-)Λ-hadron correlations in pp collisions at $\sqrt{s} = 13$ TeV," Eur. Phys. J. C **81** no. 10, (2021) 945, arXiv:2107.11209 [nucl-ex].

[139] **ALICE** Collaboration, S. Acharya et al., "Studying strangeness and baryon production mechanisms through angular correlations between charged Ξ baryons and identified hadrons in pp collisions at $\sqrt{s} = 13$ TeV," arXiv:2308.16706 [hep-ex].

[140] D. Ruggiano, "Two-particle angular correlations of identified particles in pp and p–Pb collisions at LHC energies with ALICE," arXiv:2403.02549 [hep-ex].

[141] **ALICE** Collaboration, D. Ruggiano, "Two-particle angular correlations of identified particles in pp collisions at $\sqrt{s} = 13$ TeV with ALICE," arXiv:2311.09833 [nucl-ex].

[142] **ALICE** Collaboration, J. Adam et al., "Insight into particle production mechanisms via angular correlations of identified particles in pp collisions at $\sqrt{s} = 7$ TeV," Eur. Phys. J. C **77** no. 8, (2017) 569, arXiv:1612.08975 [nucl-ex]. [Erratum: Eur.Phys.J.C 79, 998 (2019)].

[143] M. A. Janik, "Studying baryon production using two-particle angular correlations," EPJ Web Conf. **235** (2020) 01004, arXiv:2307.04534 [hep-ex].

[144] **ALICE, ATLAS, CMS, LHCb, TOTEM** Collaboration, S. Todorova-Nova, "Soft QCD," in 5th Large Hadron Collider Physics Conference. 10, 2017. arXiv:1710.05681 [hep-ex].

[145] L. Lönnblad and H. Shah, "Baryon correlations in Pythia," Eur. Phys. J. C **83** no. 12, (2023) 1105, arXiv:2309.01557 [hep-ph].

[146] N. Demazure, V. G. Sebastián, and F. J. Llanes-Estrada, "Baryon Anticorrelations in PYTHIA," Few Body Syst. **64** no. 3, (2023) 57, arXiv:2210.02358 [hep-ph].

[147] **ATLAS** Collaboration, G. Aad et al., "Rapidity gap cross sections measured with the ATLAS detector in pp collisions at $\sqrt{s} = 7$ TeV," Eur. Phys. J. C **72** (2012) 1926, arXiv:1201.2808 [hep-ex].

[148] R. J. Fries, V. Greco, and P. Sorensen, "Coalescence Models For Hadron Formation From Quark Gluon Plasma," Ann. Rev. Nucl. Part. Sci. **58** (2008) 177–205, arXiv:0807.4939 [nucl-th].

[149] Z.-w. Lin and C. M. Ko, "Partonic effects on the elliptic flow at RHIC," Phys. Rev. C **65** (2002) 034904, arXiv:nucl-th/0108039.

[150] **CMS** Collaboration, V. Khachatryan et al., "Strange Particle Production in pp Collisions at $\sqrt{s} = 0.9$ and 7 TeV," JHEP **05** (2011) 064, arXiv:1102.4282 [hep-ex].

[151] **ALICE** Collaboration, J. Adam et al., "Measurement of pion, kaon and proton production in proton–proton collisions at $\sqrt{s} = 7$ TeV," Eur. Phys. J. C **75** no. 5, (2015) 226, arXiv:1504.00024 [nucl-ex].

[152] **ARGUS** Collaboration, H. Albrecht et al., "Results on Baryon anti-Baryon Correlations in e+ e- Annihilation," Z. Phys. C **43** (1989) 45.

[153] B. Andersson, G. Gustafson, and T. Sjostrand, "Baryon Production in Jet Fragmentation and Υ Decay," Phys. Scripta **32** (1985) 574.

[154] **ARGUS** Collaboration, H. Albrecht et al., "Hyperon Production in e^+e^- Annihilation at 10-GeV Center-of-mass Energy," Z. Phys. C **39** (1988) 177.

[155] **Belle** Collaboration, R. Seidl et al., "Invariant-mass and fractional-energy dependence of inclusive production of di-hadrons in e^+e^- annihilation at $\sqrt{s} = 10.58$ GeV," Phys. Rev. D **96** no. 3, (2017) 032005, arXiv:1706.08348 [hep-ex].

[156] S. Gieseke, S. Kiebacher, S. Plätzer, and J. Priedigkeit, 2025.

[157] S. Plätzer and I. Ruffa, "Towards Colour Flow Evolution at Two Loops," JHEP **06** (2021) 007, arXiv:2012.15215 [hep-ph].

[158] S. Catani and M. Grazzini, "Infrared factorization of tree level QCD amplitudes at the next-to-next-to-leading order and beyond," Nucl. Phys. B **570** (2000) 287–325, arXiv:hep-ph/9908523.

[159] A. van Hameren and C. G. Papadopoulos, "A Hierarchical phase space generator for QCD antenna structures," Eur. Phys. J. C **25** (2002) 563–574, arXiv:hep-ph/0204055.

[160] **DELPHI** Collaboration, P. Abreu et al., "Tuning and test of fragmentation models based on identified particles and precision event shape data," Z. Phys. C **73** (1996) 11–60.

[161] P. Gras, S. Höche, D. Kar, A. Larkoski, L. Lönnblad, S. Plätzer, A. Siódmok, P. Skands, G. Soyez, and J. Thaler, "Systematics of quark/gluon tagging," JHEP **07** (2017) 091, arXiv:1704.03878 [hep-ph].

[162] A. J. Larkoski, I. Moult, and D. Neill, "Toward Multi-Differential Cross Sections: Measuring Two Angularities on a Single Jet," JHEP **09** (2014) 046, arXiv:1401.4458 [hep-ph].

[163] K. Lee, A. Pathak, I. Stewart, and Z. Sun, "Nonperturbative Effects in Energy Correlators: From Characterizing Confinement Transition to Improving α_s Extraction," arXiv:2405.19396 [hep-ph].

[164] A. J. Larkoski, G. P. Salam, and J. Thaler, "Energy Correlation Functions for Jet Substructure," JHEP **06** (2013) 108, arXiv:1305.0007 [hep-ph].

[165] J. Holguin, I. Moult, A. Pathak, M. Procura, R. Schöfbeck, and D. Schwarz, "Top Quark Mass Extractions from Energy Correlators: A Feasibility Study," arXiv:2407.12900 [hep-ph].

[166] E. Witten, "Baryons in the 1/n Expansion," Nucl. Phys. B **160** (1979) 57–115.

[167] J. R. Christiansen and P. Z. Skands, "String formation beyond leading colour," Journal of High Energy Physics **2015** no. 8, (Aug., 2015) . http://dx.doi.org/10.1007/JHEP08(2015)003.

[168] J. Altmann and P. Skands, "String junctions revisited," JHEP **07** (2024) 238, arXiv:2404.12040 [hep-ph].

[169] S. Gieseke, S. Kiebacher, and S. Plätzer, 2025.

[170] P. Agarwal and J. Nahmgoong, "Singlets in the tensor product of an arbitrary number of Adjoint representations of SU(3)," arXiv:2001.10826 [math.RT].

[171] A. Zee, Group Theory in a Nutshell for Physicists. Princeton University Press, USA, 3, 2016.

[172] **LHCb** Collaboration, R. Aaij et al., "Observation of structure in the J/ψ -pair mass spectrum," Sci. Bull. **65** no. 23, (2020) 1983–1993, arXiv:2006.16957 [hep-ex].

[173] G. Eichmann, H. Sanchis-Alepuz, R. Williams, R. Alkofer, and C. S. Fischer, "Baryons as relativistic three-quark bound states," Prog. Part. Nucl. Phys. **91** (2016) 1–100, arXiv:1606.09602 [hep-ph].

[174] **ALICE** Collaboration, S. Acharya et al., "Multiplicity-dependent production of $\Sigma(1385)$ and $\Xi(1530)^0$ in pp collisions at $\sqrt{s} = 13$ TeV," JHEP **05** (2024) 317, arXiv:2308.16116 [nucl-ex].

[175] **ALICE** Collaboration, S. Acharya et al., "First observation of strange baryon enhancement with effective energy in pp collisions at the LHC," arXiv:2409.12702 [nucl-ex].

[176] **ALICE** Collaboration, S. Pucillo, "Insights on strange quark hadronization in small collision system with ALICE: Multiple strange hadrons and $\Sigma\pm$ baryons," EPJ Web Conf. **296** (2024) 15005, arXiv:2312.14892 [hep-ex].

[177] H. He, Y. Liu, and P. Zhuang, "Ω_{ccc} production in high energy nuclear collisions," Phys. Lett. B **746** (2015) 59–63, arXiv:1409.1009 [hep-ph].

[178] S. Cho and S. H. Lee, "Production of multicharmed hadrons by recombination in heavy ion collisions," Phys. Rev. C **101** no. 2, (2020) 024902, arXiv:1907.12786 [nucl-th].

[179] G. Yang, J. Ping, P. G. Ortega, and J. Segovia, "Triply heavy baryons in the constituent quark model *," Chinese Physics C **44** no. 2, (Feb, 2020) 023102. https://dx.doi.org/10.1088/1674-1137/44/2/023102.

[180] S. Plätzer, "Summing Large-N Towers in Colour Flow Evolution," Eur. Phys. J. C **74** no. 6, (2014) 2907, arXiv:1312.2448 [hep-ph].

[181] T. Becher and M. Neubert, "Infrared singularities of scattering amplitudes in perturbative QCD," Phys. Rev. Lett. **102** (2009) 162001, arXiv:0901.0722 [hep-ph]. [Erratum: Phys.Rev.Lett. 111, 199905 (2013)].

[182] O. Almelid, C. Duhr, E. Gardi, A. McLeod, and C. D. White, "Bootstrapping the QCD soft anomalous dimension," JHEP **09** (2017) 073, arXiv:1706.10162 [hep-ph].

[183] R. Ángeles Martínez, M. De Angelis, J. R. Forshaw, S. Plätzer, and M. H. Seymour, "Soft gluon evolution and non-global logarithms," JHEP **05** (2018) 044, arXiv:1802.08531 [hep-ph].

[184] M. Arioli, B. Codenotti, and C. Fassino, "The padé method for computing the matrix exponential," Linear Algebra and its Applications **240** (1996) 111–130. https://www.sciencedirect.com/science/article/pii/0024379594001901.